Brillouin Echoes for Advanced Distributed Sensing in Optical Fibres

THÈSE N^{O} 4958 (2011)

PRÉSENTÉE LE 11 MARS 2011

À LA FACULTÉ SCIENCES ET TECHNIQUES DE L'INGÉNIEUR
INSTITUT DE GÉNIE ÉLECTRIQUE ET ÉLECTRONIQUE
PROGRAMME DOCTORAL EN PHOTONIQUE

ÉCOLE POLYTECHNIQUE FÉDÉRALE DE LAUSANNE

POUR L'OBTENTION DU GRADE DE DOCTEUR ÈS SCIENCES

PAR

Stella FOALENG MAFANG

acceptée sur proposition du jury:

Prof. T. Kippenberg, président du jury
Prof. L. Thévenaz, directeur de thèse
Prof. M. Gonzalez-Herraez, rapporteur
Prof. C. Moser, rapporteur
Prof. M. Tur, rapporteur

ÉCOLE POLYTECHNIQUE
FÉDÉRALE DE LAUSANNE

Suisse
2011

To my father Pascal Foaleng

To my mother Monique Membouet Foaleng

To my niece Tonia Djuikoua Foaleng

Abstract

Brillouin scattering is particularly efficient and attractive for the implementation of strain and temperature distributed sensing in optical fibres. Recently a trend has been observed that modern advanced applications require a substantial step towards better spatial resolution, while preserving temperature/strain precision over a long range. For this purpose the state of the art does not satisfy all these requirements. In this thesis we present a radically new approach named Brillouin Echoes distributed sensing (BEDS) that allows covering these requirements.

In the first part, we propose an updated configuration of the classical existing Brillouin sensor for time domain analysis allowing drastic noise reduction. Then we investigate the limitations (due to non-linear effects) of the classical Brillouin sensor in terms of long distance range measurements. The identified nonlinear effects are pump depletion due to SBS itself, self-phase modulation (SPM), modulation instability (MI), which occurs only in fibres presenting an anomalous dispersion at the pump wavelength and Raman scattering (RS).

We propose the modeling of the pump depletion effect to obtain analytical expressions that are useful for the proper design of a BOTDA sensor and for the determination of a very small depletion. The model confirmed by experimental measurements is informative on the conditions maximizing the depletion effect; therefore a standard configuration can be defined to test the value of the depletion in the set-up.

Furthermore, we demonstrate that SPM-induced spectral broadening can have a significant effect on the measured effective gain linewidth. Modeling and experiments have undoubtedly demonstrated that the effective gain linewidth can easily experience a two-fold increase in standard conditions when the pulse intensity profile is Gaussian. We showed that the problem can be practically circumvented by using a clean rectangular pulse with very sharp rising and falling edges

The theoretical and experimental analysis of the undesirable effects of MI and forward RS in distributed BOTDA sensors systems gives a simplified expression to predict the critical power for a given distance range. MI turns out to be the dominant nonlinear limitation since it shows the lowest critical power, but it is less critical since it can be avoided to a wide extent by using the fibre in the normal dispersion spectral region such as a DSF in the C-band. On the other hand Raman scattering can be avoided only by limiting the optical pump power and therefore is the ultimate nonlinear limitation in a distributed sensing system. Under similar conditions RS shows a critical power ~5 times larger than MI.

In the second part, we present the new approach Brillouin echo distributed sensing (BEDS) which has proved to be a powerful solution to realize sub-metric spatial resolutions in Brillouin distributed measurements. We have demonstrated both theoretically and experimentally that an optimized configuration is reached when the optical wave is π-phase shifted. The experimental tests have shown a spatial resolution down to 5 cm, with a clear margin for further improvement down to a real centimetric spatial resolution. This optimized configuration produce the best contrast independently of the pulse intensity, with a factor 2 of

improvement compared to other techniques based on the same approach (dark pulse, bright pulse). This extends the dynamic range by 3 dB, which corresponds in standard loss conditions to a 5 km extension of the sensing range. An analytical developed model has proved to be an excellent tool not only for optimizing the pumping scheme but also in post-processing the measured data.

Finally the potentialities of BEDS technology provide solutions in real contexts. Using the BEDS technology in landslide monitoring at laboratory scale, for the first time it became possible to observe the failure propagation in laboratory scale with an accurate precision. Furthermore, using BEDS we have proposed and demonstrated the possibility of mapping geometrical structure fluctuations along a photonic crystal fibre (PCF). Both long- and short-scale longitudinal fluctuations in the Brillouin frequency shift have been identify and quantify. Observation of Brillouin linewidth broadening in PCF fibre through distributed measurement of the Brillouin gain spectrum using BEDS has allowed fundamental understanding of SBS in PCF fibre and in their design in view of applications to optical-strain/temperature sensing.

Keywords: Brillouin echoes, distributed fibre sensor, optical fibre sensors, stimulated Brillouin scattering, Fibre optics, Non-linear optics, stimulated Raman scattering, modulation instability, spatial resolution, pump depletion.

Version abregée

La diffusion Brillouin est particulièrement éfficace et attractive pour l'implementation de la distribution des contraintes et de la temperature dans les capteurs à fibres optiques. La tendance observée est que les nouvelles applications nécessitent une avancée importante vers une meilleure résolution spatiale, tout en préservant la précision sur la mesure de la température et de la contrainte sur de longues distances. A cet effet, l'état de l'art ne satisfait pas ces exigences. Dans cette thèse, nous présentons une approche radicalement nouvelle appelée « Brillouin Echoes distributed sensing (BEDS)» qui permet de couvrir ces besoins.

Dans la première partie de cette thèse, nous proposons une nouvelle configuration du capteur Brillouin classique permettant la réduction du bruit. Puis nous étudions les limites de ce même capteur en termes de mesures sur de longues portées. Les effets non-linéaires les plus critiques sont l'appauvrissement de la pompe par effet Brillouin, l'auto-modulation de phase (SPM), l'instabilité de modulation (MI), qui se produit uniquement dans les fibres présentant une dispersion anormale par rapport à la longueur d'onde de la pompe et la diffusion Raman (RS).

Nous proposons la modélisation de l'effet de l'appauvrissement de la pompe pour obtenir des expressions analytiques qui sont utiles pour la bonne conception d'un capteur Brillouin et pour la détermination d'un appauvrissement très faible. Ce modèle est confirmé par des mesures expérimentales.

En outre, nous démontrons que l'automodulaton de phase peut avoir un effet significatif sur la largeur de raie mesurée du gain Brillouin éffectif. La modélisation et les expériences ont incontestablement démontré que la largeur de raie du gain éffectif peut aisément faire l'expérience d'une augmentation de deux fois dans des conditions standards lorsque le profil d'intensité d'impulsion est Gaussien. Nous montrons qu'en pratique le problème peut être contourné en utilisant une impulsion rectangulaire.

Nous étudions également les effets indésirables de l'instabilité de modulation et la diffusion Raman en avant dans les capteurs Brillouin distribués. Ces deux effets sont préjudiciables et ont été évalués expérimentalement et comparés à un modèle théorique donnant une expression simplifiée pour prédire la puissance critique pour une portée donnée. L'instabilité de modulation se révèle être la limitation dominante car montrant la plus faible puissance critique. Ce pendant elle peut être évité en utilisant une fibre optique présentant une dispersion normale comme une fibre à dispersion décalé par exemple dans la bande C. D'autre part nous montrons que la diffusion Raman ne peut être évitée qu'en limitant la puissance de pompage optique et est donc la limitation ultime non linéaire dans un système de détection distribuée. Dans des conditions similaires la diffusion Raman affiche une puissance critique d'environ 5 fois plus grande que celle de l'instabilité de modulation.

Dans la deuxième partie de cette thèse, nous présentons une nouvelle approche appellée les echoes Brillouin (BEDS) qui s'est avéré être une solution puissante pour réaliser des résolutions spatiales sub-métrique dans les mesures Brillouin distribuées. Nous avons démontré à la fois théoriquement et

expérimentalement qu'une configuration optimisée est obtenue lorsque la phase de l'onde optique est déphasée de π. Les essais expérimentaux ont montré une résolution spatiale de 5 cm. Cette configuration optimisée permet de produire le meilleur contraste, indépendamment de l'intensité des impulsions, avec un facteur 2 d'amélioration par rapport aux autres techniques basées sur la même approche (impulsion sombre, impulsion lumineuse). Cela permet ainsi d'étendre la plage dynamique de 3 dB par conséquent d'étendre la plage de détection de 5 km. Un modèle analytique développé s'est avéré être un excellent outil non seulement pour optimiser le système de pompage, mais aussi pour le traitement des données mesurées.

Les potentialités de la technologie BEDS permet de fournir des solutions dans des contextes réels. Utilisation de la technologie dans la surveillance des glissements de terrain à l'échelle du laboratoire, pour la première fois, il a été possible d'observer la propagation progressive des glissemnts de terrain à l'échelle du laboratoire avec une précision exacte. En outre avec la technologie BEDS, nous avons proposé et démontré la possibilité de cartographier les fluctuations géométriques le long d'une fibre à cristaux photoniques (PCF). Deux fluctuations à long et à courte échelle longitudinale dans le décalage Brillouin ont été d'identifier et quantifier. En fin, l'observation de l'élargissement de la largeur de raie Brillouin d'une fibre à critaux photonique a mène à la compréhension fondamentale de la difussion Brillouin stimulée dans ces fibres spéciales en vue d'applications comme capteurs ditribués de température et de contrainte.

Mots-clés: échos Brillouin, capteurs distribués à fibre, capteurs à fibres optiques, diffusion Brillouin stimulée, Fibres optiques, optique non-linéaire, diffusion Raman stimulée, instabilité de modulation, résolution spatiale.

Acknowlegments

The realization of this thesis was a wonderful opportunity to meet and talk with many people. Here I would like to extend my heartfelt thanks to those who have helped me and contributed to the development of this dissertation and the success of these remarkable Ph.D years.

I owe many thanks to Professor Luc Thévenaz, my thesis advisor from whom I received invaluable comments, guidance, extraordinary support and scientific contribution during these four years of research. Luc gave me full confidence; he has always been supportive and provided me constructive criticism which oriented my work and allowed me to grow scientifically. I would also like to acknowledge his efforts on teaching me how to think and write scientifically. I would like to express all my gratitude to him, for his understanding and kindness during difficult times. It would not have been possible to write this thesis without his insights.

I would like to thank OMNISENS SA (Dr. Marc Niklès and Dr. Fabien Briffod) which was the pillar of the whole story, National Swiss Fund and European COST Action 299 "Fides" for their financial support.

My special thanks and sympathy go to Pr. Moshe Tur (in my humble opinion) from Tel-Aviv University in Israel, not only for being kind to serve as the external reader and be part of my Ph.D defence jury but also for his continuous encouragement, precious comments and scientific discussions during his visit to our group in spring 2009 and during the two weeks that I spend in Tel-Aviv in his laboratory in Winter 2009. I would like to thank Pr. Kwong-Yong Song from Chung-Ang University in South-Korea with whom I had interesting scientific discussions during his visit in our group in Summer 2009. I also thank Pr. Lie Jin from Bucknell University in USA with whom I also had fruitful discussions during her visit in our group in Summer 2010. I am also grateful to Pr. Miguel González-Herráez and Dr. Sonia Martin-Lopez for the fruitful discussions I had with them during the last year of my research.

My acknowledgments also go to the team of Geotechnical Institute at ETH in Zurich (Pr. Sasha Puzrin, Michael Iten and Dominik Hauswirth) for the invaluable collaboration in the BEDS in-situ campaign in 2008 and 2009 in Zurich. For the collaboration we had in the microstrutured optical fibres project, I also thank the team of ST-Femto laboratory at France-Compté University in France.

I also thank all jury members of my oral examination Pr. Tobias Kippenberg, Pr. Moshe Tur, Pr. Miguel González-Herráez and Pr. Christophe Moser for accepting to read and evaluate this work.

More recently, during the concluding stage of conclusion of my thesis, my special thanks go to Barbara Althaus and also Dr. Fabien Ravet for their precious language proof reading.

I warmly thank former colleagues of the group, namly Dario, Jean-Philippe, Mario and Jean-Charles (with whom I have collaborated more) and my present colleagues, namely Sang-Hoon, Nikolay and Isabelle (I enjoyed our frequent discussions between women in a men-dominant group) for scientific discuccions, I also enjoyed our launch time. I also thank the successive secretaries of the group; I name Pierrette, Luana

and Alexandra for their administrative assistance. I thank also the two technicians Fredo and Pascal for have always given the solutions to my technical problems.

Thoughts go also to a few friends (Davide, Gustave and Christian).

Finally, I wish to thank my family in Belgium, Cameroon, Canada, Italy, France, and Switzerland for encouraging me during the doctoral processs, in particular, Kounhawa Michel, Tuekam Lucien, Toussaint Guillaume, Kemayou Fernand, Ngani Jules, and Ngani Jeanne. My brothers and sisters Foaleng Nono Irene, Foaleng Mpako Hortence, Foaleng Manesse Eric, Foaleng Djuikoua Judith, Foaleng Tafe Raoul, Foaleng Fotue Nelly, and Foaleng Tela Babeth for the unconditional help, support, encouragements and interest since the beginning. A deep thought goes to my niece Tonia. Last - but not least at all Patrick for his lovely support and patience over this adventure. The last words are unavoidably reserved to my dear parents who have sustained me throughout immensely in too many ways to sum up; I thank them for their love and for giving me a precious education.

Table of contents

1 INTRODUCTION 1

1.1 How did this happen? 2
1.2 Fibre optics sensors 2
1.3 The problem 3
1.4 In this thesis 4
Bibliography 6

2 OPTICAL EFFECTS IN OPTICAL FIBRES 9

2.1 Linear scattering effects 10
2.1.1 Elastic scattering effects 11
2.1.1.1 Rayleigh and Rayleigh wing scattering 11
2.1.2 Inelastic spontaneous scattering effects 11
2.1.2.1 Spontaneous Raman scattering in optical fibres 13
2.1.2.2 Spontaneous Brillouin scattering in optical fibres 13
2.2 Non-linear effects 19
2.2.1 Non-linear scattering: stimulated Brillouin scattering in optical fibres 20
2.2.1.1 Electrostriction 20
2.2.1.2 Stimulated Brillouin scattering through electrostriction 21
2.2.1.3 Theoretical description of SBS 23
2.2.1.4 Solutions in steady state conditions and relation between phonons life time and Brillouin line-width 25
2.2.1.5 Solutions in steady state conditions in the un-depleted pump approximation 29
2.2.1.6 Brillouin critical power 30
2.2.1.7 Brillouin antistokes 32
2.2.2 Non-linear scattering: Stimulated Raman scattering in optical fibres 33
2.2.3 Non-linear effect: Kerr effect 34
2.2.3.1 Self-phase modulation (SPM) 35
2.2.3.2 Cross-phase modulation (XPM) 35
2.2.3.3 Parametric process: Modulation instability (MI) 35
2.2.3.4 Parametric process: Four-wave mixing (FWM) 36
Bibliography 37

3 DISTRIBUTED BRILLOUIN SENSORS AND THEIR LIMITATIONS 41

3.1 How distributed Brillouin sensor can sense temperature and strain 42
3.1.1 Principle 43

3.1.2 Parameter specifications....47
3.1.3 Advantages of distributed Brillouin fibre sensors....47
3.1.4 Polarization issue....48
3.2 Time-domain approach....52
3.2.1 Brillouin optical time-domain reflectometry (BOTDR)....52
3.2.2 Brillouin optical time-domain analysis (BOTDA)....52
3.3 Frequency-domain approach....56
3.3.1 Brillouin optical frequency-domain analysis (BOFDA)....56
3.4 Correlation-domain approach....57
3.4.1 Brillouin optical correlation-domain analysis (BOCDA)....57
3.5 Range limitations of distributed Brillouin sensor....59
3.5.1 Depletion due to Brillouin sensor....60
3.5.1.1 First order approximation in the presence of one sideband CW signal 61
3.5.1.2 Extension to 2nd order correction and generalization to the presence of two sidebands....63
3.5.1.3 Relations between depletion and error on the peak of Brillouin gain spectrum....68
3.5.1.4 Experimental demonstration and discussion 72
3.5.2 Impact of self-phase modulation....78
3.5.2.1 Theory....78
3.5.2.2 Results and discussion....80
3.5.3 Impact of Raman scattering....84
3.5.3.1 Theory....84
3.5.3.2 Results and discussion....85
3.5.4 Impact of modulation instability....85
3.5.4.1 Results and discussion....87
3.6 Conclusion....89
Bibliography....91

4 BRILLOUIN ECHOES DISTRIBUTED SENSING (BEDS) 97
4.1 Broadening of the BGS and physical limitations in spatial resolution: theoretical and experimental descriptions....98
4.2 The new approach and the three ways of making Brillouin echoes....102
4.3 Physical explanation of Brillouin echo....103
4.4 Theoretical description of Brillouin echo....104
4.5 Experimental implementation....110
4.6 Experimental results and discussion....111
4.7 Issues related to the continuous activation of the acoustic wave....114
4.7.1 Continuous activation....115
4.7.2 Second echo....115
4.8 Deconvolution method....117
4.9 Differential gain approach (DGA)....120
4.9.1 Principle....120
4.9.2 Experimental results and discussion....121
4.10 Performances of the two methods....125
4.11 Conclusion....127
Bibliography....128

5 APPLICATIONS OF BEDS 131

5.1 Landslide monitoring using BEDS 132
5.1.1 Background 132
5.1.2 Detection of landslide boundaries using the BEDS system: Detection of the strain profile of a cable pulled out of sand at the geotechnical laboratory of ETHZ, Zurich 133
5.2 Brillouin gain spectrum measurements in Photonic crystal fibre using BEDS 137
5.2.1 Background 137
5.2.2 Mapping of two PCF fibres 138
5.3 Acoustic life-time and Brillouin spectrum measurement in Photonic crystal fibres using BEDS 142
5.4 Conclusion 143
Bibliography 144

6 OPTICAL SAMPLING APPLIED TO OPTICAL DISTRIBUTED FIBRE SENSORS 145

6.1 Background 146
6.2 Principle and theory 146
6.3 Experimental set-up 148
6.4 Experimental results and discussion 149
6.5 Conclusion 152
Bibliography 153

7 CONCLUSION 155
7.1 Original contributions 156
7.1.1 Brillouin sensor and its limitations 156
7.1.2 Toward high performances sensor: Brillouin Echoes 157
7.1.3 Outlook and future directions 159

APPENDIX 161
A Derivation of the three coupled waves equations 161
B Acoustic field solution 168
C General solution for Signal amplitude 168
D Impact of the coherence´s source light 171

GLOSSARY 173

List of figures

Figure 2-1: Scattered light by two volume elements dV_1 and dV_2 in the direction θ [2]. 10
Figure 2-2: Fourth spontaneous scattering features in a non-homogeneous medium: Rayleigh, Rayleigh-wing, Raman and Brillouin scatterings. 12
Figure 2-3: Illustration of the generation of a Stokes component through Brillouin scattering [2]..... 17
Figure 2-4: Illustration of the generation of an anti-Stokes component through Brillouin scattering [2]. 18
Figure 2-5: Brillouin and Rayleigh lines observed in the light backscattered from an incident lightwave (λ = 1551.84 nm) in a 20 m long single-mode optical fibre (G652A IUT). The Brillouin shift is measured to be 10.860 GHz. 19
Figure 2-6: Schematic representation of the stimulated Brillouin scattering process: Concurrent phenomena involve in the process. 22
Figure 2-7: Orientation of the waves involved in stimulated Brillouin scattering in optical fibre. 24
Figure 2-8: (a) Lorentzian distribution (solid line) drawn with measured Brillouin gain spectrum (dotted line). The measured Brillouin shift is 10.727 GHz, the linewidth is 27 MHz and the acoustic lifetime is τ_A= 5.89 ns (b). Details of experimental set-up are provided in chapter 4. 29
Figure 2-9: (a) Transmitted (cross) and backscattered power measurements as a function of the input power (circle) of 5 km fibre. The dashed curve is the 1% of the input power. Measured critical powers are 14.99 dBm (according to Bayvel) and 17.48 dBm (according to Smith). (b) - (c) Brillouin lines and Rayleigh line observed in the light backscattered from two different incident lightwave powers (λ = 1551.84 nm). The Brillouin shift was measured to 10.860 GHz. 31
Figure 2-10: Illustration of the Lorentzian shape of the Brillouin gain spectrum and Brillouin loss spectrum and of the associated non linear phase shift. Energy transfer is made from higher frequencies to lower frequencies. 32
Figure 2-11: Raman gain spectrum in fused silica (λ_p = 1μm) [25]. 34
Figure 3-1: Apparatus used for apply strain (courtesy of ETHZ-IGT). 44
Figure 3-2: Dependence of Brillouin frequency with applied strain: Brillouin gain spectrum. Frequency shift at the resonance versus strain. 45
Figure 3-3: Variations of the Brillouin gain spectrum with the temperature: (a) Brillouin gain spectra, (b) Frequency of maximum Brillouin interaction versus temperature. 46
Figure 3-4: Illustration of the resolution. Left: a) spatially and detection resolved, b) spatially unresolved and detection resolved, c) spatially and detection un-resolevd. Right: illustration of the definition of accuracy and of the precision [32]. 48
Figure 3-5: First configuration: passive polarization scrambler. 48
Figure 3-6: Brillouin gain distribution along a 1 km G652D IUT fibre for two different configurations. (a) without scrambler; (b) scrambler on pump and scrambler on probe. 49
Figure 3-7: Second configuration: passive polarization diversity. 50

Figure 3-8: Brillouin gain distribution along a 1 km G652D IUT fibre is presented for two different states of polarization represented, direct polarisation (bleu trace), cross polarisation (gray trace) and resulting average of the two direct and cross polarisation. (a) on the signal, (b) on the pump, (c) comparison between the average trace when the scrambler is on the signal (green trace) and when the scrambler is on the pump (blue trace). 51

Figure 3-9: Experimental set-up of the BOTDA technique using a single laser. Optical noise results from the bidirectional propagation of optical waves showing the same frequency along the optical fibre. 53

Figure 3-10: The new BOTDA configuration for low optical noise. Using an optical circulator, light from the upper channel is extracted at the fibre output. This signal is boosted using an EDFA (Erbium doped amplifier) and filtered using a very narrowband fibre Bragg grating filter (<0.1 nm) to transmit only one sideband onto the detector. The filtering is crucial since it eliminates the unwanted modulator sideband that reduces the measurement contrast and any presence of the pump frequency due to the finite extinction ratio of the intensity modulator that would generate substantial optical noise at detection when combined with the Rayleigh light from the pump pulse..... 54

Figure 3-11: a) 3D distribution of the gain spectrum 47 km fibre length, obtained using 7 m spatial resolution with 256 time trace averaging. b) Trace of maximum Brillouin gain along the first 5 km of the fibre. c) Resulting Brillouin frequency shift of 47 km length fibre. 55

Figure 3-12 : Basic configuration of BOFDA [35]..... 57

Figure 3-13: Experimental set-up for the correlation based stain sensing technique [39]..... 59

Figure 3-14: After propagation in a long uniform fibre, a too strong CW signal will deplete the pump that will show a power drop when the frequency difference between pump and signal correspond to the Brillouin shift of this long fibre, following a power distribution as shown on the top left curve. If such a pump interrogates a segment with a gain spectrum shifted by a small amount $\delta\nu$, as shown on left, the actual gain spectrum shows a distorted skew distribution with a slightly shifted peak position, as shown on right. The thin line represents the real gain spectrum..... 61

Figure 3-15: (a) Frequency error as a function of the depletion factors d for different approximation (black line first order approximation, red line: 2nd order approximation and yellow line: exact result by numerical maximum finding). This shows that the 2nd order approximation is very good up to d=0.25, while the first order is only acceptable up to d=0.1. (b) Dependence of the frequency error on the frequency difference $\delta\nu$ between the gain central frequency and the depletion central frequency, for four different depletion factor d. Again it is clear that the first order approximation leads to an inaccurate determination, while the matching with the 2nd order approximation is nearly perfect..... 71

Figure 3-16: (a) Sensing fibre arrangement for pump depletion demonstration and position of the pump and the signal waves. A quasi uniform 1 km SMF fibre showing a constant Brillouin shift with a short section at the far end placed in a environmental temperature condition T_2 =24 °C different than that of the rest of the fibre (T_1=34 °C). Case 1: the pump and the signal are launched respectively at the far end and the near end of the fibre. Case 2: the pump and the signal are launched respectively at the near end and the far end of the fibre. 72

Figure 3-17: Brllouin gain spectrum at one position within the10 m segment of fibre shifted by 10 degrees in temperature for different powers of the CW signal varying from 0.70 mW to ~3.5 mW and with a fix pump peak power of 69 mW. The reference is the Brillouin gain in the case 1 when the pump is launched at the far end of the fibre (gray curve). a) P_{is} = 0.70 mW, b) P_{is} = 1.10 mW, c) P_{is} = 1.75 mW, d) P_{is} = 2.32 mW e) P_{is} = 2.87 mW, f) P_{is} = 2.32 mW showing the evolution of the peak gain for different CW signal power. In each case the actual measured gain spectrum shows a distorted skew distribution with a slightly up-shifted peak position whereas the power increases when compared to the reference (gray curve). If the Brillouin loss configuration was used the peak position would be down-shifted. 73

Figure 3-18: Brllouin frequency shift as function of the position for different power P_{is} of the CW signal, (a) in the case 1, (b) closer view of a), (c) in the case 2, (d) closer view of d), In the 10 m section of

fibre the Brillouin frequency shift moves to higher frequencies for the case 2 and remains quasi constant for the case1 74

Figure 3-19: (a) Output pump peak power as function of the frequency difference of the pump and the signal for two different values of P_{is} (0.70 mW and 2.87 mW), (b) depletion factor as a function of the power of the CW signal, model (1st order approximation, gray) model (2nd order approximation, black curve) and experiments (red square), (c) frequency error as a function of the depletion factor d in the worst case situation for $\delta\nu$=10 MHz (black curve), (d) measured depletion factor d (red square), theoretical depletion factor d (2nd order approximation, black curve), and Brillouin gain (red cross) as a function of the pump peak power P_{ip} with a Cw signal power P_{is} of ~1.91 mW, the fraction of energy transfer from the pump to the signal remains the same for different pump peak power while the Brillouin gain increases. In a), b) and c) a fix input pump peak power P_{ip} of ~70 mW was used. 75

Figure 3-20: Distribution of the frequency shift along the ~1 km single mode fibre presenting a variation. 76

Figure 3-21: (a) Output pump peak power as function of the frequency difference between the pump and the signal for four different values of P_{is}, (b) Output pulse power for three different frequency detunings with P_{isL} = 14.38 mW, (c) depletion factor d as a function of the pump peak power with a CW signal power P_{is} = 1.91 mW, model (2nd order approximation, black curve), experiment (red square), (d) measured depletion factor d (red square), theoretical depletion factor d (2nd order approximation, black curve), and Brillouin gain (red cross) as a function of the pump peak power P_{ip} with a CW signal power P_{is}=2.48 mW, the amount of energy transfer from the pump to the signal increases for different pump peak power while the Brillouin gain increases In (a), (b), and (c), a fix input pump peak power P_{ip} ~60 mW was used. 77

Figure 3-22: Experimental demonstration (solid lines) and theoretical analysis (dotted lines) of the gain spectrum broadening due to SPM along 25.5 km SMF fibre (a) for different peak powers of a 30 ns FWHM Gaussian pulse (b) comparing 30 ns FWHM Gaussian and rectangular pulses of identical energy (peak power of rectangular pulse is 222 mW). 81

Figure 3-23: Brillouin gain spectral width measured close to the fibre input (100 m) and at the fibre output (25.5 km) using a 30 ns Gaussian pulse (a) Linear dependence on the pump peak power, showing that the effect of SPM is observed only at the distant end, (b) Inverse dependence of the gain linewidth on the pulse width, showing the excess broadening due to SPM at the far end (pump power is 153 mW). 83

Figure 3-24: (a) The corresponding time domain measurement waveform of the pump pulse at the output of a 13 km DSF for different pump peak powers ;(b) Brillouin gain distributed measurement showing the pump depletion by Raman scattering in a 13 km DSF for different input pump peak powers; (c) Measured power spectra at the far end of a 13 km DSF fibre in the nomal dispersion regime showing the absence of MI, in inset the Raman spectra of the same fibre; (d)Maximum distance before Raman scattering begins to deplete the pump: experimental points (*), and theoretical model (solid line). 86

Figure 3-25: (a) Measured power spectra of MI at the far end of a 25.5 km SMF in the anomalous dispersion regime. (b) Distributed Brillouin gain measurements in a 25.5 km SMF fibre showing the pump depletion due to MI after a critical distance depending on the pump peak power; (c) Experimental (*) and theoretical (×) critical power as a function of the critical distance where the pump depletion turns significant (Brillouin gain fall-off) and the ratio (◊) between theoretical and experimental values. 88

Figure 4-1: Theoretical variation of the Brillouin response versus pump pulse width for two different values of Brillouin line-width 35 MHz and 50 MHz. 100

Figure 4-2: a) Effective Brillouin response spectrum for different pump pulse width 5 ns, 10 ns, 20 ns, 30 ns and 50 ns, corresponding to the spatial resolutions of 0.5 m, 1 m, 2 m, 3 m, and 5 m, b) Variation in the Brillouin response line-width (FWHM) for various values of the pump pulse width, theoretical (solid line) and experimental (dotted line). 102

Figure 4-3: (a) Bright pulse, (b) dark pulse, (c) π phase pulse. 103

Figure 4-4: Pump coding waveform, where α, β, and γ can be either real or complex. The duration of the β part of the pump pulse, T, will determine the spatial resolution. 105

Figure 4-5: Brillouin signal from a 5 cm section, spliced in the middle, of a 40 m fibre, whose Brillouin frequency is detuned by 140 MHz from that of the 5 cm section. Ω is tuned to the 5cm section Brillouin frequency. The β pump pulse is 500 ps long. A: bright pulse; B: dark pulse; C: π phase shift pulse. 107

Figure 4-6: A 2D Distance-Frequency map of Brillouin gain from a 5 cm section, spliced in the middle of a 40 m fibre, whose Brillouin frequency is detuned by 140 MHz from that of the 5 cm section. The Ω phase shift pulse is 500 ps long. As in the experiment below, for each Ω the mean over time was removed and the redder the color the *more negative* are the values of the Brillouin signal (with respect to the signal's initial power $\left|A_S^0\right|^2$ 108

Figure 4-7: The Brillouin signal from the 5m section in a 20 m (10.73 GHz)-5 m (10.86 GHz)-20 m (10.73 GHz) fibre, probed by a 500 ps π phase shift pulse. Brillouin frequency is tuned at resonance for the 5m section (10.86 GHz). The fast-fall time is accompanied by an exponential decrease to saturation. As the π phase shift pulse leaves the 5m section and enters the 20m one, a slow recovery of the signal follows a fast rise time. The ripples are due to the relative proximity of the Brillouin frequencies (140 MHz) of the various sections, and reflect the non-zero contributions of the fairly long sections to the overall Brillouin signal. .. 109

Figure 4-8: Experimental set-up of the optimized BEDS system: EC-LD: external cavity laser diode; EDFA: erbium-doped fibre amplifier; EOM: electro-optic modulator; FBG: fibre Bragg grating; PD: photodiode. 110

Figure 4-9: (a) 3D distribution of the Brillouin response along the sensing fibre as a function of frequency and position, (b) Enlarged top view of the 3D distribution of the Brillouin gain in the vicinity of the 5 cm fibre section. Since the echo response manifests itself as an apparent loss, the signal polarity has been inverted for clarity. 112

Figure 4-10: (a) Spectral distribution of the Brillouin response measured locally by the Brillouin echo of a π-phase pulse, for a broad range of pulse width shorter than the acoustic life-time, showing that the measured line-width is unchanged and equal to the natural linewidth $\Delta\nu_B$=27 MHz; (b) theoretical and measured Brillouin response line-width as function of the pulse width for a classical BOTDA (Brillouin optical time domain analysis) and for the BEDS technique, showing the critical dependency of the linewidth on the pulse width in the case of the BOTDA. 113

Figure 4-11: (a) The scheme shows that the signal wave beats with the Brillouin spontaneous amplified emission from long homogeneous sections; the beat frequency is higher for signal frequencies spectrally more distant from the spontaneous amplified emission, giving rise to a noisy beat note jamming the response, as shown in (b). 114

Figure 4-12: 3D distribution of the Brillouin response along the sensing fibre as a function of the frequency and the position using a 500 ps π phase pulse. The fibre comprises a 1m section with ν_B of 10.86 GHz, in the middle of 40 m of fibre with ν_B=10.73 GHz. 115

Figure 4-13: Probing a 1 m section (ν_B = 10.86 GHz) in the middle of a 40 m fibre (ν_B = 10.73 GHz), using a 500 ps π phase pulse and a 256 time average for each temporal trace. (a) The Brillouin gain through the 1m section at frequency ν_B = 10.86 GHz, (1m section at resonance). The marked slow descent of the signal at the beginning of the section, and the marked slow recovery of the signal as the π phase shift pulse enters the subsequent 20 m section, both of the order of τ_A ~6 ns, are manifestations of the second echo; (b) measured Brillouin gain distribution within the 1m section at position 22.53 m showing the high quality of the measured spectrum and the unwanted presence of the second echo. Since the π phase shift pulse actually manifests itself as an apparent Brillouin loss, the signal polarity has been inverted for clarity. 116

Figure 4-14: Illustration of the convolution of Brillouin response with the impulse response of the system showing the reversibility of convolution. 118

Figure 4-15: Probing a 1 m section (ν_B = 10.86 GHz) in the middle of a 40 m fibre (ν_B = 10.73 GHz), using a 500 ps π phase pulse and a 256 time average for each temporal trace. (a) The Brillouin gain through the 1 m section at frequency ν_B = 10.86 GHz, (1 m section at resonance). Measured data (circle), processed data (star); (b) measured and processed Brillouin gain distribution within the 1 m section at position 22.53 m showing the attenuation of the second echo thanks to the procesing, the signal polarity has been inverted for clarity. 119

Figure 4-16: Illustration of the pulse configuration, as used for the differential gain approach. (a) The probing pulse, comprising a short π phase shift portion at the end of zero phase section; (b) A zero phase reference pulse. 120

Figure 4-17: The lower channel in the set-up of BEDS with differential gain approach integrated. 121

Figure 4-18: A 3D map of the Brillouin response in the 20 m-1 m-20 m fibre of Fig. 9, as obtained from the differential gain technique. No second echoes are observed. 121

Figure 4-19: Using the differential gain technique to probe a 1 m section (ν_B=10.86 GHz) in the middle of a 40 m fibre (ν_B=10.73 GHz), using a 500 ps π phase pulse and 256 time averages of each temporal trace. (a) Compare the very clean Brillouin gain trace around the 1 m section at the 1m section frequency (ν_B=10.86 GHz) with that of Fig. 10a. (b) Brillouin frequency shift as a function of position in the fibre. . 122

Figure 4-20: **(**a) 3D spectral distribution of the response as function of the position over a 5 km fibre realized with a 5 cm spatial resolution. The 5 cm segment is too small to be distinguished; (b) magnified view of the 3D distribution of the Brillouin response around the 5 cm fibre section, showing that this segment at the end of the 5 km fibre is fully resolved both in space and frequency..... 123

Figure 4-21: Two measurements without (A) and with (B) 0.5 ns π phase pulse along the 5 km long fibre. Inset: the difference between the two measurements, A and B, showing the signature of the fibre equivalent to the response of the 0.5 ns phase pulse. Measurements were performed using 256 times averaging of each temporal trace. 124

Figure 4-22: (a) Brillouin response as a function of distance in the vicinity of the 5 cm fibre section; (b)Brillouin frequency shift as a function of distance at the same positions. 124

Figure 4-23: Brillouin response applying the low pass filter on the measured data and using the differential gain technique to probe a 1 m section (ν_B=10.86 GHz) in the middle of a 40 m fibre (ν_B=10.73 GHz), using a 500 ps π phase pulse and 256 time averages of each temporal trace. (a) Compare the very clean Brillouin response trace around the 1 m section at the 1m section frequency (ν_B=10.86 GHz) of Figure 4-19(a)**Error! Reference source not found.** with that of Figure 4-13 and Figure 4-15 (a); (b) Compare the very clean Brillouin gain distribution within the 1 m section at position 22.53 m with that of Figure 4-13(b) and Figure 4-15(b). 125

Figure 4-24: 2 Magnified view of 2D spectral distribution of the Brillouin response around the 1 m fibre section as function of the position over the 40 m of fibre realized with a 5 cm spatial resolution; from left to right original data; filtered data and BEDS differential gain. 126

Figure 4-25: Comparative Brillouin response of the BEDS differential gain approach and the differential pulse-width pair technique [16], obtained under identical power and spatial resolution conditions (5 cm), clearly showing the optimized BEDS response by a 3 dB contrast improvement. 127

Figure 5-1: **(**a) Illustration of the motion of the land showing the three zones concerned (stable zone, transition zone and moving zone) and the strain transfer to the cable for a landslide at 45° angle, (b) geometry of the pullout box used the measurements: 2 m length, 0.1 m diameter and 0.1 m depth, c) geometry (cross section) of the used optical fibre cable (left) and its photograph (right) which shows the cable with the micro-anchor mounted. 134

Figure 5-2: Geotechnical measurement laboratory land-slide set-up showing a micro anchor mounted onto the optical fibre cable before recovering with sand (left), the pullout-box with optical fibre cable buried in sand (right). 135

Figure 5-3: (a) Applied displacement as a function of the measured displacement (retrieved from numerical integration of the entire strain in the cable), (b) applied force versus optically measured pullout force. The measured and the applied values are consistent. 136

Figure 5-4: Measured strain for each load step δ applied to the fibre cable: For each load step δ distributed measurements was carried out. Measured was obtained using BEDS experimental set-up with 5 cm spatial resolution allowing for at least 20 resolved points per meter. The Brillouin frequency shift was retrieved which gave the information on the amount of strain applied. In the first four steps, the strain behind the fixation point (at 2.8 m) is zero while at larger displacement steps the strain profile propagates behind the fixation point. 136

Figure 5-5: Scanning electron micrograph (SEM) of the solid core PCF fibres, a)Fibre 1: 100°m length and b)Fibre 2: 400°m length. 137

Figure 5-6: 2 D distribution of Brillouin gain along along the 100 m PCF fibre. The spatial resolution and the frequency resolution are respectively 30 cm and 2 MHz. 140

Figure 5-7: Mapping of the Brillouin frequency shift along the a) Fibre 1 and b) Fibre 2 showing the effect of in-homogeneities and strain. The insets show the Fourier transforms. 141

Figure 5-8: a) Brillouin gain spectrum at position distance of 85 m with a line-width of 50 MHz b) experimental Brillouin gain in the time domain at the fibre output end and at the peak gain frequency. The red line represents the exponential decay fit curve to estimate the acoustic lifetime. The set-up is described in Figure 4-8. 142

Figure 6-1: Set-up of generation of the optical sampling signal. 148

Figure 6-2: Complete set-up for optical sampling applied to distributed Brillouin sensing system. BOTDA: Brillouin time domain analysis. 149

Figure 6-3: Fibre sensor arrangement used for the comparative tests. At a wavelength of 1557 nm the Brillouin resonance of the fibres is ν_B = 10.693 GHz for the G652D fibre and ν_B = 10.520 GHz for the G657B fibre. 149

Figure 6-4: 3D plot of the distribution of the Brillouin gain of the central region of the fibre arrangement shown in Figure 6-3. The short segments made of distinct fibres are clearly visible. The acquisition is realized using the optical sampling technique with a 64 times averaging. 150

Figure 6-5: Brillouin gain as function of the position in the fibre at the frequency resonance of the long segment fibre (10.693 GHz) measured (a) using direct detection i.e. high frequency detector; (b) using the optical sampling technique and a low frequency detector. 151

Figure 6-6: Brillouin gain as function of the position in the fibre at the frequency resonance of the small segment fibre (10.520GHz) measured (a) using direct detection, i.e. high frequency detector; and (b) the corresponding optical signal measured using the optical sampling technique and a low frequency detector with a 64 times averaging. 151

List of tables

Table 2-1: Brillouin shift and typical characteristics of the silica at two different wavelengths 1.55 μm and 1.3 μm. 17
Table 2-2 : Raman and Brillouin typical characteristisc in silica. 33
Table 3-1: Characteristics of the SMF and the DSF fibres used for the experiments. 85
Table 4-1: Summary of the performances of the two methods. 126
Table 5-1: Parameters of PCF Fibres 1 and 2. 139
Table 5-2: Summary of the PCF fibres' retrieved characteristics 141

1 Introduction

In this opening chapter, we introduce the topic of fibre optic sensors in its historical context; we situate the problem of the spatial resolution and dynamic range required for new advanced applications. We then outline the method we are using to explore these questions and place it in its historical context. The chapter ends with an overview of the remaining chapters of this thesis.

The optical fibre, as thin as a hair and stronger than steel, remains one of the greatest technological advances of the 20th century. Developed in the 70s in the Corning Glass laboratories, optical fibres are capable of conducting light between two locations separated by hundreds or even thousands of km, as it was envisioned by Charles Kao in 1966 (Nobel prize winner physics in 2009). By enabling communications over very long distances and at speeds not previously possible, optical fibres were one of the key elements of the optical communications' revolution. This huge potential inspired 20 years later, i.e. in the 90s, the use of optical fibres as a sensor of temperature as well as strain over many kilometers. Since then several application areas have been developed, especially in the detection of oil spills, in structure health monitoring, etc.

1.1 How did this happen?

In 1922, Leon Brillouin, predicted in one of his theory that the diffraction of light by a sound wave induces a frequency shift through the light-matter interaction in the fluid. Only in 1930 and 1932, i.e. 8-10 years later, Brillouin's work was experimentally and independently verified by Goss, R. Lucas and P. Biquard (in France), and by Debye and Sears (in the USA). They have shown that the scattered spectra are composed of two shifted components and one un-shifted component. In 1935 Landau and Placzeck published a short note pointing out that the un-shifted incident light is due to the non propagating temperature fluctuations. At that moment it was not possible to study more in detail these results. The change in frequency was too small to be resolved by the detection systems available at this time. Scientists had to wait until 1960 for the advent of lasers allowing new developments in the field (Chiao 1964), such as very high resolution interferometers, thus increasing research interests related to the spectrum of light scattered by fluctuation density. This made possible more accurate measurements of frequencies, intensities and line-widths and gave access to the characterization of thermodynamic and acoustic properties as acoustic wave velocity, bulk modulus. As a direct consequence, in 1972 and 1974 respectively, Ippen and Rich observed the Brillouin effect in optical fibers. Initially considered by Smith (Smith 1972) as a major limitation for optical-fibre transmission lines, it eventually proved possible to manufacture Brillouin-optical amplifiers (Olsson 1986), fibre lasers (Bayvel 1989) and narrowband tunable filters (Tkach 1989). Recently, researchers have demonstrated that the group velocity of light could be controlled in an optical fibre using stimulated Brillouin scattering (Song et al 2005, Okawachi 2005). Among all these applications, researchers have demonstrated that the spectral characteristics of the Brillouin scattered light contain information on quantities such as ambient temperature (Horiguchi 1989) and strain (Culverhouse 1989), initiating then the field of Brillouin optical fibre sensors which has continued to grow and spread out over the world and into new fields of applications.

1.2 Fibre optics sensors

Optical fibre sensors may be defined as a system through which a physical, chemical, biological, or other quantity interacts with light guided in an optical fibre or guided to an interaction region by an optical fibre to produce an optical signal related to the parameter of interest (Culshaw 2004). In a more general view, optical fibre sensors technology can also be seen as the association of optics and

electronics or opto-electronics, every evolution of this latter given rise to interesting applications in optical fibre sensors. They can be configured in different shapes, to sense various physical disturbances, temperature, strain, pressure, acoustic field, flow rate, electric field, magnetic field, current and voltage, among which some of them are available on the market for many years. Fibre sensors have shown the advantage of being of small in size, low in weight, immune to electromagnetic interference and chemically passive and capable of remote measurement. These make them a good candidate for operating in harsh conditions or in applications that are inaccessible using alternative technologies.

They can be classified in single point fibre sensors and distributed fibre sensors.

Single point sensors as fibre Bragg gratings not often are used to sense a single point. When a large number of points must be measured, many fibres must be used to connect the sensor heads, causing a cost penalty. There is therefore an opportunity to save cost by multiplexing a number of sensing elements over a single fibre, thus forming a fibre optic sensor network distributed in space.

Distributed optical fibre sensing uses the very special properties of optical fibres to make simultaneous measurements of both the spatial and temporal behavior of a measurand field. Nowadays, the annual market for distributed fibre sensors is estimated to reach US$ 550 millions, much bigger than the annual market for point sensors (Krohn 2010). Distributed fibre sensors technology exists essentially in three types, based on either Rayleigh scattering, Raman scattering and Brillouin scattering. Optical time domain reflectometry (OTDR) based on Rayleigh scattering has given rise to the well-known method for the characterization and the monitoring of optical fibre links in the Telecommunications industry. OTDR technology (Barnosky 1976) has been developed for measuring optical fibre attenuation characteristics and overall fibre length. It allows location of losses introduced by a connector, a splice or by any default present on the fibre link. Distributed networks based on fibre Bragg gratings (Hill 1978, Stone 1987, Payne 1989, Morey 1989, Hand 1990, Morey 1991, Kashyap 1994) are essentially a network of point sensors, as mentioned in the previous paragraph. They have found applications in many areas including the monitoring of strain for smart structures. Raman scattering technology (Dakin 1985) is currently the dominant distributed photonic sensor technology for measuring temperature in the power cable and the oil and gas industries because it allows continuous sensing range of 15 km or more. Raman distributed temperature sensors have been implemented on a large scale in oils wells. Brillouin scattering technology (Horiguchi 1989, Bao 1993, Niklès 1996), which is the technology presented in this thesis, is newer and requires maybe a more expensive interrogating system than fibre Bragg grating technology and Raman based distributed sensors. However, the whole fibre acts as the sensor and it can be used to measure continuously strain as well as temperature (something not possible with Raman scattering technology) in a range of 50 km indeed 100 km.

1.3 The problem

At this point, we have to define two main performance parameters for distributed sensors and in particular for distributed Brillouin sensor measurements: the accuracy of the measurand and the spatial rsolution. The accuracy of the measurand qualitatively expresses the closeness of the measured value to the true or ideal value of the measurand. The spatial resolution is defined as the

smallest length of fibre over which any sensible change in the spatial variation of the measurand can be detected. Nowadays, modern or/and specific advanced applications have taken a substantial step towards better spatial resolution, while preserving temperature/strain precision over a long range. It has been demonstrated that, in classical configuration spatial resolution not better than ~1 m (Fellay 1999) can be obtained over a long distance range while maintaining a narrow spectrum. The reason comes from the fact that the observed Brillouin spectrum turns apparently broader as the spectrum of the pulse used to map the information becomes broader than the Brillouin resonance, since the spectral distribution of the effective gain is given by the convolution between the pulse spectrum, (broader for shorter pulse), and the natural Brillouin gain spectrum. This broadening, as a result reduces accuracy in the measurement of temperature and strain at submetric spatial resolutions, and eventually leads to a vanishing gain for ultrashort pulses.

However, this situation changed when scientific community understood that by pre-activating the acoustic wave within the Brillouin resonance, it could be possible to have a narrow Brillouin gain spectrum down to its natural line-width for spatial resolution shorter than the acoustic relaxation time. First observed in 1999 by Bao *et al* and qualitatively explained by Lecoeuche *et al* in 2000, this breakthrough opened the incredible perspective of performing high spatial resolution measurements while maintaining a sharp Brillouin resonance. They actually reported distributed measurements using pulse width down to 1.5 ns (15 cm spatial resolution) (Zou 2004). Despite the unquestionable experimental demonstration brought by the authors, these results have so far suffered from the problem that they could not be decisively reproduced with a set-up different from the original (same sources, same electro-optic modulator). In particular no one could observe this spectral narrowing at 1550 nm using semiconductor lasers with lower coherence. Moreover, no clear physical description of the experimental situation has been reported and the authors have so far justified their observations only through a numerical integration of the coupled wave equations (Zou 2005, Kalosha 2006).

1.4 In this thesis

A part of this PhD thesis is dedicated to the clarification of the results reported by Bao *et al*, through deep theoretical and experimental studies of the concept, to end up with the objective to reach experimentally very high spatial resolution in a controlled and optimized approach while maintaining a long range measurement. Another part of this thesis is dedicated to the theoretical and experimental studies of limitations upon the performances of Brillouin sensors due to some non-linear effects.

Including this introductory chapter, the thesis is organized into seven chapters. The second chapter is divided into two main parts. The first section reviews the linear effects (elastic and inelastic effects) in the optical fibre. The second part reviews the stimulated Brillouin scattering in optical fibre in order to introduce the concepts needed to understand the following chapters. We then review some of the nonlinear effects in optical fibreswhich play an important role in penalysing the performances of Brillouin sensors.

Chapter 3 in the first instance is devoted to the Brillouin sensor itself, its different variants; an updated configuration of the classical Brillouin sensor for time domain analysis allowing low noise is proposed. Then, we move on the theoretical and experimental study of the impact of non-linear effects presented in chapter 2 on the performances of the Brillouin sensor.

In Chapter 4, we present the new concept called "Brillouin echoes" also developed in this thesis. We experimentally and theoretically study the physics behind Brillouin echoes. We then present an analytical model that allows us to optimize the performance of the Brillouin sensor echo.

As an illustration, the application of the measurements system in landslide monitoring is presented in chapter 5. The mapping of photonic crystal fibre, the measurement of the Brillouin gain spectrum in this latter and the acoustic lifetime measurement in standard fibre are presented as well.

High spatial resolution distributed sensor need fast optical detection and acquisition electronics devices, that are not widely available but are expensive and limited in performance in terms of sensitivity and noise measurements interface. In chapter 6, we propose to apply a technique named optical sampling to distributed fibre sensors which give the possibility to acquire fast optical signals using low frequency electronic detection and acquisition systems. After presenting the principle and the theory, experimental implementation and results are discussed.

Chapter 7 concludes the thesis with a summary of the main achievements, a broader perspective of its implications and an outlook towards future work.

Bibliography

Bao, X., Webb, D. J., and Jackson, D. A., 1993. 32-km distributed temperature sensor based on Brillouin loss in an optical fiber. Optics Letters, 18: 1561-163.

Bao, X., Brown, A., DeMerchant, M., and Smith, J., 1999. Characterization of the Brillouin-loss spectrum of single-mode fibers by use of very short (<10 ns) pulses. Optics Letters, 24: 510-512.

Barnosky M. K. and Jensen S. M., 1976. Fibre waveguides: a novel technique for investigating attenuation. Applied Optics, 15:9.

Brillouin, L., 1922. Diffusion de la lumière et des rayons X par un corps transparent homogène. Annales de Physique, 17: 88-122.

Chiao, R.Y., Townes, C.H., and Stoicheff, B.P., 1964. Stimulated Brillouin Scattering and Coherent Generation of Intense Hypersonic Waves. Physical Review Letters, 12: 592-595.

Culverhouse, D., Frahi, F., Pannell, C.N., and, Jackson, D.A., 1989. Potential of stimulated Brillouin scattering as sensing mechanism for distributed temperature sensor. Electronics Letters, 25: 913-915.

Culshaw, B., 2004. Optical fiber sensor technologies: opportunities and-perhaps pitfalls. Journal of Lightwave Technology 22: 39-50.

Dakin, J.P., Pratt, D.J., Bibby, G.W., and Ross, J.N., 1985. Distributed optical Raman temperature sensor using a semiconductor light source and detector. Electronics Letters, 21: 569-570.

Fellay, A., Thévenaz, L., Facchini, M., Niklès, M., and Robert, P., 1997. Distributed sensing using stimulated Brillouin scattering: towards ultimate resolution. Optical Fiber Sensors, Optical Society of America Technical Digest Series, 16: 324-325.

Horiguchi, T., Kurashima, T. and Tateda, M., 1989. Tensile strain of Brillouin frequency shift in silica optical fibers. IEEE Photonics Technology Letters, 1: 107-108.

Horiguchi, T., and T., Tateda, M. Y.. 1989. BOTDA-nondestructive measurement of single-mode optical fibers attenuation characteristics using Brillouin interaction: theory. Journal of Lightwave Technology, 7: 1170-1176.

Horiguchi, T., Shimizu, K., Kurashima, T., Tateda, M., and Koyamada, Y., 1995. Development of a distributed sensing technique using Brillouin scattering. Journal of Lightwave Technology, 13: 1296-1302.

Hand D. P and Russell R. St. J., 1990. Photoinduced refractive-index changesin germanosilicate fibers. Optics Letters, 15:102.

Hill K. O. Fujii Y, Johnson D. C., and. Kawasaki B. S, 1978. Photosensitivity in optical fiber waveguides: Application to reflection filter fabrication. Applied Physics Letters, 32:647.

Ippen, E.P., and Stolen, R.H., 1972. Stimulated Brillouin scattering in optical fibers. Applied Physics Letters, 21: 539-541.

Kao C. K. and Hockham G. A., 1966. Dielectric fiber surface waveguides for optical frequencies. In Proc. Inst. Electrical Engineering, 113: 1151.

Kashyap R., 1994. Photosensitive optical fibers: Devices and applications. Optical Fiber Technology, 1: 17.

Krohn D., July 2010, Interview technology Focus, Nature Photonics 4: 436.

Lecoeuche V., Webb D. J., Pannell C. N., and Jackson D. A., 2000. Transient response in high-resolution Brillouin-based distributed sensing using probe pulses shorter than the acoustic relaxation time. Optics Letters, 25: 156-158.

Meltz G., Morey W. W., and Glenn W. H., 1989. Formation of Bragg gratingsin optical fibers by a transverse holographic method. Optics Letters, 14: 823.

Morey W. W, Meltz G., and. Glenn W. H, 1989. Fiber Bragg gratingsensors. In Proc. SPIE Fiber Optic & Laser Sensors VII, 1169: 98.

Morey W. W., Meltz G. and Glenn W. H., 1989. Bragg-grating temperature and strain sensors. In Proc. OFS'89. Paris, France, 526.

Morey W. W., Dunphy J. R., and Meltz G., Sept. 1991. Multiplexing fiber Bragggrating sensors. In Proc. SPIE Distributed and Multiplexed Fiber Optic Sensors, Boston, MA, 1586: 216.

Niklès M., Thévenaz L., and Robert P. A., 1996. Simple distributed fiber sensor based on Brillouin gain spectrum analysis. Optics Letters, 21:758–760.

Olsson, N.A., and Van Der Ziel, J.P., 1986. Cancellation of fiber loss by semiconductor laser pumped Brillouin amplification at 1.5 μm. Applied Physic Letters, 48: 1329-1330.

Okawachi, Y., Bigelow, M.S., Sharping, J.E., Zhu, Z., Schweinberg, A., Gauthier, D.J., Boyd, R.W., and, Gaeta, A.L., 2005. Tunable all-optical delays via Brillouin SlowLight in an Optical Fiber. Physical Review Letters, 94: 153902.

Payne F. P., 1989. Photorefractive gratings in single-mode optical fibers. Electronics Letters, 25: 498.

Ponikvar D. R. and Ezekiel S., 1981. Stabilized single-frequency stimulated Brillouin fiber ring. Optics Letters, 16:398-400.

Smith, R.G., 1972. Optical power handling capacity of low loss optical fibers as determined by stimulated Raman and Brillouin scattering. Applied Optics, 11: 2489-2494.

Song, K.-Y., González-Herráez, M., and Thévenaz, L., 2005. Observation of pulse delaying and advancement in optical fibers using stimulated Brillouin scattering.Optics Express, 13: 82-88.

Stone J, 1987. Photorefractivity in GeO2-doped silica fibers. Journal Applied Physic, 62:4371.

Tkach, R.W., and Chraplyvy, A.R., 1989. Fibre Brillouin amplifiers. Optical and Quantum Electronics, 1: 111-113.

Tkach, R.W., Chraplyvy, A.R., and Derosier, R.M., 1989a. Performance of a WDM network based on stimulated Brillouin scattering. IEEE Photonics Technology Letters, 21: S105-S112.

Zou, L., Bao, X., Wan, Y., and, Chen, L., 2005.Coherent probe-pump-based Brillouin sensor for centimetre-crack detection. Optics Letters 15: 370-372.

Zou, L., Bao, X., Ravet, F., and Chen, L., 2006. Distributed Brillouin fiber sensor for detecting pipeline buckling in an energy pipe under internal pressure. Applied Optics, 45:3372-3377.

2 Optical effects in optical fibres

In this chapter, different optical effects in the optical fibre will be addressed. We will review linear and non linear effects, firstly focusing on spontaneous Brillouin scattering as a linear effect and stimulated scattering as a non linear effect. We will then summarize the theoretical approach allowing the derivation of the basic equations governing the stimulated Brillouin scattering process. Secondly we will introduce other nonlinear phenomena such as stimulated Raman scattering and those originating in the optical Kerr effect such as self-phase modulation and modulation instability, which have their own responsibility in the limitations of performances of the Brillouin sensors that we will be discuss in chapter 3.

Scattering is a general physical process where waves, such as light, are forced to deviate from a straight trajectory by one or more non-uniformities present in the medium through which they pass. In 1957, Fabelinski [1] wrote that when a monochromatic light passes through a dense, transparent medium, some of the light is scattered, since the density is not uniform.

Light is considered as an electromagnetic wave. The propagation of the light in a dielectric medium may turn out to be linear or non linear, depending on the intensity of the light sent into the medium.

2.1 Linear scattering effects

Light scattering is intimately linked to the presence of in-homogeneities in the optical properties of the propagation medium. As an example, let us take the case of a plane wave illuminating a completely homogeneous medium as shown in Figure 2-1. We assume that the medium is formed of an elementary volume dV_1 which scatters light in the direction θ. However, there exists for sure an elementary volume (labeled dV_2) close to dV_1, whose scattered light interferes destructively with that from dV_1. Since a similar description can be applied to all directions, except the direct direction $\theta=0$, one can deduce that scattering exists only for the direction $\theta=0$. Now assuming that the medium is not uniform, i.e. presents fluctuations density, the total number of molecules in the volume dV_1 may not be equal to the total number of molecules in the volume dV_2. Consequently, the destructive interference between the fields scattered by these two elements in the direction $\theta\neq0$ is no longer total. To summarize, in a completely homogeneous medium, light always propagates in a single direction. However, in a non-uniform medium the light scattered results from density fluctuations of the media which modifies spatially and temporally its optical properties [2]. In addition, the scattering is linear since the intensity of the wave is very small or does not exceed a certain critical value in order not to change the intrinsic optical response of the medium. In this linear case, the susceptibility of the material remains independent of the electromagnetic field $\vec{E}$ present in the medium, and the polarization remains linearly dependent on $\vec{E}$. Two types of

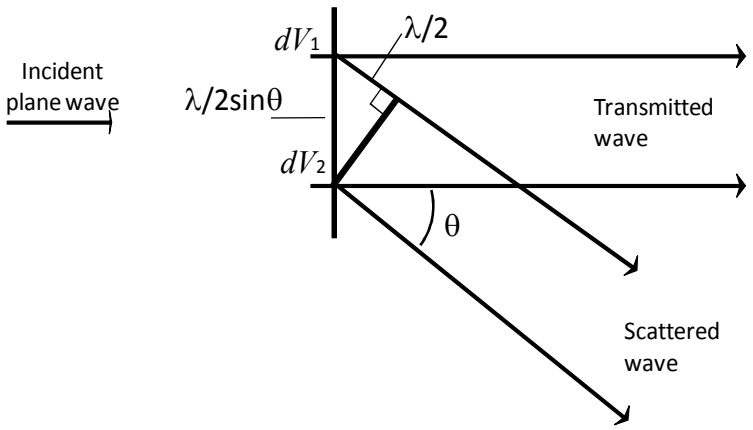

Figure 2-1: Scattered light by two volume elements dV_1 and dV_2 in the direction θ [2].

scattering can be distinguished: inelastic scattering and elastic scattering.

2.1.1 Elastic scattering effects

2.1.1.1 Rayleigh and Rayleigh wing scattering

Elastic scattering is a scattering where the light is scattered with no frequency shift. In this category we have Rayleigh and Rayleigh-wing scattering.

Rayleigh scattering is the scattering of light from non-propagating density fluctuations. Formally, it can be described as scattering from entropy fluctuations.

Rayleigh-wing scattering results from fluctuations in the orientation of anisotropic molecules. Since the molecular reorientation process is very rapid, this component is spectrally very broad. Rayleigh-wing scattering does not occur for molecules with an isotropic polarizability tensor, as is the case for glass and optical fibres (since the silica molecule is centro- symmetric).

2.1.2 Inelastic spontaneous scattering effects

Linear inelastic scatterings are characterized by their shift in frequency due to the molecular fluctuations density (optical phonons) for the Raman scattering and to the pressure fluctuations density (acoustic phonons) for the Brillouin scattering.

Under most general circumstances, the spectrum of the scattered light has the form shown in Figure 2-2 in which the four types of scattering features are represented. By definition, those components of the scattered light that are shifted to lower frequencies are known as Stokes components, and those components that are shifted to higher frequencies are known as Anti-Stokes[1] components. Eq. (2.1) describes the light propagation as an electromagnetic wave. This equation is known as a perturbed wave equation derived from the well-known Maxwell equations:

$$\nabla^2 \vec{E} - \frac{1}{c^2}\frac{\partial^2 \vec{E}}{\partial t^2} = \mu_0 \frac{\partial^2 \vec{P}}{\partial t^2}, \tag{2.1}$$

where $c = 1/\sqrt{\varepsilon_0 \mu_0} = 3\times10^8$ m/s is the speed of light in the vacuum, $\vec{P}$ is the electric polarization describing the response of the medium under the influence of the electrical wave, $\vec{E}$ is the vector field wave, $\mu_0 = 4\pi\times10^{-7}$ kg m A^{-2}s^{-2} is the magnetic permittivity in free space and $\varepsilon_0 \approx 8.85\times10^{-22}$ kg^{-1} m^{-3} A^2 s^4 is the dielectric constant in vacuum. In the linear regime, as is the case here, $\vec{P}$ depends linearly on $\vec{E}$ and is expressed as:

$$\vec{P}_L = \varepsilon_0 \chi \vec{E}, \tag{2.2}$$

[1] Stokes and anti-Stokes are of historical origin, they have no physical cause.

where χ is the linear dielectric susceptibility, ε_0 is the dielectric permittivity of free space, $\vec{P}_L$ is the linear part of the polarization.

In an isotropic and homogeneous medium, the tensor χ is reduced to a scalar and Eq. (2.1) becomes:

$$\nabla^2\vec{E}-\frac{n^2}{c^2}\frac{\partial^2\vec{E}}{\partial t^2}=0\,, \tag{2.3}$$

where n is the refractive index of the medium.

In an isotropic and inhomogeneous media, such as in optical fibres, spatial and temporal fluctuations $\Delta\chi$ of the dielectric susceptibility are taken into account, the medium therefore develops an additional polarization $\vec{P}_d$ [2], where $\vec{P}$ is then given by:

$$\vec{P}_L=\varepsilon_0\chi\vec{E}+\vec{P}_d\,,\ \text{where}\ \vec{P}_d=\Delta\varepsilon\vec{E} \tag{2.4}$$

The dielectric tensor $\Delta\varepsilon$ then contains all the information on the fluctuations (spatial-temporal) that lead to the light scattering. The light propagation is then given by Eq. (2.5):

$$\nabla^2\vec{E}-\frac{n^2}{c^2}\frac{\partial^2\vec{E}}{\partial t^2}=\mu_0\frac{\partial^2\vec{P}_d}{\partial t^2}\,, \tag{2.5}$$

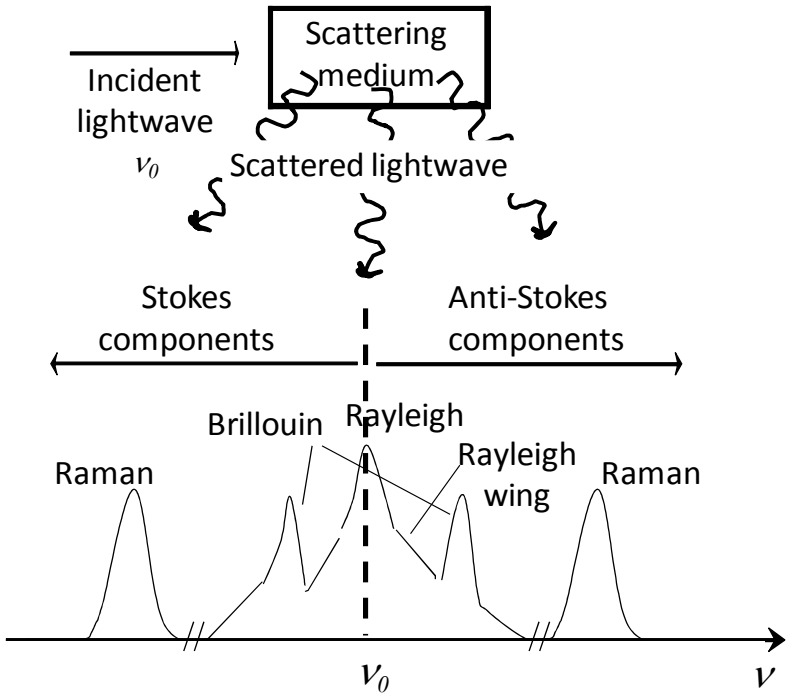

Figure 2-2: Fourth spontaneous scattering features in a non-homogeneous medium: Rayleigh, Rayleigh-wing, Raman and Brillouin scatterings.

In detail, $\Delta\varepsilon$ can be decomposed into two distinct components $\Delta\varepsilon=\Delta\varepsilon\delta_{ik}+\Delta\varepsilon\delta_{ik}^{(t)}$: a scalar contribution $\Delta\varepsilon\delta_{ik}$ and a tensor contribution $\Delta\varepsilon\delta_{ik}^{(t)}$ [2]. Fluctuations of pressure, temperature, entropy and density, i.e. all thermodynamic fluctuations, are at the origin of the scalar contribution and hence at the origin of Brillouin and Rayleigh scattering. Symmetric and anti-symmetric components are at the origin of the tensor contribution. The symmetric part $\Delta\varepsilon\delta_{ik}^{(s)}$ is associated with the reorientation of molecules and hence is at the origin of Rayleigh-wing scattering, while the anti-symmetric part $\Delta\varepsilon\delta_{ik}^{(a)}$ is associated with the polarisability change of molecules in the optical medium (in the presence of an electrical field) and hence is responsible for Raman scattering. The two scatterings of interest for us are Raman and Brillouin scattering, so we will focus on them.

2.1.2.1 Spontaneous Raman scattering in optical fibres

Raman scattering results from the interaction of light with the vibrational modes of the molecules constituting the scattering medium. As previously explained, Raman scattering can also be described as the scattering of light from optical phonons. Since spontaneous Raman scattering does not have any impact on the present work, we will not go in detail in this subject. On the other side, we will give more information in the case of stimulated Raman scattering (SRS) since its impact on the performances of the Brillouin sensor is relevant.

2.1.2.2 Spontaneous Brillouin scattering in optical fibres

- **Density fluctuations and acoustic wave**

Brillouin scattering has its origin in $\Delta\varepsilon$ variations induced by thermodynamic quantities, where density fluctuations can be described in terms of *pressure p* and *temperature T* or *entropy s* fluctuations (for convenience $\Delta\varepsilon\delta_{ik}=\Delta\varepsilon$). Because sound wave propagation is an adiabatic process, density fluctuations (noted $\Delta\rho$) should be decomposed into pressure fluctuations at constant entropy and entropy fluctuations at constant pressure [3]. Considering this, the dielectric constant fluctuations expressed as function of all these quantities can be written as:

$$\Delta\varepsilon=\left(\frac{\partial\varepsilon}{\partial\rho}\right)_T\Delta\rho+\left(\frac{\partial\varepsilon}{\partial T}\right)_\rho\Delta T\text{, where }\Delta\rho=\left(\frac{\partial\rho}{\partial p}\right)_s\Delta p+\left(\frac{\partial\rho}{\partial s}\right)_p\Delta s\text{,}\qquad(2.6)$$

Referring to the work performed by Fabelinskii in 1968 [4], the contribution of the second term of the first equation is less than 2%. Moreover, the dielectric constant is more significantly affected by density fluctuations than temperature fluctuations; hence the second term can be neglected. Eq 2.6 becomes:

$$\Delta\varepsilon=\left(\frac{\partial\varepsilon}{\partial\rho}\right)_T\left(\frac{\partial\rho}{\partial p}\right)_s\Delta p+\left(\frac{\partial\varepsilon}{\partial\rho}\right)_T\left(\frac{\partial\rho}{\partial s}\right)_p\Delta s\text{,}\qquad(2.8)$$

The frequency of the light scattered by fluctuations at constant entropy (thermal sound waves or phonons), corresponding to the first term on the right of Eq. (2.7), is shifted by an amount

proportional to the velocity of the phonons or sound wave V_a, Energy and momentum considerations require that the proportionality constant be the magnitude of the change in the wave vector of the scattered light. Two lines (or Stoke and anti-Stokes) are observed because scattering can occur from waves traveling in opposite directions but at the same speed. These lines are broadened somewhat because of the dissipative process which damp out the waves. Brillouin has suggested that light is scattered by thermal sound waves in fluid [5]. So this first term is responsible for Brillouin scattering and these lines are known as the Brillouin lines.

The light scattered by the fluctuations at constant pressure (second term of the Eq.(2.7)) is not shifted in frequency although it is broadened somewhat due to the thermal dissipative processes which damp out these fluctuations. So the second term is responsible for Rayleigh scattering.
Still focusing only on Brillouin scattering, $\Delta\varepsilon$ is reduced to the first term of Eq. (2.7) and reads as:

$$\Delta\varepsilon = \left(\frac{\partial\varepsilon}{\partial\rho}\right)_T \left(\frac{\partial\rho}{\partial p}\right)_s \Delta p = \frac{\gamma_e}{\rho_0}\left(\frac{\partial\rho}{\partial p}\right)_s \Delta p \text{ , with } \gamma_e = \rho_0\left(\frac{\partial\varepsilon}{\partial\rho}\right)_T, \tag{2.8}$$

where ρ_0 is the average density of the medium and γ_e is the electrostrictive coefficient, to be discussed in the stimulated Brillouin scattering section.

As suggested by Brillouin [5], at the thermal equilibrium, pressure variations are principally attributed to thermally-generated phonons in both fluids and optical fibres (which can be considered as a homogeneous fluid, viscous and compressible). Therefore, in a macroscopic description, the coupling between light and thermal phonons (acoustic wave) is usually introduced as a small time-varying part of the permittivity [4]. This leads to small displacements of the medium that modify locally the density in the material. These fluctuations of density are considered to be small compared to the mean density, and hence, from a macroscopic point of view, the fibre is not affected by these internal modifications. However, the spectral repartition of the thermal energy is ruled by the Bose-Einstein distribution, the average number of phonons is given by:

$$N = \frac{1}{\exp\left(\frac{hf}{kT}\right)-1} + \frac{1}{2}, \tag{2.9}$$

where h=6.626x10^{-34} J.s is the Planck constant, k=1.381x10^{-23} J.K^{-1}. N~620 is a number found at room temperature (T=298 K) and at the typical frequency of Brillouin scattering in silica (f~10GHz). In bulk silica, longitudinal and degenerated transverse modes coexist and can be observed [9]. Due to the geometry of the fibre, both cladding and core acoustic modes can propagate [6, 7, 8]. If the optical and the acoustic modes do not significantly overlap, as it is the case in the cladding of step-index fibres, the scattering is weak and can be barely detected. In the core, only forward and backward directions are of interest. Shear modes produce a scattering that can only be detected in the direction normal to the fibre axis [6, 7, 18]. Only the longitudinal mode remains which is obviously a pressure wave inducing periodic variations of the density, and hence a density wave. This explains why the dielectric constant fluctuation is written as a function of density fluctuations $\Delta\rho$ instead of pressure fluctuations Δp.

The acoustic waves represented by the local fluctuations $\Delta\rho$ of the average density of the medium ρ_0 is given by Eq (2.10):

$$\rho(z,t) = \rho_0 + \Delta\rho(z,t), \tag{2.10}$$

Eq. (2.11) describes the periodic behavior of the density fluctuations (where c.c. means conjugate complex).

$$\Delta\rho(z,t) = \frac{1}{2} Q(z,t) e^{j(\Omega t - qr)} + c.c\,, \tag{2.11}$$

where the variables Ω and q represent respectively the angular frequency and the wave vector of the acoustic wave. Finally, Eq. (2.12) represents the propagation of these density fluctuations.

$$\frac{\partial^2 \vec{\rho}}{\partial^2 t} - \Gamma'\nabla^2 \frac{\partial \vec{\rho}}{\partial t} - V_a^2 \nabla^2 \vec{\rho} = 0\,, \tag{2.12}$$

where V_a denotes the velocity of longitudinal acoustic waves which depends on the properties of the material (molecular mass, adiabatic compressibility), in fused silica for instance its value is about 5900 m/s. Γ' is the damping parameter defined as:

$$\Gamma' = \frac{1}{\rho}\left[\frac{4}{3}\eta_s + \eta_b + \frac{\kappa}{C_p}(\gamma_r - 1)\right], \tag{2.13}$$

where η_s and η_b are respectively the shear and bulk viscosity coefficients, κ is the thermal conductivity and γ_r is known as the adiabatic index.
Now we shall address the situation when the monochromatic electromagnetic wave (optical wave) travels along these thermal acoustic wave fluctuations.

- **Coupling between acoustic and optical wave**

Eq. (2.14) represents the spatial-temporal evolution of a monochromatic electromagnetic wave characterized by its wave vector k and its angular frequency ω.

$$\vec{E}(z,t) = \frac{1}{2} A(z,t) e^{j(\omega t - kr)} + c.c.\,, \tag{2.14}$$

From previous analysis, we know that the polarization in the simultaneous presence of electromagnetic waves and acoustic waves can be derived from Eqs. (2.4) and (2.8) as represented in the following equation,

$$\vec{P}_d(r,t) = \Delta\varepsilon \vec{E}(r,t) = \frac{\gamma_e}{\rho_0} \Delta\rho(z,t) \vec{E}(r,t)\,, \tag{2.15}$$

By inserting Eqs (2.11) and (2.14) in Eq. (2.15), the polarization is written as:

$$\vec{P}_d(r,t) = \frac{\gamma_e}{4\rho_0}\left[QAe^{j((\omega+\Omega)t-(k+q)r)} + Q^* Ae^{j((\omega-\Omega)t-(k+q)r)} \right] + c.c., \quad (2.16)$$

Finally, by inserting Eq. (2.16) in the perturbed wave equation (Eq. (2.1)), Eq. (2.17) is obtained and describes the spontaneous Brillouin scattering.

$$\nabla^2 \vec{E}_s - \frac{n^2}{c^2}\frac{\partial^2 \vec{E}_s}{\partial t^2} = \frac{\mu_0 \gamma_e}{4\rho_0}\left[\underbrace{(\omega+\Omega)^2 QAe^{j((\omega+\Omega)t-(k+q)r)}}_{\text{Anti-Stokes component}} + \underbrace{(\omega-\Omega)^2 Q^* Ae^{j((\omega-\Omega)t-(k+q)r)}}_{\text{Stokes component}} \right] + c.c. \quad (2.17)$$

It is clear that in the presence of the acoustic wave, there are new spectral components due to the polarization of the medium. The generated two-spectral components appear at the frequency ω-Ω and ω+Ω, usually called respectively Stokes and anti-Stokes components.

- **Stokes and anti-Stokes waves**

Here the interest is to find the relation between the frequency shifts (called Brillouin shift) introduced by the scattering and the scattering direction. From Eq. (2.17), momentum and energy conservations respectively impose that the wave vector $\vec{k}_s$ of the Stokes component is given by:

$$\vec{k}_s = \vec{k} - \vec{q}, \quad (2.18)$$

and its the angular frequency is given by:

$$\omega_s = \omega - \Omega, \quad (2.19)$$

From a quantum point of view, an incident photon is annihilated leading to the creation of anti-Stokes photon and an acoustic phonon. These Eqs (2.18) and (2.19) also show that the scattered Stoke wave is accompanied by a frequency shift corresponding to the acoustic wave frequency. Figure 2-3(a) illustrates schematically the scattering process and allows determining geometrically the direction of scattering θ as shown in Figure 2-3(b). Frequencies and vector waves of the three waves are coupled together via the dispersion relations by:

$$\left|\vec{k}\right| = \omega\frac{n}{c}, \left|\vec{k}_s\right| = \omega_s\frac{n}{c}, \left|\vec{q}\right| = \frac{\Omega}{V_a}, \quad (2.20)$$

Since the acoustic wave's frequency Ω is much smaller than that of the incident and scattered optical waves involved in the process, the approximation that $\left|\vec{k}\right| \approx \left|\vec{k}_s\right|$ can be made. The analysis of the Figure 2-3 leads to the relation $\left|\vec{q}\right| = 2\left|\vec{k}\right|\sin\left(\theta/2\right)$ for the acoustic wave vector. Using the dispersion relations, the frequency shift experienced by the Stokes wave as a function of the scattering angle θ is given by:

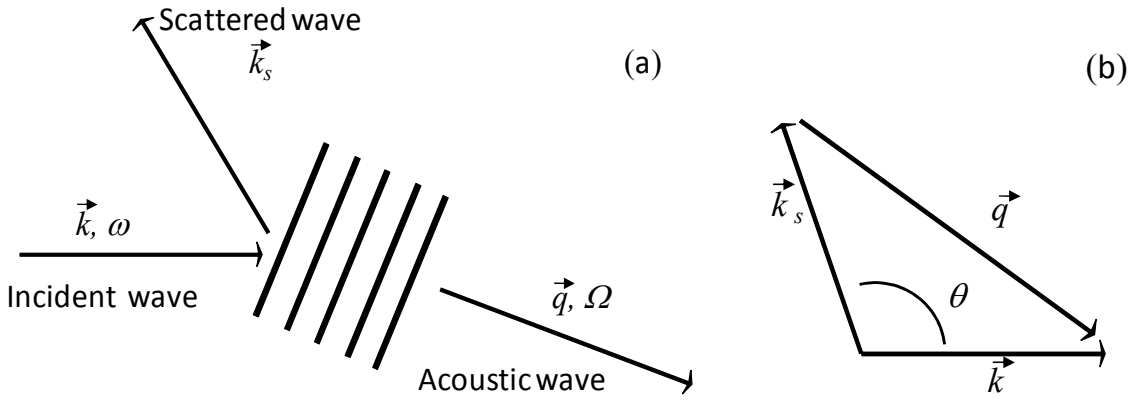

Figure 2-3: Illustration of the generation of a Stokes component through Brillouin scattering [2].

$$\Omega = 2n\omega\frac{V_a}{c}\sin\left(\theta/2\right), \tag{2.21}$$

In the forward direction, the frequency shift is equal to zero since $\theta=0$, while it is maximum in the backward direction since $\theta=\pi$. In this case the shift reads as $\Omega=2n\omega V_a/c$.

In optical fibres, Hereafter, the Brillouin shift ν_B will denoted the maximum value of Ω an given by.

$$\nu_B = \frac{\Omega}{2\pi} = \frac{2nV_a}{\lambda}, \tag{2.22}$$

where λ is the wavelength of the incident light. The typical value of the maximum Brillouin frequency shift in optical fibre is 10.8 GHz at 1.55 μm and 13 GHz at 1.3 μm, as summarised in Table 2-1.

An analogous analysis can be applied to the anti-Stokes wave. In this case the momentum and

Table 2-1: Brillouin shift and typical characteristics of the silica at two different wavelengths 1.55 μm and 1.3 μm.

Incident wavelength λ_p	1.55 μm	1.3 μm
Refractive index of the fibre n	1.46	1.46
Acoustic velocity V_a	5900 m/s	5900 m/s
Brillouin shift ν_B	10.8 GHz	13 GHz

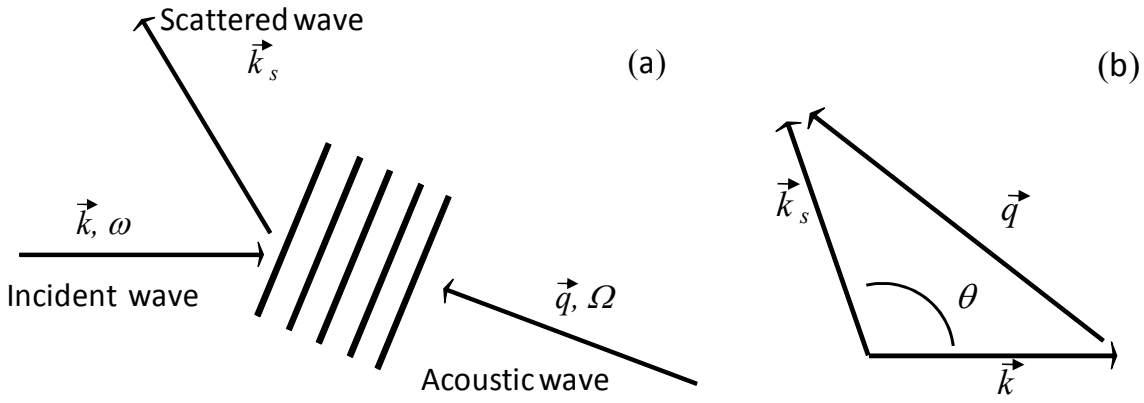

Figure 2-4: Illustration of the generation of an anti-Stokes component through Brillouin scattering [2].

energy conservations relations are expressed as:

$$\vec{k}_{as} = \vec{k} + \vec{q}\,, \tag{2.23}$$

$$\omega_s = \omega + \Omega\,, \tag{2.24}$$

Figure 2-4 illustrates schematically the process of the generation of an anti-Stokes component by an acoustic wave, and allows us to determine geometrically the direction of scattering θ.

The anti-Stokes emission is up-shifted in frequency by an amount equal to the acoustic wave frequency. From a quantum point of view, an incident photon is annihilated leading to the creation of a Stokes photon and the annihilation of an acoustic phonon.

To summarise, the Brillouin shift ν_B remains the same in absolute value for the both Stokes and anti-Stokes components while the direction of propagation of the acoustic waves implied in the two processes leads to a down shift $\nu_s = \nu - \nu_B$ (Stokes wave) and a up-shift $\nu_s = \nu + \nu_B$(anti-Stokes wave) of the optical frequency.

Figure 2-5 shows an experimental spectrum representing the elastic Rayleigh and inelastic Brillouin contributions to scattering in a single mode optical fibre (G652A IUT). The figure clearly shows that in the spontaneous regime at room temperature (as is the case here), the scattering efficiency is very small, around three orders of magnitude smaller than Rayleigh scattering. This results from the efficiency of the spontaneous Brillouin scattering that depends on the temperature or, more precisely, on the number of thermal acoustic phonons in the optical fibre. However, in a stimulated regime, the number of acoustic phonons increases rapidly and the scattering's efficiency also increases to eventually reach 100% [19].

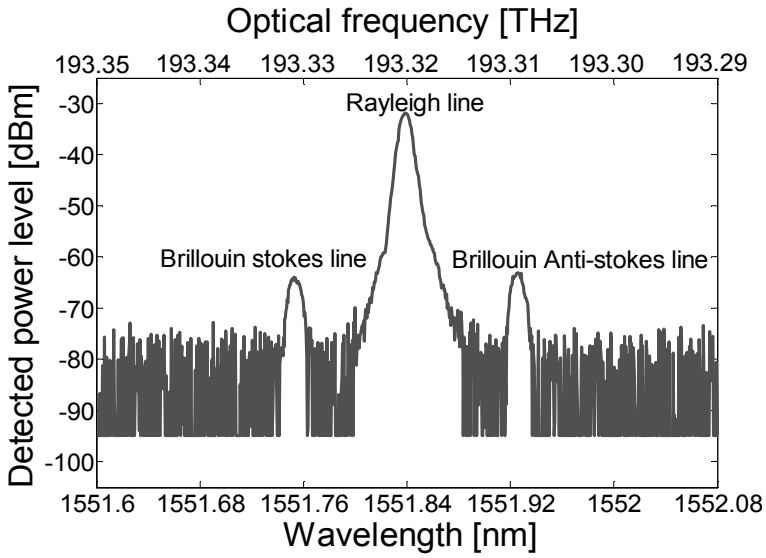

Figure 2-5: Brillouin and Rayleigh lines observed in the light backscattered from an incident lightwave (λ = 1551.84 nm) in a 20 m long single-mode optical fibre (G652A IUT). The Brillouin shift is measured to be 10.860 GHz.

2.2 Non-linear effects

Non-linear effects in a dielectric medium such as optical fibres result from the intense electromagnetic fields applied into the fibres. The intrinsic response of the medium is changed by deforming the balance of its electronic cloud of electrons, or modifies the binding of atoms constituting the molecules [11, 12]. The susceptibility of the material becomes dependent on the magnitude of the fields in the medium. As a result, the induced polarization $\vec{P}$ is no longer only a linear function of the incident electric field E but $\vec{P}$ is split in two part: linear $\vec{P}_L$ and non linear $\vec{P}_{NL}$ given by:

$$\begin{aligned}\vec{P} &= \varepsilon_0 \left(\underbrace{\chi^{(1)}.\vec{E}}_{P_L} + \underbrace{\chi^{(2)}:\vec{E}\vec{E} + \chi^{(3)}\vdots\vec{E}\vec{E}\vec{E} + \ldots}_{P_{NL}} \right), \\ &= \vec{P}_L + \vec{P}_{NL}^3\end{aligned} \tag{2.25}$$

where $\chi^{(n)}$ is the n-rank tensor of susceptibility; the symbols, : and $\vdots$ are respectively the first-rank, the second-rank and the third-rank tensorial products. The real and imaginary part of the first-rank susceptibility corresponds to the refractive index of the material $\left(n(\omega) = \sqrt{1 + \mathrm{Re}\left\{ \chi^1(\omega) \right\}} \right)$ and to the linear absorption coefficient $\left(\alpha(\omega) = \frac{\omega}{c.n(\omega)} \mathrm{Im}\left\{ \chi^1(\omega) \right\} \right)$ [13]. The second-rank susceptibility $\chi^{(2)}$ is

responsible for many effects, such as second harmonic generation (SHG) and sum frequency generation (SFG) in materials with an absence of inversion symmetry at the molecular level. The centro symmetrical character of the silica gives it the second-rank susceptibility to be equal to zero, *and, hence optical fibres do not exhibit second-order non-linear effects* [2, 15] (this explains why in Eq. (2.25) the non linear part of the polarization $\vec{P}$ is reduced to the only third order $\vec{P}_{NL}^{3}$). The third-order susceptibility $\chi^{(3)}$ is responsible for the lowest order non-linear effects in fibres: stimulated scattering effects (SBS and SRS) and optical Kerr responsible of third-harmonic generation (THG), four-wave-mixing (FWM), self-phase modulation (SPM) and modulation instability (MI). If some of these effects have generated significant scientific interests in a wide variety of applications, we will see in the second part of the next chapter that some of them such as SPM, MI and Raman effects have negative impact on the performances of the Brillouin sensor

2.2.1 Non-linear scattering: stimulated Brillouin scattering in optical fibres

Being a linear phenomenon, since the intensity incident of the light has no effects on the optical response of the material, spontaneous scattering is attributed to the presence of in- homogeneities in the medium. In this case, these in-homogeneities are attributed to the density adiabatic fluctuations i.e. thermal acoustic phonons (acoustic wave). The efficiency of this scattering in the spontaneous regime is very small, when compared to Rayleigh scattering (cf. Figure. 2-5) and depends directly on the number of thermal acoustic phonons (Section 2.1). However, in the stimulated regime, the Brillouin scattering becomes a nonlinear phenomenon since the high incident intensity light can drive the generation of acoustic phonons. Thermal motions are no longer the only source of acoustic waves in the medium, there is also the incident light. The number of acoustic phonons therefore increases and enhances the efficiency of the stimulated process. This was first observed in crystals by Chiao in 1964 [16] and in optical fibres by Ippen in 1972 [17].

There are two different physical mechanisms by which optical waves can drive acoustic waves. One is electrostriction and the other is optical absorption[2], which is less commonly used than electrostrictive SBS, since it can occur only in lossy optical media [2]. Electrostriction is the main mechanism observed in silica.

2.2.1.1 Electrostriction

Electrostriction is the tendency of materials such as silica to become compressed in the presence of an electric field. The molecules of the material are moved by a force $\vec{F}$ that attracts material to regions of a high electric field $\vec{E}$ [2, 21], to maximize the potential energy Δu. From a macroscopic point of view, we can consider that the force acting on an individual molecule. In the presence of the field, the molecule develops a dipole moment that increases its potential energy Δu given by:

[2] Optical absorption is the fact that the heat evolved by absorption in regions of high optical intensity tends to cause the material to expand in those regions. The density variations induced by this effect can excite an acoustic disturbance.

$$\Delta u=\frac{1}{2}\Delta\varepsilon\left|\vec{E}\right|^2. \tag{2.26}$$

The force acting on the dipole moment is given by:

$$\vec{F}=-\nabla u. \tag{2.27}$$

As a result of density fluctuations of the material $\Delta\rho$, the fluctuations of the dielectric constant of the medium $\Delta\varepsilon$ due to the force F, which is accompanied by an electrostrictive pressure $p_{st,}$ is given by the Eq. (2.8). The work per unit volume $\Delta\varpi$ done by the force compressing the material is directly linked to p_{st} and is given by:

$$\Delta\varpi=p_{st}\frac{\Delta V}{V}=-p_{st}\frac{\Delta\rho}{\rho_0}. \tag{2.28}$$

As a general rule $\Delta\varpi=\Delta u$, considering Eq. (2.26), the value of p_{st} can be deduced as a function of intensity of the electric field $\vec{E}$,

$$p_{st}=-\frac{1}{2}\rho_0\frac{\partial\varepsilon}{\partial\rho}\left|\vec{E}\right|^2=-\frac{1}{2}\gamma_e\left|\vec{E}\right|^2, \tag{2.29}$$

where $\gamma_e=\rho_0\,\partial\varepsilon/\partial\rho$, as already defined such as the electrostrictive constant of the material (in Section.2.1). Since p_{st} is negative, the total pressure is reduced in regions of intense electric field. As a result, the molecules will be naturally moved into these regions within the medium, so that the material density will be locally compressed in the medium. Since the molecule displacement is very slow compared to that of the optical waves, $V_a\,n/c=10^{-5}$, the effect on the material must be characterized by the time averaged value $\langle|\vec{E}|^2\rangle$ as written in Eq. (2.30) instead of the instantaneous field $|\vec{E}|^2$ as written in Eq. (2.29). This implies that, only the low frequency components of the optical intensity would give rise to an electrostrictive pressure within the medium.

$$p_{st}==-\frac{1}{2}\gamma_e\left\langle\left|E\right|^2\right\rangle. \tag{2.30}$$

2.2.1.2 Stimulated Brillouin scattering through electrostriction

From the previous section, electrostriction is the driving mechanism basis of SBS in optical fibres since it can generate a great number of acoustic phonons. The stimulation grows from the beating of the incident wave (later to be called ‘pump wave’, symbol ‘p’ is used for pump) with the Stokes wave (later to be called ‘signal wave’, to differentiate from scattered spontaneous waves, symbol ‘s’ is used for signal).

Two configurations can be distinguished; one is the Brillouin generator if the signal wave originates from the backscattered stimulated Brillouin process. In this case Brillouin shift is given

by Eq. (2.22), $\nu_B = \Omega/2\pi = 2nV_a/\lambda_p$. The other is the Brillouin amplifier if the back-propagating signal wave is externally injected into the medium. In this case, this external signal must be set at the frequency of the Stokes wave coming from spontaneous scattering in the medium that undergoes amplification through the SBS process. The maximum frequency shift is given by the of the frequency pump and signal difference equal to the maximum Brillouin shift, $\nu_p - \nu_s = \nu_B = \Omega/2\pi$.

Figure 2-6 illustrates the cycle of the SBS process where two waves, strong pump and small signal counter-propagate along the fibre. When the difference between the optical frequencies of the two waves is around the Brillouin shift of the medium (this is automatic for the Brillouin generator), electric density of energy associated with the beating signal oscillates at the frequency around that of the acoustic waves implied in the Brillouin scattering. The electrostriction then produces a pressure wave which reinforces the acoustic waves already present in the medium, and hence, enhances the efficiency of the scattering. Gradually the signal wave sees its amplitude grow as a result of the backscattering of the pump wave. At the same time, the pump wave sees its intensity decrease. It can be review that the electrostriction phenomenon is a "reservoir" of acoustic phonons producing a Bragg index grating [10] , diffracting the pump wave to the signal wave with more and more efficiency as the acoustic wave grows.

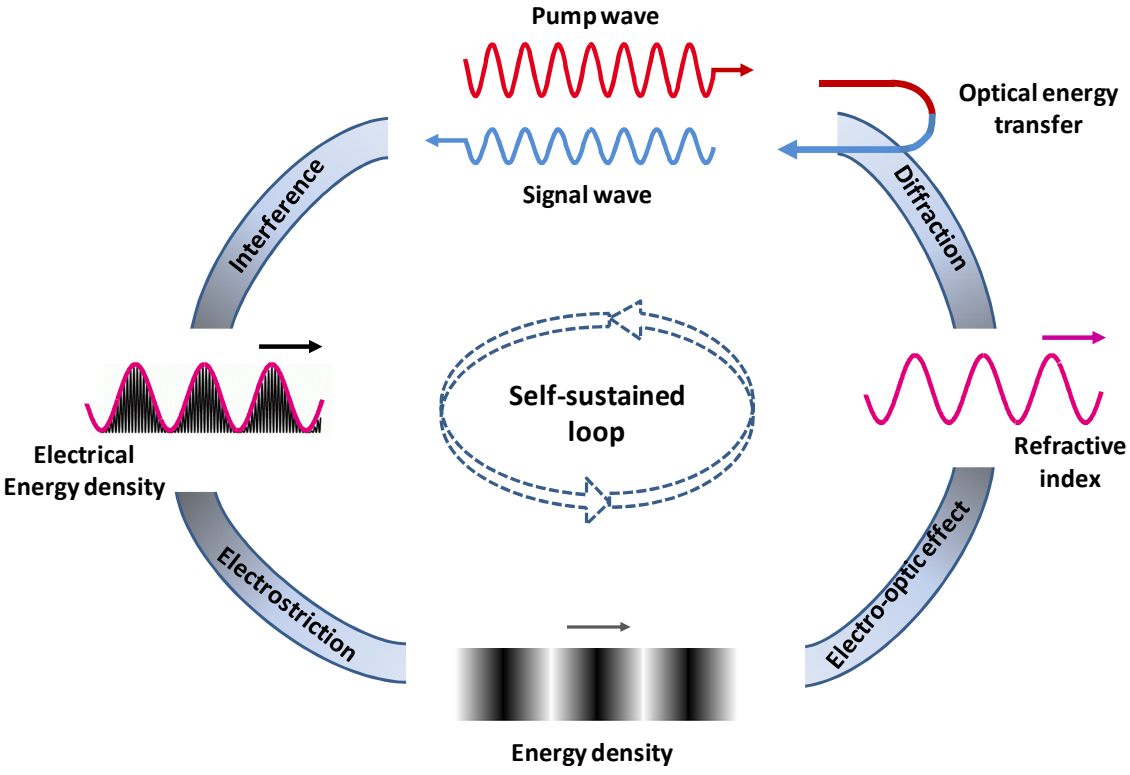

Figure 2-6: Schematic representation of the stimulated Brillouin scattering process: Concurrent phenomena involve in the process.

2.2.1.3 Theoretical description of SBS

Now it is clear that SBS involves a set of three waves (the pump, the signal and the acoustic wave) coupled together by a photon-phonon interaction. As the single mode optical fibre is the medium of propagation for this study, then the waves propagate along the fibre axis (the *z* axis). According to the phase-matching condition introduced in Section 2.1, the pump and acoustic waves are therefore co-propagating in the positive direction of the fibre (positive *z*), and the signal wave is counter-propagating as sketched in Figure 2-7.

Let us see now how address the non-linear coupling among the three interacting waves. The optical field within the Brillouin medium is represented as

$$\vec{E}=\vec{E}_p+\vec{E}_s\,, \tag{2.31}$$

where pump and signal fields are defined by:

$$\vec{E}_p=e_p A_p\left(z,t\right)\exp\left[\,j\left(\omega_p t+k_p z\right)\right]+c.c.\,, \tag{2.32}$$

$$\vec{E}_s=e_s A_s\left(z,t\right)\exp\left[\,j\left(\omega_s t-k_s z\right)\right]+c.c.\,, \tag{2.33}$$

where e_p and e_s are respectively the unit polarization vectors for the pump and the signal waves. A_p and A_s are respectively the complex envelopes of the pump and signal waves.

The acoustic wave is described in terms of the material density distribution as:

$$\Delta\rho\left(z,t\right)=Q\left(z,t\right)\exp\left[\,j\left(k_p z+\Omega t\right)+c.c.\right], \tag{2.36}$$

where $\Omega=\omega_p-\omega_s$, and ρ_0 denotes the means density of the medium.
Referring to the perturbed wave equation (Eq. (2.1)), the spatial and temporal evolution of the two optical waves is given by:

$$\nabla^2\vec{E}_p-\frac{n^2}{c^2}\frac{\partial^2\vec{E}_p}{\partial t^2}=\mu_o\frac{\partial^2\vec{P}_{NL,p}}{\partial t^2}\,, \tag{2.34.a}$$

$$\nabla^2\vec{E}_s-\frac{n^2}{c^2}\frac{\partial^2\vec{E}_s}{\partial t^2}=\mu_o\frac{\partial^2\vec{P}_{NL,s}}{\partial t^2}\,, \tag{2.34.b}$$

The spatial and temporal evolution of the acoustic wave is given by [2]:

$$\frac{\partial^2\Delta\rho}{\partial t^2}-\Gamma'\nabla^2\frac{\partial\Delta\rho}{\partial t}-V_a^2\nabla^2\Delta\rho=-\nabla.F\,, \tag{2.34.c}$$

where Γ' is a damping parameter given by Eq. (2.13). The right-hand side term of Eq. (2.34.c) consists of the divergence of the electrostrictive force $\vec{F}$ per unit volume as defined in Eq.(2.27). Considering the total field in Eq. (2.31) and considering that there is no excitation at 2 Ω. Assuming

that the waves are quasi-monochromatic, then the slowly varying envelopes approximation (SVEA) can be applied. After some calculations, $\nabla\vec{F}$ can be written as:

$$\nabla.\vec{F}=\frac{1}{2}\sqrt{\eta_p}\,\gamma_e q^2\left[A_p A_s^* \exp\left(j\left(qz-\Omega t\right)\right)+\text{c.c.}\right], \tag{2.35}$$

where $\eta_p=\left|e_p \bullet e_s\right|^2$ represent the polarization efficiency of the process. As the medium polarization was linear for spontaneous scattering, here the polarization is non linear ($\vec{P}_{NL}(r,t)$) since the susceptibility depend on E and is responsible of the coupling between the Eqs. (2.34). $\vec{P}_{NL}(r,t)$ is derived by substituting Eqs. (2.32) and (2.33) in Eq. (2.15) which leads to the following relations

$$\vec{P}_{NL,p}(r,t)=e_p\frac{\gamma_e}{\rho_0}Q(z,t)A_p(r,t)e^{j\left(\omega_p t+k_p z\right)}, \tag{2.35.b}$$

$$\vec{P}_{NL,s}(r,t)=e_s\frac{\gamma_e}{\rho_0}Q^*(z,t)A_s(r,t)e^{j\left(\omega_p t-k_p z\right)} \tag{2.35.c}$$

SVEA allows neglecting the second space and time derivatives of the optical field amplitudes. Substituting Eqs (2.31), (2.32), (2.35) and (2.34) and supposing η_p=1 (meaning that the polarizations of the two optical waves are perfectly aligned), after some calculations the system of three coupled differential equations is thus obtained [10, 30, 37, 38] which details of all calculations can be found in Appendix A1:

$$\frac{\partial A_p(z,t)}{\partial z}+\frac{1}{V_g}\frac{\partial A_p(z,t)}{\partial t}=\frac{1}{2}ig_{2,p}A_s(z,t)Q(z,t) \tag{2.36a}$$

$$\frac{\partial A_s(z,t)}{\partial z}-\frac{1}{V_g}\frac{\partial A_s(z,t)}{\partial t}=-\frac{1}{2}ig_{2,s}A_p(z,t)Q^*(z,t) \tag{2.36b}$$

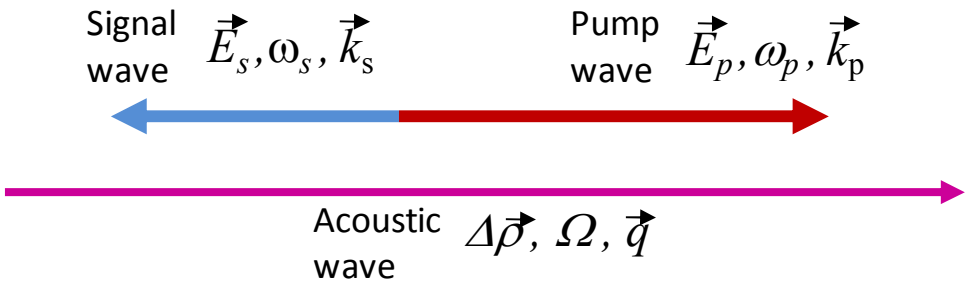

Figure 2-7: Orientation of the waves involved in stimulated Brillouin scattering in optical fibre.

$$\frac{\partial Q(z,t)}{\partial z}+\frac{\partial Q(z,t)}{\partial t}+\Gamma_A Q(z,t)=ig_1 A_p(z,t)A_s^*(z,t);$$
$$\Gamma_A=i\frac{\Omega_B^2-\Omega^2-i\Omega\Gamma_B}{2\Omega} \qquad (2.36c)$$

The last equation can be further simplified by omitting the second term in the left-hand side. In fact, the acoustic waves are attenuated over very short distance (<10 μm) such that the source term appears to be constant [2, 19]. Remaining at the Brillouin resonance, the last equation can be rearranged as

$$\frac{\partial Q(z,t)}{\partial t}+\frac{\Gamma_B}{2}Q(z,t)=ig_1 A_p(z,t)A_s^*(z,t) \qquad (2.37)$$

Notations and approximations: ω_p, ω_s and $\Omega=\omega_p-\omega_s$, are the center angular frequencies of the pump, signal and acoustic waves respectively, while k_p, k_s and $\vec{q}=\vec{k}_p-\vec{k}_s$ are their wave vectors. $g_1=\gamma_e q^2/8\pi\Omega$ and $g_2=\gamma_e\omega_{s,p}/cn\rho_0$, represent, respectively, the electrostrictive and elasto-optic coupling effects, both related to the electrostictive constant [2]. $A_p(z,t)$, $A_s(z,t)$ and $Q(z,t)$ are slowly varying complex envelopes. $\Omega_B=2\pi\nu_B$ is the Brillouin frequency shift for resonant interaction between the three waves, and $\Gamma_B=q^2\Gamma'$ is the damping acoustic wave coefficient.

2.2.1.4 Solutions in steady state conditions and relation between phonons life time and Brillouin line-width

The steady state conditions means that the system stops evolving for the three waves, i.e. all first temporal time derivatives are zero ($\partial/\partial t=0$). It must be pointed out that this approximation is valid for continuous waves (CW) or long pulse widths (much longer than the phonon lifetime).

In silica fibres, while optical waves undergo a very small attenuation, the acoustic waves undergo strong attenuation through the damping parameter $\Gamma'$and; again, propagate only over shorter distances, indeed few micrometers. Consequently the intensity of the acoustic wave undergoes an exponential decay described as following:

$$\left|\Delta\rho(t)\right|^2=\left|\Delta\rho(0)\right|^2 e^{-t/\tau_A}, \qquad (2.38)$$

where $\tau_A=1/\Gamma_B=1/\Gamma'|q|^2$ represents the average lifetime of the acoustic phonons in the fibre and is inversely proportional to the acoustic damping coefficient Γ_B. However τ_A is intimately related to the FWHM width $\Delta\nu_B$ of the Brillouin spectrum. In the literature one can find two different definitions of the acoustic phonon lifetime. Either [2]:

$$\tau_A=\frac{1}{\Gamma_B}=\frac{1}{2\pi\Delta\nu_B}, \qquad (2.39)$$

Or [23]:

$$\tau'_A=\frac{1}{\Gamma'_B}=\frac{1}{\pi\Delta\nu_B} \tag{2.40}$$

Here below, we explain that the former definition, Eq. (2.39), is the more consistent and, thus, should be adopted.

Let assume a constant signal wave, $A_s(z,t)\equiv A_s^0$, a null initial acoustic conditions, $Q(z,t=0)\equiv 0$, and a propagating pump pulse of temporal width, T. At some arbitrary point along the fibre, z_0, the time evolution of the complex envelope of the acoustic wave $Q(\Omega,z_0,t)$ at $\Omega=\omega_p-\omega_s$, is given by the direct solution of Eq. (2.36c):

$$Q(\Omega,z_0,t)=\begin{cases}\dfrac{ig_1A_p^{peak}A_s^{0*}}{\Gamma_A}\left[1-\exp\left(-\Gamma_A t\right)\right] & 0<t\le T \qquad (2.41a)\\[2ex] \dfrac{ig_1A_p^{peak}A_s^{0*}}{\Gamma_A}\exp\left(-\Gamma_A t\right)\left[\exp\left(+\Gamma_A T\right)-1\right] & t>T \qquad (2.41b)\end{cases}$$

When $\Omega=\omega_p-\omega_s$ is equal to Ω_B, $\Gamma_A=\Gamma_B/2$ is a *real* number, and the acoustic amplitude rise ($0< t <T$) and decay ($t >T$) are governed by the exponential term $\exp(-\Gamma_A t)$. Consequently, the temporal evolution of the acoustic *intensity*, $\left|Q(\Omega,z_0,t)\right|^2$ depends on $\left[\exp(-\Gamma_A t)\right]^2=\exp(-2\Gamma_A t)=\exp(-\Gamma_B t)$. In a process characterized by an exponential time build-up and decay, it is customary to define the *time constant* using the behavior of the *intensity* of the phenomenon, rather than its amplitude. Therefore, the acoustic *intensity* follows a $\exp(-t/\tau_A)$ time dependence as also shown in Eq. (2.38), whereas the acoustic amplitude is governed by $\exp(-t/(2\tau_A))$, having a twice longer time constant [22]. To relate τ_A to $\Delta\nu_B$, let us consider the case of a very long pump pulse, $T >> 2/\Gamma_B$, the acoustic wave stops growing $\partial Q/\partial t=0$ and therefore $Q(\Omega,z_0,t)$ of Eq. (2.37) becomes:

$$Q(\Omega,z_0,t)=\frac{ig_1A_p^{pulse\ peak}A_s^{0*}}{\Gamma_A} \tag{2.42}$$

Under these assumptions Eqs. (2.36a) and (2.36b) for the pump and signal waves are respectively reduced to Eqs. (2.43a) and (2.43b):

$$\begin{aligned}\frac{\partial A_p(z,t)}{\partial z} &= -i\frac{1}{2}g_2 A_s(z,t)Q(z,t)\\ &= \left[-i\frac{1}{2}g_2 A_s(z,t)\right]\left[-\frac{ig_1 A_p^{peak}A_s^{0*}}{\Gamma_A}\right]\\ &= -\frac{g_1 g_2\left|A_s^0\right|^2 A_p^{peak}}{2\Gamma_A}\end{aligned} \tag{2.43a}$$

$$\begin{aligned}\frac{\partial A_s(z,t)}{\partial z} &= -i\frac{1}{2}g_2 A_p(z,t)Q^*(z,t)\\ &= \left[-i\frac{1}{2}g_2 A_p(z,t)\right]\left[-\frac{ig_1 A_p^{peak}A_s^{0*}}{\Gamma_A}\right]^*\\ &= -\frac{g_1 g_2\left|A_p^{peak}\right|^2 A_s^0}{2\Gamma_A}\end{aligned} \tag{2.43b}$$

By deeply analyzing the form of these equations, it can be seen that the real part of the right hand members is responsible for the nergy transfer between the optical waves, while the imaginary part is responsible for a propagation phase associated to the non-linear interaction. Eq. (2.43b) can be readily solved to obtain:

$$\begin{aligned}A_s(z) &= A_s^0\exp\left[-\frac{g_1 g_2\left|A_p^{peak}\right|^2}{2\Gamma_A}z\right]\\ &= A_s^0\exp\left[-g_1 g_2\left|A_p^{peak}\right|^2\left[\frac{\Omega^2\Gamma_B}{\left(\Omega_B^2-\Omega^2\right)^2+\Omega^2\Gamma_B^2}\right]z\right],\end{aligned} \tag{2.44}$$

Remembering that the signal wave propagates in the -*z* direction, Eq. (2.44) describes the well-known exponential gain, characterizing the Brillouin process. It is possible to introduce coupled equations for the intensities of the two interacting optical waves. Taking the absolute square of the signal complex amplitude, we find the *z* dependence of the intensity given by Eq. (2.45):

$$\begin{aligned}I_s(z) = \left|A_s(z)\right|^2 &= \left|A_s^0\right|^2\exp\left[-2g_1 g_2\left|A_p^{peak}\right|^2\left[\frac{\Omega^2\Gamma_B}{\left(\Omega_B^2-\Omega^2\right)^2+\Omega^2\Gamma_B^2}\right]z\right],\\ &= \left|A_s^0\right|^2\exp\left[-g_B(\Omega)\left|A_p^{peak}\right|^2 z\right]\end{aligned} \tag{2.45}$$

Taking these considerations into account and introducing the linear loss in the fibre in equal quantities for both pump and signal ($\alpha=\alpha_p=\alpha_s$), differential coupled intensities equations are obtained in steady state conditions:

$$\frac{dI_p}{dz} = -g_B(\Omega) I_p I_s - \alpha I_p \tag{2.46a}$$

$$\frac{dI_s}{dz} = -g_B(\Omega) I_s I_p + \alpha I_s \tag{2.46b}$$

where $g_B(\Omega) = g_1 g_2 \left[\frac{\Omega^2 \Gamma_B}{\left(\Omega_B^2 - \Omega^2\right)^2 + \Omega^2 \Gamma_B^2} \right]$ is the Brillouin gain spectrum, and is known to be very narrow with respect to Ω_B so $\Omega \approx \Omega_B$. Therefore, it is common to approximate $\Omega_B^2 - \Omega^2$ by $2\Omega(\Omega_B - \Omega)$ to obtain the familiar Lorentzian lineshape:

$$g_B(\Omega) = g_B \left[\frac{\frac{\Gamma_B}{2}}{\left(\Omega - \Omega_B\right)^2 + \left(\frac{\Gamma_B}{2}\right)^2} \right], \tag{2.47}$$

where $g_B = \frac{k \gamma_e^2 \varepsilon_0 q^2}{\varepsilon \rho_0 \Omega_B \Gamma_B n c_0}$ is the centre line Brillouin gain coefficient which measured value in a single mode fibre is $1\text{x}10^{-11}$-$5\text{x}10^{-11}$ [24]. The Full Width Half Maximum (FWHM), $\Delta\Omega_B$ in rad/sec, or $\Delta\nu_B$ in Hertz, is given by:

$$\Delta\nu_B = \frac{\Delta\Omega_B}{2\pi} = \frac{\Gamma_B}{2\pi} = \frac{1}{2\pi\tau_A} \tag{2.48}$$

From Eqs. (2.47) and (2.48), the Brillouin gain spectral distribution is determined by the response to the acoustic wave *amplitude Q*, while the phonon life time τ_A is defined by the acoustic *energy* loss. As a result of the square law dependence between amplitude and energy, the rate of change on the acoustic amplitude is scaled by twice the phonon life time. This also explains the factor 2 in the expression relating the phonon lifetime τ_A to the FWHM width $\Delta\nu_B$ in Eq. (2.48), which is frequently omitted in the literature.

Figure 2.8 represents the Brillouin response to a small signal in an optical fibre, G652D IUT, at a wavelength of 1552 nm, as a function of the frequency difference between the pump and signal waves. It illustrates the match with a Lorentzian shape distribution of the Brillouin gain spectrum (BGS). The measured FWHM linewidth of this distribution is 27 MHz, resulting in $\Gamma_B = 169\,\text{MHz}$ and an acoustic phonon life time of $\tau_A \sim 5.89\,\text{ns}$ and 11.78 ns in amplitude which is about the value we find in the literature. The measured Brillouin shift of this fibre is 10.727 GHz, which of course can change according to the fibre type, which in most of cases depends on the core doping concentration.

By expressing the electrical fields in Eqs. (2.43) in terms of theirs intensities and phases as,

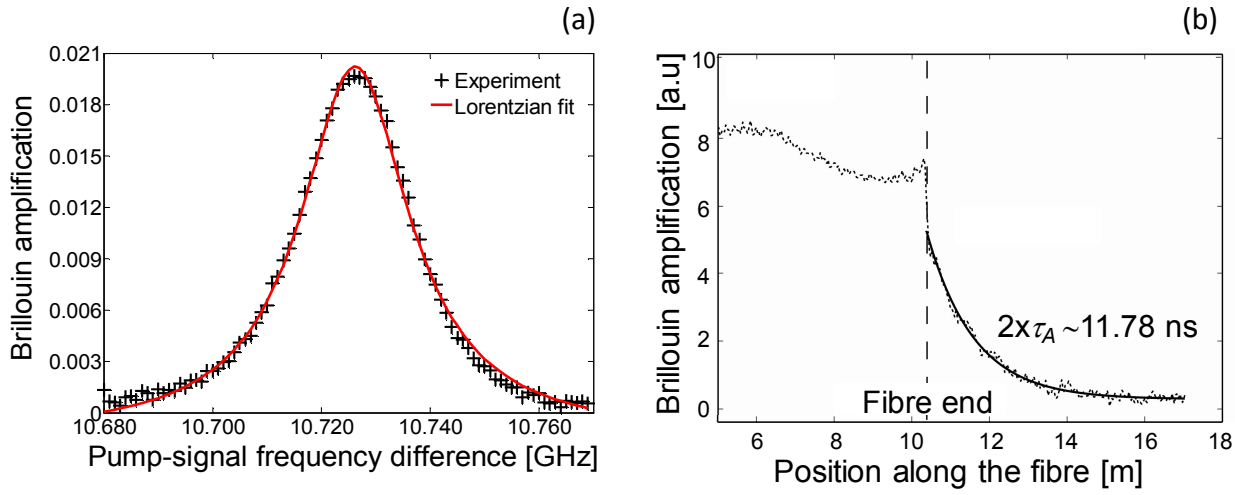

Figure 2-8: (a) Lorentzian distribution (solid line) drawn with measured Brillouin gain spectrum (dotted line). The measured Brillouin shift is 10.727 GHz, the linewidth is 27 MHz and the acoustic lifetime is τ_A= 5.89 ns (b). Details of experimental set-up are provided in chapter 4.

$$A_p(z) = I_p(z)\exp(-i\phi_p^{SBS} z), \tag{2.49.a}$$

$$A_s(z) = I_s(z)\exp(i\phi_s^{SBS} z), \tag{2.49.b}$$

and by taking the imaginary part, we easily obtain the expression for the additional phase shifts due to SBS:

$$\frac{\partial \phi_p^{SBS}}{\partial z} = g_B I_s \frac{(2\Delta\nu/\Delta\nu_B)}{1+(2\Delta\nu/\Delta\nu_B)^2}, \tag{2.50.a}$$

$$\frac{\partial \phi_s^{SBS}}{\partial z} = g_B I_p \frac{(2\Delta\nu/\Delta\nu_B)}{1+(2\Delta\nu/\Delta\nu_B)^2}, \tag{2.50.b}$$

which are usually defined in the way that a positive $\phi_{p,s}^{SBS}$ implies a supplementary positive delay. Consequently, both optical waves are retarded for a positive $\Delta\nu$ while there are advanced for a negative $\Delta\nu$ as illustrated in Figure 2-10. Recently these phase characteristics of the SBS in optical fibres has been successfully exploited to control the group velocity of optical signals [40].

2.2.1.5 Solutions in steady state conditions in the un-depleted pump approximation

Differential coupled-intensities equations (Eq. (2.4)) cannot be resolved analytically in presence of a non vanishing loss [2]. A very simple solution can be obtained by assuming that the pump is attenuated by the fibre loss only: the pump is said to be un-depleted. In these conditions, and from Eq. (2.46a), it is possible to retrieve the pump-intensity length dependence

$$I_p(z)=I_p^0\exp(-\alpha z) \tag{2.51}$$

where I_p^0 is the initial injected pump intensity at z=0. However, the Brillouin signal intensity can be obtained by inserting Eq. (2.49) into Eq. (2.46b) and integrating over the whole fibre length L. The obtained Eq. (2.52) clearly shows that, in the un-depleted approximation[3], the signal intensity grows exponentially with the initial pump intensity, the fibre length L.

$$I_s(0)=I_s^L\exp\left(g_B I_p^0 L_{eff}-\alpha L\right) \tag{2.52}$$

where I_p^0 is the initial injected signal intensity at z=L. L_{eff} denotes the effective length that can be seen as the total length over which the pump remains constant. $L_{eff.}$ is adjusted in such a way that the effect produced by a constant intensity I_p over the length L_{eff}, is equal to that produced over the real fibre length L taking into account the attenuation of the fibre α. Eq. (2.63) gives the relationship between the effective length L_{eff}, the real length L, and the attenuation α,

$$L_{eff}=\frac{1}{\alpha}\left[1-\exp(-\alpha L)\right], \tag{2.53}$$

where it can be rapidly seen that L_{eff} tends to $1/\alpha$ for large lengths, and thus does not exceed 15 km at 1.3 μm and 20 km at 1.55 μm.

Here we take advantage of also introducing the concept of effective area A_{eff}, since as with L_{eff}, A_{eff} is a very important parameter when it comes to scale non-linear effects in optical fibres which depend on intensity distribution instead of power distribution. However, the field is not uniformly distributed inside a single-mode step-index fibre. It also propagates out of the core of the fibre (transversal distributions). Since this distribution is usually not precisely known, one can consider that the intensity distribution of the mode is constant over an effective area A_{eff} which is linked to the intensity and the power by I=P/A_{eff}, and hence allowing the linking of experimental conditions with theoretical conditions. The effective core area can be expressed as [25]:

$$A_{eff}=\frac{2\pi\left[\int_0^{+\infty}I(r)rdr\right]^2}{\int_0^{+\infty}I(r)^2rdr}, \tag{2.54}$$

where I(r) is the intensity of the fundamental mode at radius r. A_{eff} can vary over a range of 20-100 μm^2 in the 1.55 μm region depending on the fibre design [25].

2.2.1.6 Brillouin critical power

[3] In the second part of the next chapter we will discuss the situation when the pump experiences depletion to the benefit of the signal and its effect on the determination of Brillouin shift and its impacts on Brillouin sensors.

According to Smith [26], the SBS critical Brillouin power is defined as the input pump power for which the backward stimulated signal power becomes comparable to the input pump power [26]. The following equation represents the Smith's relation for the SBS critical power:

$$P_{crit} \approx K_{SBS} \frac{19 A_{eff}}{g_B L_{eff}} \tag{2.55}$$

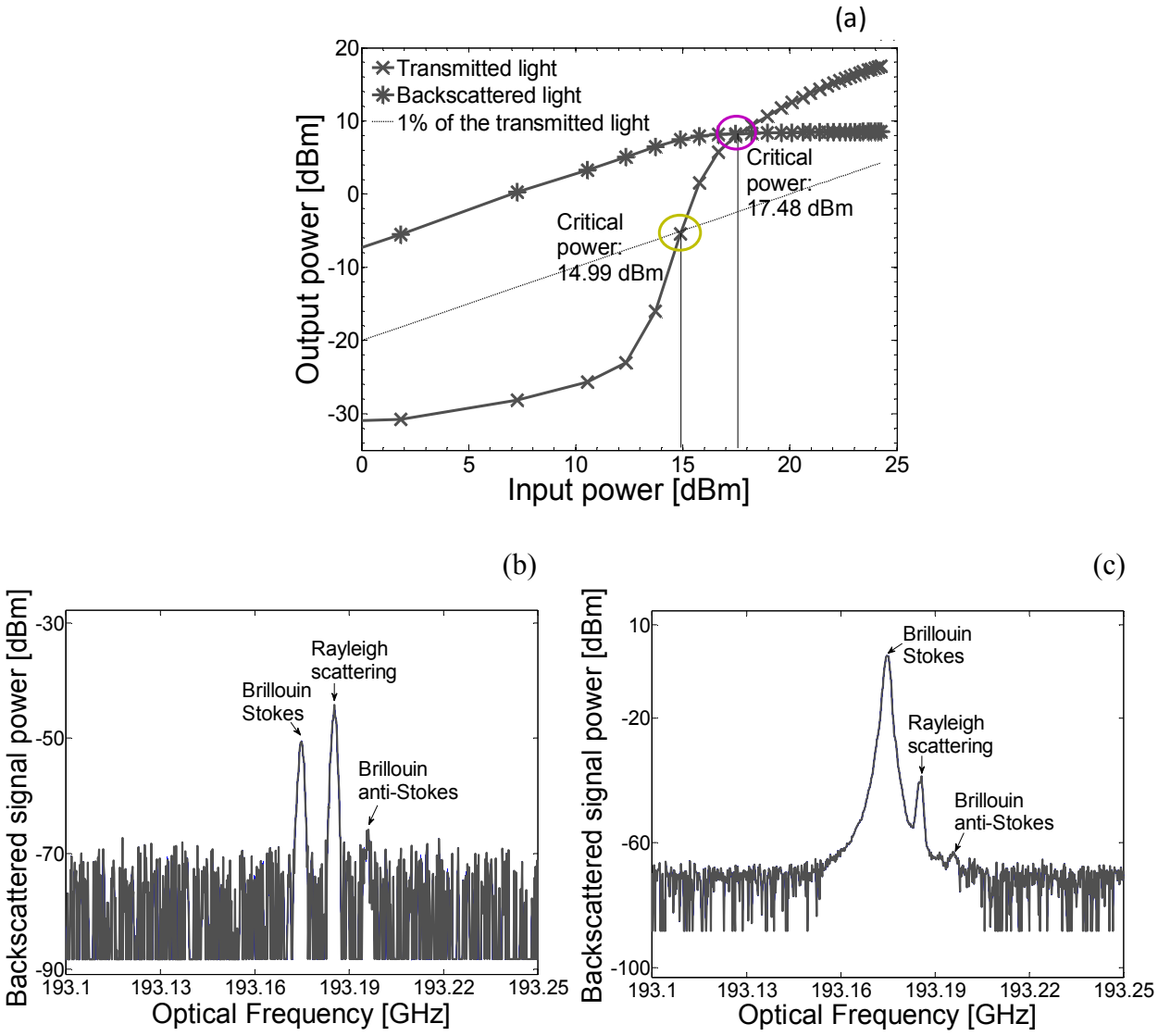

Figure 2-9: (a) Transmitted (cross) and backscattered power measurements as a function of the input power (circle) of 5 km fibre. The dashed curve is the 1% of the input power. Measured critical powers are 14.99 dBm (according to Bayvel) and 17.48 dBm (according to Smith). (b) - (c) Brillouin lines and Rayleigh line observed in the light backscattered from two different incident lightwave powers (λ = 1551.84 nm). The Brillouin shift was measured to 10.860 GHz.

where the factor K_{SBS} depends on the exact value of Brillouin gain [28,29,39].
According to *Bayvel* [27], the experimental SBS critical power is defined when the backscattered signal power reaches 1% of the input pump power. Figure 2-9 (a) shows the critical power according to Bayvel and Smith criterias.

2.2.1.7 Brillouin antistokes

It has been seen that in the spontaneous Brillouin regime the amplitude of the two components, Stokes and anti-Stokes, is low but remains comparable (cf. Figure 2-4), while the direction of propagation of acoustic waves implied in the two processes leads to a down shift $\nu_s=\nu-\nu_B$, (Stokes wave) and up shift $\nu_s=\nu+\nu_B$ (anti-Stokes wave) of the optical frequency. The efficiency is around three orders of magnitude less than Rayleigh scattering due to the number of thermal acoustic phonons in the optical fibre. However, in the stimulated Brillouin regime, when the input pump power increases, the signal grows exponentially (Figure 2-9(b)) to typically become the dominating peak of the backscattered spectrum as illustrated in Figure 2-9(c). In this figure, the line of the Brillouin anti-Stokes component has vanished. This can be understood from a quantum point of view. Let us take the case of the Stokes process first. In this case, a pump photon is annihilated to *create* a Stokes photon and an acoustic phonon, increasing rapidly the number of acoustic phonons, and hence enhancing the Stokes phonons already present in the fibre:

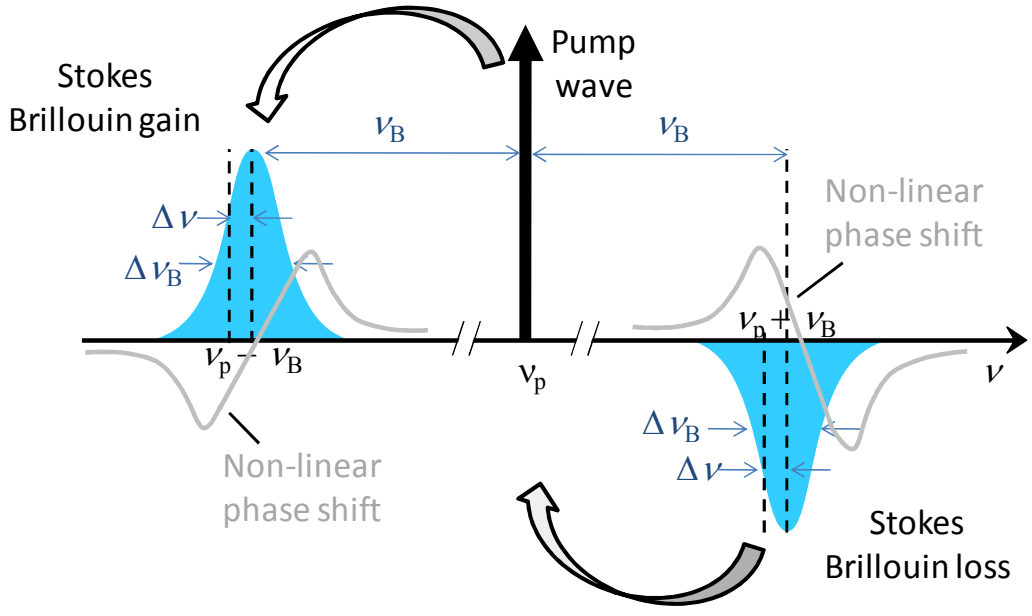

Figure 2-10: Illustration of the Lorentzian shape of the Brillouin gain spectrum and Brillouin loss spectrum and of the associated non linear phase shift. Energy transfer is made from higher frequencies to lower frequencies.

However, in the case of the anti-Stokes process a pump photon *and* an acoustic phonon are *annihilated* to *create* an anti-Stokes photon, thus decreasing the number of phonons, which leads to the vanishing of the acoustic wave and the reduction of the efficiency of the process [19, 30]. In conclusion, Stokes scattering creates phonons, while anti-Stokes scattering annihilates phonons. In SBS process the exchange of the energy of the photon with material is made from the high frequencies to lower frequencies (cf. Figure 2-10). Consequently stimulated Brillouin scattering is never an anti-Stokes process. The process is called *Brillouin gain* when the CW signal is spectrally down-shifted with respect to the pump signal and *Brillouin loss* when inversely the CW signal is spectrally up-shifted with respect to the pump signal (cf. Figure 2-10); therefore the signal experienced attenuation since the power transfer energy is fundamentally made from the CW signal to the pump light.

Table 2-2 : Raman and Brillouin typical characteristisc in silica.

Parameters	Raman	Brillouin
Incident wavelength λ_p	1.55 μm	1.55 μm
Response time T	75 fs	11.78 ns
Brillouin shift ν	13.2 THz	10.8 GHz
Linewidth	30 THz	27 MHz
Peak gain	$\sim 10^{-13}$ m/W	$\sim 10^{-11}$ m/W

2.2.2 Non-linear scattering: Stimulated Raman scattering in optical fibres

Stimulated Raman scattering (SRS) is an effect that results from the interaction between an optical wave and molecular fluctuations of the material. SRS manifests with a down shift in frequency. SRS and SBS belong to the same family of inelastic scatterings, but they are considerably different in some aspects such as the value of frequency shift, the critical power, the Raman gain value and the spectrum linewidth (see Table 2-2). Mathematically, the interaction between the pump wave and the signal wave can be expressed with analogies to SBS [2]:

$$\frac{dI_p}{dz} = -\frac{\omega_p}{\omega_s} g_R I_p I_s - \alpha_p I_p , \tag{2.56a}$$

$$\frac{dI_s}{dz} = -g_R I_p I_s - \alpha_s I_s , \tag{2.56b}$$

where g_R is the Raman gain coefficient in single mode optical fibres (that typical value can be find in Table2-2)and ω_p, ω_s the pulsations of the pump and signal waves respectively.

The critical Raman power is defined as the power for which signal power becomes as high as the input pump power. Its value can be deduced from Eq. (2.55) and reads as [2]:

$$P_{crit} \approx 16 \frac{A_{eff}}{g_R L_{eff}} \tag{2.57}$$

Figure 2-11 shows a typical measurement of the Raman gain spectrum. If the Raman process has attracted the scientific community for many applications in optical distributed sensors or amplifiers, we will see in the second part of the next chapter that it can be a limiting factor for Brillouin sensors

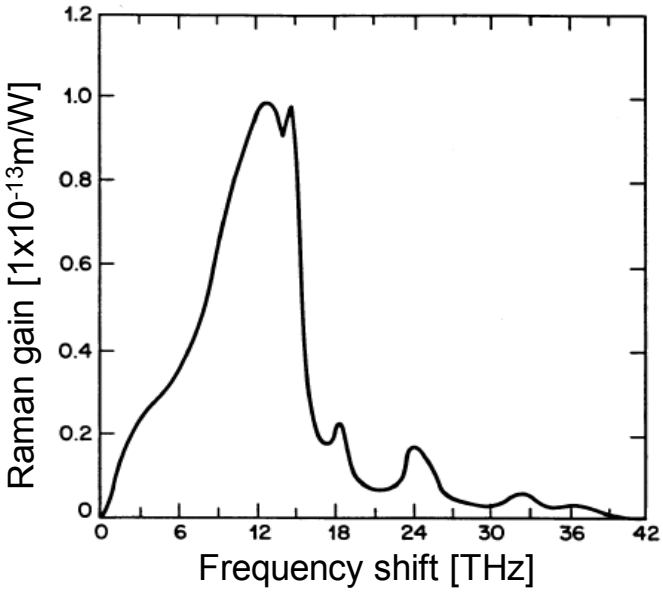

Figure 2-11: Raman gain spectrum in fused silica ($\lambda_p = 1\mu m$) [25].

2.2.3 Non-linear effect: Kerr effect

The optical Kerr is responsible of third-harmonic generation (THG), self-phase modulation (SPM), cross-phase modulation and parametric process such as four-wave-mixing (FWM), and modulation instability (MI). The optical Kerr effect refers to the dependence of the refractive index upon the intensity of the electromagnetic field:

$$n(I)=n_0+n_2 I\,, \tag{2.58}$$

where I is the optical intensity (W/m^2) inside the optical fibre, n_0 and n_2 (m^2/W) are respectively the linear part and the non-linear part of the refractive index. n_2 is related to the third-order susceptibility component $\chi^{(3)}$ by the relation $n_2=(3/8n_0)\,\chi^3_{xxxx}$. The typical value of n_2 is about 2.6x10^{-20} m^{2}W^{-1} at 1.55μm in silica doped with GeO_2 [20] and ~2.2x10^{-20} m^{2}W^{-1} pure in silica [31]. The non-linearity in optical fibres is generally defined from its non-linear coefficient γ as:

$$\gamma=\frac{n_2\omega}{cA_{eff}}, \tag{2.59}$$

where A_{eff} is the effective area of the optical mode of the fibre at the pulsation ω of the incident wave. The small value of the non linear refractive index in silica when compared to other highly non-linear materials, is largely compensated by the high confinement of the optical mode (i.e. small effective area varying from 1 to 80 μm^2) and the high interaction length over many km, over which the non-linear effects can be cumulated as a convergence of the transparency of the silice.

2.2.3.1 Self-phase modulation (SPM)

In SPM an optical field experiences a self-induced phase shift during the propagation within the optical fibre:

$$\phi_{NL}=n_2 IkL=\gamma PL\,, \tag{2.60}$$

where $k=\left|\vec{k}\right|$ is the wave number, L is the fibre length and P is the optical power. This phenomenon is responsible for symmetrical spectral broadening of the Brillouin gain in optical fibres if I is time-domain dependent.

2.2.3.2 Cross-phase modulation (XPM)

An optical field at wavelength λ_1 experiences a phase shift induced by a propagating field at a different wavelength λ_2

$$\phi_{NL}=n_2 kL(I_1+2I_2)=\gamma PL+2\gamma P_2 L\,, \tag{2.61}$$

where I_2 and P_2 are respectively the intensity and the power of the second wave.

We will focus on SPM, since XPM has no real effect on Brillouin sensors.

2.2.3.3 Parametric process: Modulation instability (MI)

MI can be addressed in a spectral approach as a FWM or SPM modulated with the dispersion [32]. An intense pump wave transfers energy to a pair of weak side-bands located symmetrically on each side of the pump wave. Modulation instability in optical fibres results from the interplay between non-linear effects and dispersion, and its typical manifestation consists of a spontaneous

breakup of the initial perturbed continuous wave into a periodic pulse. This occurs only in an anomalous dispersion regime.

2.2.3.4 Parametric process: Four-wave mixing (FWM)

When two or more waves simultaneously transmit in a non linear medium, the interactions between the waves tend to produce new frequency components that were not present in the incident field. In other words, the beating of the waves creates by means of the Kerr effect a temporal Bragg diffraction able to generate a new frequency. When the intensity of the waves is highly different, that can induce an energy transfer by the Bragg diffraction from the higher intensity wave (pump wave) to the lower intensity wave (signal wave). Actually, FWM finds its applications in wavelength division multiplexed communications systems for the potential development of a tunable light source and wavelength conversion [33-36]. The efficiency of the process is maximum when frequency- and phase-matching conditions are verified by the waves given respectively $\omega_3 + \omega_4 = \omega_1 + \omega_2$ by and $\omega_3 + \omega_4 = \omega_1 + \omega_2$.

Bibliography

[1] Fabelinskii I.L., 1956. Sov. Phys. Dokl. 1, p. 115.

[2] Boyd R. W., *Nonlinear Optics*, fourth ed. Academic press (2008).

[3] Frenkel J., 1946. Kinetic theory of liquid, 235-46.

[4] Fabelinskii I.L., 1968. *Molecular light scattering*. Plenum Press, New York, pp. 95&150.

[5] Brillouin, L., 1922. Diffusion de la lumière et des rayons X par un corps transparent homogène: Annales de Physique, 17:88-122.

[6] Rich T.C. and Pinnow D.A., 1974. Evaluation of fiber optical waveguides using Brillouin spectroscopy. Applied Physics Letters, 13: 264-266.

[7] Rowell N.L., Thomas, P.J. van Driel H.M. and Stegeman, G.I., 1979. Brillouin spectrum of single-mode optical fibers. Applied Physics Letters, 34, 2:139-141.

[8] Jen C.K., 1985. Similarities and differences between fiber acoustics and fiber optics. Proceedings of the IEEE Ultasonics Symposium: 1128-1133.

[9] Rich T.C., and Pinnow D.A., 1972. Total optical attenuation in bulk fused silica. Applied Physics Letters 20: 264-266.

[18] Thomas P.J., Rowell N.L., van Driel H.M. and Stegeman G.I., 1979. Normal acoustic modes and Brillouin scattering in single-mode optical fibers. Physical Review B, 19, 10:4986-4998.

[10] Niklès M., 1997. La diffusion Brillouin dans les fibres optiques: étude et application aux capteurs distribués. Thèse de doctorat N° 1674, Ecole Polytechnique Fédérale de Lausanne.

[11] Bloembergen N., *Nonlinear Optics*, World Scientific, New York, fourth edition (1996).

[12] Butcher P. N. and Cotter D., *The elements of nonlinear optics*. Cambridge University Press, (1990).

[13] Born M. and Wolf E., *Principles of Optics*. Pergamon Press, New York, 6th ed. (1980).

[14] Osterberg U. and Margulis W., 1986. Dye laser pumped by Nd:YAG laser pulses frequency doubled in a glass optical fiber. Optics Letters, 11, 516-518.

[15] Agrawal, G.P., *Nonlinear fibre optics*, 2nd ed. Academic Press, (2008).

[16] Chiao R.Y., Townes C.H. and Stoicheff B.P., 1964. Stimulated Brillouin Scattering and Coherent Generation of Intense Hypersonic Waves. Physical Review Letters 12: 592-595.

[17.] Ippen E.P. and Stolen R.H., (1972). Stimulated Brillouin scattering in optical fibers. Applied Physics Letters, 21: 539-541.

[19] Nikles M., Thévenaz L., and Robert P.A., 1997. Brillouin gain spectrum characterization in single-mode optical fibers. Journal of Lightwave Lightwave Technology, 15: 1842-1851.

[20] Agrawal G., *Nonlinear Fiber Optics*, 4th ed. Academic press, (2007).

[21] Buckland E.L. and Boyd R.W., 1997. Measurement of the frequency response of the electrostrictive nonlinearity in optical fibres. Optics Letters, 22:10.

[23] Pannel C. N., Russell St. J., and Newson T. P. 1993. Stimulated Brillouin scattering in optical fibres: the effects of optical amplification. JOSA B, 10:4.

[24] Niklès M., Thévenaz L. and Robert P., 1997. Brillouin Gain Spectrum Characterization in single-mode optical fibers. Journal Lightwave of Technology, 15:1842-1851.

[25] Agrawal, G.P., *Nonlinear fibre optics*, Second Edition. 3rd ed. Academic Press, (2001).

[26] Smith R.G., 1972. Optical power handling capacity of low loss optical fibers as determined by stimulated Raman and Brillouin scattering. Applied Optics, 11: 2489-2494.

[27] Bayvel P., and Radmore P.M., 1990. Solutions of the SBS equations in single-mode optical fibres and implications for fibre transmission systems. Electronics Letters 26:434-436.

[28] Deventer O.and Boot J., 1994. Polarization properties of stimulated Brillouin scattering in single-mode fibres. Journal Lightwave of Technology, 12:585-590.

[29] Aoki Y. and Kazuhito T. 1988. Stimulated Brillouin scattering in a long single-mode fiber excited with a multimode pump laser, JOSA B, 5:358-363.

[30] Ravet F., 2007. Performance of the Distributed Brillouin Sensor: Benefits and Penalties Due to Pump Depletion, Thesis dissertation 2007 University of Ottawa.

[31] Landau L. D. and Lifshitz E. M., *Statistical physics*. Butterworth-Heinemann, 3rd ed., (1984).

[32] Stolen R.H. and. Bjorkholm J.E., 1982. Parametric amplication and frequency conversion in optical fibers. IEEE Journal Quantum Electronics, 18, 7:1062-1072.

[33] Stolen R. H., Bjorkholm J. E, and Ashkin A., 1974. Phase-matched three-wave mixing in silica fiber optical waveguides. Applied Physic Letters, 24, 7:308.

[34] Inoue K., 1994. Arrangement of fiber pieces for a wide wavelength conversion range by fiber four-wave mixing. Optics Letters, 19, 16:1189-1191.

[35] Watanabe S. and Chikama T., 1994. Highly efficient conversion and parametric gain of nondegenerate forward four-wave mixing in a singlemode fibre. Electronics Letters, 30, 2:163-164.

[36] Zhang X. and Jogersen B.F., 1997. Noise Characteristics and Optimum Fiber Length of Spectral Inversion Using Four-Wave Mixing in a Dispersion-Shifted Fiber. Optics Fiber Technology. 3, 1:28-43.

[37] Alasia D., 2006. Advanced trends in nonlinear optics applied to distributed optical-fibre sensors. Thèse de doctorat N° 3648, Ecole Polytechnique Fédérale de Lausanne.

[38] Facchini M., 2001. Distributed fiber sensors based on Brillouin scattering. Thèse N° 2521 de doctorat, Ecole Polytechnique Fédérale de Lausanne.

[39] Zadok1 A., Zilka E., Eyal A., Thévenaz L., and Tur M., 2006. Vector analysis of stimulated Brillouin scattering amplification in standard single-mode fibers. Optics Express, 16:21692-21707.

[40] González-Herráez M., Song K.-Y. and Thévenaz L., 2005. Optically controlled slow and fast light in optical fibres using stimulated Brillouin scattering. Applied Physics Letters, 87, 8:081113.

3 Distributed Brillouin sensors and their limitations

Chapter 2 has allowed understanding the physical mechanism behind Brillouin scattering. It has explained how it was possible to stimulate Brillouin scattering especially in optical fibres, and has outlined others non-linear effects as Kerr effect and parametric process. The aim of this chapter[4] instead, is to provide an overview about Brillouin sensors and their limitations due to those non-linear phenomena. The chapter is divided into two parts. The subject of the first is devoted to provide through selected reference from the literature, an understanding of different class/variants of distributed Brillouin sensors. The remainder of the chapter is devoted to the study of the impact of non-linear effects, outlined in chapter 2, upon the performances of a Brillouin sensor, through experimental and analytical studies.

[4] This chapter is based on:
Diaz S., Foaleng S. M., Lopez-Amo M., and Thévenaz L., (2008). A High-Performance Optical Time-Domain Brillouin Distributed Fibre sensor. IEEE Sensors journal, 8, 7:1268-1272.

Foaleng S. M., Rodríguez-Barrios F., Martin-Lopez S., González-Herráez M., and Thévenaz L., (2011). Impact of self-phase modulation on the performance of Brillouin distributed fibre sensors. Optics Letters. 36, 2:97:99.

Foaleng S. M., Thévenaz L., (2011). Impact of Raman scattering and modulation instability on the performances of Brillouin sensors. In proceding of SPIE, 21st International Conference on Optical Fiber Sensors, Ottawa, Canada, 7753-226.

Thévenaz L., Foaleng S. M, Lin J., (2011). Impact of pump depletion on the determination of the Brillouin gain frequency in distributed fiber sensors. In proceding of SPIE, 21st International Conference on Optical Fiber Sensors, Ottawa, Canada, 7753-210.

Number of optical fibre sensors have been proposed and developed throughout the global scene [1]. Since they can operate over long distances because of the low loss of optical fibre, distributed fibre sensors are the most attractive. Their cost may be less than that of a large number of point sensors. Distributed fibre sensing techniques are commonly based on optical time domain reflectometry (OTDR) [2]. In this latter optical pulses are launched into an optical fibre and the information is retrieved thanks to the variations in backscattering intensity induced by the measurand that is detected as a function of time. Hartog and Payne were the first to use optical fibres to sense temperature [3] in 1982. For that demonstration, they exploited the induced variation of the Rayleigh scattering coefficient along the length of liquid and silica fibres. Even though liquid-core fibres have larger coefficient than silica fibres, the fact that their reliability is not well known can limit their exploitation.

Few years later (i.e. 1985), Dakin *et al* [4] have also demonstrated temperature profiles measurement, this time using the variation in the Raman backscattering coefficients of anti-Stokes and Stokes lights. This approach is very practical because conventional silica optical fibres can be used as sensor. The anti-Stokes Raman backscattering light is about 30 dB weaker than the Rayleigh backscattering light. However, its sensitivity to temperature is large. Systems based on Raman scattering have been commercialized by several manufacturers.

The latest in date class of distributed fibre optics sensor uses Brillouin scattering which is about 20 dB weaker than Rayleigh scattering (cf. Figure 2.5 in Chapter 2). However, Brillouin scattering can be enhanced by the stimulated Brillouin scattering process (cf. Section. 2.2 in Chapter 2) making the sensor technologies using the Brillouin technique more practical than the others since in addition of distributed strain [5], as well as distributed temperature [6-7] measurement can be performed. Nowadays there are three ways to evaluate the Brillouin information locally: time domain, frequency domain and using correlation.

3.1 How distributed Brillouin sensor can sense temperature and strain

Developed in 1976 by Barnosky [2], OTDR has given rise to the well-known method for the characterization and the monitoring of optical fibre links in the telecommunications industry. Based on the measurement of the Rayleigh backscattering signal when an optical pulse is launched into the fibre, OTDR technique has been developed for measuring optical fibre attenuation characteristics, junction losse and reflections as well as total fibre length. It allows locating of losses introduced by a connector, a splice or by any default present on the fibre link.

Even if OTDR makes possible the spatial distribution measurement of losses, breaks, discontinuities along the fibre and the fibre length measurement, it does not allow performing distributed strain or temperature measurements. Distributed Brillouin analysis was first proposed in the 90s as an alternative method. It rapidly turned out that it had many more potentialities for sensing, since Brillouin scattering is intrinsically very sensitive to temperature [6-7] and the deformations [5] experienced by the sensing fibre. This comes from the fact that Brillouin scattering must satisfy a very strict phase matching condition, making the interaction manifest itself as a spectral narrow resonance.

3.1.1 Principle

As explained in the previous chapter, in stimulated Brillouin regime (Brillouin amplificator case), a weak signal wave will experience a sharp gain if it is spectrally positioned at a frequency shifted by ν_B below a strong pump propagating in the opposite direction (their frequency difference $\omega=\omega_p-\omega_s$ needs to be close to the peak of the Brillouin spectrum ν_B; (cf. Section 2.2.1 of Chapter 2). The maximum Brillouin frequency shift is obtained when defined as $\omega_p-\omega_s=\nu_B=2nV_a/\lambda_p$ (in Eq. (2.22)).

From the theory of elasticity, the speed of the acoustic wave is also related to the density of the material ρ as defined in the following relation:

$$V_a=\sqrt{\frac{\partial p}{\partial \rho}\Big|_s}=\sqrt{\frac{k}{\rho}}=\sqrt{\frac{1}{C_s\rho}}, \tag{3.1}$$

where k is the bulk modulus and C_s is the adiabatic compressibility. The intrinsic material properties are function of the temperature and strain. This means each extrinsic change, either in temperature or in strain or pressure applied to the material, will change the Brillouin frequency shift in optical fibre ν_B through V_a. This can be explicitly seen in the following equation [19]:

$$V_a=\sqrt{\frac{E(1-k)}{(1+\kappa)(1-2\kappa)\rho}}, \tag{3.2}$$

where E is the Young modulus, and κ is the Poisson ratio. Mallinder *et al* have observed variations of the Young modulus and the Poisson ratio with strain for fused silica fibres [8]. The refractive index n will also depends on the fluctuations of the density and will change through the elasto-optic effect which is mathematically described by the elasto-optic tensor. Since the optical fibre is an isotropic material, the elasto-optic tensor for optical fibre is reduced to only two components and therefore, the refractive change in the optical fibre is reduced to [9]:

$$\delta n=-\frac{n^2}{2}\left[p_{12}-\kappa(p_{11}+p_{12})\right] \tag{3.3}$$

where p_{11} and p_{12} are the elasto-optics coefficients. Bertholds *et al* have experimentally found the values of these two parameters and κ [10, 5]. It was found that the Brillouin frequency shift increases linearly with strain [5, 11] and temperature according to Eqs. (3.4) and (3.5) [11-12]:

$$\nu_B(\varepsilon)=\nu_B(1+C_s\varepsilon) \tag{3.4}$$

$$\nu_B(t)=\nu_B(t_r)\left[1+C_t(t-t_r)\right] \tag{3.5}$$

where ε is the tensile strain[5], C_s is the normalized strain coefficient, C_t is the normalized thermal coefficient compared to the room temperature t_r and, t is the variable temperature.

Variations of the Brillouin gain spectrum with the strain

The strain coefficient C_s is written as:

$$C_s = \frac{1}{\nu_B}\frac{\partial \nu_B}{\partial \varepsilon} = \frac{1}{n}\frac{\partial n}{\partial \varepsilon} + \frac{1}{V_a}\frac{\partial V_a}{\partial \varepsilon} \tag{3.6}$$

From Eq. (3.2) the second term can be calculated:

$$\begin{aligned}\frac{1}{V_a}\frac{\partial V_a}{\partial \varepsilon} &= \frac{1}{\nu_B}\left(\frac{\partial V_a}{\partial E}\frac{\partial E}{\partial \varepsilon} + \frac{\partial V_a}{\partial \kappa}\frac{\partial \kappa}{\partial \varepsilon} + \frac{\partial V_a}{\partial \rho}\frac{\partial \rho}{\partial \varepsilon}\right) \\ &= \underbrace{\frac{1}{2E}\frac{\partial E}{\partial \varepsilon}}_{\delta E} + \underbrace{\frac{\kappa(2-\kappa)}{(1-\kappa^2)(1-2\kappa)}\frac{\partial \kappa}{\partial \varepsilon}}_{\delta \kappa} - \underbrace{\frac{1}{2\rho}\frac{\partial \rho}{\partial \varepsilon}}_{\delta \rho}\end{aligned} \tag{3.7}$$

From Ref. [8], using n=1.46 and λ_p=1.55µm, then $\frac{1}{E}\frac{\partial E}{\partial \varepsilon}$=5.75 and $\frac{\partial \kappa}{\partial \varepsilon}$=3.07. From Ref. [10], κ=0.16, p_{11}=0.113 and p_{12}=0.252, then δn=–0.32, δE=2.875, $\delta \kappa$=1.364, $\delta \rho$=0.34, and therefore

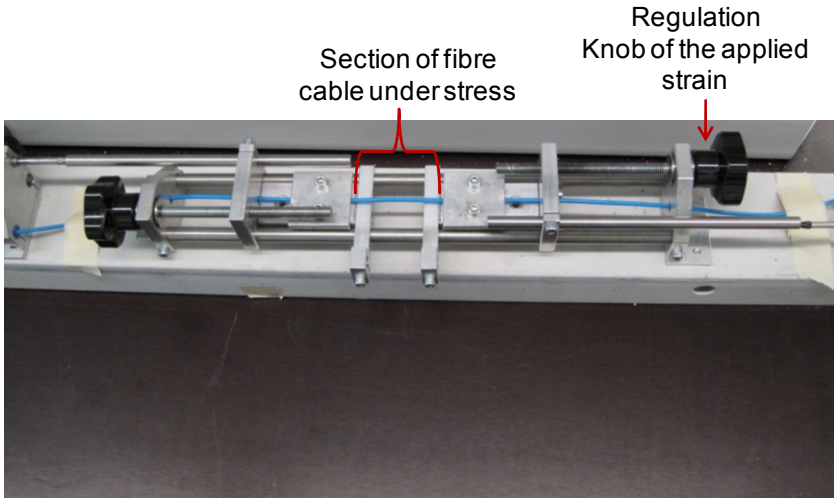

Figure 3-1: Apparatus used for apply strain (courtesy of ETHZ-IGT).

[5]It must be pointed out that strain refers to longitudinal strain induced, by stress along the fibre, and does not mean strain induced by lateral pressure. It has been found that lateral pressure up to 2.2 kg/m has little effect on the Brillouin frequency shift [22]. However many studies are looking to use lateral pressure to build a sensor [31].

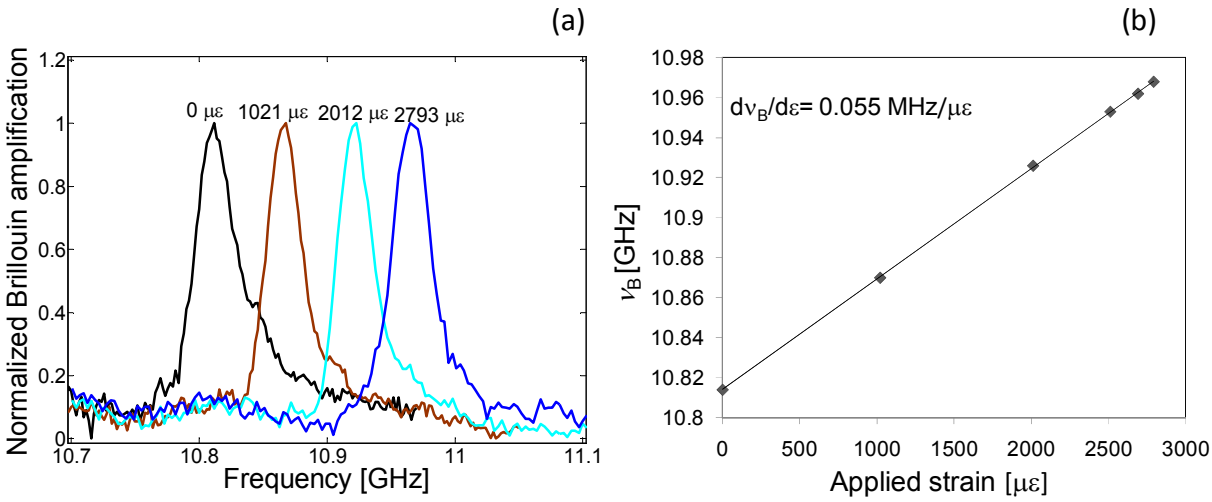

Figure 3-2: Dependence of Brillouin frequency with applied strain: Brillouin gain spectrum. Frequency shift at the resonance versus strain.

C_s=4.26. Comparing the values of δn with the three other values of $\delta E, \delta\kappa, \delta\rho$, it can be said that the change of ν_B with strain comes mainly from the change in the acoustic velocity rather than the change in the refractive index of fibres [11].

The applied strain has the effect of linearly shifting the Brillouin frequency to a higher frequency [5]. Figure 3-1 shows the strain part of the set-up used for experimental strain measurements of a 6 cm SMF fibre in which six different strain values were applied. The complete set-up used for these measurements is described in Section 4.9. The measurement results are represented in Figure 3-2 showing the normalized Brillouin gain spectrum of an unstrained fibre together with the strained fibres as well as the linear dependence between strain and ν_B with a slope of 551.86 MHz/(%ε). In the literature, one can find value as 594.1 MHz/(%ε) [14] (the discrepancy with the previous value is due to the composition of the fibre material).

Variations of the Brillouin gain spectrum with the temperature

For change in temperature, the variation of the Brllouin frequency with the temperature is written as [19]:

$$\frac{\partial \nu_B}{\partial T} = \frac{2}{\lambda_p}\left[V_A \frac{dn}{dT} + n\frac{dV_A}{dT}\right]. \tag{3.8}$$

From 20°C to 1620°C temperature change, the variations in the speed of the acoustic wave with the temperature is only 7% [13] when compared to the variations in the refractive index meaning that in this range of temperature, the variations of ν_B will strongly depend on the refractive index. In high temperature conditions the peak of the Brillouin gain moves to higher frequencies while its linewidth decreases and the parameters Lorentzian distribution of the Brillouin gain spectrum change. The inverse effect is produced at lower temperatures; i.e. the peak of the Brillouin gain moves to lower frequencies while its linewidth increases [14]. However, Brillouin gain does not

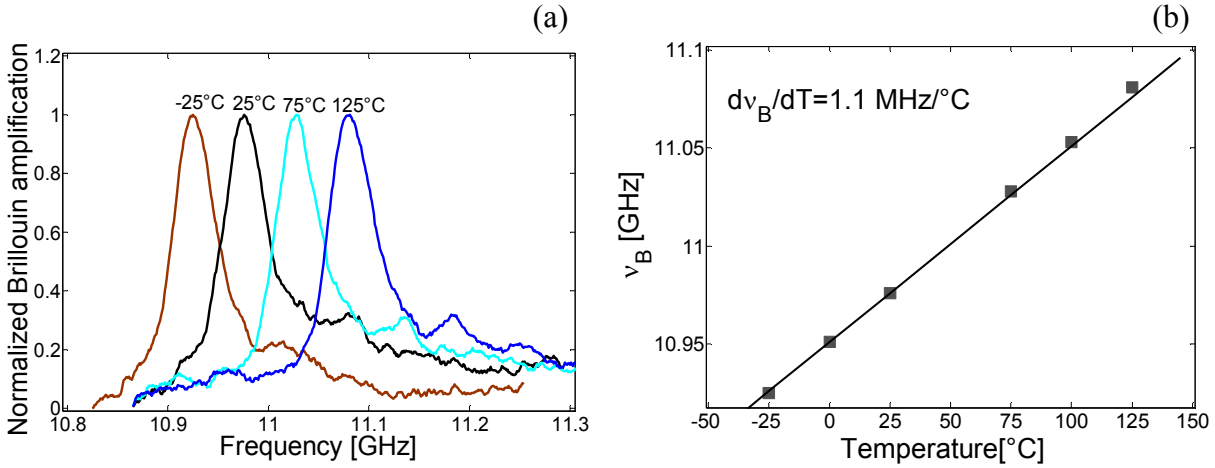

Figure 3-3: Variations of the Brillouin gain spectrum with the temperature: (a) Brillouin gain spectra, (b) Frequency of maximum Brillouin interaction versus temperature.

depends on the temperature; the apparent growth of its amplitude is exactly compensated by the narrowing of its linewidth. This observation means that the electrostriction efficiency does not depend on the temperature [14-15].

The change in temperature remains linear only in the range from 200 K to 600 K [16]. The Brillouin line-width is related to the lossy propagation of acoustic waves, i.e. to their damping rate. The fact that the linewidth increases for low temperature means that the damping rate of the acoustic waves increases when the temperature decreases [14]. The temperature coefficients of Brillouin frequency shift change for different fibres [12] (e.g. at λ_p=1.32 μm, for a GeO_2 doped core/pure-silica cladding fibre, the slope vary from 1.17MHz/°C to 1.36MHz/°C [12-14]. For a pure-silica core/F-doped cladding fibre, the slope is 1.33MHz/°C [12]. Nonetheless, the discrepancy between them is caused by the inhomogeneous refractive index profiles of the optical fibres, the variation in dopant concentrations [12, 14, 30] and the residual stress [17] along the overall fibre. Brillouin gain spectrum performed with the configuration set-up of Figure 3-10 at different temperatures of a 20 m photonic crystal fibre with pure silica core are shown in Figure 3-3.

The measurement series were performed by placing the fibre under test inside a temperature chamber with a sweep from -20°C to 150°C. The first graph shows the Brillouin gain spectrum, normalized to their maximum at the resonant frequency ν_B. In the second graph, the values of ν_B for each temperature are given, showing a linear behavior as previously mentioned. Referring to this graph, the slope is C_t=1.1 MHz/°C which is not so different from that find in the litterature.

However, not only strain and temperature can change the Brillouin shift. There are other factors such as the types and the doping concentrations of the fibre [18]. For instance for a type doping Germanium which is used in single mode fibre, the Brillouin peak decreases with an amount of -94 MHz/(mol%GeO_2) and its line-width increases with an amount of 1.4 MHz/(%mol GeO_2) [14].

On the other hand, Brillouin shift can be different for optical fibres having the same material composition; this is due to the variations of residual stress in fibre manufacturing, or of the tensile strain applied to fibre when the fibre is wound on a drum [5].

3.1.2 Parameter specifications

Here below, we reproduce the specifications of the study group of the COST 299 [32].

- Spatial resolution

The spatial resolution is specified for an optical fibre by the minimum distance between two step transitions of the measurand (it can also be defined as the smallest length of fibre over which any sensible change in the spatial variation of the measurand can be detected). The measuring spatial resolution is the minimum distance over which the system is able to indicate the value of the measurand within the specified uncertainty (cf. Figure 3-4 (right)). The detection spatial resolution is the minimum distance that generates results that are within 5% of the measurand transition amplitude.

- Accuracy

The accuracy of measurand qualitatively expresses the closeness of the measured value to the true or ideal value of the measurand. Accuracy represents the difference between the measured result and the true value and is affected by both bias and precision. Accuracy should not be confused with the term precision as illustrated in Figure 3-4 (left).

- Precision

It describes how repeatable a measurement result is. Precision is expressed by the estimated standard deviation of a specified series of measurements. Sometimes precision is expressed as a multiple of the estimated standard deviation, e. g. 2σ (meaning that about 95% of the measured values are within the mean value $\pm 2\sigma$). The smaller is the dispersion of the measured values, the better the precision; precise measurement results need not to be necessarily accurate (due to the bias). Therefore, a result of a single measurement should be interpreted as drawn from an ensemble with the measured standard deviation.

- Stability

The stability is the ability of a measurement system to maintain its metrological characteristics and meet other specifications over the intended service time.

- Measurement or distance range

The distance range is the fibre length over which the measurement can be performed within the stated uncertainty and spatial resolution.

3.1.3 Advantages of distributed Brillouin fibre sensors

- Low loss fibre is used, kilometers range of measurements, compatibility with telecommunications components
- Frequency-based technique instead of intensity based technique as Raman sensor
- More accurate measurements, more long term stability system since intensity-based technique suffer from a higher sensitivity to drifts and from a potential biasing by any step loss.
- Time measurement relatively low.

- Possibility to integrate many sensors in one sensor.

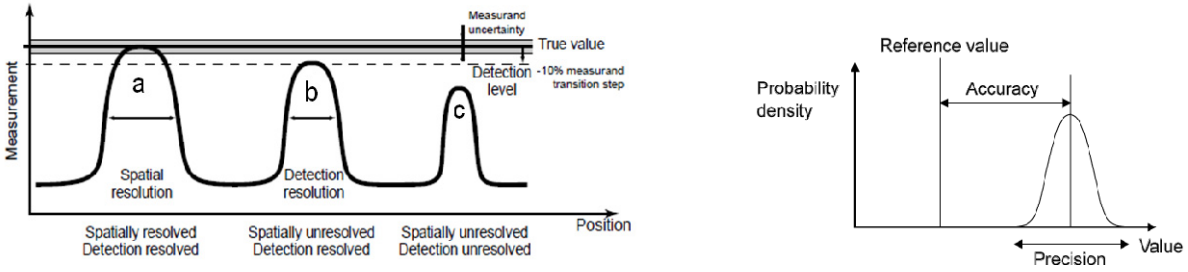

Figure 3-4: Illustration of the resolution. Left: a) spatially and detection resolved, b) spatially unresolved and detection resolved, c) spatially and detection un-resolevd. Right: illustration of the definition of accuracy and of the precision [32].

3.1.4 Polarization issue

Polarization scrambler is a module which allows controlling the state of polarization of the light at any time during its propagation in the fibre. In distributed Brillouin fibre sensor it is used to avoid any gain fading effects resulting from the polarization-dependent Brillouin interaction.

In the frame work of this thesis, a passive polarization scrambler and a polarization diversity were successfully implemented, resulting in a perfectly flat amplification profile along the fibre and reducing polarization fading to zero.

- First configuration:

The principle of the passive scrambler is represented in Figure 3-5. It is based on an unbalanced Michelson interferometer. There are two branches: the first contains 140 m standard low birefringence single mode optical fibre (SMF) and a faraday mirror, the second contains a polarization (PM) optical mirror. The arm length difference is much larger than the coherence length of the laser, so that they combine incoherently in the PM 50/50 coupler.

After passing through the appropriated length of 140 m birefringence SMF fibre in order to randomize the phase of light, the polarization of the light changes and becomes orthogonal as a

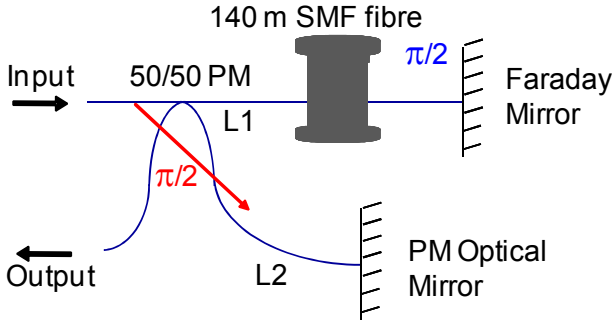

Figure 3-5: First configuration: passive polarization scrambler.

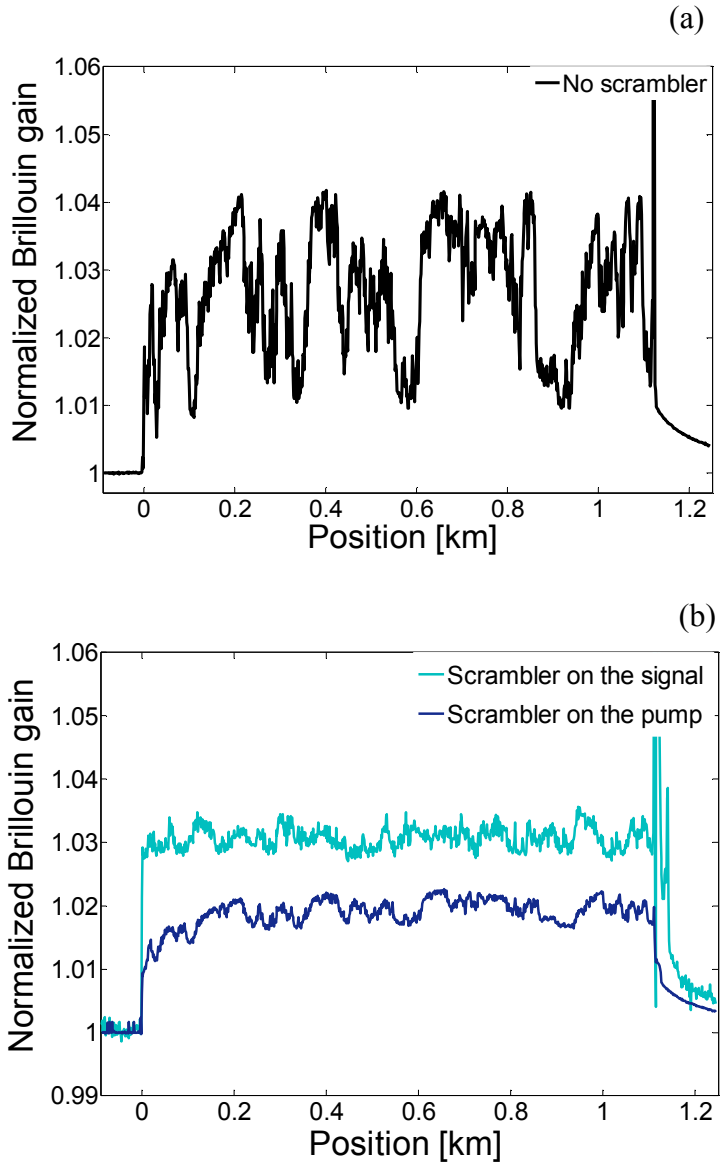

Figure 3-6: Brillouin gain distribution along a 1 km G652D IUT fibre for two different configurations. (a) without scrambler; (b) scrambler on pump and scrambler on probe.

result of the PM Faraday mirror placed at the one end of the optical fibre.

In the second arm, the light is reflected by a PM optical mirror. Therefore, the polarization of the light remains orthogonal to the light on the first arm, and there will not be any interference between each other. The connection with the PM Faraday Mirror were adjusted to compensate the loss in the delaying fibre, so that the same amount of power is obtained from the two arms after the recombination to secure a uniform scrambling.

The proposed passive scrambler configuration was implemented in the set-up described in Figure 3-1. The results obtained with and without the polarization scrambler are compared in Figure 3-6 (a) and (b). As shown in Figure 3-6 (b), the results are greatly improved when the polarization scrambler is used. However, the flat curve is obtained with the scrambler on the signal while the

better performance in term of noise is reached with the scrambler on the pump. This can be explained as follow: first, there is always noise since the polarization of the light over the Michelson's coupler is not perfectly orthogonal. In fact when this noisy signal is used as signal wave, the noise is present at the detection. In addition, in the arm of the signal any polarizing element will decrease the efficiency of the scrambling. When the same signal is used as pump, the impact of the noise becomes negligible.

- Second configuration

The configuration 2 of the passive diversity depicted in Figure 3-7 which is similar to the configuration 1: The 50/50 PM coupler was replaced by a polarisation switch and a circulator capable to transmit two different states of polarisations. By implementing the polarisation switch in a proper manner, it was possible to detect the signal from the first arm (the direct polarisation) and from the second arm (the cross polarisation) independently as shown in Figure 3-8 (a) when the scrambler was placed on the signal and in Figure 3-8 (b) when the scrambler was placed on the pump. The resulting amplification profile shown in Figure 3-8 (a) is obtained by averaging the two (cross and direct) amplification profiles. A very flat curve is reached with the scrambler on the signal and on the pump and the better performance in term of noise is obtained with the scrambler on the pump.

In summary a passive scrambler system all fibred was obtained. It has the advantage to be robust over time respect to the traditional active system. Therefore the passive scrambler we built is less expensive less than 1000 USD compared to the active scrambler which the prize is up to 3000 USD. On the other hand, we must address the fact that this passive srambler system it is bulky. Also one must be sure that the polarizations are perfectly orthogonal and the fibres elements have to be polarization maintained. However with the recent technologies it is possible to have a whole integrated system using MEMs which can bring a huge advantage in terms of bulky and probably increase the signal to noise ratio (SNR).

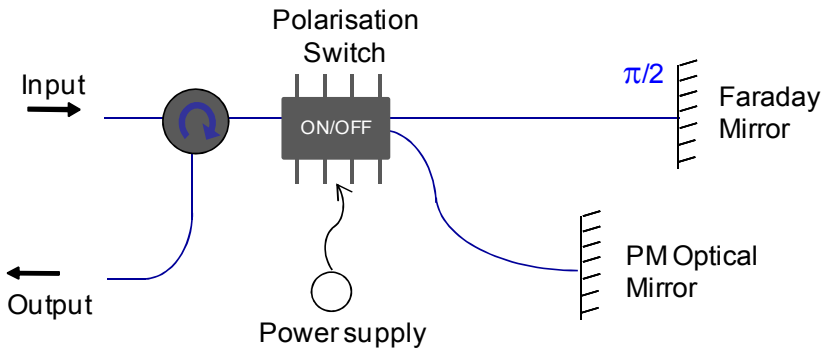

Figure 3-7: Second configuration: passive polarization diversity.

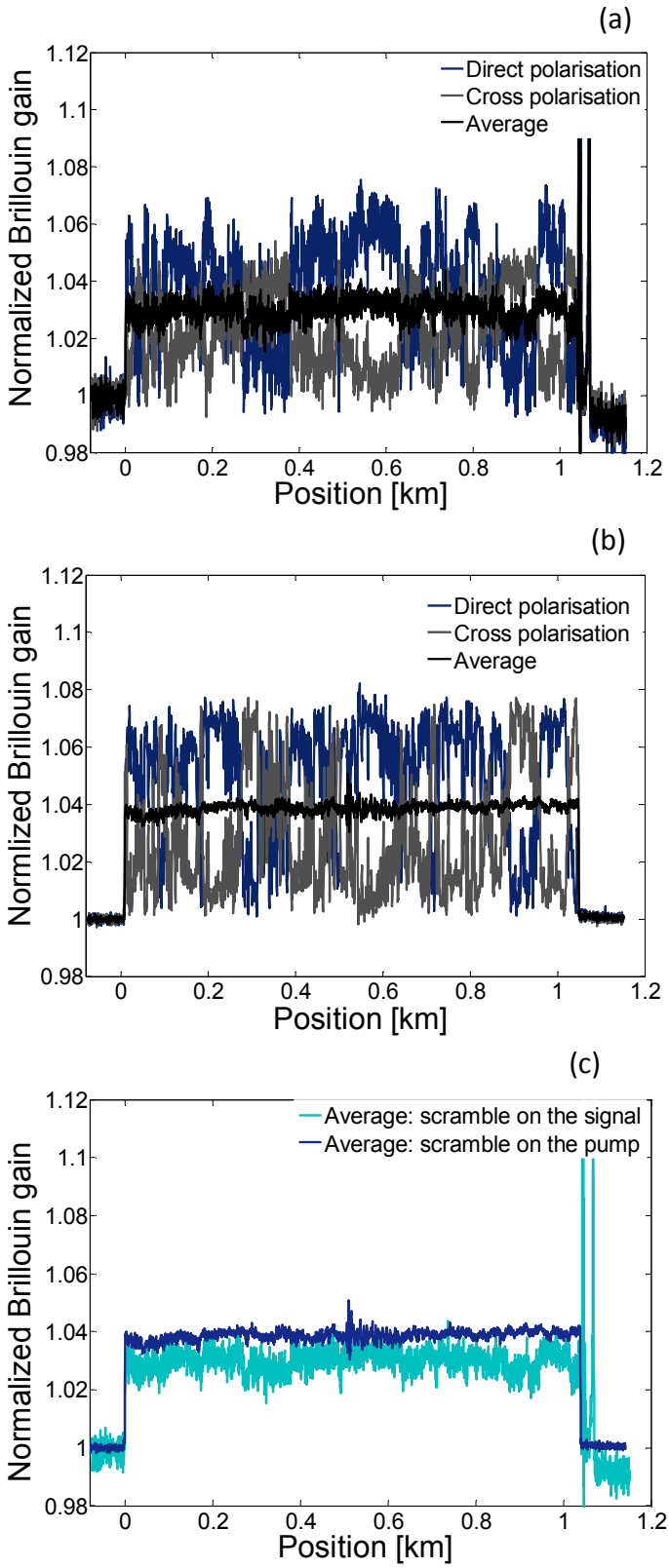

Figure 3-8: Brillouin gain distribution along a 1 km G652D IUT fibre is presented for two different states of polarization represented, direct polarisation (bleu trace), cross polarisation (gray trace) and resulting average of the two direct and cross polarisation. (a) on the signal, (b) on the pump, (c) comparison between the average trace when the scrambler is on the signal (green trace) and when the scrambler is on the pump (blue trace).

3.2 Time-domain approach

Time domain approach uses a light pulse as pump which interacts with a counter-propagating continuous wave (CW) in the Brillouin gain configuration. As addressed in Chapter 2, the process is called Brillouin gain when the CW signal is spectrally down-shifted with respect to the pump pulse signal and Brillouin loss when inversely the CW signal is spectrally up-shifted with respect to the pump pulse signal. At each instant during the pulse light propagation through the fibre, stimulated Brillouin scattering occurs only in the region where the two waves are overlapping. This detected temporal trace provides the spatial information along the fibre, since the pulse time of flight can be used to convert the temporal coordinate to a spatial coordinate. The Brillouin interaction occurs at a particular section of the fibre if the two counter-propagating wave's frequencies match the local Brillouin frequency shift. Techniques based on spontaneous Brillouin scattering for Time Domain Reflectometry (BOTDR) [4] require only one access point to the test fibre to launch the pump wave, while those using SBS for Brillouin Analysis (BOTDA) must access both ends of the test fibre to launch the pump pulse and CW signal, [1-3]. However, the first and main advantage of BOTDA over BOTDR lies in the stimulated nature of the Brillouin interaction. Since BOTDR relies on spontaneous effect while BOTDA uses stimulation of the Brillouin intraction which enhances the signal, consequently, much higher SNR is achieved.

3.2.1 Brillouin optical time-domain reflectometry (BOTDR)

The BOTDR system was first developed by Kurashima in 1992 [21]. The principle of BOTDR is based on the OTDR technique but here the system uses Brillouin scattering instead of Rayleigh scattering. The Brillouin backscattered intensity from an intense pulse is recorded as a function of time. The optical wave is divided into two optical waves, one is modulated into a pulse and the other one is used as a reference light wave. The pulse power is amplified by an Erbium amplifier and launched into a test fibre. The Brillouin shift is determined by scanning, step by step, the frequency and by recording for each step the detected signal (using for instance a coherent and heterodyne receiver [22]). The frequency distribution of the Backscattered signal can then be reconstructed at each position by analyzing for each time step the amplitude as a function of the frequency and determining the peak value. With the coherent detection, the Brillouin backscattering signal (which is 100 times smaller than Rayleigh backscattering) does not suffer from noise fading thus no need of polarization scrambler or polarization diversity is needed. 1 m spatial resolution over a 10 km range was obtained with this system. However other improvements have been made and have increased the spatial resolution to 2 m over 30 km [23]. These performances can be improved through Raman amplification but require complex equipments [24]. Having the advantage of the one-end access system, we will see that the spatial resolution cannot be better than 1 m.

3.2.2 Brillouin optical time-domain analysis (BOTDA)

BOTDA was first proposed as a nondestructive attenuation measurement technique for optical fibres [5]. By clarifying the strain and temperature dependence of the Brillouin frequency shift [5-6], BOTDA has been used as strain and distributed strain and temperature measurement techniques. Initially, two distinct lasers for generating pump and signal waves were used. This causes problems

of frequency drifts between the lasers. Niklès *et al* [25] suggested resolving the problem by using a microwave generator and a LiNbO3 electro-optic modulator (EOM) to generate pump and signal waves from a *single* light source, as shown in Figure 3-9. The EOM modulates the laser light at a frequency near the Brillouin frequency shift to generate a signal wave. The same EOM also produces a pump pulse by applying an electrical pulse to the EOM electrodes. The modulator is biased to operate in a suppressed carrier scheme, so that the lower modulation sideband can be used as a signal wave while the upper sideband is suppressed by an optical filtering. Nowadays the BOTDA system provides access to both fibre ends with the Nikles'[s] solution for better performances, since the pump pulse and the CW signal must counter-propagate in the sensing fibre. The electrostriction that stimulates the acoustic wave is driven by the interferences between pump and signal, so that their states of polarization must be preferably aligned to create the maximum gain [26]. Orthogonal polarizations will result in a totally vanishing gain, and since the polarization normally varies randomly along an optical fibre [26], a non-zero gain can only be secured using polarization scrambling or a polarization-diversity scheme. This polarization dependence can also be favorably used to efficiently and rapidly measure the local birefringence properties along an optical fibre [27].

However the configuration shown in Figure 3-9 suffers from sensitivity to optical noise, as a result of the bidirectional propagation of optical waves showing the same frequency along the optical fibre:

(i) Interference between the 10% of the upper sideband transmitted by the Bragg grating filter and the same signal coming out from the fibre which creates reflexion over the fibre.

(ii) Interference between the modulation signal after the filter and the signal coming out from the fibre.

A sensor configuration was entirely revisited to reach a lower noise level for observing high contrast signals and a new configuration was proposed in Ref. [28] as depicted in Figure 3-10. This

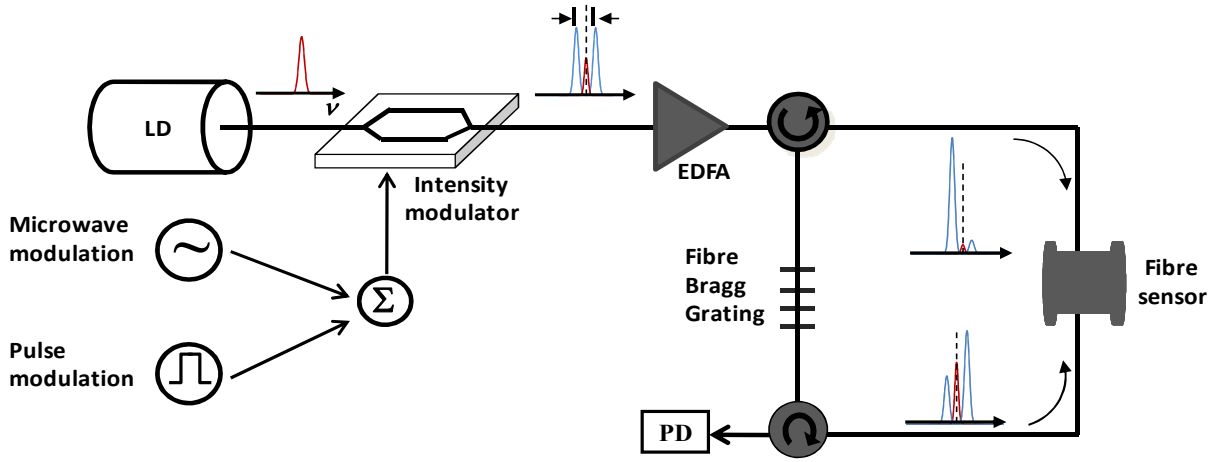

Figure 3-9: Experimental set-up of the BOTDA technique using a single laser. Optical noise results from the bidirectional propagation of optical waves showing the same frequency along the optical fibre.

configuration avoids as much as possible the bidirectional propagations of waves showing the same optical frequency [29]. It also drastically reduces the optical noise resulting from the superposition of coherent waves with same frequency and showing a random fluctuation of the phase difference generated from spurious optical reflections and Rayleigh scattering in the system. The random phase difference generates an important noise intensity and is frequently observed in bidirectional fibre optics systems.

Using the configuration presented on the Figure 3-10 measurements were carried out over a 47 km sensing range with 7 m spatial resolution thanks to the massive noise reduction by more than 15 dB down to optical shot noise. To maintain a sufficient gain, the pump pulse must be made longer enough. For this system, the pulse width was set to 70 ns corresponding to a spatial resolution of 7 m.

The overall information was obtained by performing a frequency sweep of the signal wave (as shown in Figure 3-11(b), single traces were acquired with a 125 MHz detector and 256 averaging). The scan in time/distance and frequency domain can be viewed as a 3D distribution in Figure 3-11(a) representing the spectral distribution of the Brillouin gain at any location along the fibre. The resulting maximum Brillouin frequency shift over the fibre length of 47 km (accuracy of less than 1 MHz) is shown in Figure 3-11(c). The change of the curve shape at the 25 km position is due

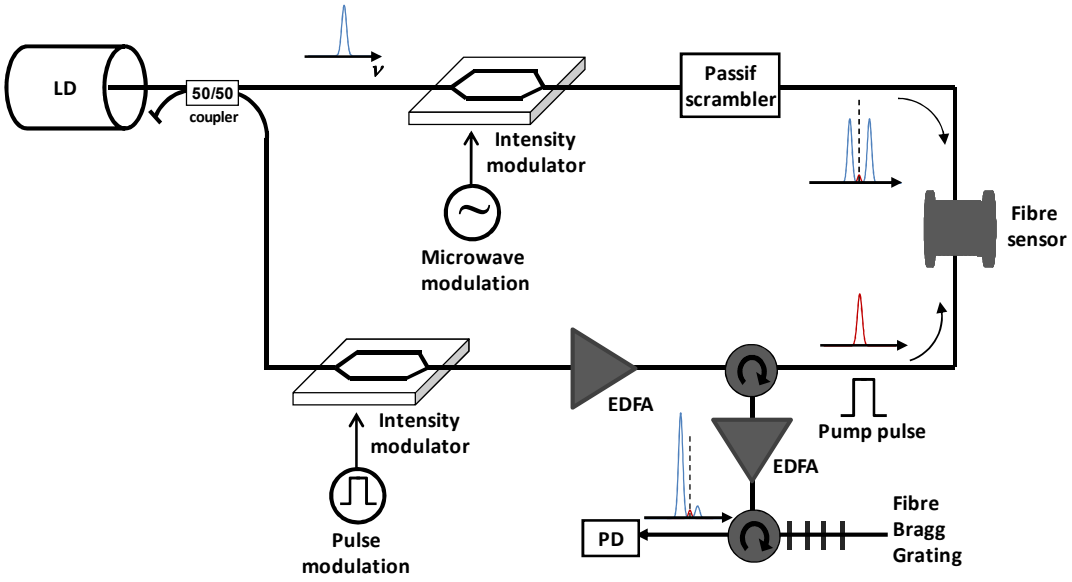

Figure 3-10: The new BOTDA configuration for low optical noise. Using an optical circulator, light from the upper channel is extracted at the fibre output. This signal is boosted using an EDFA (Erbium doped amplifier) and filtered using a very narrowband fibre Bragg grating filter (<0.1 nm) to transmit only one sideband onto the detector. The filtering is crucial since it eliminates the unwanted modulator sideband that reduces the measurement contrast and any presence of the pump frequency due to the finite extinction ratio of the intensity modulator that would generate substantial optical noise at detection when combined with the Rayleigh light from the pump pulse.

to the non uniformity doping concentration in the used single mode fibre. It must be pointed out that the range is limited by high power, which leads to non-linear effects, Raman scattering and/or modulation instability depending on the fibre type (fibres with normal or anormal dispersion). Studies on this issue in Brillouin sensor based time domain will be carried out in the second part of this chapter.

BOTDA system has the same limitation of a spatial resolution of 1 m as BOTDR system, limited by the gain spectrum broadening due to the pump spectral broadening for short pulses. This 1 m spatial resolution can be secured up to a distance of 30 km and requires an average of less than 1000 to get performances identical to a BOTDR system.

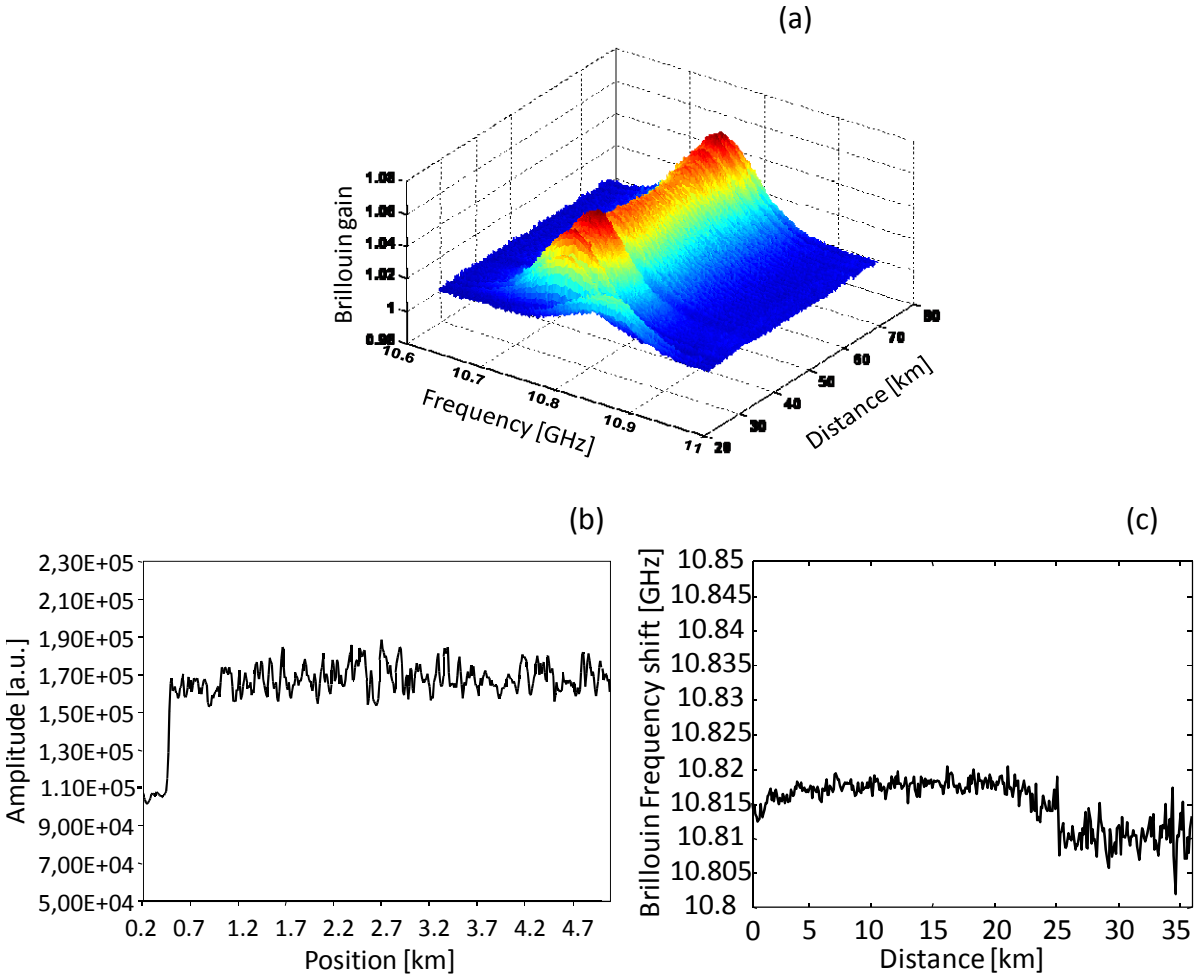

Figure 3-11: a) 3D distribution of the gain spectrum 47 km fibre length, obtained using 7 m spatial resolution with 256 time trace averaging. b) Trace of maximum Brillouin gain along the first 5 km of the fibre. c) Resulting Brillouin frequency shift of 47 km length fibre.

3.3 Frequency-domain approach

3.3.1 Brillouin optical frequency-domain analysis (BOFDA)

Unlike BOTDA method, BOFDA use the frequency domain which determines the transfer function of a fibre. Optical frequency domain reflectometry (OFDR) was first analyzed by Ghafoori-Shiraz *et al* [33]. Brillouin optical domain reflectometry (BOFDA) was then proposed 10 years later by Dieter *et al*. [34, 35]. BOFDA system is based on the measurement of a complex baseband transfer function that relates the amplitudes of a counter-propagating pump and signal waves along a fibre length. The basic experimental configuration of a BOFDA is depicted in Figure 3-12 [35]. The CW lights from two lasers are coupled at two ends of a single mode optical fibre (SMF). As for BOTDA, the frequency of the signal is downshifted, compared with that of the pump, by an amount corresponding to the Brillouin frequency shift of the fibre. The signal is then modulated in amplitude by an electro optic modulator (EOM) with a variable modulation frequency f_m.

For each value of f_m, the modulated signal intensity that equals $I_s(L,t)$ at $z=L$ and the alternating part of the transmitted modulated pump intensity $I_p(L,T)$ are recorded. These two output signals which are proportional to the modulated pump and signal intensities at $z=L$ passed through the photodetectors (PD), are fed into a network analyzer (NWA). The network analyzer determines the baseband transfer function of the sensor fibre. The output of the NWA is digitized by an analog to digital converter (A/D) and fed to a signal processor which calculates the Inverse fast Fourier transform (IFFT). For a linear system, this IFFT is a good approximation of the pulse response h(t) of the sensor fibre and allow retrieve informations in temperature and strain distribution along the fibre.

Author claimed that that BOFDA is more advantageous than BOTDA since it offers the possibility of narrow-band operation, and hence the improvements of the signal-to-noise ratio. However it must be pointed out that the measurement time using BOFDA is relatively higher than that of time domain approach, since it requires many measurements at different frequencies to obtain the baseband transfer function with a sufficient spectral resolution. Thus as far as the repeatability of the measurement is concerned, the temperature and the strain of the sensor fibre are constant. Secondly, the narrow band operation is the same as the BOTDA system since for a 1 m spatial resolution, at least a 100 MHz bandwidth (BW) photodetector is required just like in the BOTDA case. Eq. (3.9) gives the expression of the spatial resolution in the case of BOFDA:

$$\Delta z = \frac{V_g}{2} \frac{1}{f_{m\,max} - f_{m\,min}} \tag{3.9}$$

where $f_{m,max}$ and $f_{m,min}$ denote respectively the maximum and minimum modulation frequency. It can be seen that the former is the limiting factor. When its value is much greater than the narrow Brillouin gain spectrum line-width (30 MHz in the SMF fibre), the sidebands of the signal spectrum fall outside the Brillouin gain spectrum, inducing a distortion of the baseband transfer functions measured, for a number of pump-signal frequency offsets. So, the BOFDA has the same limitation of a spatial resolution of 1 m as BOTDR and BOTDA systems. Recently research have been carried

out in BOFDA systems to increase the performances in terms of the SNR, playing on the post processing including the de-convolution method to extract the data [36].

3.4 Correlation-domain approach

3.4.1 Brillouin optical correlation-domain analysis (BOCDA)

From the previous sections, both the time domain and frequency techniques discussed suffer from the limitation related to the spectral broadening for short pulses and the subsequent loss of measurement contrast. Furthermore the backscattered signal is generally too weak so that the response to the optical pulses needs to be integrated several times. It would thus take at least several minutes to complete the measurement, which is not an advantage for dynamic applications sensors, for instance. In 2000, Hotate *et al* proposed an interesting technique based on the correlation control of two synchronous continuous frequency modulated waves to overcome this limitation (BOCDA) [37]. Brillouin scattering can thus be generated locally along the fibre and the use of the pulsed lightwave is no longer required.

The configuration of the BOCDA technique is describes in the Figure 3-13. As in BODTA and BOFDA, the laser light is split into two waves (pump and signal waves). The signal wave has the frequency shifted from the pump wave by an amount of the Brillouin frequency. In order to resolve the position of the applied strain or change in temperature, the pump and signal waves are sinusoidally frequency-modulated, producing periodical correlation peaks along the optical fibre. The resulting effect is such that the Brillouin scattering only occurs at specific positions in the fibre. At the position where the correlation peak takes place, the frequency of the two waves change synchronously, and their frequency difference remain constant. In this case the signal waves will be

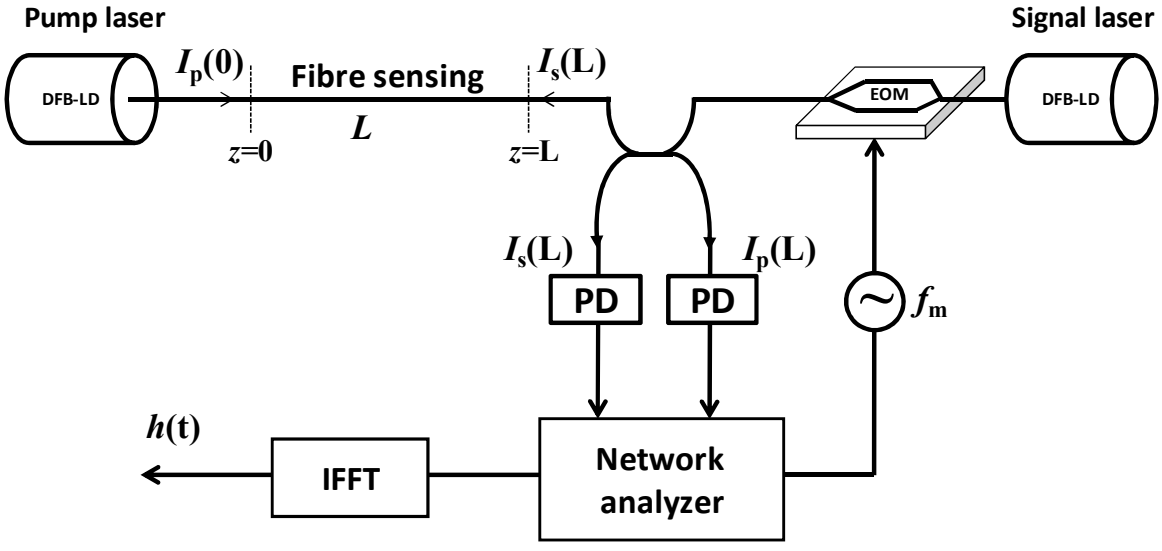

Figure 3-12 : Basic configuration of BOFDA [35].

subject to Brillouin gain only at correlation points and will carry the information about the Brillouin properties only at those positions. However, at different positions where the correlation is low, the frequency of the signal relative to the pump changes continuously, thus resulting in very low gain. To remove ambiguities, the modulation frequency of the waves f_m and the fibre arrangement must be controlled to allow only one correlation point to be present in the segment under test. This determines practically the range of the modulation frequency f_m that will be used. A standard lock-in detection stage is then used to chop the pump at low frequency, modulate the gain and discriminate the signal fraction that is amplified from the important continuous background.

The spatial resolution in correlation approach is given by the spatial range Δz around the correlation point, over which the broadening of the beat signal is small enough not to cause significant spreading and reduction of the effective Brillouin gain:

$$\Delta z \approx \frac{V_g \Delta \nu_B}{\pi \Delta f \, f_m} \tag{3.10}$$

As we have seen $\Delta \nu_B$ is the Brillouin gain linewidth in optical fibres. From Eq. 3.10 one can rapidly see that, for the best spatial resolution, the modulation amplitude Δf and the modulation frequency f_m must be as high as possible. Nonetheless, these two parameters cannot be increased arbitrarily since the distance L between two correlation points depends essentially on f_m defined as follow $L=V_g/2f_m$. On the other hand, Δf is not limited [38], but cannot be higher than the Brillouin frequency shift of the optical fibre to overcome crosstalk. Taking into account these considerations, N_R (the number of effective sensing points) has been defined as the evaluation parameter of the system, and is given by the ratio between L and Δz (Eq. 3.10):

$$N_R = \frac{L}{\Delta z} = \frac{\pi \Delta f}{\Delta \nu_B} \tag{3.12}$$

N_R has been calculated to a fixed approximate value of 570 *[39]*. Typical values for parameters appearing in these 3 equations are f_m=30MHz, Δf=2.5GHz resulting in a spatial resolution of 1cm and a measurement range of 3 m [40]. As it can see in Eq. 3.12 in order to achieve a better range, N_R must be increased, the same technique has been used with a multiple modulation schemes [41], and N_R was increased three times [42]. Recently, the same group upgraded the BOCDA technique to the BOCDR technique (enabling them to perform one access measurement [42]). With the double modulation scheme [42], they could increase the number of points N_R by m times [6] to 5690 points with m~10.4 and upgrade the performances of the system to 27 cm spatial resolution over a 1.5 km measurement range [42].

[6] It must be point out that as m increase, the SNR is deteriorated due to the following reasons [42] (i) the remaining peak noise become larger, (ii) the spatial resolution becomes higher while reducing the Brillouin gain spectrum signal power, and hence deteriorating the measurement accuracy.

One can observe that the problem of spatial resolution is solved at the expose of measurement range which is limited by the number of resolved points.

The Next chapter will be devoted to address a new technique (time-domain based), which has the requisites of high spatial resolution while maintaining a sharp Brillouin resonance over a many km range of measurement.

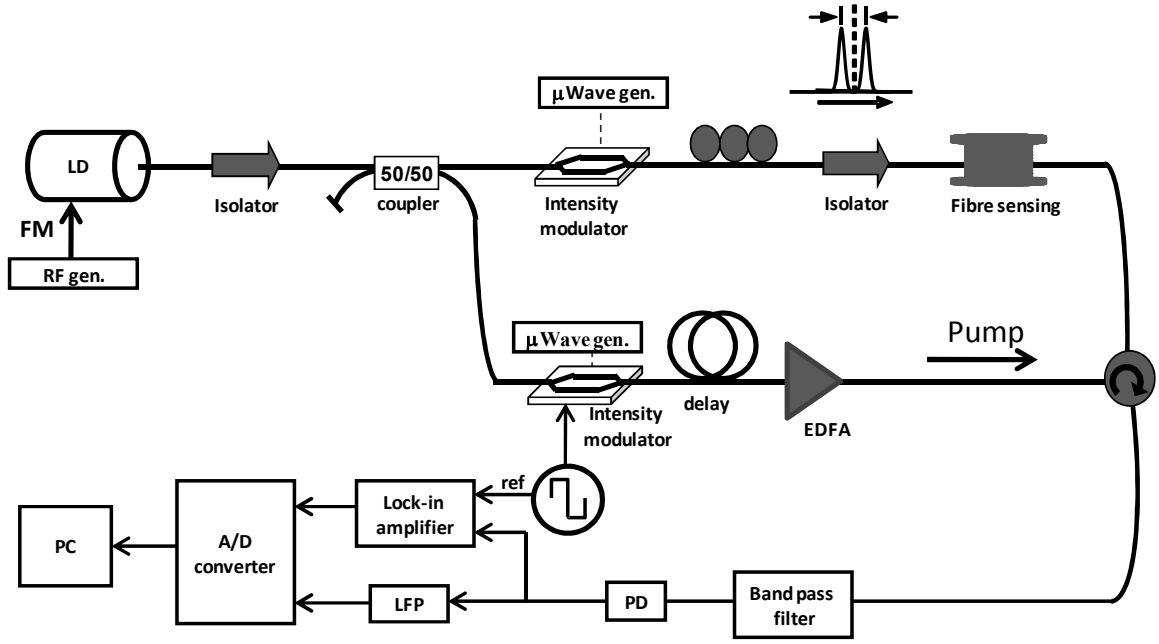

Figure 3-13: Experimental set-up for the correlation based stain sensing technique [39].

3.5 Range limitations of distributed Brillouin sensor

The distance range is a key parameter that must be made as long as possible. The recent raising interest in Brillouin fibre sensors for application in civil engineering, in oil & gas industry, in perimeter security and in intrusion detection has stimulated the research efforts to extend the distance range. As formerly seen in time-domain approach pulses are used to interrogate locally the interaction along the fibre. In order to achieve better performances in terms of range and spatial resolution, pump pulse and signal powers must be raised to maintain the signal changes above the noise level. These powers cannot be made arbitrarily large and must be kept below the observation threshold of any other noise-fed nonlinear effects. In these systems the most critical nonlinear effects are those in which a signal wave is amplified through a forward interaction, in other words when the background noise is amplified while co-propagating with the pump pulse. In such a situation the interaction length may cover many tens of kilometers and even a weak nonlinear amplification much less efficient than stimulated Brillouin scattering (SBS) may result in a large amplified spontaneous signal that eventually depletes the pump. The identified nonlinear effects are

pump depletion due to SBS itself, self-phase modulation (SPM), modulation instability (MI), which occurs only in fibres presenting an anomalous dispersion at the pump wavelength and Raman scattering (RS).

A spectral self-broadening of the pump due to MI has been observed in sensors based on spontaneous Brillouin scattering [43], whereas a rapid pump depletion has been observed in the case of BOTDA sensing system [44]. Similar observations have been realized in the case of RS in which the Brillouin gain has been observed to abruptly fall to zero [45] after several kilometers, severely limiting the distance range that turns highly dependent on the pump pulse power. Although former works [44-45] have shown a correct intuition based on experimental observations to address qualitatively the issue, we present here a quantitative model to control the pump depletion, to show the self-phase modulation and to anticipate the detrimental impact of MI and RS, validated by experimental demonstrations.

3.5.1 Depletion due to Brillouin sensor

The effect resulting from the gradual power transfer from the higher frequency wave to the lower frequency wave has not been considered so far as a major point by the community since it is more insidious and does not prevent the basic operation of the sensor. However, its detrimental impact has been rightfully mentioned at a relatively early stage during the development of Brillouin sensing [11, 50]. As a result of the increased range and accuracy, some recent reports have clearly focused on this effect by proposing a correction procedure based on an algorithm[51], by explicitly checking its absence of negative impact through a proper scaling of the signal powers[46-49] or by showing and evaluating experimentally its biasing effect[52].

We propose here to further develop and tried to complete the work performed in Ref. 8 and 9 by building a full model that addresses the impact of the power transfer between the pump and the signal in the case of a BOTDA sensor. The analytical model not only can be used to evaluate the error on the determination of the maximum gain frequency in a given experimental configuration, but also defines the worst case condition with the maximal error. In addition, this model reveals the tolerable power transfer for a given maximum error. In the situation addressed by the model, a pulse and a CW wave counter-propagate in the fibre and interact through SBS. Again, the fibre sensor is defined to be in a gain configuration if the pulse frequency is higher than the CW wave frequency, otherwise in a loss configuration as addressed in Chapter 2 (Section 2.2.1). The tiny CW wave intensity change observed in the time domain gives a measure of the interaction intensity at the crossing point of the pulse and the CW wave. This distributed intensity change actually is entirely compensated by an equivalent cumulated energy change in the pulse wave. The effect on the pulse amplitude can be quite massive with two identical power waves interacting over a long length, so that a bright design always employs an intense pump pulse and a weak CW wave to minimize the relative impact on the pulse amplitude. A significant change of the pulse power is detrimental because this power not only scales the strength of the interaction but also affects the response at the far end of the fibre. More concretely the output pulse power varies when the frequency difference between the two interacting waves is scanned. The variation inevitably leads to a spectral distortion of the gain spectrum at a given position. It must be mentioned that both the gain and the loss configurations lead to an equally distorted gain spectrum, so that none of these configurations can

be claimed to offer a decisive advantage. This conclusion is fully supported by the results of our model, so we shall address hereafter the case of a gain configuration without loss of generality. The power transfer from the pulse to the CW wave will in this section be designated as *pump depletion*.

3.5.1.1 First order approximation in the presence of one sideband CW signal

The pump pulse is chosen to be launched at the near end of the fiber (z=0), the CW wave entering at the far end (z=L) and is made of one single frequency, as created by the two sidebands of a modulator usually filtered by a FBG before intering in the fibre.

The common sense shows that the worst case is the situation of a uniform fibre showing a constant Brillouin shift, although presenting a short section at the far end with different environmental conditions [50-52], so that the cumulated depletion effect on the pulse is maximized at the maximum gain frequency. If ever the short section at the far end presents a gain spectrum that is slightly shifted with respect to the long uniform preceding section, it will be spectrally scanned by a pump with a frequency varying power as shown in Figure 3-14. This results in a measured skew spectrum in the short section and the determination of the peak gain frequency will be biased. *Here we shall only consider this worst case, all other situations leading to a less severe error*.

As depicted in Figure 3-14, the amount of depletion can be characterized by a dimensionless coefficient d:

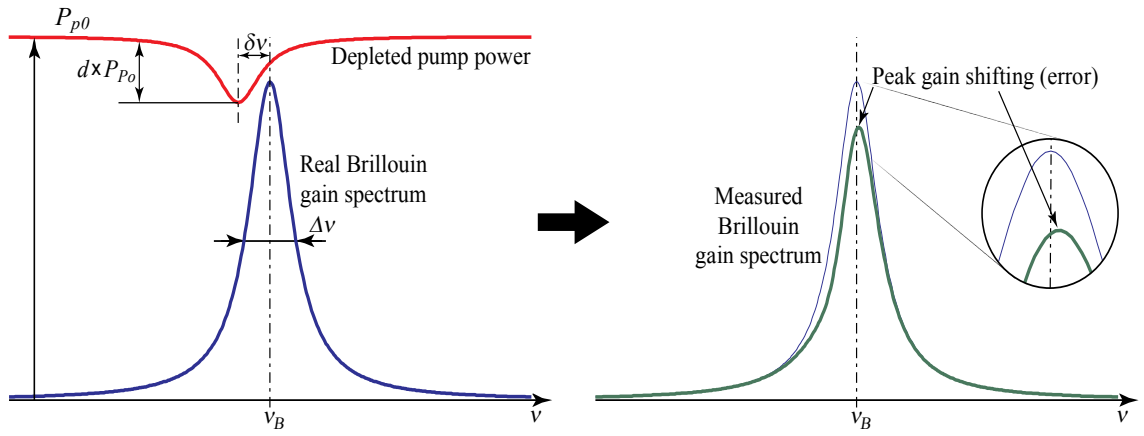

Figure 3-14: After propagation in a long uniform fibre, a too strong CW signal will deplete the pump that will show a power drop when the frequency difference between pump and signal correspond to the Brillouin shift of this long fibre, following a power distribution as shown on the top left curve. If such a pump interrogates a segment with a gain spectrum shifted by a small amount $\delta\nu$, as shown on left, the actual gain spectrum shows a distorted skew distribution with a slightly shifted peak position, as shown on right. The thin line represents the real gain spectrum.

$$d = (P_{Po} - P_P) / P_{Po}\,, \tag{3.13}$$

where P_{Po} is the pump power in absence of Brillouin interaction (absence of gain or no signal wave) and P_P is the pump power in presence of maximum interaction at the Brillouin peak gain frequency.

Assuming the effect of the interaction has negligible impact on the power P_S of the CW signal wave (in small gain condition less than 10%), the signal launched at the far end at $z=L$ will only experience an exponential decay due to the linear attenuation α, so that $P_S(z) = P_{iS}\,\mathrm{e}^{-\alpha(L-z)}$ with $P_{iS} = P_S(L)$ as the input signal power. Then the pump power distribution $P_P(z)$ can be calculated by solving the basic equations for the Brillouin interaction (defined in Eqs. (2.36)), including the linear attenuation term:

$$dP_P = -\alpha P_P(z)\,dz - \frac{g_B}{A_{eff}} P_P(z) P_s(z)\,dz\,, \tag{3.14}$$

where g_B and A_{eff} were defined to be the Brillouin linear gain and the nonlinear effective area of the propagating mode in the fibre(as defined in Chapter 2) , respectively. It must be pointed out that g_B is considered here as position-independent, since the maximal depletion effect will be observed in the worst case scenario when the gain is maximal at any position.

By inserting Eq.(3.13) into Eq.(3.14) and performing the integration, an exact solution $P_P(z)$ can be found, that gives the following final expression for the residual output pump power $P_P(L)$ after fixing the initial condition $P_{iP}=P_P(0)$:

$$P_P(L) = P_{iP}\, e^{-\alpha L} e^{-\frac{g_B}{\alpha A_{eff}} P_{is}\left(1-e^{-\alpha L}\right)} = P_{iP}\, e^{-\alpha L} e^{-\frac{g_B}{A_{eff}} P_{is} L_{eff}}\,, \tag{3.15}$$

where the non-linear effective length of the fibre L_{eff} was defined in Eq. (2.53). Eq. (3.15) simply shows that the pump experiences a loss equivalent to the gain experienced by a small signal giving negligible pump depletion. This is the translation into the situation of a negligible gain on the signal.

The output pump power with a zero gain interaction reads simply $P_{P0}(L) = P_{iP}\, e^{-\alpha L}$ from Eq. (2.51), so that the depletion factor d can be easily derived by inserting $P_{p0}(L)$ and Eq. (3.15) into Eq. (3.13):

$$1 - d = \frac{P_P(L)}{P_{Po}(L)} = \mathrm{e}^{-\frac{g_B}{A_{eff}} P_{iS} L_{eff}}\,, \tag{3.16}$$

and hence the maximum input signal power P_{iS} for a given tolerable depletion factor d is given by:

$$P_{is} < -\ln(1-d)\frac{A_{eff}}{g_B L_{eff}} \overset{L\to\infty}{=} -\ln(1-d)\frac{A_{eff}}{g_B}\alpha\,, \tag{3.17}$$

This result is very crucial, since it shows of a single sideband used as CW signal, the maximum CW signal power P_{iS} is totally independent of the pump power P_{iP} and the pulse width T of the pump. It only depends on the fibre properties for a given depletion factor d.

The expression in Eq. (3.16) can be rewritten differently to use more practical quantities, since frequently the gain coefficient g_B and the effective mode area A_{eff} are actually difficult to evaluate. In a small gain situation, the signal will experience a gain G caused by the pump pulse (peak power P_{iP}, duration T), easily observable and measurable on the signal waveform:

$$G = \frac{g_B}{A_{eff}} P_{iP} \frac{V_g T}{2}, \tag{3.18}$$

where V_g is the group velocity or phase velocity. So that the condition given by Eq. (3.17) can be rewritten as $\frac{P_{iS}}{P_{iP}} < -\ln(1-d)\frac{V_g T}{2G L_{eff}} \overset{L\to\infty}{=} -\ln(1-d)\frac{V_g T}{2G}\alpha$.

3.5.1.2 Extension to 2nd order correction and generalization to the presence of two sidebands

The model above can be made more general to take into account the effect of the gain (or loss) on the signal, so that the signal is no longer assumed to depend only on the attenuation. Nevertheless we shall keep assuming that the gain is small, so that the exponential gain can be write as $e^x \approx 1+x$. Simultaneously we shall include the possibility that the signal is made of two frequencies as created by the two sidebands of a modulator, one experiencing gain (the lower sideband with power P_{isL}), the other experiencing loss (the upper sideband P_{isU}). This is a common experimental situation and it alleviates a lot the effect of depletion. We can nevertheless set the power of any sideband to zero in the expressions, to address the case of a pure gain or loss on a single sideband.

The signals power dependence on z will then be expressed by:

$$P_{SL}(z) = P_{iSL}\, e^{-\alpha(L-z)}[1+\frac{g_B}{A_{eff}} P_p(z)\frac{V_g T}{2}] = P_{iSL}\, e^{-\alpha(L-z)}[1+\frac{g_B}{A_{eff}} P_p(z)\, l], \tag{3.19a}$$

$$P_{SU}(z) = P_{iSU}\, e^{-\alpha(L-z)}[1-\frac{g_B}{A_{eff}} P_p(z)\frac{V_g T}{2}] = P_{iSU}\, e^{-\alpha(L-z)}[1-\frac{g_B}{A_{eff}} P_p(z)\, l], \tag{3.19b}$$

where $l=V_gT/2$. The rate equation for the pump can be completed with the contribution of the upper sideband:

$$dP_P = -\alpha\, P_P(z)\, dz - \frac{g_B}{A_{eff}} P_P(z)\, P_{SL}(z)\, dz + \frac{g_B}{A_{eff}} P_P(z)\, P_{SU}(z)\, dz, \tag{3.20}$$

By substituting Eqs. (3.19) into Eq. (3.20) we obtain:

$$dP_P = -\alpha\, P_P(z)\, dz - \frac{g_B}{A_{eff}} P_P(z)[P_{iSL} - P_{iSU}]\mathrm{e}^{-\alpha(L-z)}\, dz - \frac{g_B^2}{A_{eff}^2} P_P^2(z)[P_{iSL} + P_{iSU}]\mathrm{e}^{-\alpha(L-z)}\, l\, dz\,, \quad (3.21)$$

The last right-hand term is a 2nd order term and is normally much smaller than the two other terms, except in the situation when $P_{iSL} \cong P_{iSU}$. This is exactly the situation when we propagate the two sidebands and we filter out one of the sideband just before detection, as in Figure 3-9. If the sidebands have equal amplitudes, the 1st order term vanishes and, according to our previous modeling (Eq. (3.16) to Eq. (3.17)), we should observe no depletion!. We see the very positive impact of propagating the two sidebands, since the depletion on the pump created by the lower sideband is exactly compensated by the gain on the pump created by the upper sideband, to 1st order.

At first glance, there is no general solution for Eq. (3.21), so we shall consider the 2nd order term as a perturbation. The unperturbed solution P_P^0 is given by Eq. (3.17) and is repeated here by extending to the presence of two sidebands:

$$P_P^0(z) = P_{iP}\, e^{-\alpha L} e^{-\frac{g_B}{\alpha A_{eff}}[P_{isL} - P_{isU}]e^{-\alpha L}\left(e^{+\alpha z} - 1\right)}\,, \quad (3.22)$$

We see clearly that the pump experiences no depletion for sidebands of equal amplitude in a first order approximation.

Then let the general solution to be:

$$P_P(z) = C(z) P_P^0(z)\,, \quad (3.23)$$

By inserting Eq. (3-23) into Eq. (3-21) leads:

$$\frac{dP_P}{dz} = P_P^0(z)\frac{dC}{dz} + \cancel{C(z)\frac{dP_P^0}{dz}} = \cancel{-\alpha\, C(z) P_P^0(z)} - \cancel{\frac{g_B}{A_{eff}} C(z) P_P^0(z)[P_{iSL} - P_{iSU}]\mathrm{e}^{-\alpha(L-z)}} - \frac{g_B^2}{A_{eff}^2} C^2(z) P_P^{02}(z)[P_{iSL} + P_{iSU}]\mathrm{e}^{-\alpha(L-z)}\, l\,, \quad (3.24)$$

Three terms can be eliminated since they correspond to the unperturbed equation once $C(z)$ is placed as a multiplying factor, so that it remains the following equation to be solved for C:

$$\frac{dC}{dz} = -\frac{g_B^2}{A_{eff}^2} C^2(z) P_{iP}[P_{iSL} + P_{iSU}]\mathrm{e}^{-\alpha L}\, l\, \mathrm{e}^{-\frac{g_B}{\alpha A_{eff}}[P_{iSL} - P_{iSU}]\mathrm{e}^{-\alpha L}(\mathrm{e}^{+\alpha z} - 1)}\,, \quad (3.25)$$

This differential equation has unfortunately no analytical solution without further approximation. The problem comes from the exp(exp(z)) functional dependence that has no analytical primitive. The challenge is to find the approximation that makes sense.

(i) Situation 1

By checking real values, if we assume the reasonable situation that the power difference between the two sidebands does not exceed 0.1 mW, the argument of the exponential of Eq. (3.25) is of the order of 0.1 or less. So we can use the usual expansion $e^x \cong 1+x$ and rewrite Eq. (3.25) as:

$$\frac{dC}{dz} = -\frac{g_B^2}{A_{eff}^2} C^2(z) P_{iP} [P_{iSL} + P_{iSU}] e^{-\alpha L} \, l \, e^{\frac{g_B}{\alpha A_{eff}} [P_{iSL} - P_{iSU}] e^{-\alpha L}} \left\{ 1 - \frac{g_B}{\alpha A_{eff}} [P_{iSL} - P_{iSU}] e^{-\alpha (L-z)} \right\}, \quad (3.26)$$

This equation contains a lot of constant terms and can be rewritten to simplify the calculation:

$$\frac{dC}{C^2} = -A(1 - B\, e^{\alpha z})\, dz, \quad (3.27)$$

with

$$\begin{aligned} A &= \frac{g_B^2}{A_{eff}^2} P_{iP} [P_{iSL} + P_{iSU}] e^{-\alpha L} \, l \, e^{\frac{g_B}{\alpha A_{eff}} [P_{iSL} - P_{iSU}] e^{-\alpha L}} \\ B &= \frac{g_B}{\alpha A_{eff}} [P_{iSL} - P_{iSU}] e^{-\alpha L} \end{aligned}, \quad (3.28)$$

The general solution of Eq. (3.27) is then:

$$\frac{1}{C} - K = A\left(z - \frac{B}{\alpha} e^{\alpha z}\right), \quad (3.29)$$

where K is an arbitrary integration constant.

Since $P_P(z=0) = P_{iP}$ and according to Eq. (3.22) and Eq. (3.23), we must have $C(z=0) = 1$, so K can be determined:

$$K = 1 + \frac{AB}{\alpha} \quad \text{and} \quad C = \frac{1}{1 + Az + \frac{AB}{\alpha}(1 - e^{\alpha z})}, \quad (3.30)$$

The general solution for $P_P(z)$ can be written finally as:

$$P_P(z) = \frac{P_{iP}\, e^{-\alpha z}\, e^{-\frac{g_B}{\alpha A_{eff}} [P_{iSL} - P_{iSU}] e^{-\alpha L} (e^{+\alpha z} - 1)}}{1 + \frac{g_B^2}{A_{eff}^2} P_{iP} [P_{iSL} + P_{iSU}] e^{-\alpha L} \, l \, e^{\frac{g_B}{\alpha A_{eff}} [P_{iSL} - P_{iSU}] e^{-\alpha L}} \left\{ z - \frac{g_B}{A_{eff}} [P_{iSL} - P_{iSU}] \frac{e^{-\alpha L}}{\alpha^2} (e^{+\alpha z} - 1) \right\}}, \quad (3.31)$$

The interesting value for evaluating depletion is the pump power at the fiber far end:

$$P_P(L)=\frac{P_{iP}\,\mathrm{e}^{-\alpha L}\,\mathrm{e}^{-\frac{g_B}{A_{eff}}[P_{iSL}-P_{iSU}]L_{eff}}}{1+\frac{g_B^2}{A_{eff}^2}P_{iP}[P_{iSL}+P_{iSU}]\mathrm{e}^{-\alpha L}\,l\,\mathrm{e}^{\frac{g_B}{\alpha A_{eff}}[P_{iSL}-P_{iSU}]\mathrm{e}^{-\alpha L}}\left\{L-\frac{g_B}{A_{eff}}[P_{iSL}-P_{iSU}]\frac{L_{eff}}{\alpha}\right\}}, \quad (3.32)$$

Since the denominator now contains an additive term that depends on the input pump power, the depletion with the 2nd order correction is no longer independent of the pump power. The expression is quite complicated, but it can be simplified according to the situation. The numerator of Eq. (3.32) is the 1st order correction as found in Eq. (3.15) that remains a good evaluation when only one signal is present (lower or upper sideband). *The 2nd order correction is minor and is maximum when the fibre length is equal to 1/α.* The expression in Eq. (3.16) for the depletion remains valid. In presence of two sidebands of equal power (P_{iSL}=P_{iSU}) the 2nd order correction must be taken in to account, however many terms vanish in Eq. (3.32). In this particular case, the pump power at the far end can be expressed as:

$$P_P(L)=\frac{P_{iP}\,\mathrm{e}^{-\alpha L}}{1+\frac{g_B^2}{A_{eff}^2}P_{iP}[P_{iSL}+P_{iSU}]\mathrm{e}^{-\alpha L}\,l\,L}, \quad (3.33)$$

so the depletion factor can be then expressed as:

$$1-d=\frac{P_P(L)}{P_{Po}(L)}=\frac{1}{1+\frac{g_B^2}{A_{eff}^2}P_{iP}[P_{iSL}+P_{iSU}]\mathrm{e}^{-\alpha L}\,l\,L}=\frac{1}{1+G\frac{g_B}{A_{eff}}[P_{iSL}+P_{iSU}]\mathrm{e}^{-\alpha L}\,L}, \quad (3.34)$$

where the expression in Eq. (3.18) for the gain at the fibre input has been inserted. The second term in the denominator is maximum when L=1/α. This can be explained as follow: the depletion naturally increases with the fibre length when the effect of attenuation is small, so for short fibre length. Then, for longer fibres, the attenuation experienced by the signal and the pump limits the product of their power at any location along the power.

To establish for the two sidebands case *of equal amplitude* an expression similar to Eq. (3.17), the tolerable signal power for a given depletion d can be expressed as:

$$P_{iSL}+P_{iSU}<\frac{d}{\frac{g_B^2}{A_{eff}^2}P_{iP}(1-d)\mathrm{e}^{-\alpha L}\,l\,L}=\frac{d}{G\frac{g_B}{A_{eff}}(1-d)\mathrm{e}^{-\alpha L}\,L}\overset{L=1/\alpha}{=}\frac{e\,\alpha\,d}{G\frac{g_B}{A_{eff}}(1-d)}=\frac{e\,\alpha\,d\,P_{iP}\,l}{G^2(1-d)}, \quad (3.35)$$

(ii) Situation 2

If the power difference between the two sidebands is larger than 0.1 mW (case of a single sideband for example), but the propagation is over a distance short compared to the typical attenuation distance α^{-1} (1 km fibre for example), the expression in Eq. (3.25) can be simplified differently: $\mathrm{e}^{\alpha z}-1\approx\alpha z$ and Eq. (3.26) can be rewritten in this case as:

$$\frac{dC}{dz} = -\frac{g_B^2}{A_{eff}^2} C^2(z) P_{iP} [P_{iSL} + P_{iSU}] \mathrm{e}^{-\alpha L} \, l \, \mathrm{e}^{-\frac{g_B}{A_{eff}} [P_{iSL} - P_{iSU}] \mathrm{e}^{-\alpha L} z}, \tag{3.36}$$

Such an equation can be used for instance to evaluate the 2nd order correction in the single sideband case. The differential equation is simplified by grouping the constant terms:

$$\frac{dC}{C^2} = -A' \mathrm{e}^{-B'z} \, dz, \tag{3.37}$$

with:

$$\begin{aligned} A' &= \frac{g_B^2}{A_{eff}^2} P_{iP} [P_{iSL} + P_{iSU}] \mathrm{e}^{-\alpha L} \, l \\ B' &= \frac{g_B}{A_{eff}} [P_{iSL} - P_{iSU}] \mathrm{e}^{-\alpha L} \end{aligned}. \tag{3.38}$$

The general solution of Eq. (3.37) is:

$$\frac{1}{C} - K' = \frac{A'}{B'} \mathrm{e}^{-B'z}, \tag{3.29}$$

where K' is an arbitrary integration constant.

Since $P_P(z=0) = P_{iP}$ and according to Eq. (3.22) and Eq. (3.23), we must have $C(z=0) = 1$, so K' can be determined:

$$K' = 1 - \frac{A'}{B'} \quad \text{and} \quad C = \frac{1}{1 - \frac{A'}{B'}(1 - \mathrm{e}^{-B'z})}. \tag{3.40}$$

The general solution for $P_P(z)$ can be written finally as:

$$P_P(z) = \frac{P_{iP} \, \mathrm{e}^{-\alpha z} \, \mathrm{e}^{-\frac{g_B}{\alpha A_{eff}} [P_{iSL} - P_{iSU}] \mathrm{e}^{-\alpha L} (\mathrm{e}^{+\alpha z} - 1)}}{1 + \frac{g_B}{A_{eff}} P_{iP} \frac{P_{iSL} + P_{iSU}}{P_{iSL} - P_{iSU}} \, l \, [1 - \mathrm{e}^{-\frac{g_B}{A_{eff}} [P_{iSL} - P_{iSU}] \mathrm{e}^{-\alpha L} z}]}. \tag{3.41}$$

The interesting value for evaluating depletion is the pump power at the fiber far end:

$$P_P(L) = \frac{P_{iP} \, \mathrm{e}^{-\alpha L} \, \mathrm{e}^{-\frac{g_B}{A_{eff}} [P_{iSL} - P_{iSU}] L_{eff}}}{1 + \frac{g_B}{A_{eff}} P_{iP} \frac{P_{iSL} + P_{iSU}}{P_{iSL} - P_{iSU}} \, l \, [1 - \mathrm{e}^{-\frac{g_B}{A_{eff}} [P_{iSL} - P_{iSU}] \mathrm{e}^{-\alpha L} L}]}. \tag{3.42}$$

In the presence of a single sideband (e.g. $P_{iSU}=0$), this expression is reduced to:

$$P_P(L)=\frac{P_{iP}\,\mathrm{e}^{-\alpha L}\,\mathrm{e}^{-\frac{g_B}{A_{eff}}P_{iSL}\,L_{eff}}}{1+\frac{g_B}{A_{eff}}P_{iP}\,l\,[1-\mathrm{e}^{-\frac{g_B}{A_{eff}}P_{iSL}\,\mathrm{e}^{-\alpha L}\,L}]}, \tag{3.43}$$

and the depletion factor in this case reads as:

$$1-d=\frac{P_P(L)}{P_0(L)}=\frac{\mathrm{e}^{-\frac{g_B}{A_{eff}}P_{iSL}\,L_{eff}}}{1+\frac{g_B}{A_{eff}}P_{iP}\,l\,[1-\mathrm{e}^{-\frac{g_B}{A_{eff}}P_{iSL}\,\mathrm{e}^{-\alpha L}\,L}]}, \tag{3.44}$$

The numerator of Eq. (3.44) is the 1st order correction as found in Eq. (3.15) and the denominator corresponds to the 2nd order approximation.

3.5.1.3 Relations between depletion and error on the peak of Brillouin gain spectrum

Let consider the Brillouin gain spectrum in a short section at the far end of the fibre to be:

$$g(\nu')=g_B\frac{1}{1+\left[\left(\nu'-\nu_B\right)/\Delta\nu/2\right]^2}, \tag{3.45}$$

where ν_B is the Brillouin shift corresponding to the maximal gain in the short section and $\Delta\nu$ the FWHM width of this gain spectrum. To make it simpler, the frequency scale is shifted to $\nu=\nu'-\nu_B$, (maximum gain at the frequency origin).

If the maximal Brillouin gain frequency in the long uniform segment is shifted by $\delta\nu$ and the FWHM width $\Delta\nu$ is identical to the short segment, the pump intensity follows this distribution when the effect of depletion is small (d<0.2):

$$I_p(\nu)=I_{P_{is}}\left[\,1-\frac{d}{1+\left(\frac{\nu-\delta\nu}{\Delta\nu/2}\right)^2}\,\right]. \tag{3.46}$$

Assuming a very small gain in the percent range during the interaction over the pulse width T, the net signal gain can be reasonably expressed by a first order expansion of the exponential amplification:

$$G(\nu)=1+g(\nu)I_P(\nu)\frac{V_gT}{2}=1+g_B\frac{V_gT}{2}I_{P_{is}}\frac{1}{1+\left(\frac{\nu}{\Delta\nu/2}\right)^2}\left[\,1-\frac{d}{1+\left(\frac{\nu-\delta\nu}{\Delta\nu/2}\right)^2}\,\right]. \tag{3.47}$$

This distribution is represented in Figure 3-15 and presents a maximum that is shifted with respect to the *d=0* situation. The amount of shifting depends on the magnitude of the depletion *d* and the relative shift $\delta\nu$ of the maximum gain frequencies of the two segments. The gain FWHM width $\Delta\nu$ is just a scaling factor and all results can be expressed as normalized to $\Delta\nu$. The error is found by calculating ν giving the maximum of the expression in Eq. (3.47). The solution turns out to be the root of a 5th order polynomial given by Eq. (3.48) that cannot be extracted analytically [9]:

$$\begin{aligned}&\nu^5-4\delta\nu\,\nu^4+\left(6\delta\nu^2+2\Delta\nu^2-2d\,\Delta\nu^2\right)\nu^3+\left(3d\,\delta\nu\,\Delta\nu^2-4\delta\nu^3-4\delta\nu\,\Delta\nu^2\right)\nu^2\\&+\left(\delta\nu^4+2\Delta\nu^2\,\delta\nu^2+\Delta\nu^4-2d\,\Delta\nu^4-d\,\Delta\nu^2\,\delta\nu^2\right)\nu+d\,\delta\nu\,\Delta\nu^4=0.\end{aligned} \tag{3.48}$$

Let express Eq. (3.48) in normalized quantities by defining $y=\frac{\nu_e}{\Delta\nu/2}$ and $e=\frac{\delta\nu}{\Delta\nu/2}$. Eq. (3.48) can be written in a condensed manner as $a_o+a_1y+a_2y^2+a_3y^3+a_4y^4+y^5=0$, with: $a_o=d\,e$, $a_1=(1+e^2)^2-d(2+e^2)$ and $a_2=-e\left[4(1+e^2)-3d\right]$, ….

Let assume that *y* is very small: $y\sim 0$, that is very reasonable since we expect the peak of the resonance to be only slightly shifted by the effect of depletion. In that case, a first order solution can be found out by neglecting all terms higher than the first degree in the polynomial expression in Eq. (3.48). The solution can be found immediately:

$$y'=-\frac{a_o}{a_1}=-\frac{d\,e}{(1+e^2)^2-d(2+e^2)}, \tag{3.49}$$

and

$$\nu_e\cong-\frac{d\,\delta\nu}{\left(1+\left(\frac{\delta\nu}{\Delta\nu/2}\right)^2\right)^2-d\left(2+\left(\frac{\delta\nu}{\Delta\nu/2}\right)^2\right)}. \tag{3.50}$$

The minus sign indicates the maximum gain is logically shifted to higher frequencies when the long segment presents a peak gain at lower frequencies than in the short segment. For a small depletion *d*, the right term of the denominator can be neglected. Then the expression is maximal when:

$$\delta\nu=\Delta\nu\sqrt{\frac{d+2}{24}}=\frac{\Delta\nu}{2\sqrt{3}} \tag{3.51}$$

This result simply means that the error is maximal when the shift between the peaks of the two segments spectra is about a quater of the full width, while the error vanishes if there is no shift or a shift much larger than the gain spectral width (no more overlap). Inserting Eq. (3.51) into Eq. (3.50) leaves the following inequality:

$$|\nu_e| < \left| -\frac{27\, d\, \Delta\nu}{169 - 484 d} \right| \approx 0.16 |d| \Delta\nu \,. \tag{3.52}$$

It will be shown that this approximation is not precise enough for the typical values of observed depletion. A plain second order solution will lead to a too complicated mathematical expression, but a perturbation approach gives a somehow simpler relation. For this we state that the second order solution y'' is just a small correction to the first order one y', so that $y'' = y' + \varepsilon$. Eq. (3.48) reduced to the second order can be expressed as:

$$\begin{aligned} a_o + a_1 y'' + a_2 y''^2 &= a_o + a_1 (y' + \varepsilon) + a_2 (y' + \varepsilon)^2 \\ &= \underbrace{a_o + a_1 y'}_{=0,\ \text{by def. of 1st order solution}} + a_1 \varepsilon + a_2 y'^2 + 2 a_2 y' \varepsilon + \underbrace{\cancel{a_2 \varepsilon^2}}_{\text{neglected, } \varepsilon << y'} \,, \\ &= (a_1 + 2 a_2 y')\varepsilon + a_2 y'^2 = 0 \end{aligned} \tag{3.53}$$

$$\Rightarrow \quad \varepsilon = -\frac{a_2 y'^2}{a_1 + 2 a_2 y'} = -\frac{a_2\, a_o^2}{a_1^3 - 2 a_o a_1 a_2} \,, \tag{3.54}$$

and,

$$\Rightarrow \quad y'' = y' + \varepsilon = y' \left[1 - \frac{a_2 y'}{a_1 + 2 a_2 y'} \right] = y' \left[\frac{a_1 + a_2 y'}{a_1 + 2 a_2 y'} \right] = -\frac{a_o}{a_1} \frac{a_1^2 - a_o a_2}{a_1^2 - 2 a_o a_2} \tag{3.55}$$

The final expression for y'' reads:

$$y'' = -\frac{d\, e}{(1+e^2)^2 - d(2+e^2)} \frac{\left[(1+e^2)^2 - d(2+e^2) \right]^2 + d e^2 \left[4(1+e^2) - 3d \right]}{\left[(1+e^2)^2 - d(2+e^2) \right]^2 + 2 d e^2 \left[4(1+e^2) - 3d \right]} \,, \tag{3.56}$$

with $y = \dfrac{\nu_e}{\Delta\nu/2}$ and $e = \dfrac{\delta\nu}{\Delta\nu/2}$.

Figure 3-15 (a) shows for different depletion factors *d* the plot in different approximation (yellow line: exact result by numerical maximum finding, black line: first order approximation, red line: 2nd order approximation) for $\Delta\nu$=40 MHz and $\delta\nu$=10 MHz. This shows that the 2nd order approximation is very good up to *d*=0.25, while the first order is acceptable up to *d*=0.1. On the Figure 3-15 (b) it is shown for $\Delta\nu$=40 MHz the dependence of the frequency error with the frequency difference $\delta\nu$ (between the gain central frequency and the shift central frequency), for four different depletion factors *d*. Again it is clear that the first order approximation leads to an inaccurate determination for d>0.1, while the matching with the 2nd order approximation is nearly perfect. It should be mentioned that the maximum frequency error occurs when $\delta\nu \sim \Delta\nu / 4$ instead of $\delta\nu \sim \Delta\nu / 2\sqrt{3}$ as determined by the 1st order approximation.

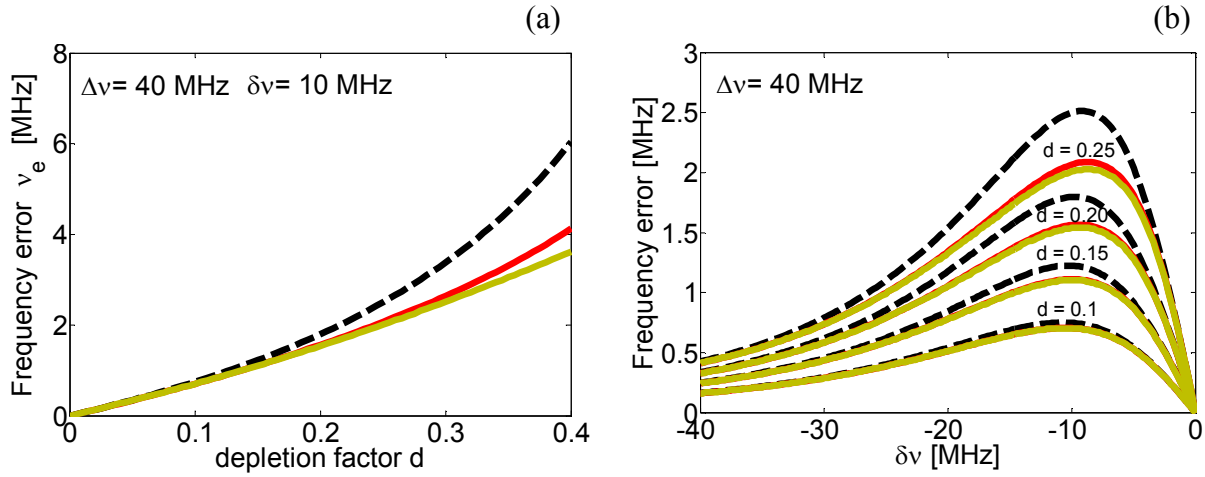

Figure 3-15: (a) Frequency error as a function of the depletion factors *d* for different approximation (black line first order approximation, red line: 2nd order approximation and yellow line: exact result by numerical maximum finding). This shows that the 2nd order approximation is very good up to *d*=0.25, while the first order is only acceptable up to *d*=0.1. (b) Dependence of the frequency error on the frequency difference $\delta\nu$ between the gain central frequency and the depletion central frequency, for four different depletion factor *d*. Again it is clear that the first order approximation leads to an inaccurate determination, while the matching with the 2nd order approximation is nearly perfect.

An interesting result would be to determine the tolerable amount of depletion that would ensure that the error will never exceed a given value ν_e. Fortunately the 5th order polynomial (Eq. (3.48)) shows a linear dependence on the parameter *d*, so an exact solution can be extracted. given by:

$$d=\frac{\nu^5-4\delta\nu\,\nu^4+\left(6\delta\nu^2+2\Delta\nu^2\right)\nu^3+\left(-4\delta\nu^3-4\delta\nu\,\Delta\nu^2\right)\nu^2+\left(\delta\nu^4+2\Delta\nu^2\,\delta\nu^2+\Delta\nu^4-d\,\Delta\nu^2\,\delta\nu^2\right)\nu}{-\left(2\Delta\nu^2\right)\nu^3+\left(3\delta\nu\,\Delta\nu^2\right)\nu^2-\left(2\Delta\nu^4\right)\nu+\delta\nu\,\Delta\nu^4} \tag{3.57}$$

The expression is quite lengthy as can be seen. Following the same procedure as for the perturbation approach before, a robust 2nd order approximation solution can be find which is given here:

$$d_{\max}=\frac{\left(1+e^2\right)\left[4ey^2-\left(1+e^2\right)y\right]}{3ey^2-\left(2+e^2\right)y+e} \text{ with } e=\frac{\delta\nu}{\Delta\nu/2} \text{ and } y=\frac{\nu_e}{\Delta\nu/2} \tag{3.58}$$

It must be mentioned that all results shown above equally applies for a loss configuration. In that case a negative value for the depletion factor *d* has to be inserted in all expressions, leading to similar errors for small *d*.

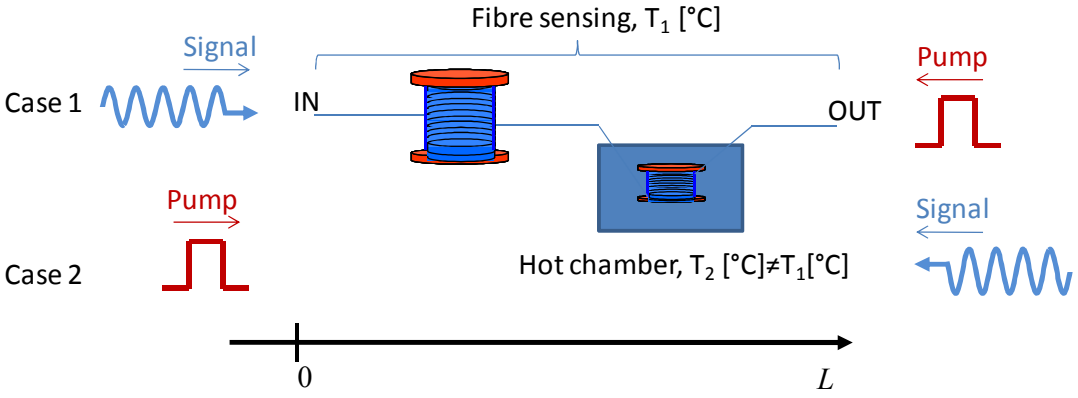

Figure 3-16: (a) Sensing fibre arrangement for pump depletion demonstration and position of the pump and the signal waves. A quasi uniform 1 km SMF fibre showing a constant Brillouin shift with a short section at the far end placed in a environmental temperature condition T_2 =24 °C different than that of the rest of the fibre (T_1=34 °C). Case 1: the pump and the signal are launched respectively at the far end and the near end of the fibre. Case 2: the pump and the signal are launched respectively at the near end and the far end of the fibre.

3.5.1.4 Experimental demonstration and discussion

For a demonstration of the effect of pump depletion, a 50 ns pulse width (corresponding to a spatial resolution of 5 m) was used to avoid a broad pulse bandwidth which may bias the retrieved information on the Brillouin shift. The measurements were realized using a ~1 km long single mode standard fibre (presenting a quasi uniform Brillouin shift oscillating between 10.726 GHz and 10.730 GHz at the far end of the fibre). The fibre was placed at room temperature (T_1 =34 °C) and a 10 m segment of the same fibre was placed in a hot chamber with a temperature controlled at T_2 =24 °C. This latter was chosen according to our model, the 2nd order approximation where $\delta\nu = \Delta\nu/4$, so that the Brillouin frequency shift along this segment is up-shifted by ~10 MHz corresponding to the maximum effect of depletion.

Since for the frequency error it does not matter if one or two sidebands are used as CW signal, we chose to carry out the measurements using one sideband as CW signal. The set-up described in Figure 3-10 was used with two minor modifications: the FBG was placed on the upper arm before the fibre allowing this way to have only one sideband and the scrambler was placed on the pump). Distributed measurements of the Brillouin frequency shift of the fibre were done varying the power P_{is} of the CW signal from 0.70 mW to about 3.50 mW with a fix pump peak power P_{iP} of ~70 mW ensuring a Brillouin gain at the fibre input of 3% (so the small gain assumption is valid).

The first measurements were carried out by launching the pump at the far end of the sensing fibre (case 1) as depicted in Figure 3-16. The same measurements were carried out by launching the pump from the near end the sensing fibre as sketched in Figure 3-16 (case 2). Figure 3-17 (a) to (d) show the Brillouin gain spectrum taken at one position within the 10 m section placed in the hot chamber. First of all, when we look at all graphs, they are all shifted by at least 10 MHz corresponding to the 10°C. Secondly, it can be seen that when the power of the signal increases, the

actual measured peak gain is up-shifted from the expected position (the reference, gray curve) while the Brillouin gain value decreases.

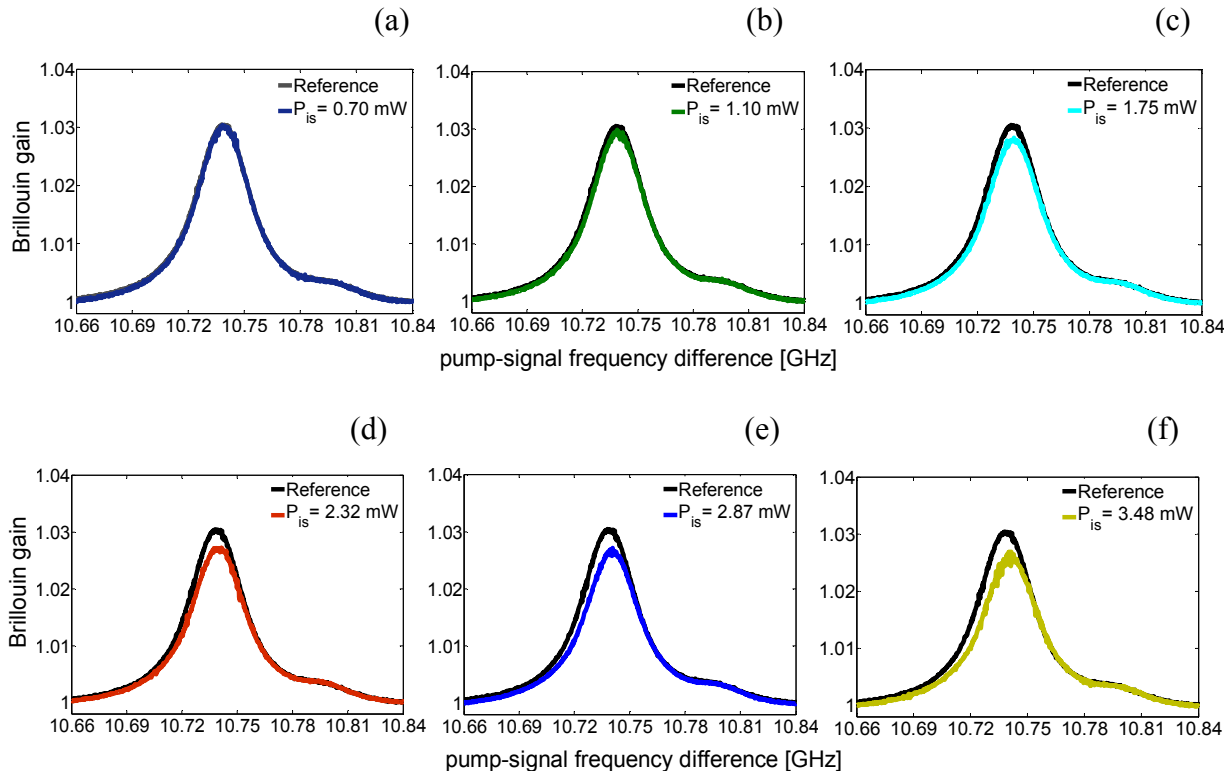

Figure 3-17: Brllouin gain spectrum at one position within the10 m segment of fibre shifted by 10 degrees in temperature for different powers of the CW signal varying from 0.70 mW to ~3.5 mW and with a fix pump peak power of 69 mW. The reference is the Brillouin gain in the case 1 when the pump is launched at the far end of the fibre (gray curve). a) P_{is} = 0.70 mW, b) P_{is} = 1.10 mW, c) P_{is} = 1.75 mW, d) P_{is} = 2.32 mW e) P_{is} = 2.87 mW, f) P_{is} = 2.32 mW showing the evolution of the peak gain for different CW signal power. In each case the actual measured gain spectrum shows a distorted skew distribution with a slightly up-shifted peak position whereas the power increases when compared to the reference (gray curve). If the Brillouin loss configuration was used the peak position would be down-shifted.

The measured Brillouin frequency shift along the sensing fibre in both cases is represented in Figure 3-18 (a) and (c). The Brillouin frequency shift of the 10 m segment of fibre is shifted to ~10.739 GHz, which shows a difference of about 10 MHz with respect to the Brllouin frequency of the rest of the fibre. As we expected from our prediction, for different powers P_{is} of the CW signal, the Brillouin frequency shift moves to higher frequencies for the case 2 and remains quasi constant for the case1 as can be better seen in the closer views shown in Figure 3-18 (b) and (c). This was already observed in the Brillouin spectrum graphs, as already explained this behavior is due to the depletion of the pump trough SBS by the signal as illustrated in Figure 3-19 (a).

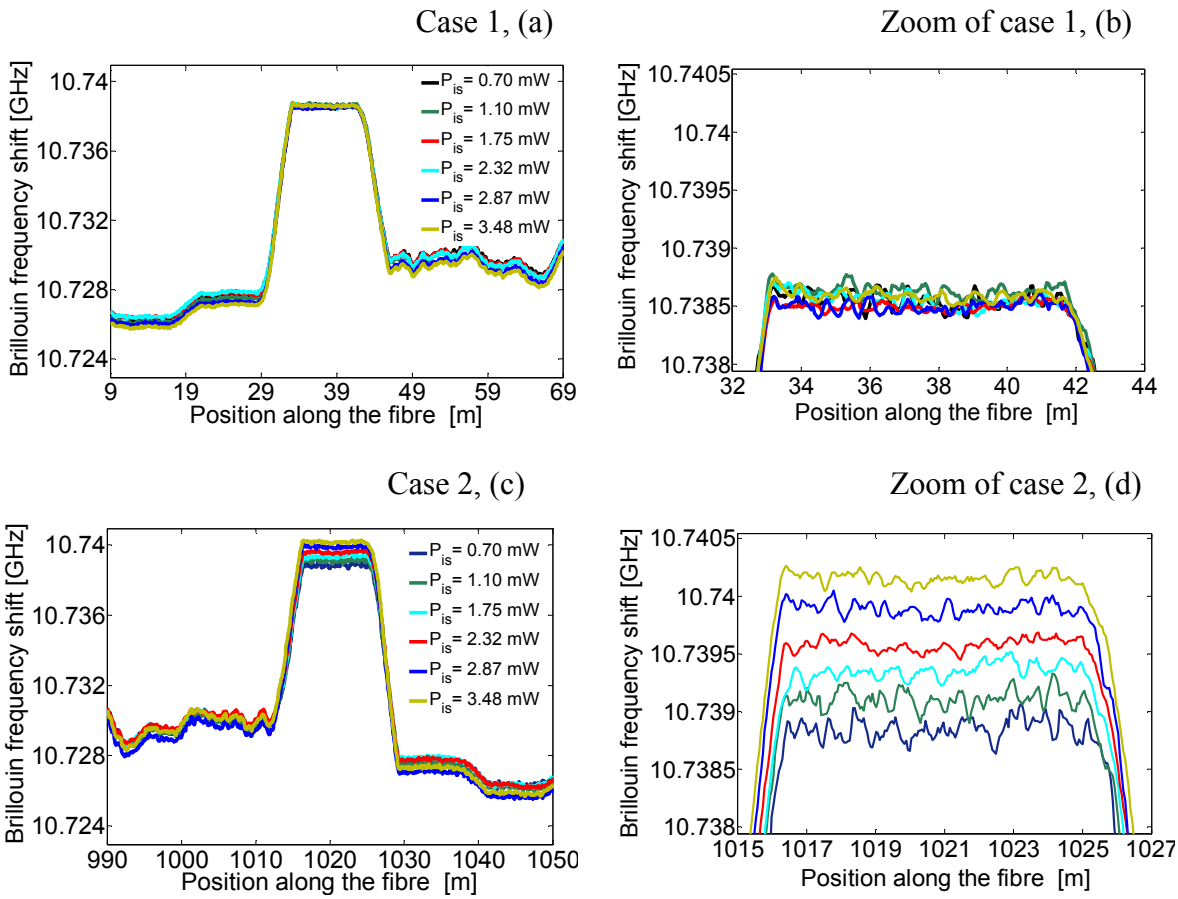

Figure 3-18: Brllouin frequency shift as function of the position for different power P_{is} of the CW signal, (a) in the case 1, (b) closer view of a), (c) in the case 2, (d) closer view of d), In the 10 m section of fibre the Brillouin frequency shift moves to higher frequencies for the case 2 and remains quasi constant for the case1.

The output power of the pump was measured for different frequencies with a detuning of 100 MHz and represented in Figure 3-19 (a). At 100 MHz detuning, the pump is not yet depleted by the signal, but as soon as the detuning becomes close to zero, the pump power gradually drops. In the case that P_{is} = 0.70 mW, the pump power loss is 4.3 % and 20% when P_{is} = 2.87 mW. The depletion factor d was calculated for each signal power P_{is} using the expression in Eq. (3.13). Figure 3-19 (b) represents the measurements of the depletion factor for different CW signal power P_{is} (red square) and the theoretical curves (gray curve: first order approximation, black curve: second order approximation) obtained using the expressions in Eq. (3.16) and Eq. (3.44), respectively. First of all, there is no much difference between the first and the second order approximation before a depletion factor of about 0.2 since we remember that our model is valid for d<0.2. The measurement curve and the theoretical fittings show the same trend. In this figure, we can see that the experimental data are below the theoretical fitting curves. This can be expected since the model address the worst case situation (it supposes that the gain is maximal all over the

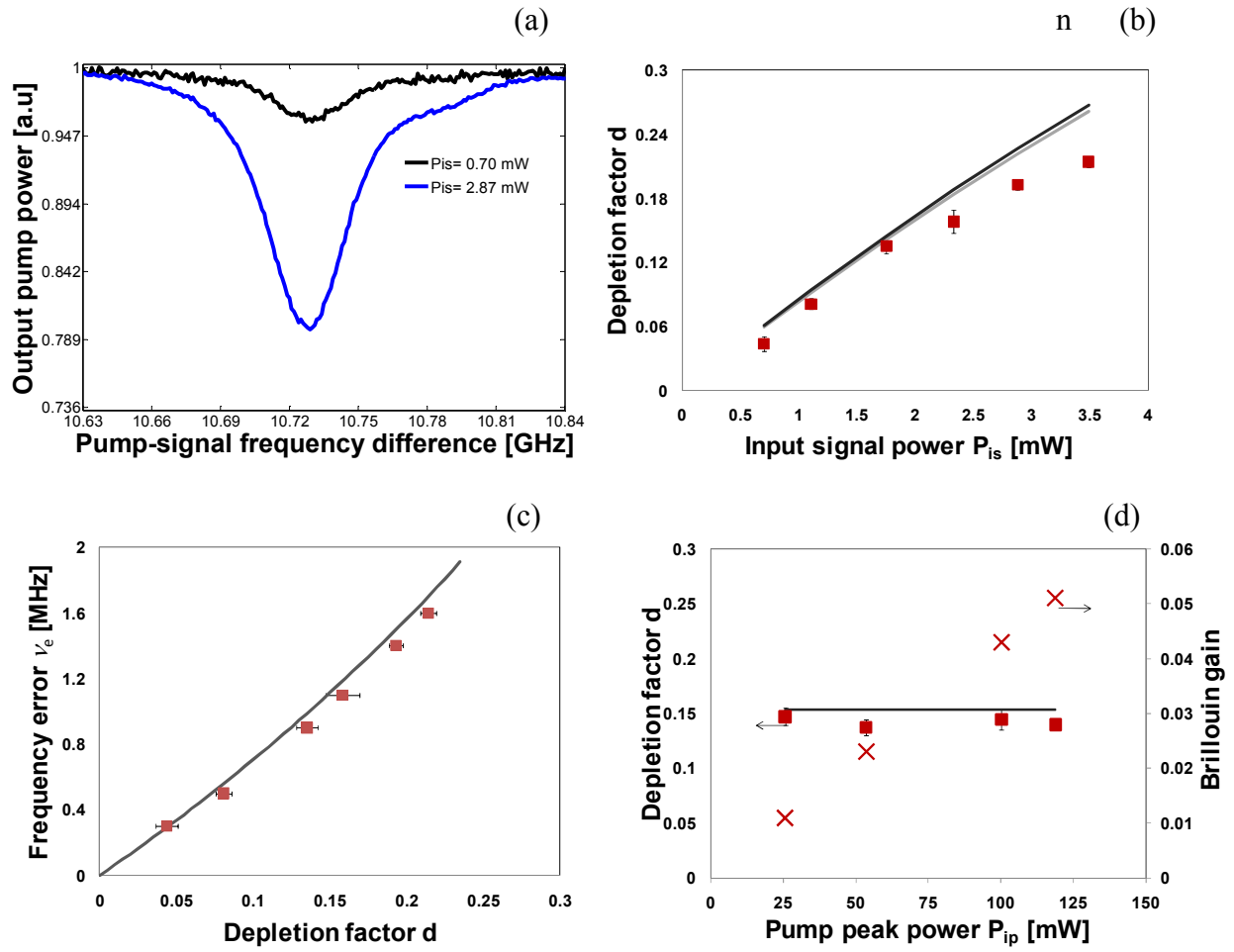

Figure 3-19: (a) Output pump peak power as function of the frequency difference of the pump and the signal for two different values of P_{is} (0.70 mW and 2.87 mW), (b) depletion factor as a function of the power of the CW signal, model (1st order approximation, gray) model (2nd order approximation, black curve) and experiments (red square), (c) frequency error as a function of the depletion factor *d* in the worst case situation for $\delta\nu$=10 MHz (black curve), (d) measured depletion factor *d* (red square), theoretical depletion factor *d* (2nd order approximation, black curve), and Brillouin gain (red cross) as a function of the pump peak power P_{ip} with a Cw signal power P_{is} of ~1.91 mW, the fraction of energy transfer from the pump to the signal remains the same for different pump peak power while the Brillouin gain increases. In a), b) and c) a fix input pump peak power P_{ip} of ~70 mW was used.

fibre). However when looking at Figure 3-20 the Brillouin shift is not totally uniform, so that the Brillouin gain would not be maximal at each position over the fibre, as assumed in the model.

The average value of the frequency shift of the 10 m segment of fibre was calculated and compared in both cases. Figure 3-19 (c) shows the obtained frequency error as a function of the depletion factor (red square). These experimental data were compared to the theoretical modeling (black curve) using the expression in Eq. (3.56). As can be seen, the results obtained experimentally

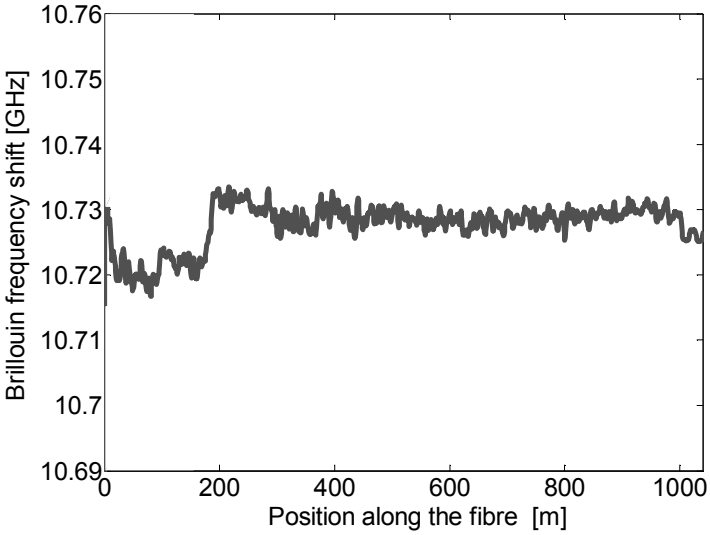

Figure 3-20: Distribution of the frequency shift along the ~1 km single mode fibre presenting a variation.

are confirmed by the theoretical studies. A depletion of about 0.043 gives a frequency error of about 0.4 MHz. from Figure 3-19 (b), this value corresponds to a CW signal power of about 1 mW, meaning that if this latter is used the Brillouin frequency shift will be up-shifted of about 0.4 MHz from its real value, what must be taken into account when setting up the sensor.

We also investigate the pump depletion induced by the signal for different pump peak power. The depletion factor d and the Brillouin gain were measured. The pump peak power P_{ip} was then varied from 26 mW to ~120 mW leaving constant the CW signal power P_{is} to 1.91 mW and ensuring that the gain remains below the 10% given by the small gain assumption. Figure 3-19 (d) shows the measured depletion factor (red square) and Brillouin gain for different input pump power (red cross). We observed that the depletion factor remains constant as the power increases (what is not obvious to understand at the first glance). This means that the proportion of energy transfer from the pump to the signal remains the same for different pump peak power even though the Brillouin gain increases. This is also verified theoretically by Eq. (3.16) showing clearly that the depletion factor d is only dependent on P_{is} and the intrinsic characteristics of the fibre. Even though in the second order approximation in Eq. (3.44).the term P_{ip} appears in the denominator, it remains of negligible influence in the general solution as proved by the black curve in Figure 3-19 (d).

We have also investigated the depletion factor in the case where two sidebands are launched in the far end of the sensing fibre. The experimental results are shown in Figure 3-21 and it turn out that in this case the behavior is different from what has been just discussed in the previous paragraph. When we look at Figure 3-21(a) which represents the output pump power at the far end of the sensing fibre for different powers of the CW signal varied from about 1 mW to about 14.5 mW (only the power of the lower sideband is represented in the figure), the curves look very different from what is presented in Figure 3-19 (a) for the same measurements in the case when one

sideband was used. This can be explained by the shape of the pulse at the output end of the fibre represented in Figure 3-21 (b) for a P_{isL} ~14.5 mW.

For each frequency detuning the pulse presents a different shape. The rising question is the presence of the oscillations observed at 100 MHz far from the central frequency. One explanation could be the interplay between the spontaneous Brillouin generated by the upper sideband (which frequency shift falls just near the frequency of the pump wave) and the pump wave. We have also

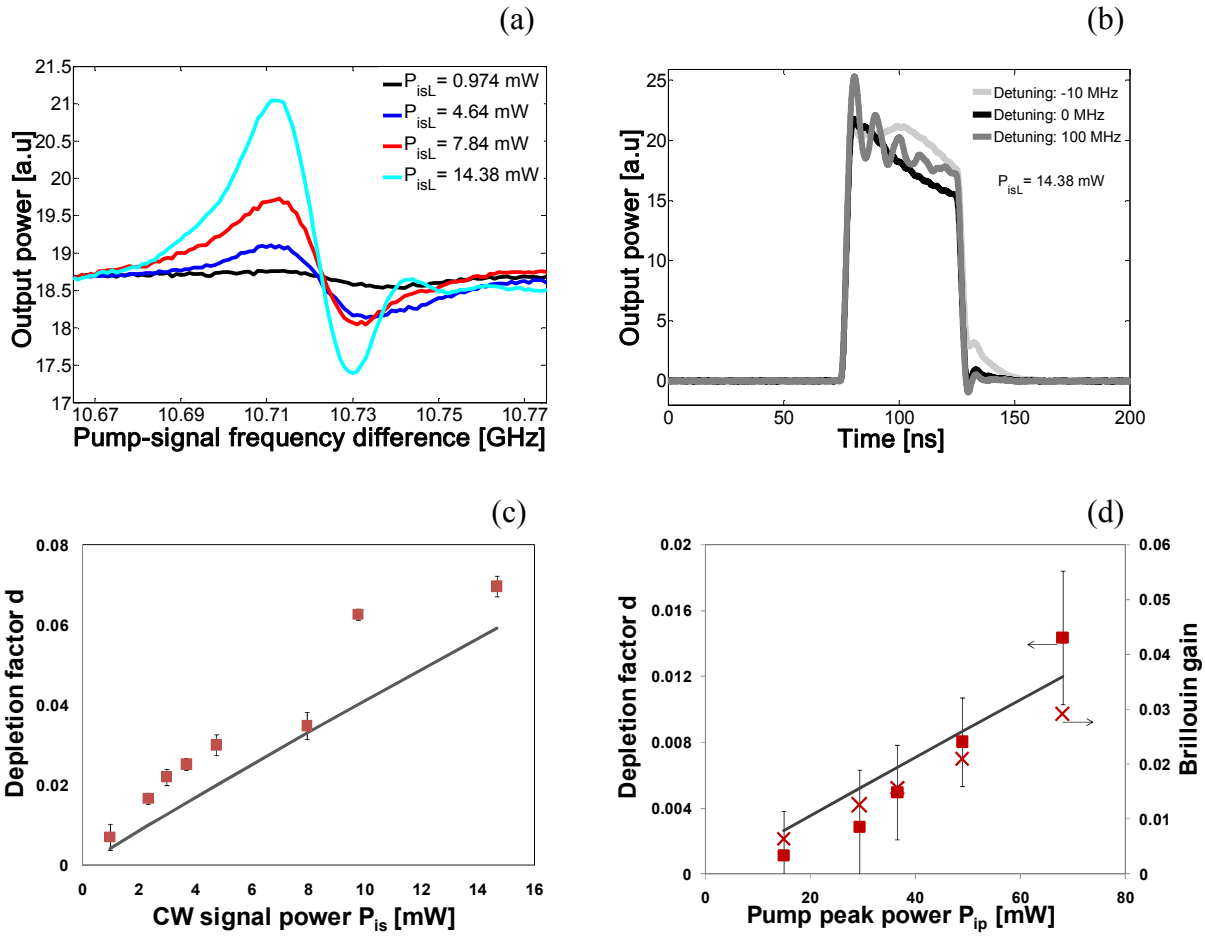

Figure 3-21: (a) Output pump peak power as function of the frequency difference between the pump and the signal for four different values of P_{is}, (b) Output pulse power for three different frequency detunings with P_{isL} = 14.38 mW, (c) depletion factor d as a function of the pump peak power with a CW signal power P_{is} = 1.91 mW, model (2nd order approximation, black curve), experiment (red square), (d) measured depletion factor d (red square), theoretical depletion factor d (2nd order approximation, black curve), and Brillouin gain (red cross) as a function of the pump peak power P_{ip} with a CW signal power P_{is}=2.48 mW, the amount of energy transfer from the pump to the signal increases for different pump peak power while the Brillouin gain increases In (a), (b), and (c), a fix input pump peak power P_{ip} ~60 mW was used.

two main differences: the depletion is much smaller. For example with P_{is} below 1 mW, the depletion is six times smaller (see Figure3-21(c)) than what is observed in the same conditions when one sideband is used. Additionaly the depletion increases with the pump peak power (see Figure 3.21 (d)). The power misbalance between the two sidebands is about 2.2%, so Eq. (3.34) was used for the theoretical fitting. In Figures 21 (c), the theoretical fitting underestimates the measured value of the depletion. This may due to the fact that the model does not take into account the effect of the amplified spontaneous scattering that starts to be important for signal powers above 1 mW. The impact of amplified spontaneous scattering may explain the unexpected response in Figure 3-21(a), but this study is out of the scope of this thesis and requires futher investigations.

3.5.2 Impact of self-phase modulation

3.5.2.1 Theory

The accuracy on the measurand is scaled by the spectral spreading of the effective gain, which in turn is given by the convolution between the pulse spectrum and the natural Brillouin gain spectrum (BGS). According to the standard time-bandwidth relations:

$$\text{Gaussian pulse} \quad \Rightarrow \frac{440MHz}{T}, \tag{3.59a}$$

$$\text{Rectangular pulse} \Rightarrow \frac{880MHz}{T}, \tag{3.59b}$$

the spectral BW of a Gaussian pulse is 2 times lower than that of the rectangular case. So the Gaussian pulse is presumably the best candidate for this interrogation when compared to other profiles (rectangular, triangular). However, we show here that this is not the best choice when addressing long ranges, because this pulse shape leads to a significant spectral broadening of the BGS along the fibre. An observed broadening of the BGS was suspected to be caused by self-phase modulation (SPM) in an early work by Lecoeuche et al [53] and by Izumita et al [54] in coherent OTDR system. SPM leads to small phase chirps during intensity transitions in the pump pulse (leading and trailing edges) that eventually become important in long fibres. The frequency broadening associated with this phase modulation leads to a reduced peak gain and uncertainties in the determination of the Brillouin shift ν_B, but leaves the temporal intensity distribution of the pump pulse unchanged and hence the spatial resolution is preserved. While the former [53-54] works showed a correct intuition addressing qualitatively the issue, no theoretical model was given. We present here a quantitative model of the detrimental impact of SPM supported by a clear experimental demonstration [55]. Two optical pulses with different temporal profiles were judiciously chosen (rectangular and Gaussian) showing the same full width at half maximum (FWHM) and carrying the same energy, to evenly study and compare the SPM impact on their spectrum. Then we clearly experimentally demonstrate the spectral broadening of the BGS due to SPM in a Brillouin distributed fibre sensor in various conditions in terms of pump pulse temporal profiles, power and width. The results are compared with a theoretical model showing good agreement.

SPM is a consequence of the nonlinear Kerr effect in the fibre that results in an intensity-dependent refractive index. It leads an optical pulse to modulate its own optical phase according to its intensity profile. Since the pulse creates a time-dependent refractive index variation, higher for larger intensities, it leads to a time-dependent nonlinear phase shift that translates into variations of the instantaneous frequency (frequency chirp) along the pulse. Let us consider the propagation of an optical pulse through a fibre characterized by a nonlinear refractive index $n(t)=n_0+n_2\,I(t)$ as defined in Eq. (2.58). After propagation over a distance z, the optical pulse accumulates an additional nonlinear phase [56] due to the intensity-dependent part of the refractive index written as $\phi_{NL}=n_2\,(\omega/c_0)\,z\,I(t)$ defined in Eq. (2.60) which creates a variation in its instantaneous frequency given by:

$$\Delta\omega(t)=\frac{d\phi_{NL}(z,t)}{dt}=-n_2\frac{\omega}{c_0}z\frac{dI(t)}{dt} \tag{3.60}$$

Eq. (3.60) clearly shows that SPM will have more impact on fast signals constantly showing temporal transitions, with no interval of constant intensity. For our study we have compared two different temporal profiles (rectangular and Gaussian) showing the same width (for equal spatial resolutions) and the same energy (to make gains equal). The rectangular pulse offers constant intensity intervals only while the Gaussian pulse varies constantly in intensity but shows the best time-bandwidth product (and thus the best time-frequency resolution). Since the intensity is constant at any time for the rectangular profile (assuming instantaneous transitions), $\Delta\omega(t)=0$ and no pulse spectral broadening should therefore be observed. The situation will be drastically different in the Gaussian case showing continuous time transitions. Since it can be entirely described analytically, let consider a pulse with a Gaussian envelope, $E(0,t)=A\exp(-t^2/\tau^2)$, so, $I(t)=|A\exp(-t^2/\tau^2)|^2=I_0\exp(-2t^2/\tau^2)$ with a $1/e$ width τ. The instantaneous frequency chirp imposed on the Gaussian pulse by SPM using Eq. (3.60) can be find in equation below:

$$\Delta\omega(t)=4n_2\frac{\omega}{c_0}zI_0\frac{t^2}{\tau^2}\exp(-2t^2/\tau^2)=4\gamma zP\frac{t}{\tau^2}\exp(-2t^2/\tau^2) \tag{3.43}$$

where c_0 is the vacuum light velocity, ω is the central angular frequency of the optical pulse, I_o and P are, respectively, the peak intensity and peak power of the optical pulse, A_{eff} is the effective area of the fibre mode and $\gamma=n_2\omega/c_0A_{\text{eff}}$ is the fibre nonlinear coefficient given by Eq. (2.59). In a long fibre segment the distance z must be replaced by the effective nonlinear distance $z_{eff}=[1-\exp(-\alpha L)]/\alpha$ already given in Eq. (2.53) where L is the physical length and α in the linear loss of the fibre. The peak excursion of the instantaneous frequency is $\Delta\omega_{\max}=2\gamma Pz_{eff}/\sqrt{e}\,\tau=1.43\gamma Pz_{eff}/T$ offset by $\tau_{\max}=T/\sqrt{8\ln 2}$ from the pulse centre and, as scale factor, gives a good estimate of the real spectral broadening. For typical values in conventional long-range BOTDA systems ($\gamma=1\ \text{W}^{-1}\cdot\text{km}^{-1}$, P=100 mW, z_{eff}=20 km and T=10 ns), this quantity amounts to 2π 29 MHz, which is similar to the Brillouin natural linewidth.

A more precise evaluation of the spectral broadening can be obtained by computing the pulse spectrum evolution along the fibre. The actual frequency spectrum of the Gaussian pulse after

experiencing SPM in the fibre is given by the Fourier transform of the output pulse amplitude according to the following equation:

$$g_{\mathrm{SPM}}(\Delta\nu)=FT\left\{\underbrace{A\,\exp\left(-t^2/\tau^2\right)}_{\text{Gaussian amplitude term}}\underbrace{\exp\left[i\gamma L_{eff}P\exp\left(-2t^2/\tau^2\right)\right]}_{\text{SPM term}}\right\} \tag{3.44}$$

where, for convenience, the time origin is considered always placed at the pulse centre. The effective Brillouin gain linewidth is given by the convolution between the real pump source spectrum after SPM, $g_{\mathrm{SPM}}(\Delta\nu)$, and the natural BGS. It must be noted that all along this derivation we have neglected the effect of chromatic dispersion. This is due to the comparatively long pulse lengths used in BOTDA systems (tens of ns) for long range measurements. It can be easily shown that in these conditions the dispersion length far exceeds the nonlinear length and thus dispersion effects can be neglected [56]. In relation to this, modulation instability (which results from SPM phase-matched by anomalous dispersion) is known to impose a limit on the peak gain of the pump pulses used in Brillouin sensors due to non-linear pump depletion. The observed effect here is radically different from the one observed in MI since it depends not only on the pulse power but also on the pulse shape and duration, and causes a smooth broadening of the BGS which was not observed in the case of MI (this issue is addressed in Section 3.5.4).

3.5.2.2 Results and discussion

The experimental study of the SPM impact on Brillouin fibre sensors has been carried out through a 25.5 km standard SMF fibre. The experimental implementation used for this study was based on a minor adaptation of the high performance pump and probe set-up described in Figure 3-10. A 1552 nm DFB laser is used as the light source. The pump pulse was shaped by an intensity modulator which was driven by an arbitrary waveform generator. The pulses produced have 30 ns FWHM optical pulse duration corresponding to 3 m spatial resolution. This duration was carefully chosen for a better demonstration as a trade-off between temporal transitions fast enough to show the SPM effect and long enough to keep the original spectrum sufficiently narrow (to avoid an excessive broadening of the effective BGS).

The BGS is determined by scanning the microwave generator frequency around the Brillouin shift ν_B. The net Brillouin gain is then measured using a detection stage comprising a 125 MHz bandwidth photoreceiver and a digital oscilloscope synchronously triggered by the arbitrary waveform generator. The distributed nature of the measurements makes possible to retrieve the effective BGS at any position along the fibre, and thus to observe the gradual impact of SPM. Depletion is avoided by using sufficiently low probe power levels (in the microwatt level) to guarantee depletion values below 1%.

Figure 3-22(a) shows the effective gain linewidth (solid lines) along the fibre using 30 ns FWHM Gaussian pulses for increasing pump peak power from 98 mW to 276 mW. The graph shows clearly a quasi-linear increase in the effective gain linewidth caused by the pump spectral broadening due to SPM along the fibre. The same figure represents the calculation of the effective gain linewidth (FWHM) as a function of the distance (dotted lines) showing a good match between the

experimental result and the theoretical model with γ=0.9 $W^{-1}km^{-1}$. This value of γ is a bit small in comparison with the values reported usually in conventional SMF ($1.1W^{-1}km^{-1}$), but the design of this fiber turns out to be quite outdated (manufactured in 1992) and the relatively low measured Brillouin gain suggests a nonlinear effective area for this fibre larger than usual. Figure 3-22(b) represents the evolution of the effective gain linewidth along the fibre using 30 ns FWHM

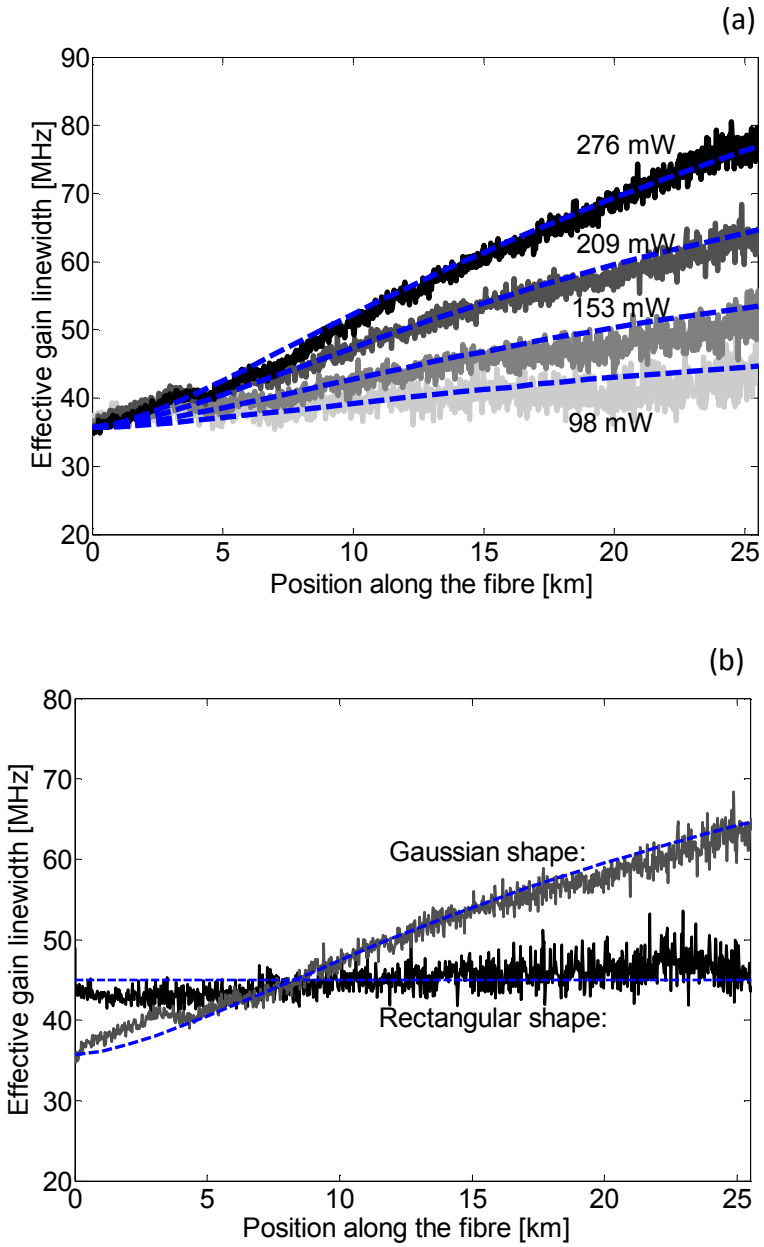

Figure 3-22: Experimental demonstration (solid lines) and theoretical analysis (dotted lines) of the gain spectrum broadening due to SPM along 25.5 km SMF fibre (a) for different peak powers of a 30 ns FWHM Gaussian pulse (b) comparing 30 ns FWHM Gaussian and rectangular pulses of identical energy (peak power of rectangular pulse is 222 mW).

rectangular and Gaussian pulses of identical energy (peak power of rectangular pulse is 222 mW). It can be observed that the gain spectral width is doubled after 25.5 km for the Gaussian pulse, while it remains nearly unchanged for the rectangular pulse as predicted by the model (dotted lines). The residual broadening of the spectrum in the square pulse is probably due to a non-ideal shape in the rectangular pulse used (the rise and fall edges are not ideally sharp). This incidentally confirms a negligeable pump depletion that would instead broaden the effective linewidth of the gain spectrum near the fibre end, independently of the pulse shape. The benefit of a better time-bandwidth product using the Gaussian pulse turns out to be entirely cancelled by SPM after less than 10 km.
From the Figure 3-22(a), and considering the extreme case of 276 mW peak power, the contrast loss can be estimated at the output of the fibre (25.5 km) to be 2 dB, which is equivalent to 10 km distance penalty in standard conditions.
Figure 3-23(a) represents comparative measurements of the gain spectral width measured for a Gaussian pulse at the fibre input (dark gray diamonds) and output (light gray squares), respectively, for different peak powers, demonstrating the clear signature of SPM by the absence of effect at short distance and through the linear dependence on power at long distances.

As shown in Figure 3-23(b) the effective Brillouin gain linewidth varies in inverse proportion to the optical pulse duration T at both the fibre input and output, but with a different slope. An excess broadening is present at the output as a result of the pump spectral spreading. This excess broadening becomes larger for shorter pulses, showing also a $1/T$ slope, in good agreement with the theory above.

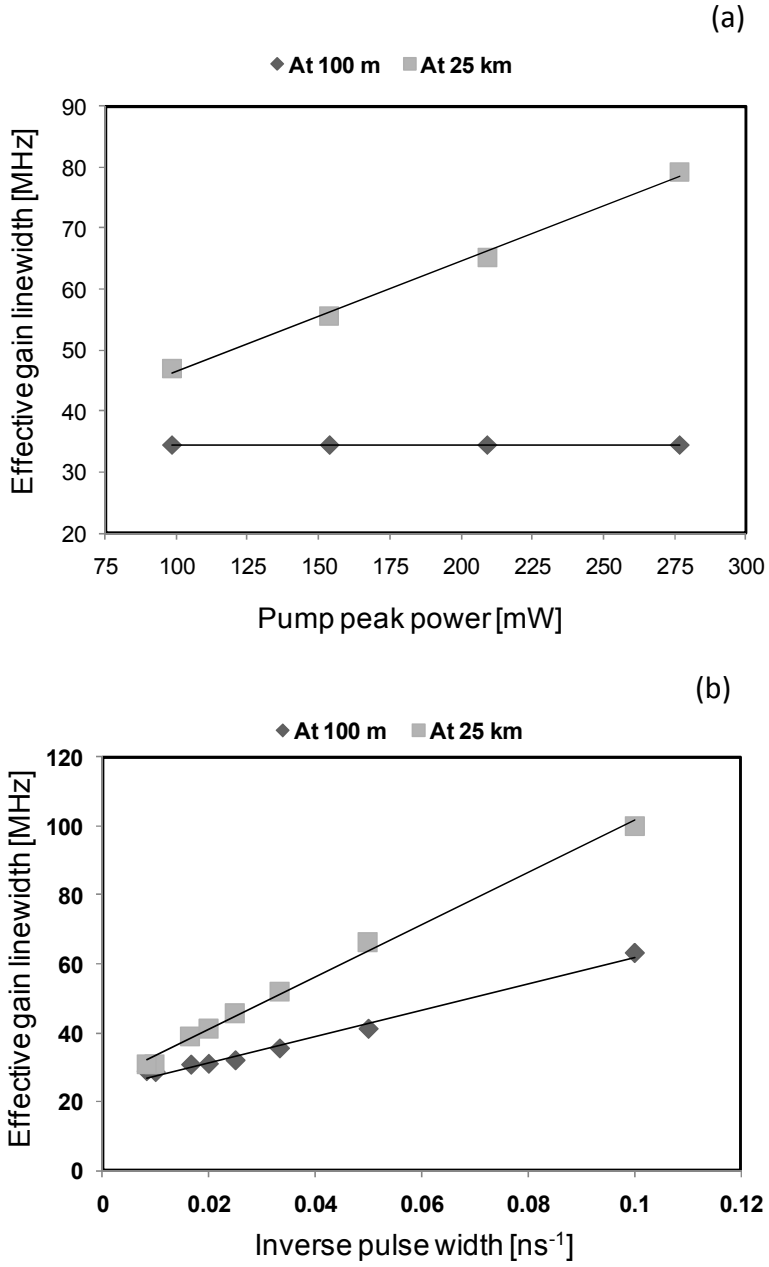

Figure 3-23: Brillouin gain spectral width measured close to the fibre input (100 m) and at the fibre output (25.5 km) using a 30 ns Gaussian pulse (a) Linear dependence on the pump peak power, showing that the effect of SPM is observed only at the distant end, (b) Inverse dependence of the gain linewidth on the pulse width, showing the excess broadening due to SPM at the far end (pump power is 153 mW).

3.5.3 Impact of Raman scattering

Raman scattering (RS) [57] has fundamental similarities with Brillouin scattering, both resulting from the interaction between light and phonons, though showing distinct features as summarized in

Table **3-1**. The most noticeable difference is the frequency shift experienced by the scattered light (13 THz for Raman, 11 GHz for Brillouin scattering), but another important distinct feature is the less strict phase matching condition in RS that makes possible forward scattering. In this latter case the input pump pulse and the Raman-generated signal are co-propagative and may interact over long distance or even the entire fibre length (unlike the case of the backward-only Brillouin scattering where the interaction length is limited to the pump pulse width). The modeling of a signal building from noise through forward Raman scattering has been proposed by Smith [58] in 1972 and has proved to be robust. In our modeling we use the expressions derived by Smith for forward Raman scattering and interpret them in the particular context of distributed Brillouin fibre sensors. Then we adapt this modeling to the particular case of modulation instability, following the same approach, to establish new relations valid to predict the observation threshold for MI.

3.5.3.1 Theory

Let us consider a fibre with a nonlinear effective area A_{eff} and of length L with a linear attenuation α. Let the pump pulse enter the fibre at $z = 0$, traveling in the $+z$ direction with a power P_p and an effective intensity $I_p=P_p/A_{eff}$. Under forward Raman amplification, the output signal power P_s due to amplified spontaneous Raman scattering produced by the incident pump intensity for an effective nonlinear distance L_{eff} by Eq. (2.61) is scaled by the peak Raman gain coefficient g_R and its effective bandwidth:

$$B_{eff} = \frac{\sqrt{\pi}}{2} \frac{\Delta \nu_{\mathrm{FWHM}}}{\sqrt{g_R I_p(0) L_{eff}}}, \tag{3.45}$$

where $\Delta\nu_{\mathrm{FWHM}}$ is the full width at half maximum of the spontaneous gain spectrum. A critical pump power P_{crit} is defined as the fictitious case where this pump amplifies the spontaneous signal to make it as large as the pump power, deliberately neglecting the effect of pump depletion. Actually this critical power P_{crit} is a good estimation of the pumping level giving rise to an amplified noise with power comparable to the pump and thus evidently depleting the pump. This leads to the following nonlinear equation to be solved for P_{crit}:

$$\frac{\sqrt{\pi}}{2}(h\nu_s)\frac{g_R}{A_{eff}} L_{eff} \Delta\nu_{\mathrm{FWHM}} = \left[\frac{g_R P_{\mathrm{crit}} L_{eff}}{A_{eff}}\right]^{3/2} \exp\left[-\frac{g_R P_{\mathrm{crit}} L_{eff}}{A_{eff}}\right], \tag{3.46}$$

from which an approximate simplified equality can be obtained using the Raman spectral characteristics in silica fibers:

$$P_{crit}^{R} \approx \frac{16A_{eff}}{g_R L_{eff}}. \quad (3.47)$$

3.5.3.2 Results and discussion

To evaluate the impact of forward Raman scattering (RS), it is necessary to avoid modulation instability by propagating the pump in normal dispersion conditions. For this purpose a 13 km DSF fiber was used and the same set of measurements at different powers was carried out. We measured series of power spectra using an optical spectrum analyzer at the output fibre end for various input pulse peak power (~400 mW to 2.16 W) as shown in Figure 3-24(c). It can be seen that there is no effect of MI, but in the inset we can see that the Raman effect takes place around 1672 nm gradually as the pump peak power increases. As a consequence the present depletion was purely due to RS by observing the presence of a strong signal at 1672 nm and by observing the depletion of the pump pulse at the initial wavelength, as shown in Figure 3-24(a). The pump pulse undergoes strong distortions as the input pump power increases and the group velocity difference at the pump and Raman wavelength causes a differential depletion over the pulse duration, even leaving a very short un-depleted section at the front edge of the pulse.Figure 3-24(b) shows the effective Brillouin gain as a function of the position in the DSF fiber for a pump peak power from ~400 mW to 2.16 W. The graph shows clearly the gradual drop of the gain after 3.4 km for a 664 mW pump power which turns more pronounced and abrupt for higher pump powers.

The absence of Raman effect is observed below a 400 mW pump power, we will see in the next setion that this power is higher than that observed for MI as anticipated by the model. Figure 3-24 (c) represents the graph of the pump power versus critical distance for experimental data (*) and for model prediction using Eq. (3.47) (solid line) showing an excellent agreement between the experimental result and the theoretical expression (using the fibre characteristics shown in Table **3-1**).

3.5.4 Impact of modulation instability

If the modulation instability phenomenon has been extensively exploited for the generation of ultrashort pulses with high repetition rate [61] and more recently as a basis for the generation of supercontinuum sources [62], in Brillouin sensors this phenomenon is not welcome. A very similar behavior observed for Raman scattering is also observed for modulation instability, which is a consequence of the interaction between Kerr effect and anomalous dispersion, giving rise to a train of solitons self-building from noise. In that case the signal manifests as spectral side lobes around

Table 3-1: Characteristics of the SMF and the DSF fibres used for the experiments.

Fibre type	Fibre loss (dB/km)	Effective area (μm^2)	Dispersion @ 1550nm (ps/km nm)	Raman Gain coef. (m/W)
SMF	0.22	~80	17	~$1e^{-13}$
DSF	0.14	~50	-2	~$4e^{-13}$

the pump frequency that extends over many tens of GHz, depending on the pump power and the medium chromatic dispersion that must be anomalous (D_λ>0).

In total analogy a similar relation can be established for MI. The essential step is to determine the effective bandwidth B_{eff} that is directly related to the spectral characteristics of the broadband gain due to MI. From the analysis of the non-linear Schrödinger equation for anomalous dispersion, we can find the MI gain spectrum $G(\omega)=|\beta_2\omega|\sqrt{\omega_c^2-\omega^2}$, where $\omega_c=(4\gamma P_p/\beta_2)^{1/2}$ is the critical frequency, β_2 the dispersion coefficient, γ the nonlinear parameter and P_p the input power. The

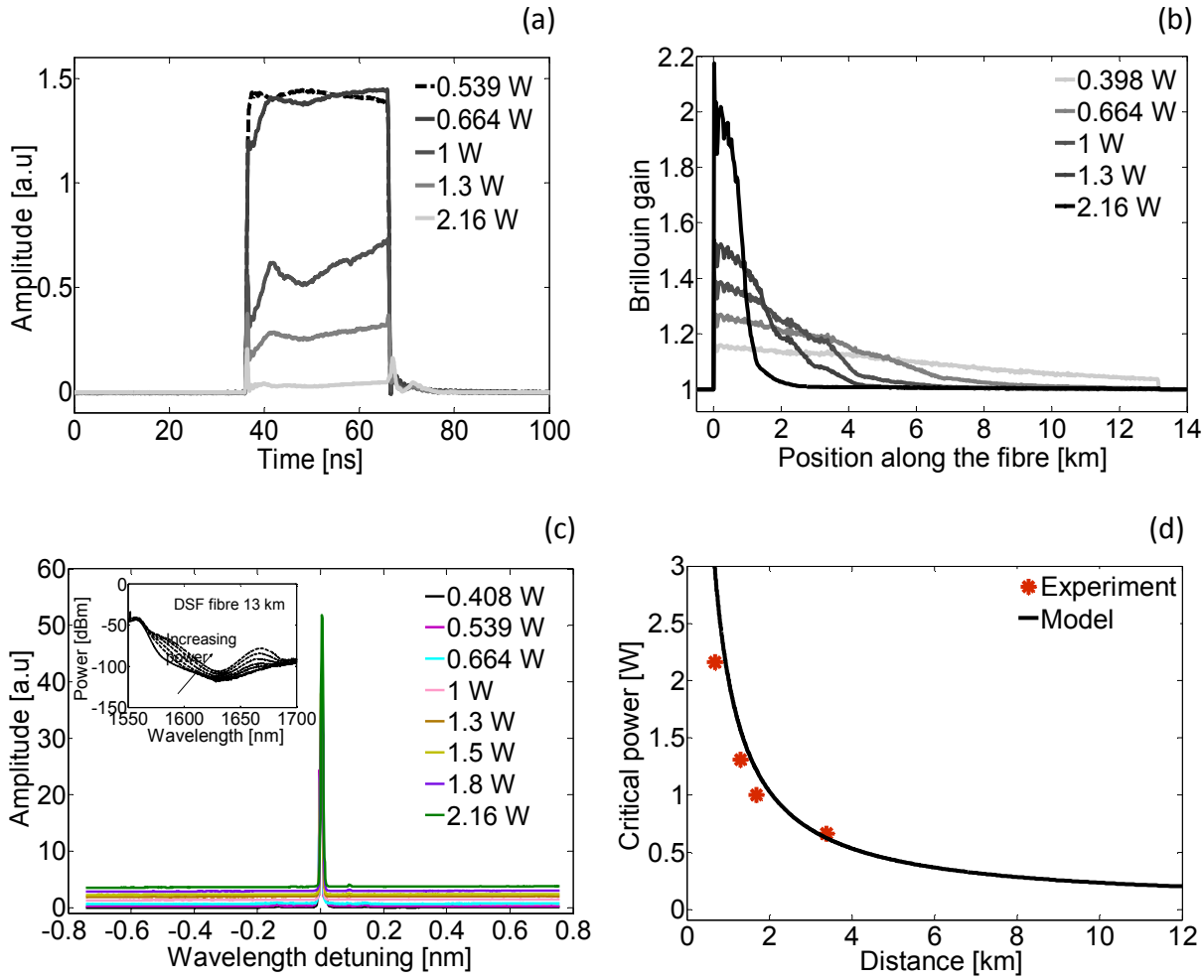

Figure 3-24: (a) The corresponding time domain measurement waveform of the pump pulse at the output of a 13 km DSF for different pump peak powers ;(b) Brillouin gain distributed measurement showing the pump depletion by Raman scattering in a 13 km DSF for different input pump peak powers; (c) Measured power spectra at the far end of a 13 km DSF fibre in the nomal dispersion regime showing the absence of MI, in inset the Raman spectra of the same fibre; (d)Maximum distance before Raman scattering begins to deplete the pump: experimental points (*), and theoretical model (solid line).

maximum gain is $G_{max}=2\gamma P_p$. From this gain spectrum the effective bandwidth B_{eff} can then be calculated:

$$B_{eff}=\frac{1}{\pi}\sqrt{\frac{4\gamma P_p}{|\beta_2|}}, \tag{3.48}$$

To establish a nonlinear equation for the critical power similar to Eq. (3.47),

$$\frac{1}{\pi}(h\nu_s)\sqrt{\frac{2}{\beta_2 L_{eff}}}=\sqrt{2\gamma P_{\text{crit}} L_{eff}}\,\exp\left[-2\gamma P_{\text{crit}} L_{eff}\right], \tag{3.49}$$

that also leads to a simplified equality valid to determine the critical power for modulation instability under the condition of anomalous dispersion ($\beta_2<0$):

$$P_{crit}^{MI}\approx\frac{20}{2\gamma L_{eff}} \tag{3.50}$$

In standard fibers at 1550nm the dispersion is anomalous and $P_{crit}^{MI}\sim 0.78P_{crit}^{R}$ using standard parameters, so that MI will always be observable at lower power than RS and will be therefore the dominating limitation.

3.5.4.1 Results and discussion

These theoretical expressions were compared to experimental data obtained using a classical Brillouin optical time-domain analyzer based on a high performance pump and probe configuration described in Figure 3-10. The duration of the rectangular pump pulses (30 ns corresponding to 3 m spatial resolution) was carefully chosen to produce clean signals with an important gain for a better demonstration. The signal power is kept low enough at 56 μW to avoid any depletion effect resulting from the Brillouin interaction.

We investigated the effect of MI using a 25.5 km standard SM fibre with relevant characteristics listed in Table 3-1. The fibre length is longer than the maximum nonlinear length $1/\alpha$=22 km, so that results can be considered as representative for any very long fibres. To observe the MI sidebands appearing symmetrically around the pump frequency, we measured series of power spectra using an optical spectrum analyzer at the output fibre end for various input pulse peak power (~160 mW to 1.6 W), shown in Figure 3-25(a). It can be seen that the MI effect becomes more pronounced as the power increases. The sidebands which appear symmetrically around the pump frequency become broader for higher pump power, leading gradually to pump depletion. The influence of MI on the distributed Brillouin amplification was then measured by varying the input pump peak power from 270 mW to 2.3 W. Figure 3-25(b) shows the effective Brillouin gain as a function of the position in a 25.5 km SM fibre for four pump peak powers. The graph demonstrates clearly the gradual drop of the gain after 10.52 km for a 497 mW pump that turns more pronounced and at shorter distance for higher pump powers. It can be seen that no gain fall-off is observed at 270 mW pump power, so we can deduce the absence of MI at this power level.

Since MI can be interpreted in the spectral domain as resulting from an energy transfer between the fundamental mode constituting the initial continuous wave and high-order modes [44, 60], several theoretical studies have shown that, after a definite propagation length, the energy spread over different frequencies eventually returns to the initial mode [59-60] (this reversible behavior of MI is known as Fermi-Pasta-Ulam recurrence FPU). This is experimentally observed in Figure 3-25(c) and (b) for pump power higher than 500 mW in which a ripple is observed. In Figure 3-25(c) is represented the pump power as a function of a critical distance evaluated as the position where the Brillouin gain starts to drop. On the same graph is calculated from the model the

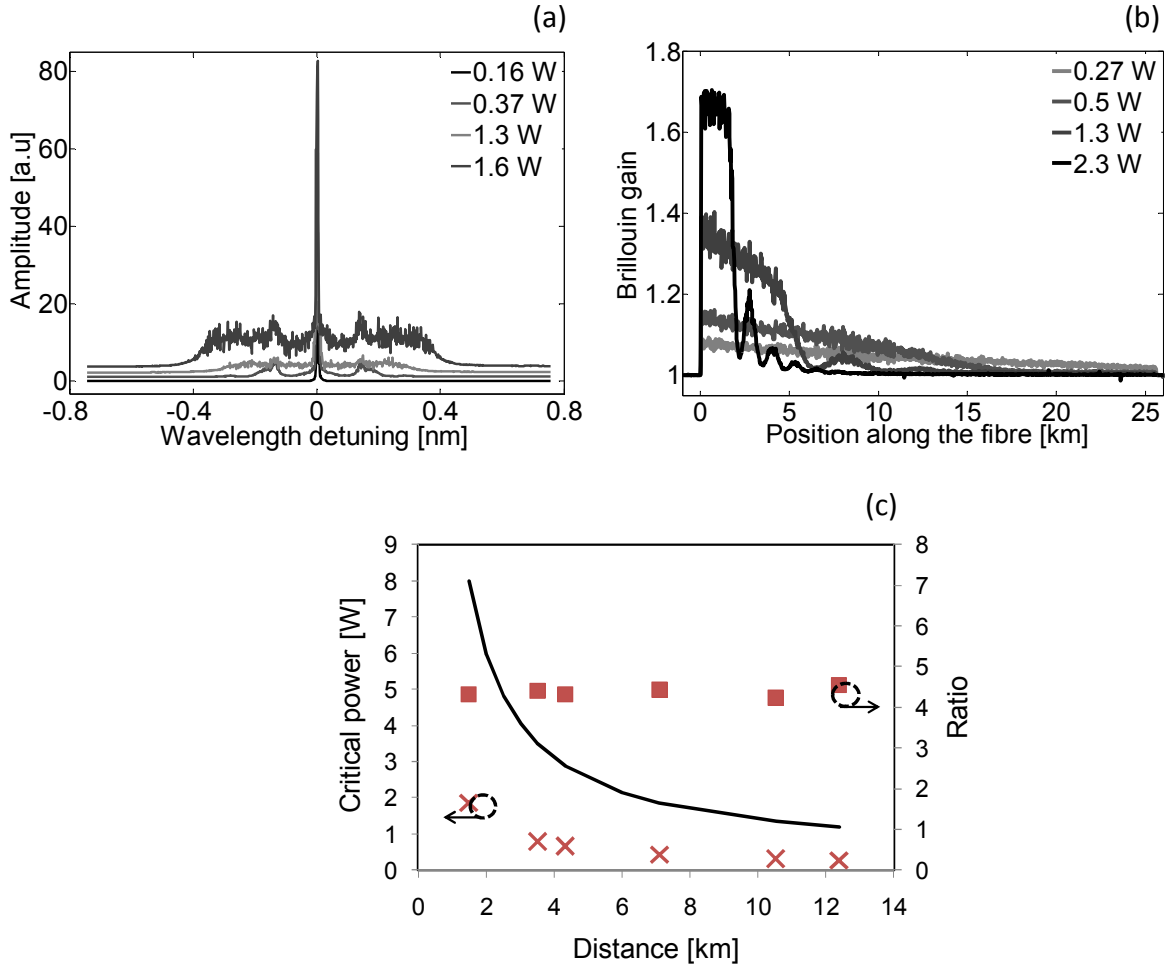

Figure 3-25: (a) Measured power spectra of MI at the far end of a 25.5 km SMF in the anomalous dispersion regime. (b) Distributed Brillouin gain measurements in a 25.5 km SMF fibre showing the pump depletion due to MI after a critical distance depending on the pump peak power; (c) Experimental (*) and theoretical (×) critical power as a function of the critical distance where the pump depletion turns significant (Brillouin gain fall-off) and the ratio (◊) between theoretical and experimental values.

critical power P_{crit}^{MI} using Eq. (3.50) for each critical distance measured experimentally. Finally the ratio between these theoretical and experimental values is represented and takes a constant value close to 4. This shows that the critical power given by the model is over-evaluated and in the reality the depletion effect on the pump by MI takes place at a power lower than the value given by the model critical power. The discrepancy may come from the fact that the MI emission keeps spreading over a broadband, as illustrated in Figure 3-25 (c) (a), and no clear dynamic spectral narrowing of the amplified spontaneous emission is observed, so that a corrective empirical factor must be preferably inserted in Eq. (3.50) to give a good prediction, yielding this final expression:

$$P_{crit}^{MI} \approx \frac{5}{2\gamma L_{eff}}, \tag{3.21}$$

Nevertheless the fact that the ratio keeps constant for a large range of pump powers proves the robustness of the model.

3.6 Conclusion

In conclusion, the modeling of the pump depletion effect has been pushed to obtain analytical expressions that are useful for the proper design of a BOTDA sensor and for the determination of its immunity to the depletion. This model is informative on the conditions maximizing the depletion effect; therefore a standard configuration can be defined to test the immunity of a set-up to depletion, made of a long uniform fibre having a length equivalent to the claimed range. The Brillouin frequency at the far end of this fibre is shifted by locally modifying the temperature or the applied strain over a short section, albeit longer than the spatial resolution. The amount of shift must be $\delta\nu=\Delta\nu/4$ and the measured Brillouin shift must correspond to the real value that can be obtained by measuring the short segment only. Moreover, the depletion does not depend on the power in the case that one sideband is used as CW signal and the contrary effect has been observed in the case that two sidebands are used. However in this latter the depletion is much smaller in the comparative situations (for example with P_{is} below 1 mW, the depletion is six times smaller).

A common accuracy claimed in most reports and commercialized instruments are 1 MHz on the peak gain frequency. Assuming an effective FWHM gain linewidth of $\Delta\nu$=40 MHz and the worst case situation $\delta\nu=\Delta\nu/2$=10 MHz, we find that the maximum depletion factor must be $d_{\max}$=0.14 (- 0.8 dB) by Eq. (3.58). Inserting this value into Eq. (3.16) and taking realistic values for a standard fibre (A_{eff}/ g_B =0.086 $W^{-1}m^{-1}$, α=5.07e^{-5} m^{-1}), we can determine that the CW signal power P_{is} must not exceed 95 µW (-10.2 dBm) to ensure that the depletion never exceeds 0.14 in a very long fibre ($L >> L_{eff}$ =20 km). This value is fairly low and is actually far from being proved to be met in the vast majority of publications and commercial instruments. They are thus all potentially subject to biasing errors related to depletion, errors that are only rarely observed since the worst case situation is very unlikely to occur in real conditions.

Afterwards, it has been demonstrated that SPM-induced spectral broadening can have a significant effect on the effective gain linewidth measured by Brillouin sensors. Modeling and experiments have undoubtedly demonstrated that the effective gain linewidth can easily experience

a two-fold increase in standard conditions when the pulse intensity profile is Gaussian. At power and spatial resolutions used in standard configurations, spectral broadening can be observed typically from a 5 km distance. Practically the problem can be circumvented by using a clean rectangular pulse with very sharp rising and falling edges. The benefit of a narrower spectrum for an identical pulse width brought by the Gaussian pulse is rapidly cancelled after about 10 km for 209 mW pump peak power.

The investigation the undesirable effects of modulation instability and forward Raman stimulated scattering in distributed BOTDA sensors systems have been also done. Both effects are detrimental and have been evaluated experimentally and compared to a theoretical model giving a simplified expression to predict the critical power for a given distance range. In a practical sensor the critical distance must be longer than the actual fibre length and is bound by the nonlinear fibre length, fixing a maximum pump power. MI turns out to be the dominant nonlinear limitation since it shows the lowest critical power, but it can be avoided to a wide extent by using the fibre in the normal dispersion spectral region such as a DSF in the C-band. On the other hand even though the critical power for Raman scattering remains high, ~5 times larger than MI undere similar conditions, it must be avoided. For now the only way to avoid it is limiting the optical pump power and is therefore the ultimate nonlinear limitation in a distributed sensing system.

Bibliography

[1] Dakin J., Culshaw B., (1988), Eds., Optical Fiber Sensors: Principles and Components, Vol. 1, Artech House, Boston. AND Culshaw B., Dakin J., (1989), Eds., Optical Fiber Sensors: Systems and Applications, Vol. 2, Artech House, Boston, “optical fibre sensors”, vol 1&2.

[2] Barnosky M.K. and Jensen S.M., 1976. Fibre waveguides: a novel technique for investigating attenuation. Applied Optics, 15:9.

[3] Hartog A.G. and Payne D.N., 1982. Remote Measurement of Temperature Distribution Using an Optical Fiber. In Technical Digest, Eigth European Conference on Optical Communication, Cannes, pp.215.

[4] Dakin J. P., Pratt D. J., Bibby G. W. and Ross J. N., 1985. Dakin distributed fibre Raman temperature sensor using a semiconductor light source and detector. Electronics Letters, 21:569-570.

[5] Horiguchi T., Kurashima T., Tateda M., 1989. Tensile Strain Dependence of Brillouin Frequency Shift in Silica Optical Fibres. IEEE Photonics Technology Letters, 1:5.

[6] Cuverhouse D., Farahi F., Pannel C. N., and Jackson D. A., 1989. Potential of stimulated Brillouin scattering as sensing mechanism for distributed temperature sensors. Electronics Letters, 25:913-915.

[7] D. Cuverhouse, F. Farahi, C. N. Pannel, and D. A. Jackson, 1989. Stimulated Brillouin scattering: A means to realize tunable microwave generator or distributed temperature sensor. Electronics Letters, 25:915-916.

[8] Mallinder F.P. and. Procter B. A, 1964. Elastic constants of fused silica as a function of large tensile strain. Physic Chem. Glasses, 5:91-103.

[9] Thévenaz L., 1988. Effet et mesure de la dispersion dans les guides d’ondes optiques. Thèse N°2294, Université de genève.

[10] Bertholds A. and Dändliker R., 1988. Determination of the individual strain-optic coefficients in single-mode optical fibers. IEEE Journal Lightwave Technology, LT-6:17.

[11] Horuguchi T., Shimuzi k., Kurashima T., Tateda M. and Koyamada Y., 1995. Development of a Distributed Sensing Technique Using Brillouin Scattering. Journal of Lightwave Technology, 13:1296-1302.

[12] Kurashima T., Horuguchi T. and Tateda M., 1990. Thermal Effects of Brillouin Gain Spectra in Single-Mode Fibres. IEEE Photonics Technology Letters, 2:10.

[13] Bucaro and J.A. H.D., 1974. High-temperature Brillouin scattering in fused quartz. Journal Applied physics, 45:5324-5329.

[14] Niklès M. 1977. La Diffusion Brillouin Dans Les Fibres Optiques: Étude et Application Aux Capteurs Distribués. EPFL, Thèse de doctorat N°1674, Ecole Polytechnique Fédérale de Lausanne.

[15] Facchini M., 2001. Distributed Optical Fibre Sensors Based on Brillouin Scattering. EPFL, Thèse de doctorat N°2521, Ecole Polytechnique Fédérale de Lausanne.

[16] Fellay A., 2003. Extreme Temperature Sensing using Brillouin Scattering in Optical Fibers. EPFL, Thèse de doctorat N°2728, Ecole Polytechnique Fédérale de Lausanne.

[17] Hibino Y., Edahiro T., Horiguchi T., Azuma Y., and Shibata N., 1989. Evaluation of residual stress and viscosity in SiO_2,-core/F-SiO_2 clad single-mode optical fibers from Brillouin gain spectra. Journal Applied Physics, 66:4049-4052.

[18] Shibata N., Waarts R. G., Braun R. P., 1987. Brillouin-gain spectra for single-mode fibres having pure-silica, GeO2-doped, and P2O5-doped cores. Optics Letters, 12:4.

[19] Timoshenko S.P. and Goodier J. N., 1970. Theory of Elasticity, 3rd edition, McGraw Hill.

[20] Kurashima T., Horiguchi T. and Tateda M., 1990. Distributed-temperature sensing using stimulated Brillouin scattering in optical silica fibres. Optics Letters, 15:18.

[21] Kurashima T., Horiguchi T. and Koyamada Y., 1992. A new technique to shift lightwave frequency for DOFS. Proc. SPIE 1797, 18-30.

[22] Shimizu, 1994 .Coherent Self-Heterodyne Brillouin OTDR for Measurement of Brillouin Frequency Shift Distribution in Optical Fibers. Journal of Lightwave Technology, vol. 12, n° 5.

[23] Kurashima T., Tateda M., Horiguchi T., 1997. Performance Improvement of a Combined OTDR for Distributed Strain and Loss Measurement by Randomizing the Reference Light Polarization State. IEEE Photonics technology Letters, 9:3.

[24] Alahbabi M. N., Cho Y. T., Newson T. P., 2005. 150-km-range distributed temperature sensor based on coherent detection of spontaneous Brillouin backscatter and in-line Raman amplification. Journal of the Optical Society of America B, 2005, 22, 6:1321–1324.

[25] Nikles M., .Thevenaz L., Robert P. A., 1997, "Brillouin gain spectrum characterization in single-mode optical fibers," Journal of Lightwave Technology, 15, 10:1842–1851.

[26] Van M. O. Deventer, Boot A. J., 1994. Polarization properties of stimulated Brillouin scattering in single-mode fibers," Journal of Lightwave Technology, 12, 4: 585–590.

[27] Thevenaz L., Foaleng S. M., Nikles M., 2007. Fast measurement of local PMD with high spatial resolution using stimulated Brillouin scattering. In Proceedings of the 33rd European Conference on Optical Communication, 10.1.2, Berlin, Germany.

[28] Diaz S., Foaleng S. M., Lopez-Amo M., and Thévenaz L., 2008. A High performance Opticla Time-Domain Brillouin Distributed fiber Sensor. IEEE Sensors Journal, 8, 7:1268-1272.

[29] Diaz S., Foaleng Mafang S., Lopez-Amo M., and Thévenaz L., 2007. High performance Brillouin distributed fibre sensor. In Proceding of the European Workshop on Optical Fibre Sensors, Naples, Italy.

[30] Lecoeuche V., Webb D.J., Pannell C.N., Jackson D.A., 1999. 25 km Brillouin based single-ended distributed fibre sensor for threshold detection of temperature or strain. Optics Communication, 168, 95-102.

[31] Tanaka Y. and Ogusu K., 1998. Temperature Coefficient of Sideband Frequencies Produced by Depolarized Guided Acoustic-Wave Brillouin Scattering. IEEE Photonics Technology Letters, vol. 10, no. 12,

[32] Guideline COST 299, 2009

[33] Ghafoori-Shiraz H., and Okoshi T., 1986. Fault location in optical fibers using optical frequency domain reflectometry. Journal Lightwave Technology, 4, 3:416-422.

[34] Garus D., Krebber K., Schliep F., Gogolla T., 1996. Distributed sensing technique based on Brillouin optical-fiber frequency-domain analysis. Optics Letters, 21, 17:1402-1404.

[35] Garus D., Gogolla T., Krebber K. and Schliep F., 1997. Brillouin optical-fiber frequency domain analysis for distributed temperature and strain measurements. Journal Lightwave Technology, 15, 4:654-662.

[36] Nöther N., 2010. Distributed Fiber Sensors in River Embankments: Advancing and Implementing the Brillouin Optical Frequency Domain Analysis. BAM, Thesis D 83, Berlin.

[37] Hotate K., and Hasegawa T., 2000. Measurement of Brillouin gain spectrum distribution along an optical fiber using a correlation-based technique – proposal, experiment and simulation. IEICE Trans. Electronics, E83-C, 405-412.

[38] Hotate K., and Tanaka M., 2002. Distributed fiber Brillouin strain sensing with 1-cm spatial resolution by correlation-based continuous-wave technique. IEEE Photonics Technology Letters, 14, 2:197-199.

[39] Mizuno Y., Zou W., He Z., and Hotate K., 2008. Proposal of Brillouin optical correlation-domain reflectometry (BOCDR). Optics Express, 16, 16:12148-12153.

[40] Mizuno Y., He Z., and Hotate K., 2009. One-end-access high-speed distributed strain measurement with 13-mm spatial resolution based on Brillouin optical correlation-domain reflectometry. IEEE Photonics Technology Letters, 21, 7:474-476.

[41] Mizuno Y., He Z., and Hotate K., 2010. Measurement range enlargement in Brillouin optical correlation-domain reflectometry based on double-modulation scheme. Optics Express, 18, 6:5926-5933.

[42] Mizuno Y., He Z., and Hotate K., 2009. Stable entire-length measurement of fiber strain distribution by Brillouin optical correlation-domain reflectometry with polarization scrambling and noise-floor compensation. Applied Physics, 2, 6:062403.

[43] Alahbabi M.N., Cho Y. T. and Newson T. P., 2004. Influence of modulation instability on distributed optical fibre sensors based on spontaneous Brillouin scattering. JOSA B, 21, 6:1156-1160.

[44] Alasia D., González-Herráez M., Abardi L., Martin-López S., Thévenaz L., 2005. Detrimental effect of modulation instability on distributed optical fibre sensors using stimulated Brillouin scattering. In Proceding of SPIE 5855, 587-590.

[45] Fellay A., Thévenaz L., Facchini M. and Robert P., 1999. Limitation of Brillouin time-domain analysis by Raman scattering. In Proceding of the 5th Optical Fibre Meas. Conference, Nantes, France, 110-113.

[46] L. Thévenaz, 2010. Brillouin distributed time-domain sensing in optical fibers: state of the art and perspectives. Frontiers of Optoelectronics in China 3, 1:13-21.

[47] Soto M. A., Bolognini G., Di Pasquale F. and Thévenaz L., 2010. Long-range Brillouin optical time-domain analysis sensor employing pulse coding techniques. Measurement Science and Technology 21, 9:094024

[48] Liang H., Li W., Linze N., Chen L. and Bao X., 2010. High-resolution DPP-BOTDA over 50 km LEAF using return-to-zero coded pulses. Optics Letters 35, 10:1503-1505.

[49] Martin-Lopez S., Alcon-Camas M., Rodriguez F., Corredera P., Ania-Castañon J. D., Thévenaz L. and Gonzalez-Herraez M., 2010. Brillouin optical time-domain analysis assisted by second-order Raman amplification. Optics Express 18, 18:18769-18778.

[50] Geinitz E., Jetschke S., Röpke U., Schröter S., Willsch R. and Bartelt H., 1999. The influence of pulse amplification on distributed fibre-optic Brillouin sensing and a method to compensate for systematic errors. Measurement Science and Technology 10, 2:112.

[51] Minardo A., Bernini R., Zeni L., Thevenaz L. and Briffod F., 2005. A reconstruction technique for long-range stimulated Brillouin scattering distributed fibre-optic sensors: Experimental results. Measurement Science & Technology 16, 4:900-908.

[52] Dong Y., Chen L. and Bao X., 2010. System optimization of a long-range Brillouin-loss-based distributed fiber sensor. Applied Optics 49, 27:5020-5025.

[53] Lecoeuche V., Webb D.J., Pannell C.N., Jackson D.A., 1999. 25 km Brillouin based single-ended distributed fibre sensor for threshold detection of temperature or strain. Optics Communications 168, 1-4:95-102.

[54] Izumita H., Koyamada Y., Furukawa S., Sankawa I., 1994. The performance Limit of Coherent OTDR Enhanced with Optical Fibre Amplifiers due to Optical Nonlinear Phenomena. Journal Lightwave Technology 12, 7:1230-1238.

[55] Foaleng S. M., Rodríguez F., Martin Lopez S., González Herráez M., Thévenaz L., 2010. "Impact of self phase modulation on the performance of Brillouin distributed fibre sensors. Optics Letters, 36, 2:97-99.

[56] Boyd R. W.. *Nonlinear Optics*, fourth ed. Academic Press (2008).

[57] Agrawal G.. *Nonlinear Optics*, fourth ed. Academic Press, (2008).

[58] Smith R.G., 1972. Optical Power Handling Capacity of Low Loss Optical Fibers as Determined by Stimulated Raman and Brillouin Scattering. Applied Optics 11, 11:2489-2494.

[59] Fermi E., Pasta J., Ulam H. C., 1965. Studies of nonlinear problems. In Collected Papers of Enrico Fermi, E. Serge Ed., 2, 977-988.

[60] Symaeys G.V., Emplit Ph., Haelterman M., 2001. Experimental demonstration of the Fermi-Pasta-Ulam recurrence in a modulationally unstable optical wave. Physics Review Letters, 87, 3.

[61] Tai K., Tomita A., Jewell J. L., and Hasegawa A., 1986. Generation of subpicosecond solitonlike optical pulses at 0.3 THz repetition rate by induced modulational instability. Applied Physics Letters, 49, 5:236–238.

[62] González-Herráez M., Martín-López S., Corredera P., Hernanz M. L. and Horche P. R., 2003. Supercontinuum generation using a continuous-wave Raman fiber laser. Optics Communications, 226, 1-6:323–328.

4 Brillouin Echoes Distributed Sensing (BEDS)

Chapters 2 and 3 provided a detailed analysis of Brillouin scattering (spontaneous and stimulated) and of different variants of the classical Brillouin sensor. Considering this later, it has been explained that high spatial resolution and the measurement range are two quantities that will never match. In this Chapter[1], we present a new concept, called "Brillouin echoes", developed in the frame of this thesis. With this concept, we demonstrate that the trade-off between the two parameters (high spatial resolution and long measurement range) can be improved. We study experimentally and theoretically the physics behind Brillouin echoes. Through these studies, an analytical model is developed, which allows us to optimize the performances of the Brillouin sensor.

[1] This chapter is based on:
Foaleng S. M., Tur M., Beugnot J.-C., and Thévenaz L. (2010). High spatial and spectral resolution long-range sensing using Brillouin echoes. IEEE Journal Lightwave Technology, 28, 20:2993-3003.

J-C Beugnot, Tur M, Foaleng S.M. and Thévenaz L. Distributed Brillouin sensing with sub-meter spatial resolution: Modeling and Processing. In preparation.

As explained in chapter 3, techniques based on spontaneous Brillouin for Time Domain Reflectometry (BOTDR) [4] require only one access point to the test fibre to launch the pump wave, while those using SBS for Brillouin Analysis (BOTDA) must access both ends of the test fibre to launch the pump pulse and CW signal, [1]-[3]. Both types of instruments offer good accuracy for temperature and strain measurements, albeit at spatial resolutions not better than ~1 m [5]. The reason comes from the fact that the observed Brillouin spectrum broadens as the pulse width decreases, since the spectral distribution of the effective gain is given by the convolution between the pulse spectrum, broader for shorter pulses, and the natural Brillouin gain spectrum (~30 MHz in silica fibres at λ_p = 1550 nm, determined by the phonon lifetime $\tau_A \cong 6$ ns) [6]. This broadening leads to a reduced peak gain and uncertainties in the determination of the Brillouin shift ν_B, and consequently to a reduced accuracy in the measurement of temperature and strain at submetric spatial resolutions. A natural limit is given by the situation when pump pulse and Brillouin gain spectra show a comparable bandwidth, corresponding to a pump pulse showing a duration equal to a double phonon lifetime $2\times\tau_A \cong 12$ ns (see section.4-1), or ~1 meter spatial resolution. Frequency-domain and correlation-based techniques have been developed to circumvent the phonon lifetime limitations and exhibit enhanced spatial resolutions down to 1cm for the latter [7]. Nevertheless, in chapter 3 we have explained that both these techniques introduce their own complexities, including a trade-off between spatial resolution and range.

4.1 Broadening of the BGS and physical limitations in spatial resolution: theoretical and experimental descriptions

Until now, we have given a literal definition of the spatial resolution, and said that it is limited to ~1 m in the classical Brillouin distributed sensing. In this section, we will confirm this by theoretical and experimental descriptions. In section 2.2.1, we have seen that the process of Brillouin scattering in optical fibres can be stimulated involving an electrostrictively-induced acoustic wave, generated through the interference between the pump and signal waves. There is an amplification of the signal when the phase-matching condition is reached (i.e. when the frequency difference between the pump and signal is around the Brillouin frequency of the fibre).

Mathematically, the assumed co-polarized but counter-propagating pump and signal waves, $A_p(z,t)\exp[i(k_p z+\omega_p t)]$ and $A_s(z,t)\exp[i(k_s z-\omega_s t)]$, will generate an acoustic field, $Q(z,t)\exp\left[i\left(qz+\Omega t\right)\right], q=k_p+k_s, \Omega=\omega_p-\omega_s$, which will then couple the two optical fields according to the Eqs. (2.36a, b) and (2.37) that for convenience we will repeat here as Eqs (4.1):

$$\frac{\partial A_p(z,t)}{\partial z}+\frac{1}{V_g}\frac{\partial A_p(z,t)}{\partial t}=i\frac{1}{2}g_2 A_s(z,t)Q(z,t); \tag{4.1a}$$

$$\frac{\partial A_s(z,t)}{\partial z}-\frac{1}{V_g}\frac{\partial A_s(z,t)}{\partial t}=-i\frac{1}{2}g_2 A_p(z,t)Q^*(z,t); \tag{4.1b}$$

$$\frac{\partial Q(z,t)}{\partial t}+\Gamma_A Q(z,t)=ig_1 A_p(z,t)A_s^*(z,t);$$
$$\Gamma_A=i\frac{\Omega_B^2-\Omega^2-i\Omega\Gamma_B}{2\Omega} \qquad (4.1c)$$

Notations and approximations: ω_p, ω_s and $\Omega=\omega_p-\omega_s$, are the centre angular frequencies of the pump, signal and acoustic waves respectively, while k_p, k_s and $q=k_p+k_s$ are their wavenumbers. $g_1(=\gamma_e q^2/(8\pi\Omega))$ and $g_{2,s,p}=\frac{\gamma_e\omega_{s,p}}{4Q_0 n c}$ represent respectively the electrostrictive and elasto-optic coupling constants. $A_p(z,t)$, $A_s(z,t)$ and $Q(z,t)$, are slowly-varying complex envelopes. $\Omega_B=2\pi\nu_B$ is the Brillouin frequency shift for resonant interaction between the three waves, and $\Gamma_B=1/\tau_A=2\pi\Delta\nu_B$ is the acoustic damping constant, intimately related to the phonon life time τ_A and the FWHM width of the Brillouin gain spectrum $\Delta\nu_B$ (see Section. 2.2.1.4). By excluding derivatives with respect to z in Eq. (2.36c) (which have allowed derive Eq. (2.37)), we have assumed that an induced acoustic disturbance at (z_0, t_0) will remain spatially local and will not propagate along the fibre. This common approximation is quite justified in our case, where due to the relatively minuscule value of the acoustic velocity with respect to that of light, the generated acoustic envelope at z_0 barely moves (<100μm) while a pump pulse - as long as ten nanoseconds, completes its voyage over z_0 - , thereby ceasing its interaction with the practically spatially-static acoustic disturbance at that point.

The interaction between the pump and signal waves under steady-state conditions is governed by the Eqs. (2.55). Due to the exponential decay of the acoustic waves in the fibre core (see Section. 2.2.1.4), the Brillouin gain spectrum (g_B) has a Lorentzian spectral profile given by Eq. (2.56). We have also seen that in the steady-state conditions and assuming an un-depleted pump, the Brillouin signal intensity can be expressed by Eq. (2.52) (see Section 2.2.1.5).

As the pump wave is a pulse wave, the length of the fibre over which an interaction between the two optical waves can occur is reduced to the length that the two waves cross together. In our case this length is related to the pulse width (T) and corresponds to the spatial resolution Δz which is given by:

$$\Delta z=\frac{1}{2}\frac{c}{n}T\cong T\,10^8\,\mathrm{m/s}, \qquad (4.2)$$

where the attenuation over this short segment has been neglected. The spectral width of the pulse will increase as the pulse width is reduced. Assuming a perfectly rectangular pulse, the spectral profile of the pulse $S_p(\nu)$, is given by the Fourier transform of the temporal pulse:

$$S_p(\nu)=\int_{-T/2}^{T/2}P_p e^{-i2\pi\nu t}dt=\frac{P_p}{\pi\nu}\sin(\pi\nu T), \qquad (4.3)$$

The resulting observed Brillouin gain spectrum will be given by the convolution of the pulse spectrum with the natural Brillouin gain spectrum $g_B(\nu)$, yielding the following spectrum:

$$g(\nu)= 2\mathrm{e}^{-\pi\Delta\nu_B T}\left[\cosh\left(\pi\Delta\nu_B T\right)-\cos\left(2\pi\left(\nu-\nu_B\right)T\right)\right]g_B\left(\nu\right), \tag{4.4}$$

The theoretical spectra (in Figure 4-2(a)) were generated using Eq. (4.4). As the pulse width approaches the phonon lifetime $2x\tau_A$~12 ns, the Brillouin spectrum broadens and reaches about 80 MHz (see Figure 4-2(a), (b)). Therefore, the resulting maximum Brillouin gain decreases due to the spectral broadening (as shown Figure 4-1). The mathematical expression of the maximum Brillouin response (i.e. at the resonance when $\nu=\nu_B$) can be found in the following equation:

$$g_{\max}(\nu=\nu_B)= 2\mathrm{e}^{-\pi\Delta\nu_B T}\left[\cosh\left(\pi\Delta\nu_B T\right)-1\right]g_B\left(\nu_B\right), \tag{4.5}$$

To understand the behaviour of the acoustic wave in these two cases (long and short pulse than $2x\tau_A$), let us assume a constant signal wave $A_s(z,t)\equiv A_s^0$, null initial acoustic conditions $\mathrm{Q}\left(z,t=0\right)\equiv 0$, and a propagating pump pulse of temporal width T. At some arbitrary point along the fibre, z_0 the time evolution of the complex envelope at $\Omega=\omega_p-\omega_s$, $Q(\Omega,z_0,t)$ was formerly given by Eqs. (2.41) that for convenience we will repeat here as Eqs (4.6):

$$Q\left(\Omega,z_0,T\right)=\begin{cases}\dfrac{ig_1A_p^{\mathrm{peak}}A_s^{0*}}{\Gamma_A}\left[1-\exp(-\Gamma_A t)\right] & 0<t\le T \qquad (4.6a)\\ \dfrac{ig_1A_p^{\mathrm{peak}}A_s^{0*}}{\Gamma_A}\exp(-\Gamma_A t)\left[\exp(+\Gamma_A T)-1\right] & t>T \qquad (4.6b)\end{cases}$$

The dynamic characteristics of the solutions of Eq. (4.1) heavily depend on $\mathrm{Re}(\Gamma_A)=\Gamma_B/2$. We

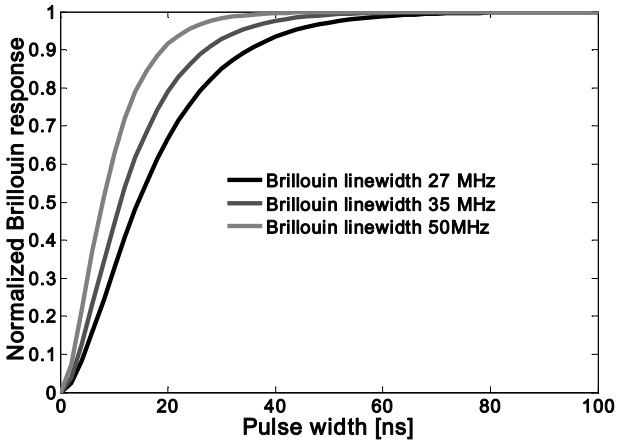

Figure 4-1: Theoretical variation of the Brillouin response versus pump pulse width for two different values of Brillouin line-width 35 MHz and 50 MHz.

will, therefore, examine two extreme cases:

(a) For a pump pulse much longer than $1/\mathrm{Re}(\Gamma_A)=2/\Gamma_B=2\tau_A$, $Q(\Omega,z_0,t)$ of Eq. (4.1a) reaches its maximum magnitude long before the pulse is over, attaining a frequency-dependent value of:

$$\begin{aligned}\left|Q(\Omega,z_0,T)\right| &= \frac{\left|g_1 A_p^{peak} A_s^{0*}\right|}{\left|\Gamma_A\right|} \\ &\approx \frac{\left|g_1 A_p^{peak} A_s^{0*}\right|}{\sqrt{(\Omega-\Omega_B)^2+(\Gamma_B/2)^2}}; \quad \text{for } T>>\frac{2}{\Gamma_B}\end{aligned} \tag{4.7}$$

In classical Brillouin distributed sensing, Ω is scanned through a range of optical frequencies to precisely determine Ω_B. The range of information is obtained from the pulse time of flight data and the spatial resolution is determined by the pulse width. According to Eq. (4.8), long pulses - while having very poor spatial resolution -, will give rise to acoustic field amplitudes *sharply* peaked at $\Omega=\Omega_B$, allowing the sensor to resolve local temperature - (and/or strain) that induces changes in Ω_B, with a sensitivity limited only by the natural Brillouin linewidth Γ_B and that of the processing electronics.

(b) For a pump pulse shorter than $1/\mathrm{Re}(\Gamma_A)=2/\Gamma_B=2\tau_A$, Eq. (4.6) can be approximated in the vicinity of Ω_B (i.e., when $|\Omega_B-\Omega|T<1$) by:

$$\begin{aligned}\left|Q(\Omega,z_0,T)\right| &\approx \left|\frac{ig_1 A_p^{\mathrm{peak}} A_s^{0*}}{\Gamma_A}(\Gamma_A T)\right| = \\ &= \left|g_1 A_p^{\mathrm{peak}} A_s^{0*} T\right|; \quad \text{for } T<<2/\Gamma_B\end{aligned} \tag{4.8}$$

Eq. (4.8) states that the magnitude of the acoustic field $|Q(\Omega,z_0,T)|$ does not depend on Ω_B in the vicinity of Ω_B. Here, high spatial resolution of the sensor is achieved at the expense of losing all spectral sensitivity (see Figure 4-2 and Figure 4-1)

This analysis has led manufacturers of Brillouin time-domain analyzers to compromise on pump pulse widths not shorter than 5 ns ~ $1/\Gamma_B$, limiting the spatial resolution of the instrument to ~0.5 m. Recently, a radically new approach has been presented for time-domain measurements, relying on the pre-activation of the acoustic field within the Brillouin frequency resonance. In this way high-spatial resolution could be obtained, while keeping the Brillouin gain profile at its natural narrow width. This is the subject of the next section.

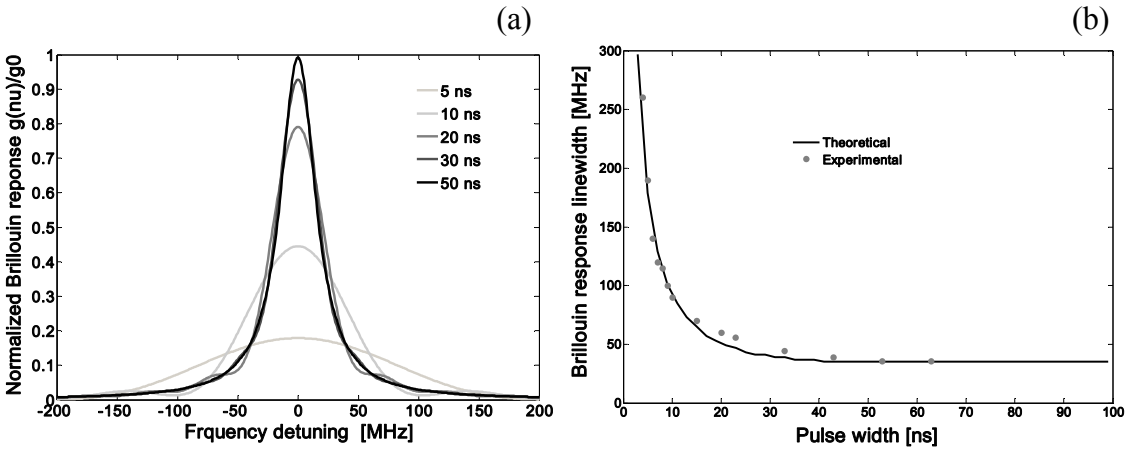

Figure 4-2: a) Effective Brillouin response spectrum for different pump pulse width 5 ns, 10 ns, 20 ns, 30 ns and 50 ns, corresponding to the spatial resolutions of 0.5 m, 1 m, 2 m, 3 m, and 5 m, b) Variation in the Brillouin response line-width (FWHM) for various values of the pump pulse width, theoretical (solid line) and experimental (dotted line).

4.2 The new approach and the three ways of making Brillouin echoes

In this new approach, a pre-activated acoustic field is electrostrictively generated through the interference between a CW pump wave (or a long pulse of duration $>>\tau_A$) and a counter-propagating CW signal wave, properly frequency shifted from the pump wave. Once the acoustic wave has fully developed, a very fast change (shorter than τ_A) in the pump signal can imprint a corresponding equally fast time-stamp on the amplified signal wave, without significantly affecting the acoustic field [10]. Being excited by CW (or quasi CW) waves, the natural Brillouin linewidth is preserved and the observed time-stamp will have narrow frequency characteristics resulting in high sensitivity to temperature and strain, while simultaneously providing high-spatial resolution determined by the fast features of the time stamp.

Several options exist as to the nature of the fast change imposed on either the pump or signal waves. A spatial resolution of 15 cm was demonstrated using a bright pulse on top of a continuous wave [9, 11] (see Figure 4-3(a)), while a dark pulse technique, i.e. shutting down one of the CW waves for a very brief time could resolve 2 cm [12] (see Figure 4-3(b)). A variant of the bright pulse technique, PPP-BOTDA [13], employs a Pulse Pre-Pump of lower intensity to activate the acoustic field before a stronger interrogating pulse arrives. By analyzing the physical principles behind these processes in the framework of this thesis, we have proposed a more recent configuration which optimizes the response by modulating the pump using a π phase pulse (see Figure 4-3(c)), a configuration we call a Brillouin Echo Distributed Sensing (BEDS) [14-15]. This denomination comes from the formal analogy in the equations with the spin echoes, as observed in nuclear magnetic resonance, and more straightforwardly highlights the physical fact that the time stamp on the pump experiences a pure reflection on the acoustic wave and is thus echoed on the signal

(a) Bright pulse configuration: the electro-optic modulator can be adequately set to allow a continuous flow of pump light to activate the acoustic wave, giving constant background amplification on the signal. The additional pump light in the pulse is reflected and its effect is observed as an additional amplification. This configuration is less efficient if the peak power of the pump is fixed.

(b) Dark pulse: the pump is turned off for a short period of time, so that no light is reflected and the constant background amplification is stopped. The acoustic wave continues vibrating during the dark pulse and the background amplification is restored when the pump light is turned on again. The effect of the dark pulse is observed as a "negative" gain (actually it is an absence of gain).

(c) Phase pulse: a π phase shift is applied to the pump for a short time, so that the reflected light interferes destructively with the signal, equivalent to a Brillouin loss process. The response is identical to the dark pulse, but is twice as large for an identical pump power and is thus most efficient.

Figure 4-3: (a) Bright pulse, (b) dark pulse, (c) π phase pulse.

4.3 Physical explanation of Brillouin echo

The implementation of BEDS is realized by propagating continuous pump and signal waves through the sensing fibre at the proper frequencies for the Brillouin interaction and by abruptly and briefly shifting the phase of the CW pump wave by π during a time much shorter than the phonon lifetime τ_A. During this very short period of time, the acoustic wave does not have time to noticeably change its phase and amplitude thanks to its inertial behaviour, so that the pump will be reflected completely out of phase during the brief π phase shift, when compared to the normal steady-state gain situation. A destructive interference on the signal results from this pump reflection observed as a small apparent loss on the signal waveform. This brief reflection on the pre-existing acoustic wave is called the first echo and its magnitude is proportional to the amplitude of the steady acoustic wave generated by the continuous counter-propagating optical waves. When the phase of the pump returns to its initial state, the normal steady state gain situation is restored. Nevertheless, the acoustic wave slightly changes its amplitude and phase during the pump phase

pulse and then returns slowly to its initial state during a typical time on the order of a few τ_A. This creates a small deficit in gain during this period, which manifests itself as a trailing and decaying loss over the signal waveform. This effect is observed as a long-lasting second echo and is clearly detrimental to the measurement, since it gives a trailing signal that may interfere at later positions with the correct information given by the first echo. While the relative importance of the second echo, when compared to the first main echo, decreases for shorter pulses, it is highly desirable to completely eliminate its effects.

Here, we further investigate the Brillouin back-scattered signals, following π phase shifted pump pulses and we show an optimized implementation that gives real metrological measurements, while detailing the reasons for the physical response of the system. Experimentally, we demonstrate a spatial resolution down to 5 cm (with only 256 averages), with a Brillouin linewidth identical to the natural one, thereby simultaneously achieving high sensitivity for temperature/strain measurements and high spatial resolution. Using a physical filtering method, measured data can be processed resulting in attenuated second echoes, as well as using an experimentally double pulse technique [14], later judiciously implemented in a pure intensity-based scheme [16], second echoes can be totally screened. The 5cm spatial resolution capabilities of BEDS extended to 5 km without any pump depletion penalty.

4.4 Theoretical description of Brillouin echo

As addressed in Section 4.2, recent developments have concentrated on separating the generation of the acoustic field from its probing by superimposing a pulse on the CW pump. This scenario can be mathematically investigated by solving the three coupled Eqs. (4.1). Since we are interested in high-spatial resolution, where a CW or quasi-CW pump pulse wave is comparable/shorter than the acoustic lifetime τ_A, the steady state condition valid as stated in Section. 2.2.1.4 is no longer valid, thus the transient analysis of Eqs. (4.1) must be carried out. Besides the approximation made on the acoustic wave, the following three other reasonable approximations were considered before finding a general analytic solution.

(i) The effect of linear attenuation of light is neglected over the region where the waves interact.

(ii) (ii) The interaction is supposed to be weak enough that the pump depletion can be neglected, i.e. $A_p(z)$ becomes constant and, hence, Eq. (4.1a) does not need to be taken into account.

(iii) (iii) The signal gain is so small that its wave amplitude can be approximated using a perturbation approach by $A_s(z,t)=A_s^0+a_s(z,t)$ with $|a_s(z,t)|<<|A_s^0|$, where A_s^0 is a continuous constant wave and $a_s(z,t)$ is a small varying term resulting from the Brillouin amplification. Consequently, A_s can be considered as a constant in the right terms of Eqs. (2.41), and only a_s is considered when A_s is differentiated, as in the left-hand term of Eq. (2.41b).

Under these assumptions, Eqs. (2.41) become:

$$\frac{\partial a_s(z,t)}{\partial z}-\frac{1}{V_g}\frac{\partial a_s(z,t)}{\partial t}=-i\frac{1}{2}g_2A_p(z,t)Q^*(z,t); \tag{4.9a}$$

$$\frac{\partial Q(z,t)}{\partial t}+\Gamma_A Q(z,t)=ig_1A_p(z,t)A_s^{0*}; \tag{4.9b}$$

To calculate the analytical solution of Eqs. (4.9), let us consider a very short segment of fibre extending from position z_0 to $z_0+\Delta z$ being much shorter than the distance over which light propagates during the pump pulse length T, and the acoustic lifetime τ_A. The rest of the fibre is then assumed to be off resonance for stimulated Brillouin scattering and no elctrostriction is observed (g_1=0). The interaction area is represented by a bounded distribution of the electrostriction ($g_1(z)=g_1^0\left[u(z-z_0)-u(z-z_0-\Delta z)\right]$), where u conventionnally represents the Heaviside unit step function. Here we point out that there is no loss of generality in considering an isolated interaction over one segment, since the system of equations subject to our approximations is linear in g_1. If the fibre comprises any number of concatenated segments with arbitrary g_1, Ω_B and Γ_B, the solution can be found separately for each segment and the total solution for a_s is simply given by the sum of the separated solutions.

Since the pump has been considered un-depleted, the pump envelope $A_p(z,t)$ is thus only function of the quantity t-$z/(V_g=c/n)$. Figure 4-4 represents the general situation of a time-domain pump pulse coding. The pump wave amplitude for a general square pulse can be expressed by

$$A_p^0(z,t)=A_p^0\left[\alpha u\left(t+t_0-\frac{z}{V_g}\right)+(\beta-\alpha)u\left(t-\frac{z}{V_g}\right)+(\gamma-\beta)u\left(t-T\frac{z}{V_g}\right)\right], \tag{4.10}$$

where the dimensionless α, β, γ are arbitrary (including complex) amplitudes and durations. Therefore a solution covering all configurations reported in the literature [9, 12-15] could be established. The time when the pulse enters the fibre is represented by t_0. The pump wave is starting since long time ($t>>t_0=2z_0/V_g$) because only the impact of pump variation on the signal was

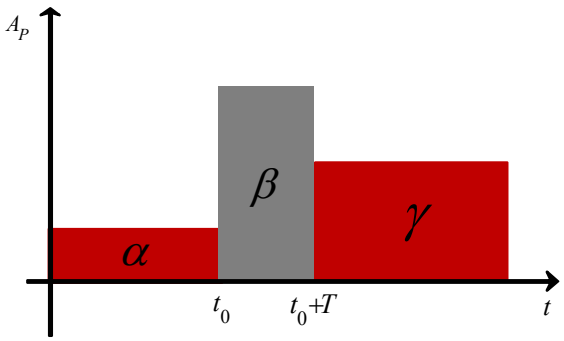

Figure 4-4: Pump coding waveform, where α, β, and γ can be either real or complex. The duration of the β part of the pump pulse, T, will determine the spatial resolution.

considered. Moreover, we assume an infinite rise-time waveform to simplify the pump equation. Using this pump temporal distribution, Eqs.(4.9) were solved analytically in the Laplace domain (see Appendix B and C). Thus, the general analytical solution for a CW input signal and a pump wave comprising three concatenated square pulses having arbitrary (including complex) amplitudes and durations for a short interaction length Δz, (impulse response), is given by:

$$a_s(z,t) = -\frac{1}{2} g \left|A_p^o\right|^2 A_s^o \Delta z \left\{ \begin{array}{l} \alpha^2 \left[u\left(t - \frac{z}{V_g}\right) - u\left(t - T - \frac{2z_o - z}{V_g}\right)\right] \\ +\beta\left[\beta^* - (\beta-\alpha)\mathrm{e}^{-\Gamma_A\left(t-\frac{2z_o-z}{V_g}\right)}\right]\left[u\left(t - \frac{2z_0 - z}{V_g}\right) - u\left(t - T - \frac{2z_o - z}{V_g}\right)\right] \\ +\gamma\left[\gamma^* - \beta^*\left(1 - e^{\Gamma_A^* T}\right) - \left(\alpha - \gamma^* e^{\Gamma_A^* T}\right)\mathrm{e}^{-\Gamma_A\left(t-\frac{2z_o-z}{V_g}\right)}\right] u\left(t - T - \frac{2z_o - z}{V_g}\right) \end{array} \right\}, \quad (4.11)$$

where $g=g_1g_2$. This expression is clearly made of three different terms (which vanish respectively for $\alpha=\beta=\gamma=0$). Eq. (4.11) is explained as follow: First, a constant gain is observed before the presence of the pulse represented by the factor α^2. Secondly, the interaction starts with the onset of the second term that manifests itself as an abrupt signal amplitude change accompanied by exponential growths during the pump pulse duration T. Thirdly, when the pump pulse ends, the second term stops contributing and the third term takes place over the step amplitude that shows the same slow exponential growth. The general analytical solution for a homogeneous long and finite segment can be found in Appendix C (Eq. (B.11)).

For the three way of making Brillouin echoes, the parameters α, β, γ are set are follow:

$\alpha = 1, \beta = 2, \gamma = 1$, is the optimum setting for the bright pulse (4.12a)

$\alpha = 1, \beta = 0, \gamma = 1$, is the setting for the dark pulse (4.12b)

$\alpha=1, \beta=-1, \gamma=1$, is the setting for the π phase shift pulse (4.12c)

We will analyze here a particular situation, where a 5 cm fibre section with $\Omega_B(5\text{cm})/2\pi=10.86$GHz is spliced between two longer sections, 20 m each, of a different fibre, having $\Omega_B(20\text{ m})/2\pi=10.73$GHz. Both fibres share a Brillouin bandwidth of 27 MHz. The power of the signal as it emerges from the fibre is given by:

$$\begin{aligned} P_s(z=0,\Omega,t) \propto \left|A_s\right|^2 &= \left|A_s^0 + a_s\right|^2 \\ &\approx \left|A_s^0\right|^2 + 2\,\mathrm{Re}\left[A_s^{0*} a_s(z=0,\Omega,t)\right] + \left|a_s\right|^2 \\ &\equiv \left|A_s^0\right|^2 + P_{Brillouin} \end{aligned} \quad (4.13)$$

since $|a_S|^2 << \mathrm{Re}\left[A_s^{0*} a_s(z=0,\Omega,t)\right]$, $|a_S|^2$ was taken to be equal to zero.

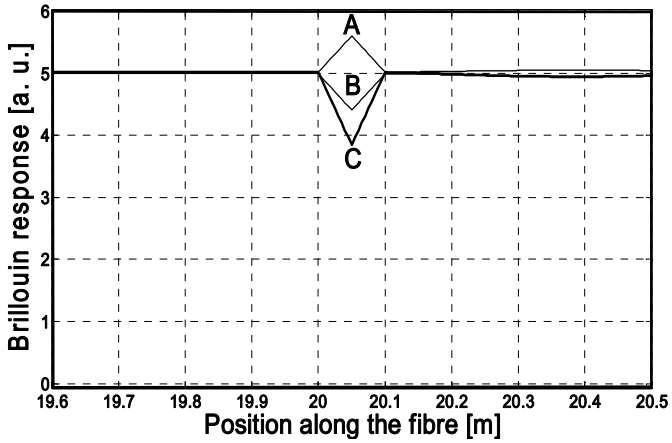

Figure 4-5: Brillouin signal from a 5 cm section, spliced in the middle, of a 40 m fibre, whose Brillouin frequency is detuned by 140 MHz from that of the 5 cm section. Ω is tuned to the 5cm section Brillouin frequency. The β pump pulse is 500 ps long. A: bright pulse; B: dark pulse; C: π phase shift pulse.

Figure 4-5 presents the results for the pulse of Figure 4-4 with $t_0 >> \tau_A$ (to allow full pre-activation of the acoustic field), T= 500 ps and $\Omega=\Omega_B(5\text{cm})/2\pi=10.86$GHz. Results for the Brillouin signal, $P_{\text{Brillouin}}$, are shown for a bright pulse, a dark pulse, and a π phase shift pulse with the setting parameters defined in Eqs. (4.12).

Originally a function of time, the curves of Figure 4-5 monitor the interaction of the narrow β pump pulse with the counter-propagating signal wave. When the propagating narrow β pulse resides in either of the 20 m sections (i.e., at distances outside the 5 cm section), it marginally affects the Brillouin signal, which is mainly due to the off-resonance (ν_B(5 cm)– ν_B(20 m)=140 MHz) action of the α and γ pulses in the two long 20 m sections, with a relatively small portion being contributed by the on-resonance but very short 5 cm section. Thus, as long as the β pulse is away from the 5 cm section, the Brillouin signal can be expressed by:

$$P_{\text{Brillouin}}(\beta \text{ pulse outside the 5 cm section}) = 2\,\mathrm{Re}\left(a_{s,2X\,20\text{ m}}(\alpha,\gamma) + a_{s,5\text{ cm}}(\alpha,\gamma)\right) \qquad (4.14)$$

for clarity we have assumed that $A_S^{0*}=1$, $a_{s,2X\,20\text{ m}}(\alpha,\gamma)$ and $a_{s,5\text{ cm}}(\alpha,\gamma)$ are the Brillouin contributions of the 20 m and 5 cm, respectively, and we ignored the contribution of the short detuned β pulse to the Brillouin signal from the long sections. When the β pulse resides in the 5cm section, the section contribution varies with the coding scheme, resulting in (note: $a_{s,5\text{cm}}(\beta=1) = a_{s,5\text{cm}}(\alpha=1,\ \gamma=1) = -a_{s,5\text{cm}}(\beta=-1)$ and $a_{s,5\text{cm}}(\beta=2) = 2a_{s,5\text{cm}}(\beta=1)$) as shown in the following equation:

$$P_{\substack{\text{Brillouin}\\(\beta\text{ pulse inside}\\5\text{cm section})}} = \begin{cases} 2\,\mathrm{Re}\left(a_{s,2X20\mathrm{m}}(\alpha=1,\gamma=1)+2a_{s,5\mathrm{cm}}(\alpha=1,\gamma=1)\right) & \text{Bright pulse } (\beta=2) \\ 2\,\mathrm{Re}\left(a_{s,2X20\mathrm{m}}(\alpha=1,\gamma=1)\right) & \text{Dark pulse } (\beta=0) \\ 2\,\mathrm{Re}\left(a_{s,2X20\mathrm{m}}(\alpha=1,\gamma=1)-a_{s,5\mathrm{cm}}(\alpha=1,\gamma=1)\right) & \pi \text{ shift pulse } (\beta=-1) \end{cases} \quad (4.15)$$

Thus, at the resonance frequency of the 5 cm section (see Figure 4-5) the Brillouin signal associated with this section (Eq. (4.15)) differs from the corresponding signal from the surrounding sections (Eq.(4.14)) by (Eq.(4.16)) below:

$$P_{\substack{\text{Brillouin}\\(\beta\text{ pulse inside}\\5\text{cm section})}} - P_{\substack{\text{Brillouin}\\(\beta\text{ pulse outside}\\5\text{cm section})}} = \begin{cases} 2\,\mathrm{Re}\left(a_{s,5\mathrm{cm}}(\alpha=1,\gamma=1)\right) & \text{Bright pulse } (\beta=2) \\ -2\,\mathrm{Re}\left(a_{s,5\mathrm{cm}}(\alpha=1,\gamma=1)\right) & \text{Dark pulse } (\beta=0) \\ -4\,\mathrm{Re}\left(a_{s,5\mathrm{cm}}(\alpha=1,\gamma=1)\right) & \pi \text{ shift pulse } (\beta=-1) \end{cases} \quad (4.16)$$

Eq. (4.16), as well as Figure 4-5, clearly demonstrates that the π phase shift pulse provides twice the contrast of the other methods. Thus, while all three coding schemes resolve the 5 cm section, the π phase shift technique results in the highest signal-to-noise ratio. As $|\beta|$ increases, the performance of the bright pulse method will asymptotically approach that of the π phase shift one.

The triangular shape of the calculated response from the 5 cm section is due to the fact that it takes time for the pulse to fully enter the section, and then to fully clear it. The initial build-up of the Brillouin pulse is not faster than the minimum between the pulse duration and the section length. In our example, they are identical: 5 cm are translated to 500 ps and *vice versa*. Upon leaving the section, the transition time is at least the pulse duration. Figure 4-6 shows the Brillouin

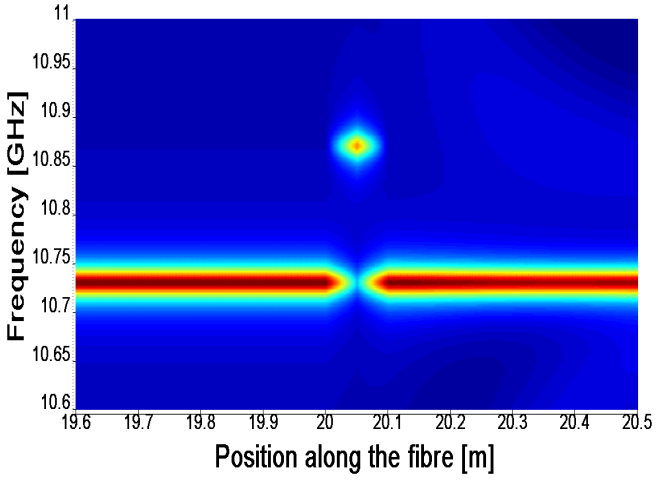

Figure 4-6: A 2D Distance-Frequency map of Brillouin gain from a 5 cm section, spliced in the middle of a 40 m fibre, whose Brillouin frequency is detuned by 140 MHz from that of the 5 cm section. The Ω phase shift pulse is 500 ps long. As in the experiment below, for each Ω the mean over time was removed and the redder the color the *more negative* are the values of the Brillouin signal (with respect to the signal's initial power $|A_S^0|^2$.

signal for the π phase shift pump as a function of both the distance ($=V_g t/2$) and frequency detuning Ω ($=\omega_p$-ω_s) for the same conditions as above. Similar to the other coding methods, the 5 cm section is well resolved not only in the time but also in frequency in spite of the very narrow probing pulse (0.5 ns$=T<<\tau_A=6$ ns). But the β pulse, while probing the pre-excited acoustic field, also slightly modifies it, resulting in an observed trailing edge, designated as the second echo. This effect is clearly observed when the section under test is longer than the probing pulse.

Consider Figure 4-7, where the 5 cm section has been replaced by a 5 m one. During the entrance of the π phase shift pulse (of duration T) into the 5 m section, the signal level sharply drops (within T) to a level dictated by the Brillouin contributions of the β pulse at the first 5 cm of the section and of the α pulse at the rest of the 5 m section (as well as the contributions from the α and γ pulses at the 20 m sections). As the β pulse continues its travel through the section, any length of fibre cleared by the β pulse becomes populated by the $\gamma(=\alpha)$ pulse, and therefore the signal level should not have changed. Instead, it continues to decrease until it saturates after a distance equivalent to a time lapse of a few tens of nanoseconds. This behaviour is a direct consequence of the effect of the β pulse on the pre-excited acoustic field: the $\gamma(=\alpha)$ pulse, which follows the moving βpulse, meets a modified acoustic field, which is no longer fully matched to the counter-propagating pump, and signal waves, and therefore, contributes *less* to the Brillouin signal. Saturation is achieved only after a few acoustic lifetimes when the β pulse has propagated deep enough into the 5 m section so that the acoustic field at the beginning of the section has resumed its

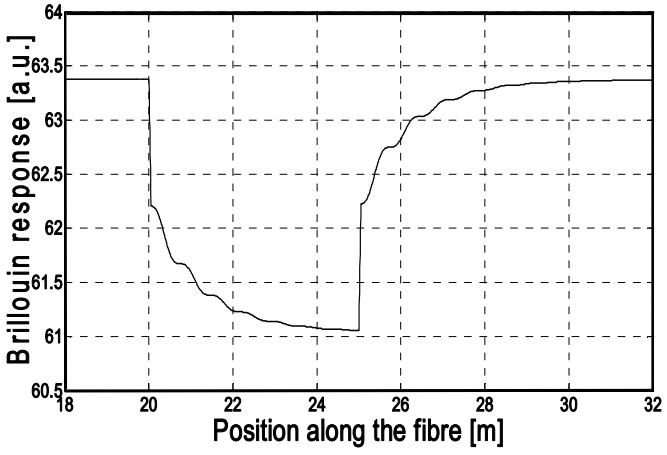

Figure 4-7: The Brillouin signal from the 5m section in a 20 m (10.73 GHz)-5 m (10.86 GHz)-20 m (10.73 GHz) fibre, probed by a 500 ps π phase shift pulse. Brillouin frequency is tuned at resonance for the 5m section (10.86 GHz). The fast-fall time is accompanied by an exponential decrease to saturation. As the π phase shift pulse leaves the 5m section and enters the 20m one, a slow recovery of the signal follows a fast rise time. The ripples are due to the relative proximity of the Brillouin frequencies (140 MHz) of the various sections, and reflect the non-zero contributions of the fairly long sections to the overall Brillouin signal.

pre-β pulse value. Once the β pulse left the 5 m section, there is again a fast rise of the signal (of duration T) and then the above described process also manifests itself as a slow ascent of the signal to its value characteristic of the long sections: again, for a while, the 5 m section does not contribute its original share to the Brillouin signal. These manifestations of the second echo, and in particular the last one, may conceal true variations of Ω_B or may be erroneously identified as such. It must be mentioned that the demonstration shows fibre segments with spectrally well separated Brillouin gains. This choice was made to distinctly show the effect of the second echo on the response, but the second echo remains equally detrimental when the gains spectrally overlap. An improved pulse version of the BEDS method, with no secondary echoes will be described in Section. 4.9.

4.5 Experimental implementation

Our BEDS experimental configuration, shown in Figure 4-8, is based on a simple modification of the high-performance pump and probe set-up described in Section 3.2.2. A 1552 nm 11 mW compact external-cavity laser diode (Redfern Integrated Optics PLANEX™ RIO0095) is used as the light source, having an enhanced coherence (linewidth $\Delta\nu$=23 kHz). In fact a coherence time, τ_C =1/ $2\pi\Delta\nu$ (cf. Appendix D), much longer than the phonon lifetime, τ_A, is required to ensure a stable pre-activation of the acoustic wave through optical interference between the pump and signal waves. The polarized output of the laser diode is split into two distinct channels to allow both the pump and signal waves to be derived from the same optical source (Section 3.2.2). The signal is generated in the upper channel, where an integrated electro-optic intensity modulator, driven by a microwave signal in a suppressed carrier configuration, creates sidebands which are launched into one end of the sensing fibre. The lower channel is connected to the opposite end of the sensing fibre to launch a continuous pump wave that is periodically modulated by a phase modulator, to produce

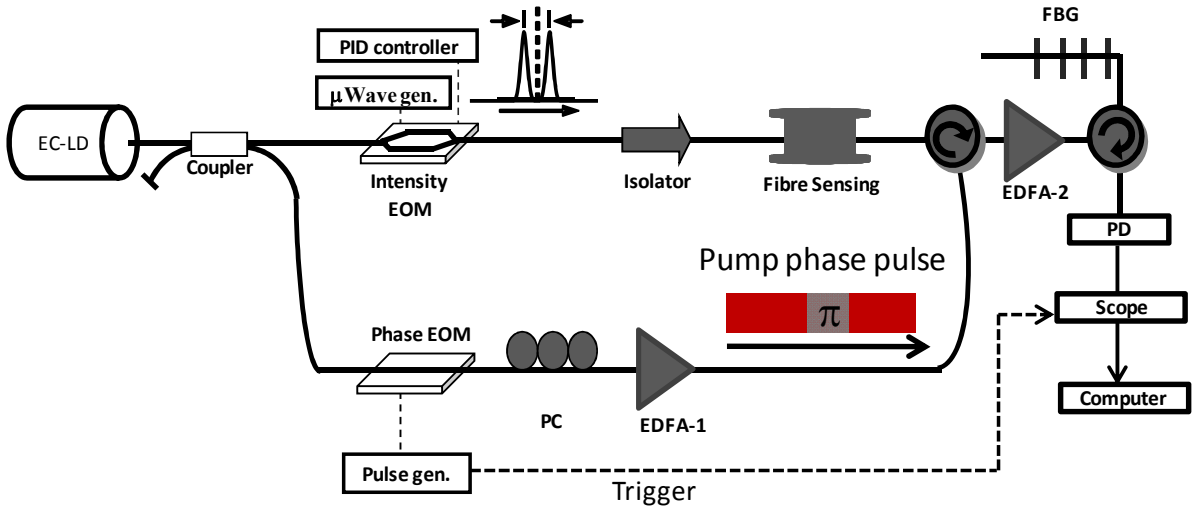

Figure 4-8: Experimental set-up of the optimized BEDS system: EC-LD: external cavity laser diode; EDFA: erbium-doped fibre amplifier; EOM: electro-optic modulator; FBG: fibre Bragg grating; PD: photodiode.

very short π phase pulses. Electrical pulses from a fast pulse generator (500 ps minimum pulse duration, corresponding to a spatial resolution of 5 cm), are then applied to the phase modulator. The output light is controlled by a polarization controller to best align pump and signal polarizations to maximize the SBS interaction, and then boosted to 20 dBm by a high-power EDFA-1. In order to be not limited by the electronic noise of the wideband photodetector module, the signal at the output of the circulator, modified by the Brillouin interaction, is further amplified by EDFA-2. Finally, a fibre Bragg grating filter (bandwidth 10 GHz) is placed in front of the detector to eliminate the upper sideband from the signal and any residual and Rayleigh backscattered light from the pump.

In this set-up, all stray forward propagating waves other than the signal, such as residual light due to the finite extinction ratio of the modulator, as well as spurious reflections and Rayleigh backscattering of the counter-propagating strong pump, all spectrally positioned at the pump frequency, are highly suppressed by the Bragg grating, thereby minimizing optical noise [19].

The Brillouin gain spectrum is determined by scanning the microwave generator around the Brillouin shift ν_B. The net Brillouin gain is then measured by converting the optical signal using a DC-1 GHz amplified photodiode module (PD), followed by a high-pass electronic filter. The 1 GHz bandwidth corresponds to a 350 ps rise time that is sufficient to resolve a 500 ps transition. For each pre-set microwave frequency, the signal is acquired in the time domain by a 4 GHz digital oscilloscope, synchronously triggered by the π shift pulse. EDFA 2 was placed at the output of the circulator, rather than before the sensing fibre in the signal channel, in order to avoid pump depletion so that the intensity of the signal does not become comparable to that of the pump, thereby limiting the detection range and the sensing accuracy [21]-[22]. On the other hand, the configuration of Figure 4-8 will suffer more from the optical ASE noise generated by the amplifier EDFA-2, see Section.4.7.1.

4.6 Experimental results and discussion

To study the performance of the BEDS system, a test fibre comprising a 5 cm section of G652A fibre, spliced in the middle of a 40 m G652D fibre, was fabricated. This creates an abrupt Brillouin frequency shift at the transition to the centimetric section from 10.730 GHz (G652D fibre) to 10.860 GHz (G652A fibre), as a simple consequence of the difference in core doping concentration (see Figure 4-9(b) below). An averaging of 256 waveforms per frequency step was performed, resulting in a total acquisition time of about 8 min. Most of this time was associated with the slow setting time of the microwave generator and the data transfer to the computer. The actual amount of time strictly needed to fully analyze the fibre (considering 256 averages and 256 frequency steps) is less than 10 s.

Figure 4-9a. shows the enlarged top view of the 3D distribution of the Brillouin response in the vicinity of the 5 cm fibre section and also the calculated Brillouin frequency shift, as a function of position (solid line) around the 5 cm fibre section. The central frequency of the Brillouin gain was determined by fitting the raw data to a Lorentzian distribution. The uncertainty was about 0.5 MHz, corresponding to a temperature accuracy of about 0.5 C and strain accuracy of about 8.75 με. The figure clearly shows that each fibre section is fully resolved both spatially and spectrally.

Measurements were performed using a 500 ps phase pulse (5 cm resolution). The observed dynamic margin is quite large, indicating that a still higher spatial resolution is possible, albeit with a lower amplitude. This comes essentially from the fact that a standard DFB laser was used for those measurements, leading to a less efficient build-up of the acoustic wave and, consequently, a more noisy response.

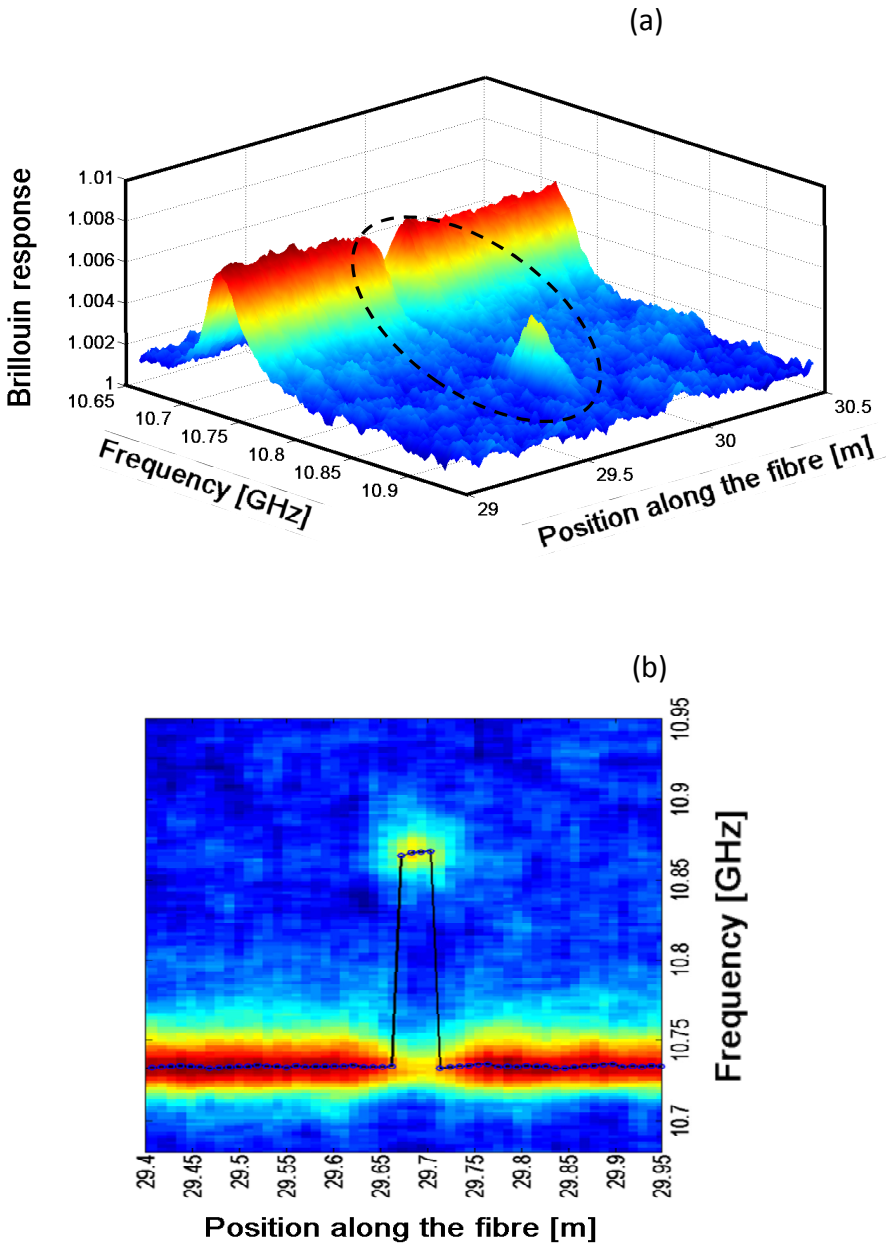

Figure 4-9: (a) 3D distribution of the Brillouin response along the sensing fibre as a function of frequency and position, (b) Enlarged top view of the 3D distribution of the Brillouin gain in the vicinity of the 5 cm fibre section. Since the echo response manifests itself as an apparent loss, the signal polarity has been inverted for clarity.

We could experimentally confirm that the Brillouin gain spectrum remains undistorted for any pulse width, and that the linewidth of the measured spectrum obtained by BEDS is essentially independent of the pulse duration, as illustrated in Figure 4-10(a). Clearly, this is not the case for a classical BOTDA method, where the linewidth is very dependent of the pulse width, and increases as the pulse width decreases, as shown in Figure 4-10(b).

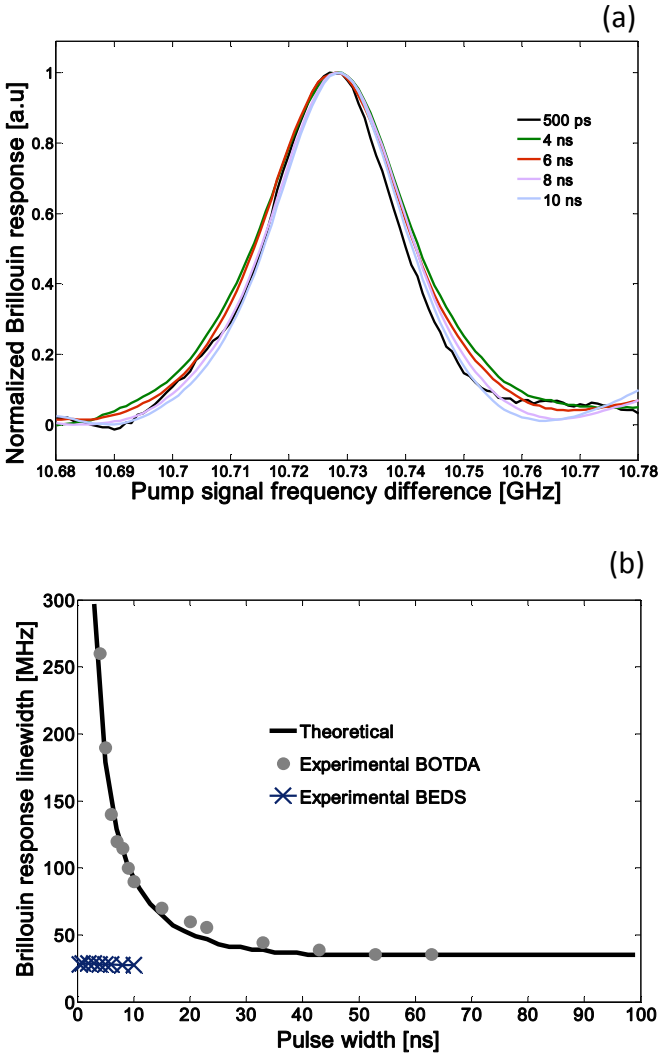

Figure 4-10: (a) Spectral distribution of the Brillouin response measured locally by the Brillouin echo of a π-phase pulse, for a broad range of pulse width shorter than the acoustic life-time, showing that the measured line-width is unchanged and equal to the natural linewidth $\Delta\nu_B$=27 MHz; (b) theoretical and measured Brillouin response line-width as function of the pulse width for a classical BOTDA (Brillouin optical time domain analysis) and for the BEDS technique, showing the critical dependency of the linewidth on the pulse width in the case of the BOTDA.

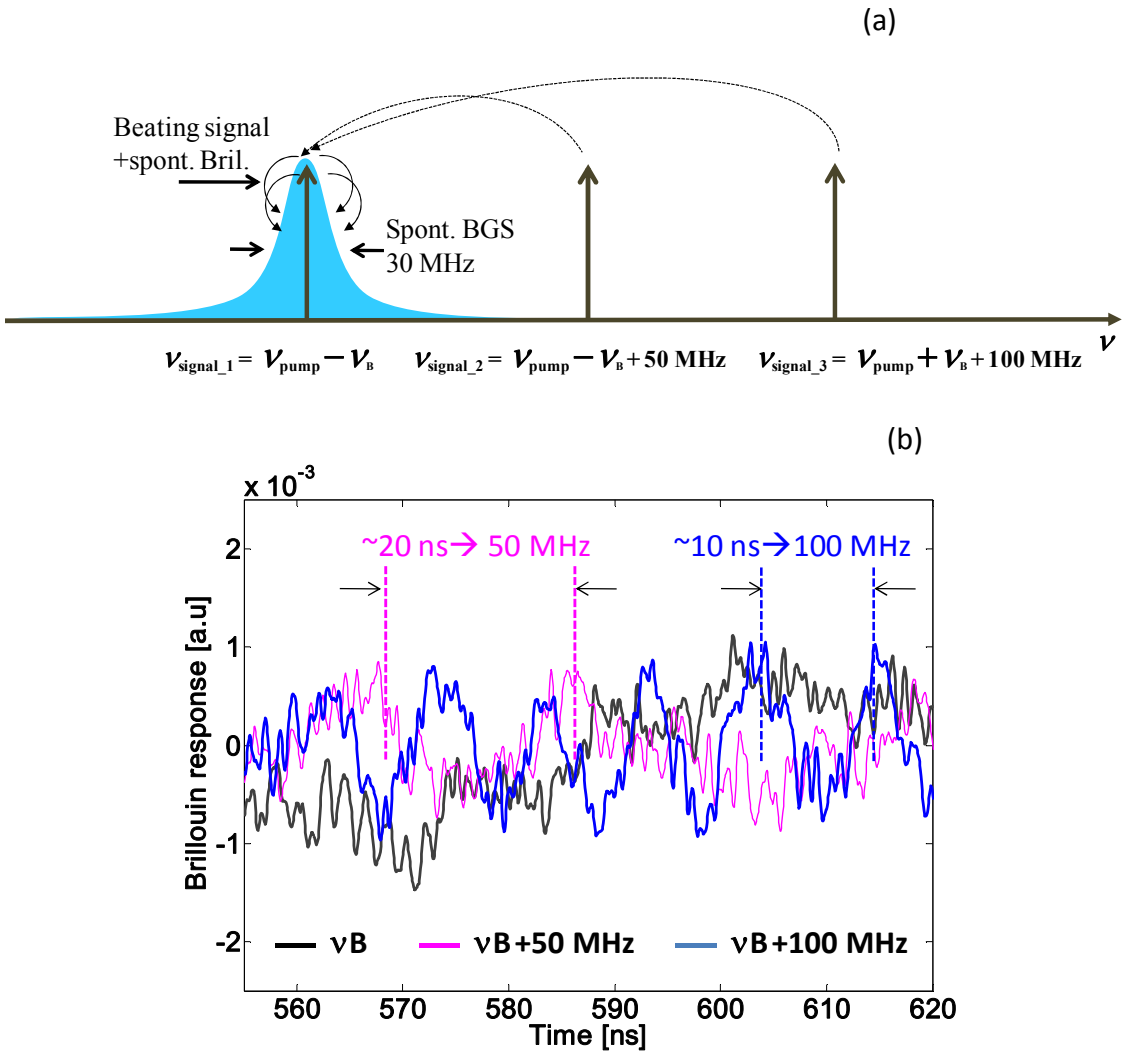

Figure 4-11: (a) The scheme shows that the signal wave beats with the Brillouin spontaneous amplified emission from long homogeneous sections; the beat frequency is higher for signal frequencies spectrally more distant from the spontaneous amplified emission, giving rise to a noisy beat note jamming the response, as shown in (b).

4.7 Issues related to the continuous activation of the acoustic wave

While the underlying principle of the BEDS technique has been experimentally validated, its application to practical sensing requires some modifications. The implementation of Figure 4-8 in fact suffers from the following penalties:

4.7.1 Continuous activation

So far, pre-activation of the acoustic field has been realized through the interference of a continuous signal with a continuous pump. However, this continuous interaction along the full length of the fibre gives rise to several detrimental effects:

(i) Pump depletion (presented in chap3), which limits both the sensing range and sensing accuracy [21-22]. To minimize pump depletion in the set-up of Figure 4-8, EDFA-2 could not precede the fibre under test. Its current position, after the circulator, comes at the expense of a less attenuated amplified spontaneous emission at the detector, resulting in higher signal-beat noise. More averaging could reduce the impact of this noise but requires longer acquisition times;

(ii) Spontaneous Brillouin noise – A continuous pump, energizing the whole length of the fibre, generates at each section of the fibre a spontaneous Brillouin signal, centered around the local Brillouin frequency of the section. This accumulated parasitic signal interferes with the continuous probe wave, as it scans the frequency range of interest, to produce optical noise, see Figure 4-11. For a long fibre with length-varying ν_B, and a detector, which is spectrally wide open (1 GHz) to accommodate fast β pulses, this type of optical beat noise may limit the noise floor of the sensor [23-24].

4.7.2 Second echo

As theoretically explained in Section. 4.4, the propagating β pulse slightly modifies the acoustic field, resulting in a non-local response of the Brillouin sensor, i.e. the measured level of the β pulse at a given spatial point is distorted by contributions from neighboring points. The longer the β pulse, the more severe is the effect.

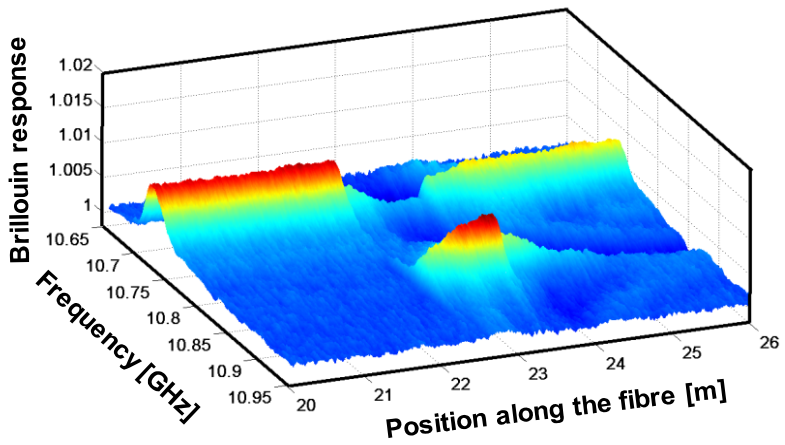

Figure 4-12: 3D distribution of the Brillouin response along the sensing fibre as a function of the frequency and the position using a 500 ps π phase pulse. The fibre comprises a 1m section with ν_B of 10.86 GHz, in the middle of 40 m of fibre with ν_B=10.73 GHz.

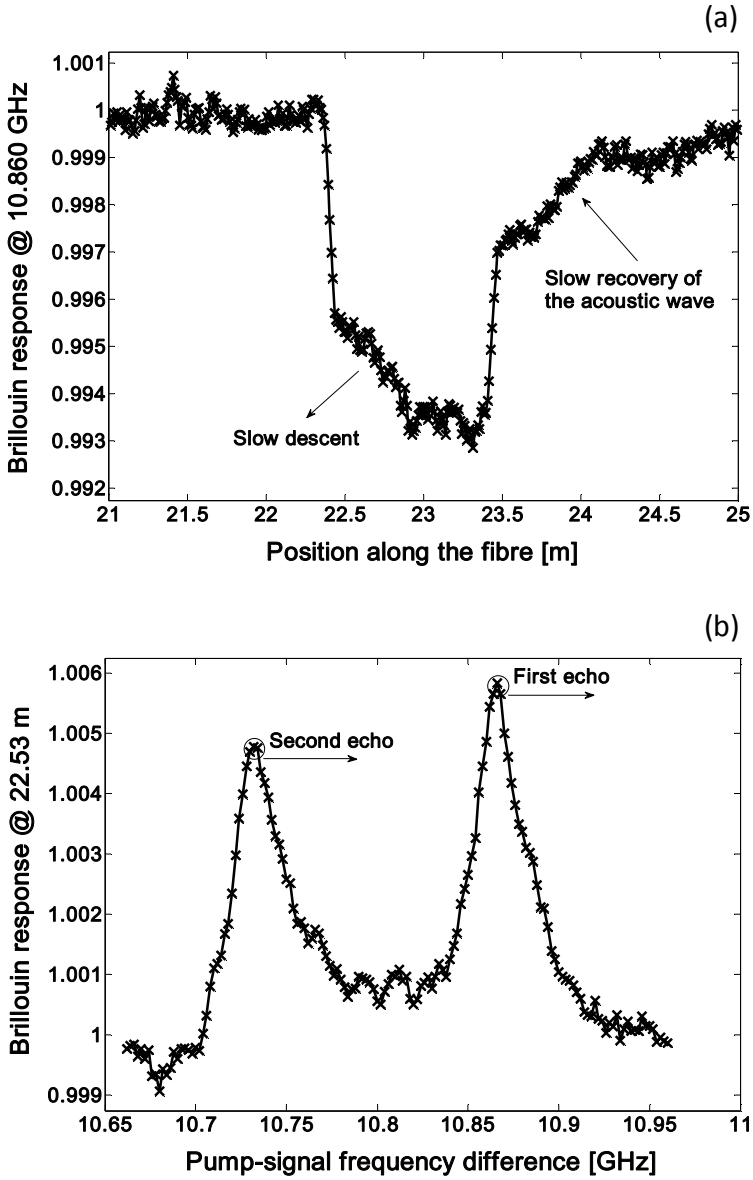

Figure 4-13: Probing a 1 m section (ν_B = 10.86 GHz) in the middle of a 40 m fibre (ν_B = 10.73 GHz), using a 500 ps π phase pulse and a 256 time average for each temporal trace. (a) The Brillouin gain through the 1m section at frequency ν_B = 10.86 GHz, (1m section at resonance). The marked slow descent of the signal at the beginning of the section, and the marked slow recovery of the signal as the π phase shift pulse enters the subsequent 20 m section, both of the order of τ_A ~6 ns, are manifestations of the second echo; (b) measured Brillouin gain distribution within the 1m section at position 22.53 m showing the high quality of the measured spectrum and the unwanted presence of the second echo. Since the π phase shift pulse actually manifests itself as an apparent Brillouin loss, the signal polarity has been inverted for clarity.

Figure 4-12 and Figure 4-13 show experimental results for a 500 ps phase pulse, probing a 1m length fibre (ν_B=10.86 GHz), placed in the middle of a 40 m fibre with ν_B=10.73 GHz. The 3D distribution of the Brillouin response along the sensing fibre is shown in Figure 4-12 as a function of both the frequency and spatial position. The spatial dependence of the Brillouin gain ν_B=10.86 GHz is shown in Figure 4-13(a) (i.e. a cut through Figure 4-12 with the original polarity conserved) and favorably compares with Figure 4-7. (Note that in the latter, the fibre segment was chosen to be longer (5 m) in order to exhibit the saturation characteristics of the signal.)

Instead of assuming a constant lower value throughout the 1 m section (excluding the very short (~5 cm) fall and rise times), the signal demonstrates a slow descent towards a saturation value, not actually reached for the 1 m section. Furthermore, following the exit of the β pulse, the signal returns to its proper value only after a slow recovery. As explained in Section 4.4, this behavior is a manifestation of the second echo: the slow descent in the 1 m section originates from a β-induced perturbation of the acoustic field along a short segment of the 20 m fibre just preceding the 1 m section. Similarly, the β-modified acoustic field in the 1 m section is responsible for the slow recovery of the signal in the 20 m section following the 1 m section. The time scale of saturation and recovery is essentially in the order of $2\times\tau_A$. For the same reason, the Brillouin response at ν_B = 10.73 GHz, Figure 4-12, still shows a non-zero signal in the 1 m section, resulting in an ambiguous spectrum measured well within the short segment where the signal was supposed to show a single peak at ν_B = 10.86 GHz, as illustrated in Figure 13(b).

After having discuss the problems of continuous activation (which limits both the sensing range and sensing accuracy) and second echo (without doubt detrimental to information retrieval), we are now going to present in the next two sections two tools developed to avoid them: the de-convolution method based on the post processing of the measured data by simply applying a digital filter and the differential pulsed pump approach, capable of alleviating the detrimental effects of the continuous pump, as well as eliminating the aftermath of the second echo.

4.8 Deconvolution method

In Eq. (4.10), we have clearly seen that the echo decays after each phase change, which is due to the exponential terms related to the slow inertial acoustic moving. The full knowledge of the time-domain response of the distributed Brillouin echo sensor (based on a given coding) allows de-convolving the interfering effect of the second echo that seriously screens the real Brillouin response of the system. Therefore, in time-domain, the measured data is the convolution between the impulse response and real data as sketched in Figure 4-14. Thus, an operation corresponding to an inverse convolution will reconstruct the original Brillouin response for each measurement (that means the filter function simply processes data by making the z-transform). Here we will address the case of the π phase pulse that is the most interesting case as formerly described. In this case, the impulse response is obtained by simply using the setting defined in Eq. (4.12c) in Eq. (4.11), thus leading to the equation:

$$a_s(z,t) = -\frac{1}{2} g\, I_p^o\, A_s^o \Delta z \left\{ 1 - 2\left[1 - \mathrm{e}^{-\Gamma(t-\frac{2z_o - z}{V_g})} \right] \left[u(t - \frac{2z_o - z}{V_g}) - u(t - T - \frac{2z_o - z}{V_g}) \right] \right. \\ \left. - 2\,\mathrm{e}^{-\Gamma(t-\frac{2z_o - z}{V_g})} (1 - \mathrm{e}^{-\Gamma T}) u(t - T - \frac{2z_o - z}{V_g}) \right\}, \quad (4.17)$$

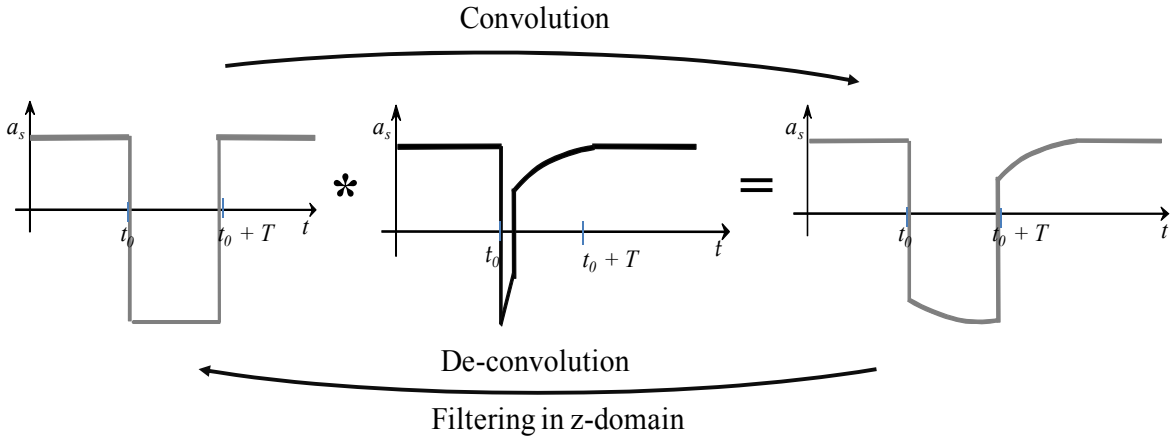

Figure 4-14: Illustration of the convolution of Brillouin response with the impulse response of the system showing the reversibility of convolution.

Figure 4-15 (a) and (b) representing respectively the BEDS original data and the BEDS data after filtering (the test fibre is the sensing fibre described in Section 4.7.2). Being a digital hygh-pass filter, this latter suppresses all continuous components, $2\alpha^2 \Delta z / V_g$, on the signal gain in Eq. (A.10) and, hence, the recovery of the acoustic wave vanishes as shown in Figure 4-15 and (b). The second echo, more visible in the classical BEDS, is now five times smaller when compared to the filtered data. The residual second echo observed in the same figure is due to the accumulated numerical error.

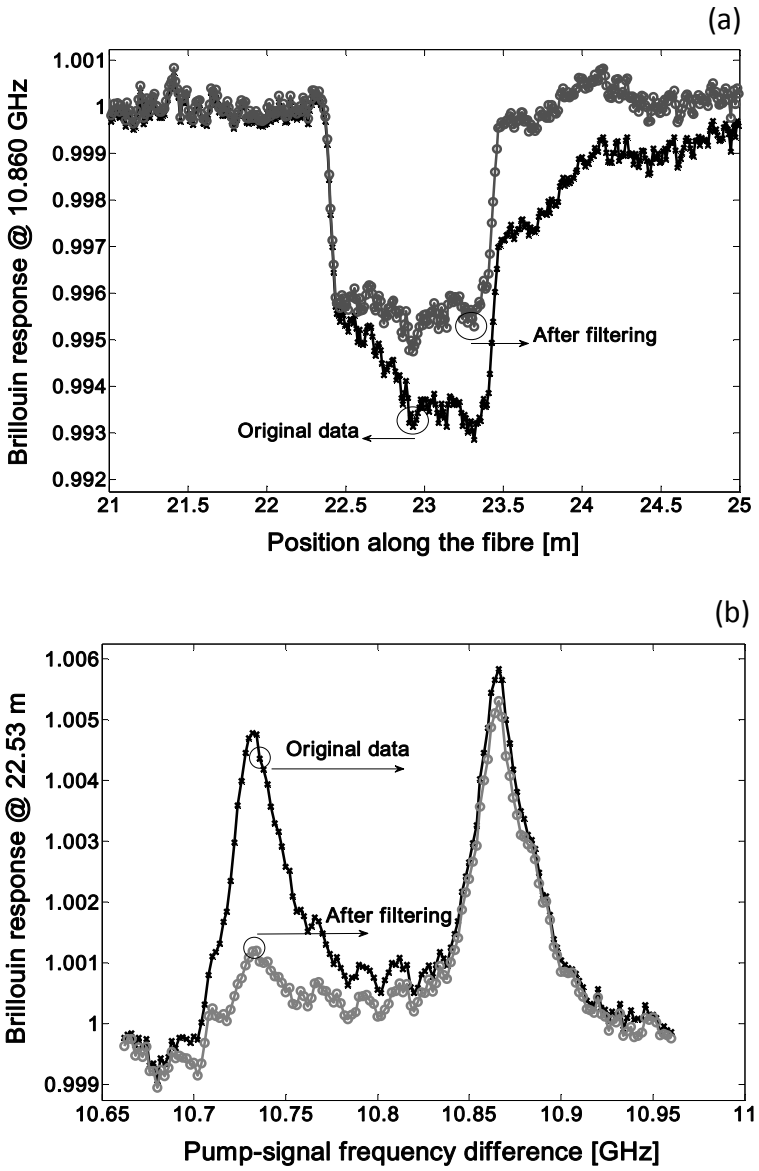

Figure 4-15: Probing a 1 m section (ν_B = 10.86 GHz) in the middle of a 40 m fibre (ν_B = 10.73 GHz), using a 500 ps π phase pulse and a 256 time average for each temporal trace. (a) The Brillouin gain through the 1 m section at frequency ν_B = 10.86 GHz, (1 m section at resonance). Measured data (circle), processed data (star); (b) measured and processed Brillouin gain distribution within the 1 m section at position 22.53 m showing the attenuation of the second echo thanks to the procesing, the signal polarity has been inverted for clarity.

4.9 Differential gain approach (DGA)

4.9.1 Principle

The effects of the second echo can be experimentally eliminated by extinguishing the pump at the end of the β pulse (*i.e.* considering γ=0 in Figure 4-4). Thus, in the absence of any pump light (no right term in Eq. (4.1a)), the back-propagating signal wave no longer experiences Brillouin interaction at all points where the β pulse has already passed through. Using an additional intensity modulator in front of the phase modulator in the pump path of Figure 4-8, the α pulse is also made finite, long enough (~30 ns) to substantially activate the acoustic wave but not too long in order to minimize pump depletion and optical beat noise (see Section. 4.7). Launching the pulse of Figure 4-16(b), comprising a ~30 ns long pulse, for which the last portion has been inverted (π phase shift) will actually activate the acoustic field and probe it without the parasitic second echo. However, the unique contribution of the short π phase shift portion of the pulse cannot be extracted unless extra measurements are taken.

The experimental configuration is based on the set-up of Figure 4-8. The lower channel was replaced by the branch in Figure 4-17, where an additional intensity modulator, synchronized with the phase modulator through the pulse generator, was used to generate the β pulse and obtained the pulse configuration shown in Figure 4-16. Since SBS is inherently dependent on the polarization [25], a passive polarization scrambler (see Section 3.1.4, Figure 3-7) was placed after the pump to achieve a non-vanishing average gain at every fibre location, regardless of the actual signal polarization at the same spatial point. In our differential gain method, two measurements are carried out: the first measurement is performed by using the pulse described in Figure 4-16(b), while a second measurement records the response to a uni-polar pulse, Figure 4-16(a), of the same length as the first pulse. Taking the difference between these two measurements results in a clean Brillouin trace characterized by a high spatial resolution, a high spectral resolution and a long range capability.

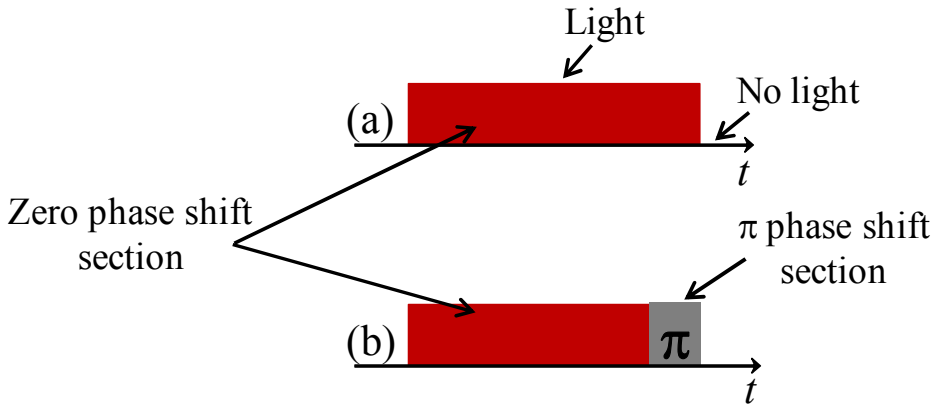

Figure 4-16: Illustration of the pulse configuration, as used for the differential gain approach. (a) The probing pulse, comprising a short π phase shift portion at the end of zero phase section; (b) A zero phase reference pulse.

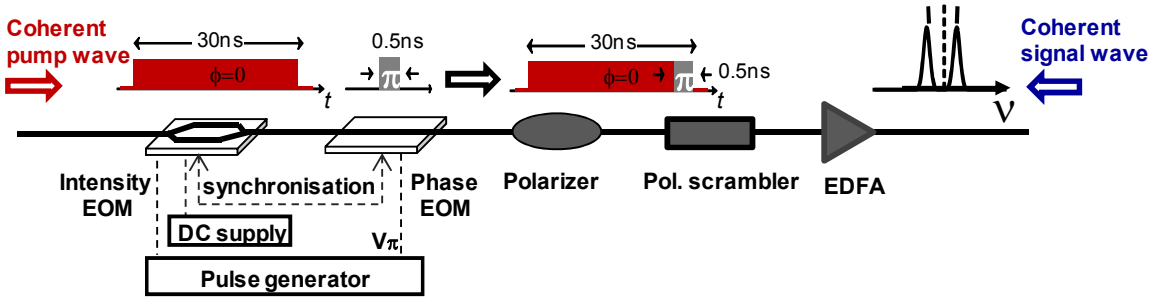

Figure 4-17: The lower channel in the set-up of BEDS with differential gain approach integrated.

4.9.2 Experimental results and discussion

Figure 4-18 and 19 show the application of the technique to the 20 m - 1 m - 20 m fibre of Figure 4-12 and Figure 4-13. As described above, measurements were carried out in two steps. First, the pump power was turned on for 30 ns, resulting in a classical Brillouin trace with a low spatial resolution as large as 3 m. Then the 30 ns compound pulse, comprising the original 29.5 ns zero phase and an appended 0.5 ns π phase shift pulse, was launched into the fibre and this new obtained trace was subtracted from the first one, giving the resulting response of the sole ultra short phase pulse. The rise/fall time of the pulses is particularly critical to secure the spatial resolution and was limited to 200 ps by our pulse generator, reasonably shorter than the π phase shift pulse width. No second echo is observed in Figure 4-18 and Figure 4-19(a), and the Brillouin sensing is actually strictly local.

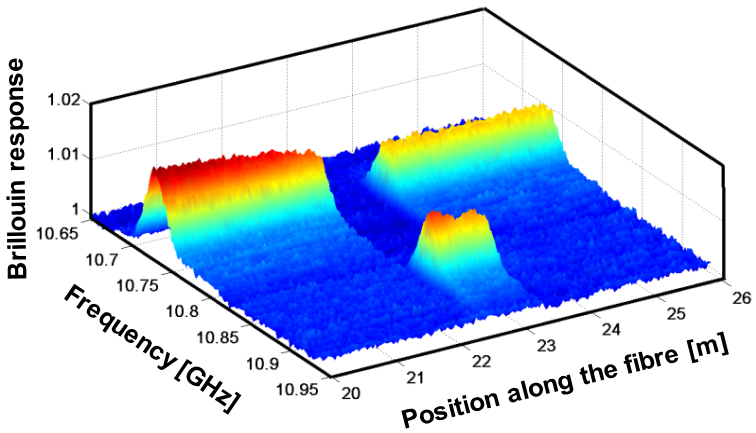

Figure 4-18: A 3D map of the Brillouin response in the 20 m-1 m-20 m fibre of Fig. 9, as obtained from the differential gain technique. No second echoes are observed.

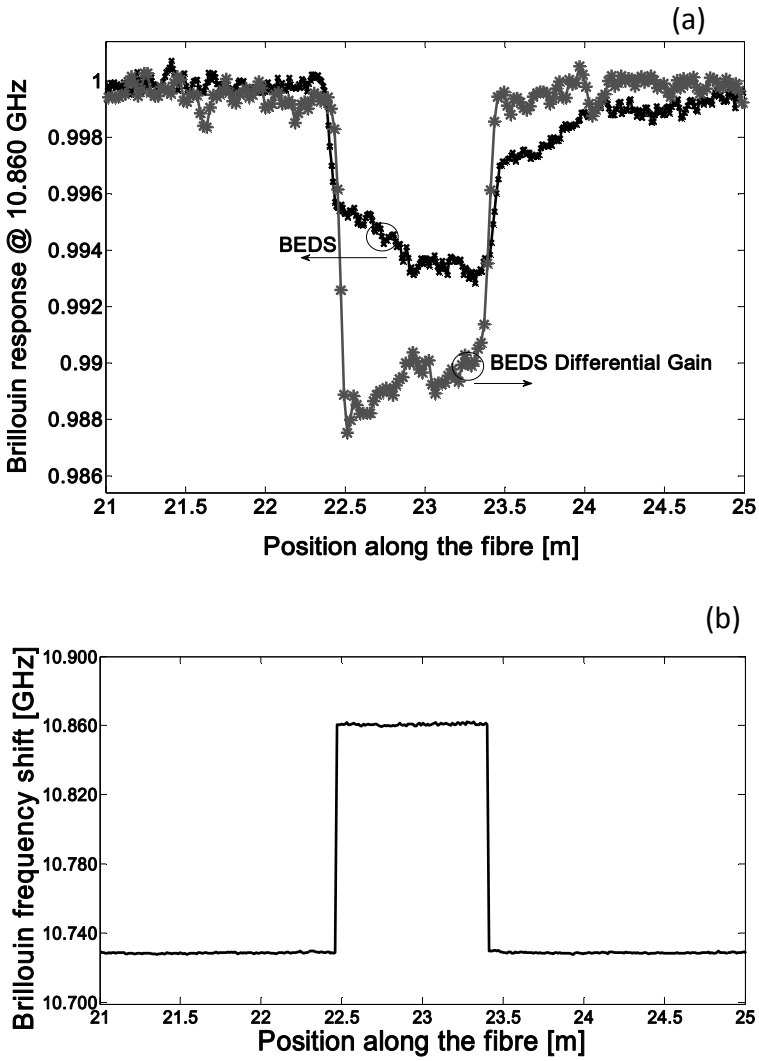

Figure 4-19: Using the differential gain technique to probe a 1 m section (ν_B=10.86 GHz) in the middle of a 40 m fibre (ν_B=10.73 GHz), using a 500 ps π phase pulse and 256 time averages of each temporal trace. (a) Compare the very clean Brillouin gain trace around the 1 m section at the 1m section frequency (ν_B=10.86 GHz) with that of Fig. 10a. (b) Brillouin frequency shift as a function of position in the fibre.

Using the same pulse parameters, the method has been also applied to a 5 km fibre (ν_B=10.42 GHz), where a 5 cm fibre with ν_B=10.30 GHz, was spliced near the far end of the long fibre.The differential pulse-width pair technique described in Ref. 16 can be seen as a simplification of the differential method detailed here, in which the π phase shift pulse is replaced by a dark pulse making the actual pump pulse shorter. A 3D view is provided in Figure 4-20 (a) and (b) where again, the 5 cm section is spatially well resolved, while preserving the ~30 MHz natural line-width of the Brillouin gain spectrum.

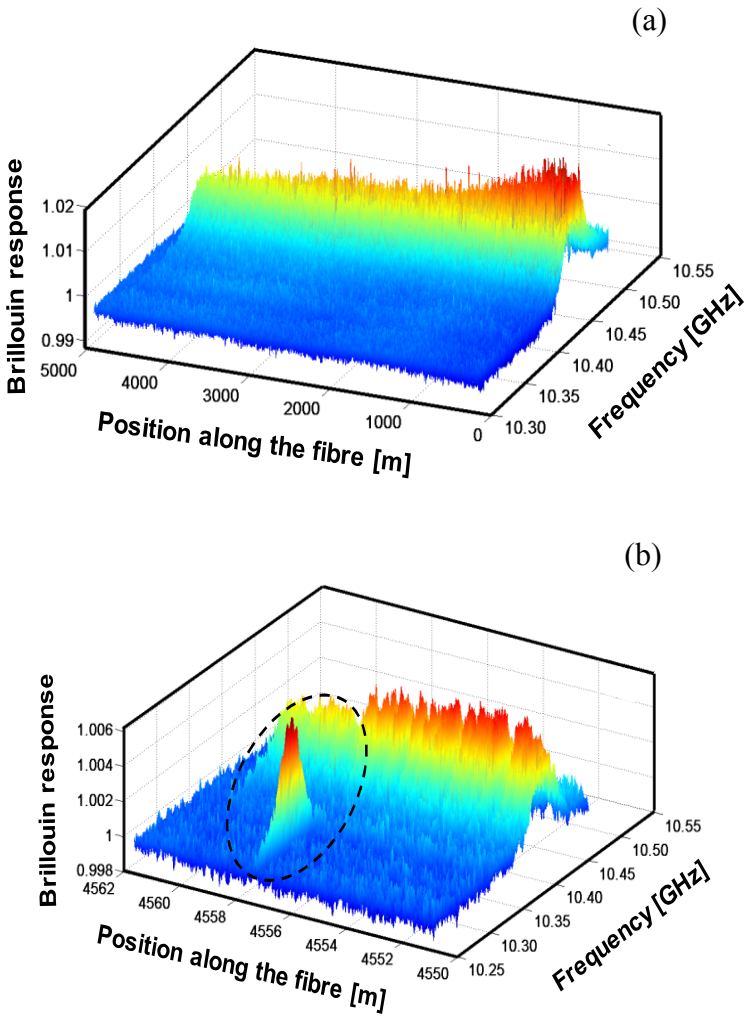

Figure 4-20: (a) 3D spectral distribution of the response as function of the position over a 5 km fibre realized with a 5 cm spatial resolution. The 5 cm segment is too small to be distinguished; (b) magnified view of the 3D distribution of the Brillouin response around the 5 cm fibre section, showing that this segment at the end of the 5 km fibre is fully resolved both in space and frequency.

Time traces shown in Figure 4-21 document consecutive measurements performed along the 5 km long fibre with (B) and without (A) the 0.5 ns π phase pulse, together with their difference, the bottom curve and the inset (Figure 4-22 depicts a close-up view of the (A-B) curve of Figure 4-21, at the Brillouin resonance of the small section fibre, around the position of the 5cm section, exhibiting excellent spatial and spectral resolution). Figure 4-22(a) shows the gain as a function of the position around the 5 cm section, when the frequency is tuned to be at the peak frequency of the short segment, while Figure 4-22(b) describes the Brillouin frequency shift around the 5 cm fibre section, as a function of distance, after processing of the raw traces. The 5 cm section is very well resolved and the accuracy of the measurement is calculated to be ±3°MHz for 2 standard deviations σ, corresponding to ±3°C.

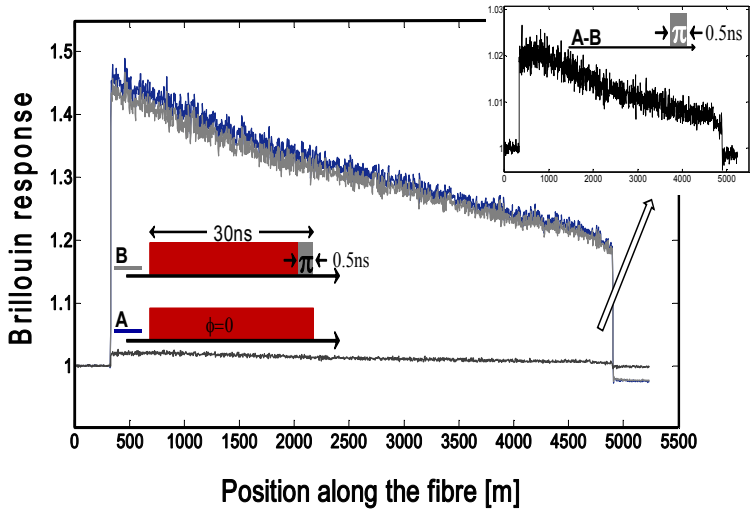

Figure 4-21: Two measurements without (A) and with (B) 0.5 ns π phase pulse along the 5 km long fibre. Inset: the difference between the two measurements, A and B, showing the signature of the fibre equivalent to the response of the 0.5 ns phase pulse. Measurements were performed using 256 times averaging of each temporal trace.

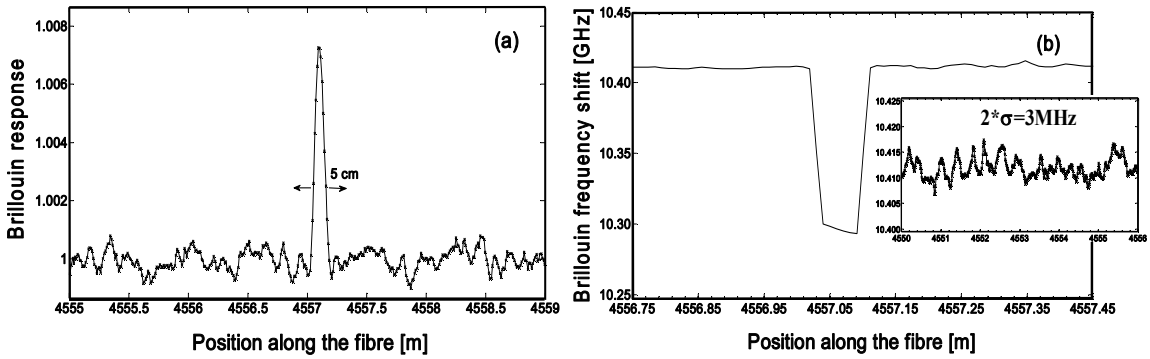

Figure 4-22: (a) Brillouin response as a function of distance in the vicinity of the 5 cm fibre section; (b)Brillouin frequency shift as a function of distance at the same positions.

4.10 Performances of the two methods

In Figure 4-24(a) and (b), we can see respectively comparative pictures of the Brillouin response and the Brillouin gain spectrum for the classical BEDS, the BEDS after processing and the BEDS differential gain approach. The summary of the performances of the de-convolution method and the differential gain approach is detailed in Table 4-1.

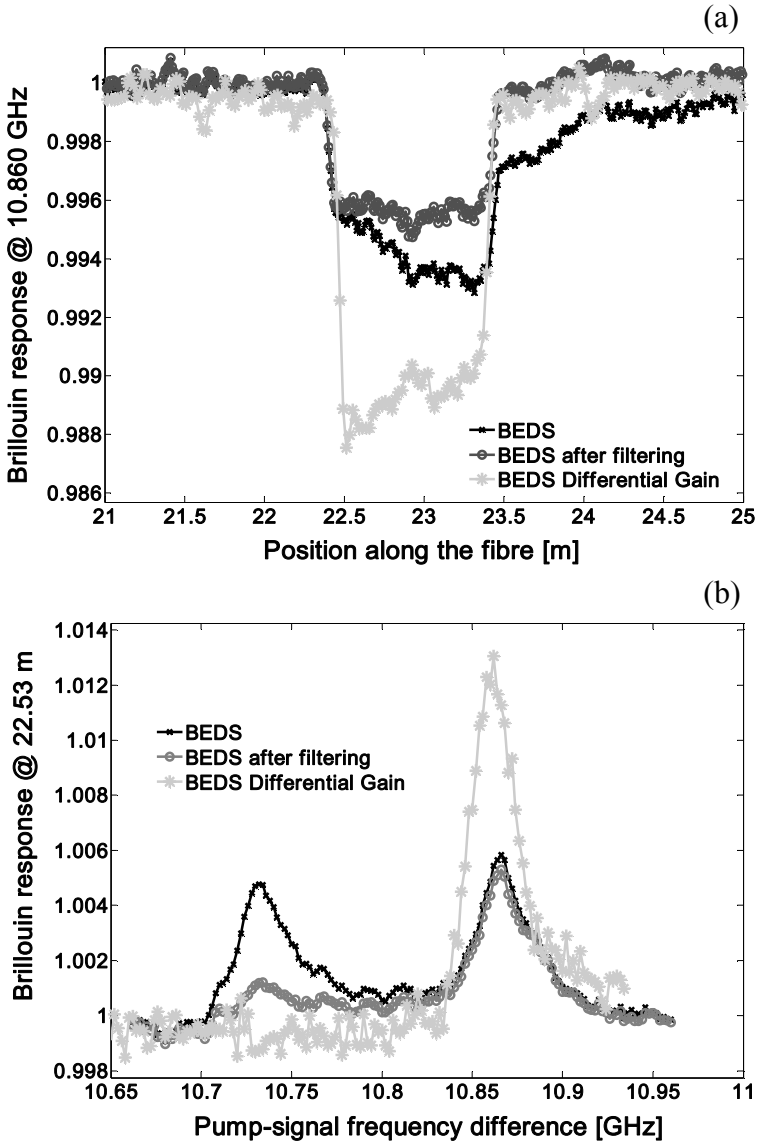

Figure 4-23: Brillouin response applying the low pass filter on the measured data and using the differential gain technique to probe a 1 m section (ν_B=10.86 GHz) in the middle of a 40 m fibre (ν_B=10.73 GHz), using a 500 ps π phase pulse and 256 time averages of each temporal trace. (a) Compare the very clean Brillouin response trace around the 1 m section at the 1m section frequency (ν_B=10.86 GHz) of Figure 4-19(a) with that of Figure 4-13 and Figure 4-15 (a); (b) Compare the very clean Brillouin gain distribution within the 1 m section at position 22.53 m with that of Figure 4-13(b) and Figure 4-15(b).

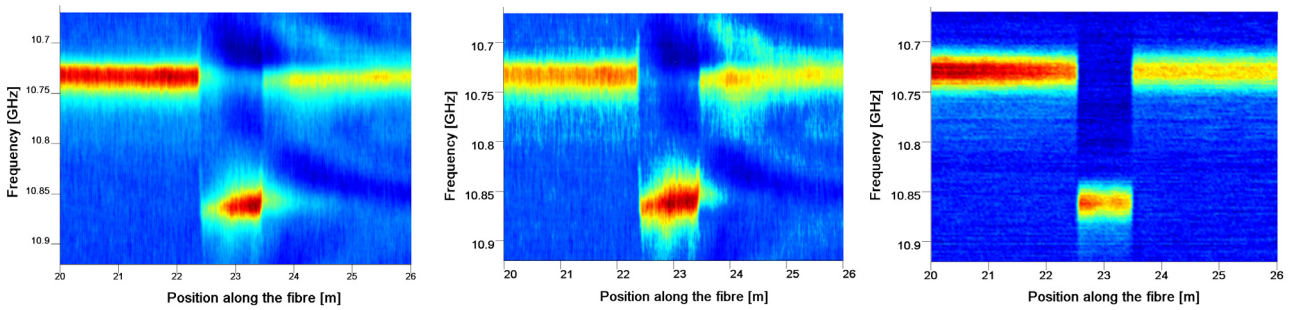

Figure 4-24: 2 Magnified view of 2D spectral distribution of the Brillouin response around the 1 m fibre section as function of the position over the 40 m of fibre realized with a 5 cm spatial resolution; from left to right original data; filtered data and BEDS differential gain.

Table 4-1: Summary of the performances of the two methods.

Methods	Using de-convolution	Using DGA
Second echo	Strongly but not totally	Totally eliminated
Range	Limited to maximum 1 km due to the pump depletion	5 km with 5cm spatial resolution
Acquisition time	Time required for post-processing ~2 s	Double time
Measurement contrast	Constant contrast	Constant contrast

In Ref 16, a method called differential pulse-width pair is reported. This technique though is presented by the authors with a different point of view, in which the π phase shift pulse is replaced by a dark pulse making the actual pump pulse shorter. In Figure 4-25, a comparative measurement to the response of these two differential techniques is presented, showing that the phase pulse actually optimizes the response by improving the contrast by a factor 2, as expected from the analysis in Section 4.4.

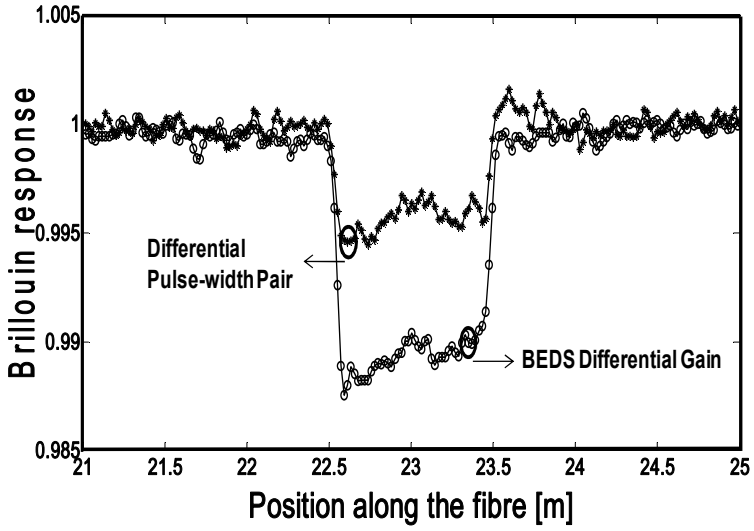

Figure 4-25: Comparative Brillouin response of the BEDS differential gain approach and the differential pulse-width pair technique [16], obtained under identical power and spatial resolution conditions (5 cm), clearly showing the optimized BEDS response by a 3 dB contrast improvement.

4.11 Conclusion

Brillouin echo distributed sensing (BEDS) has proved to be a powerful solution to realize sub-metric spatial resolutions in Brillouin distributed measurements. An optimized configuration, using π-phase pump pulses, was experimentally tested down to a spatial resolution of 5 cm, with a clear margin for further improvement down to a real centimetric spatial resolution. This optimized configuration will produce the best contrast independently of the pulse intensity, with a factor 2 of improvement compared to other techniques based on the same approach (dark pulse, bright pulse). This extends the dynamic range by 3 dB, which corresponds in standard loss conditions to a 5 km extension of the sensing range.

Major difficulties related to the restoring of the acoustic wave which manifests itself as a secondary trailing echo in the response, were successfully alleviated using a differential gain approach. This has limited excessive pump depletion and made it possible to extend the range to 5 km, which was limited to much less than 1 km using a continuous pump or a de-convolution method. This corresponds to 100,000 independent resolved points along the fibre and a range extension to 10 km looks perfectly feasible, so that a system with one million resolved points along a standard single mode fibre is likely to be proposed in the near future. It appears that BEDS systems can become a key and powerful configuration for the next generation of Brillouin fibre distributed sensors, combining simplicity in the hardware implementation, kilometric sensing ranges and centimetric spatial resolution, with a temperature/strain resolution unchanged when compared to a classical BOTDA system.

Bibliography

[1] Kurashima T., Horuguchi T. and Tateda M., 1990. Distributed-temperature sensing using stimulated Brillouin scattering in optical silica fibres. Optics Letters, 15, 18:1038–1040.

[2] Bao X., Webb D.J., and Jackson D.A., 1993. 32-Km distributed temperature sensor using Brillouin loss in optical fibre. Optics Letters, 18, 18:1561-1563.

[3] Nikles M., Thévenaz L., and Robert P. A., 1996. Simple distributed fibre sensor based on Brillouin gain spectrum analysis. Optics Letters, 21, 10:758:760.

[4] Kurashima T., Horiguchi T., Izumita H., Furukawa S., and Koyamada Y., 2008. Brillouin optical fibre time domain reflectometry. IEICE Transactions on Communication, E76-B, 4:382-390.

[5] Fellay A., Thévenaz L., Facchini M., Niklès M. and Robert P., 1997. Distributed sensing using stimulated Brillouin scattering: towards ultimate resolution. 12th International Conference on Optical Fibre Sensors, 324-327.

[6] . Agrawal G.. *Nonlinear Optics.* Chap.9, 3rd ed. (2008).

[7] Garus D., Gogolla T., Krebber K., and Schliep F., 1997. Brillouin optical fibre frequency-domain analysis for distributed temperature and strain measurements. Journal of Lightwave Technology, 15, 4:654-662.

[8] Hotate K. and Tanaka M., 2002. Distributed fibre Brillouin strain sensing with 1-cm spatial resolution by correlation-based continuous-wave technique. IEEE Photonic Technology Letters, 14, 2:179–181.

[9] Bao X., Brown A., DeMerchant M. and Smith J., 1999. Characterization of the Brillouin-loss spectrum of single-mode fibres by use of very short (10-ns) pulses. Optics Letters, 24, 8:510-512,

[10] V. Lecoeuche, D. J. Webb, C. N. Pannell, and D. A. Jackson, 2000. Transient response in high-resolution Brillouin-based distributed sensing using probe pulses shorter than the acoustic relaxation time. Optics Letters, 25, 3:156-158.

[11] Zou L., Bao X., Wan Y., and Chen L., 2005. Coherent probe-pump-based Brillouin sensor for centimeter-crack detection. Optics Letters, 30, 4:370-372.

[12] Anthony W. Brown and Bruce G. Colpitts, 2007. Dark-Pulse Brillouin optical Time-Domain Sensor with 20-mm Spatial Resolution. Journal of Lightwave Technology, 25, 1:381-386,

[13] Kishida K. and Li C-H., 2006. Pulse pre-pump-BOTDA technology for new generation of distributed strain measuring system. In Structural Health Monitoringand Intelligent Infrastructure, Vol. 1, J.P. Ou, H. Li and Z.D. Duan (Eds), Taylor & Francis group, London, 471-477.

[14] Thévenaz L., Foaleng S. M., 2008. Distributed fibre sensing using Brillouin echoes. 19th International Conference on Optical Fibre Sensors, SPIE, Perth, WA, Australia, 70043N-70044.

[15] Foaleng S. M., Beugnot J-C, Thévenaz L., 2009. Optimized configuration for high resolution distributed sensing using Brillouin echoes. 20th International Conference on Optical Fibre Sensors, SPIE, Edinburgh, UK, Scotland, 7503, 75032C-4.

[16] Li W., Bao X., Li Y., and Chen L., 2008. Differential pulse-width pair BOTDA for high spatial resolution sensing. Optics Express, 16, 26:21616-21625.

[17] Boyd R. W., *Nonlinear Optics*, 4th ed. Chap.9, (2008).

[18] Thévenaz L. and Beugnot J-C, 2009. General analytical model for distributed Brillouin sensors with sub-meter spatial resolution. In Proceedings of SPIE, 20th International Conference on optical fibre sensors, UK, Edinburgh 7503, 75036A.

[19] Diaz S., Foaleng S. M., Lopez-Amo M., and Thévenaz L., 2008. A High-Performance Optical Time-Domain Brillouin Distributed Fibre sensor. IEEE Sensors journal, 8, 7:1268-1272.

[20] Niklès M., Thévenaz L. and Robert P., 1997. Brillouin Gain Spectrum Characterization in single-mode optical fibres. Journal of Lightwave Technology, 15, 10:1842-1851.

[21] Horiguchi T., Shimizu K., Kurashima T., Tateda M. and Koyamada Y., 1995. Development of a Distributed Sensing Technique Using Brillouin Scattering. Journal of Lightwave Technology 13, 7:1296:1302.

[22] Geinitz E., Jetschke S., Röpke U., Schröter S., Willsch R. and Bartelt H., 1999. The influence of pulse amplification on distributed fibre-optic Brillouin sensing and a method to compensate for systematic errors. Measurement Science and Technology, 10, 112-116.

[23] Tkach R. W. and Chraplyvy A. R., 1989. Fibre Brillouin amplifiers. Optical and Quantum Electronics, 21, 1:S105-S112.

[24] Olsson N. A. and Van Der Ziel J. P., 1987. Characteristics of a Semiconductor Laser Pumped Brillouin Amplifier with Electronically Controlled Bandwidth. Journal of Lightwave Technology, 5, 1:147-153.

[25] Thévenaz L., Foaleng S. M. and Niklès M., 2007. Fast measurement of local PMD with high spatial resolution using stimulated Brillouin scattering. In Proceding ECOC'07, 10.1.2

5 Applications of BEDS

Som applications of BEDS technology in real situations will now be presented. This chapter[8] is the outcome of the collaboration between our laboratory, GFO (Group for Fibre Optics), and two others laboratories, the Geomechanics research group for the institute from Geotechnical Engineering (IGT) at ETHZ and the Femto-ST laboratory at Besançon University in France.

[8] This chapter is based on:

Iten M., Puzrin A.M., Hauswirth D., Foaleng-Mafang S., Beugnot J.C. and Thévenaz L. (2009). Study of a progressive failure in soil using BEDS. Proc. of SPIE, Vol. 7503, OFS20, Edinburgh, UK.

Stiller B., Foaleng S. M, Beugnot J.-C., Lee M. W., Delqué M., Kudlinski A., Thévenaz L., Maillotte H. and Sylvestre T.(2010). Photonic crystal fiber mapping using Brillouin echoes distributed sensing. Optics Express, 18, 19:20136-20142.

Beugnot J-C., B. Stiller, Foaleng S. M., Won Lee M., Delqué M., Kudlinski A., Maillotte H., Laude V., Thévenaz L.and Sylvestre T. (2010). Observation of Brillouin linewidth broadening in photonic crystal fiber. In proceding of 36th European Conference and Exhibition on Optical Communication, pp. 1-3.

5.1 Landslide monitoring using BEDS

5.1.1 Background

Nobody will forget the BP (British Petroleum) catastrophe which happened this year (2010) in the Gulf of Mexico and the damage caused worldwide by oil spills. Other recent events remind us that the cost of a bridge or structure collapsing is much more than economic; it affects people's lives, shutting down communications networks, as dramatically demonstrated by the collapses of the Laval's La Concorde overpass in fall 2006, the Minneapolis bridge in summer 2007 and the Korba chimney in autumn 2009.

This means monitoring of structures such as bridges, buildings, dams, highways, tunnels, pipelines, containers and subseas etc. is useful from the economic and security points of view [1-3]. With a proper sensing system, it is possible to obtain information about the health of a structure which can be used for designing repair schedules and for giving early warnings of degradation that might lead to a catastrophic failure in the long-term [2].

Several techniques exist, including satellite photos, geodetic techniques and inclinometers. However, with these techniques, spatial resolution ranging from 5m down to 2 m is not the only problem, there is also much uncertainty due to the hazard environment, and manpower cost is not negligible, thus generating very high costs.

Throughout this thesis, we have studied the Brillouin fibre optic sensors in its entirety, we have seen it shows a huge potential in the monitoring of temperature and stress allowing a pluridisciplinary range of applications. As a result, Brillouin sensing (using standard techniques such as BOTDA, BOTDR or BOFDA) has been developed for applications in areas such as the oil industry and civil engineering to monitor pipeline [4-6], and the gas industry to monitor gas leaks, perimeter security and intrusion.

Furthermore, for new applications we have mentioned that high spatial resolution of measurement while maintaining a good accuracy and a large dynamic range are the key elements. These requirements are not possible using classical systems such as BOTDA as described in chapter 3, where the spatial resolution is limited to 1m (this limitation is caused by Brillouin spectrum broadening which degrades the accuracy), or other techniques such as BOCDR, this time limited by the number of resolve points. In geotechnical engineering for example, to monitor structures and soils, the mitigation of geohazards is an important problem. Heavy rains, typhoons and earthquakes are the main causes of geohazards. Due to climatic changes in and extreme weather, geohazards are spreas all over the world. To monitoring the movement of land, the current challenge lies in the ability to distinguish the boundary between the location of the soil, which undergoes a shift, and the part that suffers from no moving (Figure 5-1 a), meaning that a large amount of strain gauges is required per unit length/area of the structure. Landslides need to be detected at an early stage of their development, when the motions are still shorter than 1m, i.e. an order of magnitude lower than a typical strain resolution obtained using traditional BOTDA systems. This imposes constraints on the interrogator and the fibre optic cable. It implies that the interrogator must have the ability to resolve sub-metric faults.

BEDS technology developed in the framework of this thesis was a solution to this problem since it offers sub-metric spatial resolution and an operation principle equivalent to a classical BOTDA

system, an essential quality for tests in a real environment. With the team of Prof. Puzrin, (from Geotechnical laboratory at ETHZ) we were able to prove the applicability of BEDS for the study of progressive failure in soil structure interaction. For the first time it became possible to accurately observe the failure propagation at the laboratory scale [7].

5.1.2 Detection of landslide boundaries using the BEDS system: Detection of the strain profile of a cable pulled out of sand at the geotechnical laboratory of ETHZ, Zurich

The laboratory measurement system was realized at ETHZ and consisted of two parts: a optical one and a geotechnical one.

- The optical part was realized out by our laboratory using the BEDS experiment described in chapter 4, with 5 cm spatial resolution allowing for at least 20 resolved points per meter. The optical fibre cable itself is the sensor and therefore does not affect the stiffness of the cable or the soil. A photograph of the configuration is shown in Figure 5-2 (a). The acquisition resolution was set to 25 ps (equivalent to 0.25 cm) to realize a good oversampling and to be only limited by the instrumental spatial resolution of 5 cm.
- The geotechnical part was carried out by the specialists from the ETHZ laboratory, a photograph of the configuration is shown in Figure 5-2 (b). For the laboratory testing, a 2m long, 0.1m wide and 0.2m deep pullout box was used (Figure 5-1 (b)). The idea is that a structural part embedded in soil (e.g. an anchor or a cable buried at a depth of 0.1m in sand) can be pulled out of the soil-filled box. The pulling force was applied by a step motor at the front tip of the box. This motor allows for controlled pullout by displacement δ. The following two tests were performed first: a free cable test and buried cable test.
  - (i) Free cable test: This test is performed to obtain the stiffness (strain-stress dependency) for an optical cable section of length ΔL. For this test, the box remains empty and an optical fibre cable is connected to a fixing point on the step motor and to another fixing point at a chosen distance ΔL from the step motor. The section ΔL can then be subjected to strain controlled by displacement δ of the step motor. At each strain step, optical measurements are carried out.
  - (ii) Buried cable test: In this test the cable is buried in sand and displacement δ was applied to the cable by the step motor. After a preset displacement, optical measurements are carried out. The buried cable test allows for the specification of the distribution of shear stresses between the cable surface and the sand along the cable length. For softer cables this information is of crucial importance for understanding and modeling the progressive failure phenomenon.
- Another aspect of importance for the laboratory measurement is the optical fibre cable. It must be pointed out that such an extreme spatial resolution requires particularly cautious handling and positioning of the fibre cable, since any bending of the optical cable induces a strain that is clearly observed in the distributed measured Brillouin spectrum. This fact is essential to interpret correctly the measured strain distributions, since very few sections

show a uniform strain and the value of the zero-strain frequency is particularly hard to determine. A partner company has produced a special strain sensing optical fibre cable for the laboratory tests (Figure 5-1 c) without loss due to micro-bending, allowing unproblematic handling. The cable is basically a well-protected single-mode fibre which shows very good strain transmission properties from the outer jacket to the fibre core.

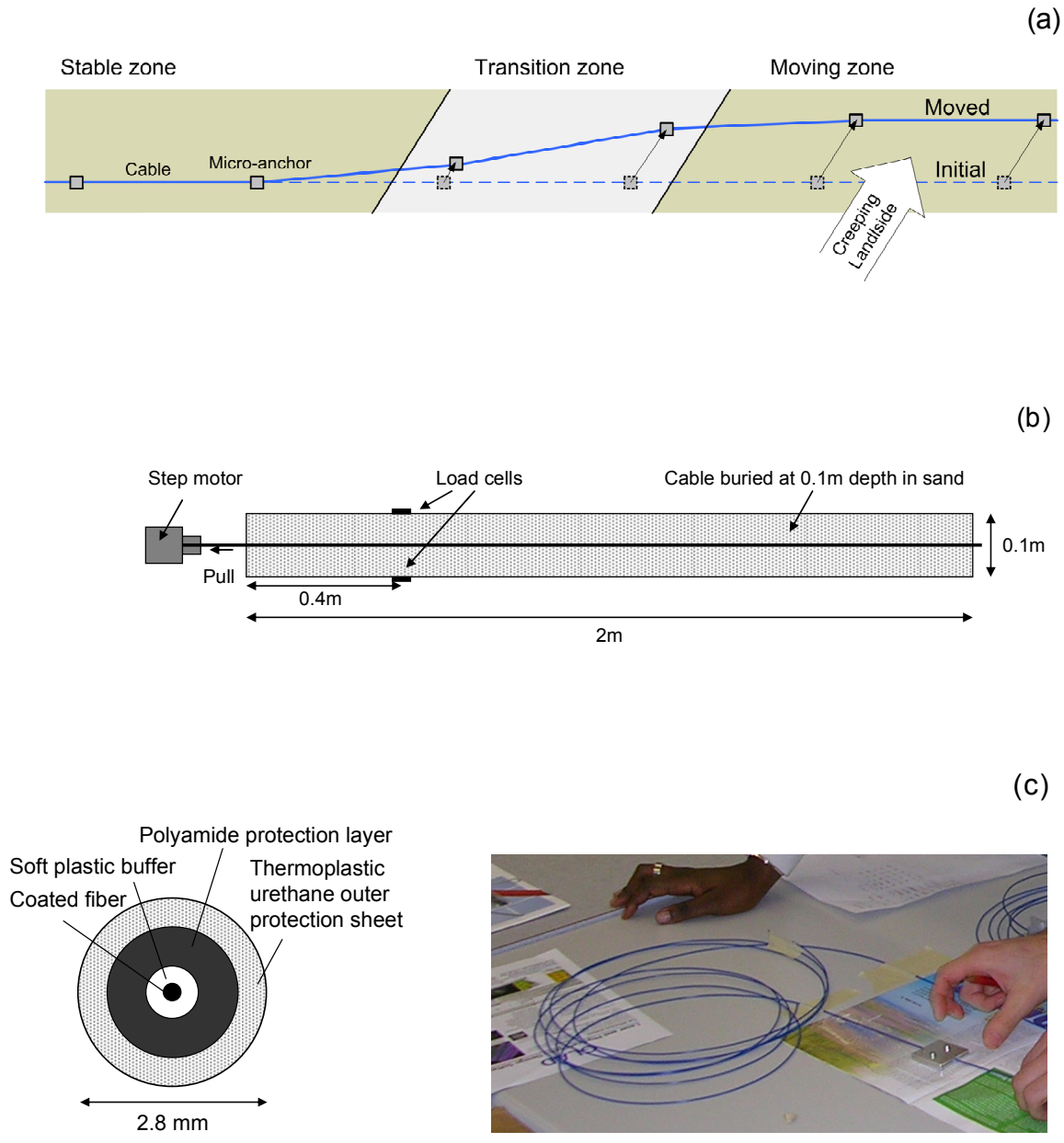

Figure 5-1: (a) Illustration of the motion of the land showing the three zones concerned (stable zone, transition zone and moving zone) and the strain transfer to the cable for a landslide at 45° angle, (b) geometry of the pullout box used the measurements: 2 m length, 0.1 m diameter and 0.1 m depth, c) geometry (cross section) of the used optical fibre cable (left) and its photograph (right) which shows the cable with the micro-anchor mounted.

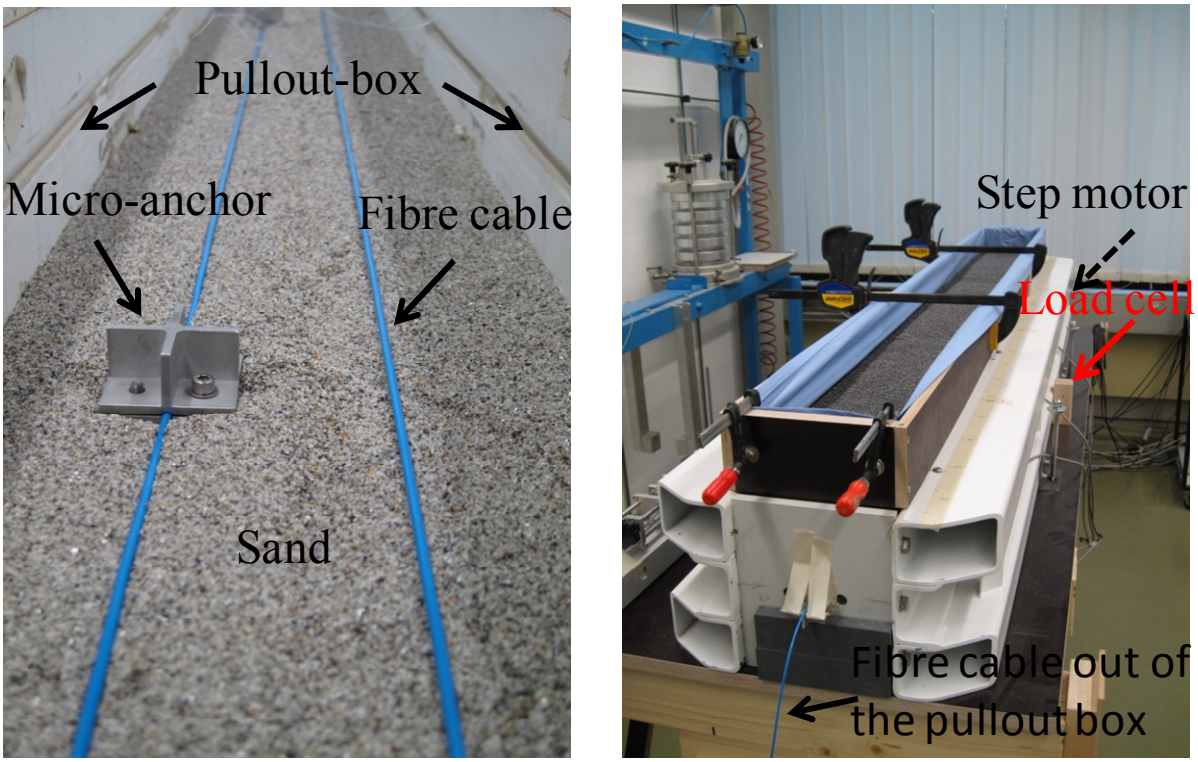

Figure 5-2: Geotechnical measurement laboratory land-slide set-up showing a micro anchor mounted onto the optical fibre cable before recovering with sand (left), the pullout-box with optical fibre cable buried in sand (right).

Free cable testing

Free cable testing was realized over a 2 m section of the cable. A comparison with similar testing using BOTDA technology showed an excellent correlation. Small fibre slippage inside the protection layer at relatively high strains (>1.5%) was detected. Below that value, strain applied to the cable jacket was directly transferred to the fibre core. The data from the free cable tests was then used to back calculate stresses and forces from the optical measurements, which could be evaluated as a function of the independently measured load cell forces.

Buried cable testing

Buried cable testing was realized by pulling out a 2 m long cable section buried at a depth 0.1 m in sand.Figure 5-4 shows the obtained strain data (relative to the zero strain measurement) along the optical fibre cable for eight displacement steps controlled by the step motor. The fixation of the cable to the step motor is at a distance of 2.83 m from the measuring unit. As can be seen in the same figure, in the first four steps, the strain behind the fixation point is zero. At larger displacement steps the strain profile propagates behind the fixation point, most probably due to the slippage of the glass fibre inside the cable.

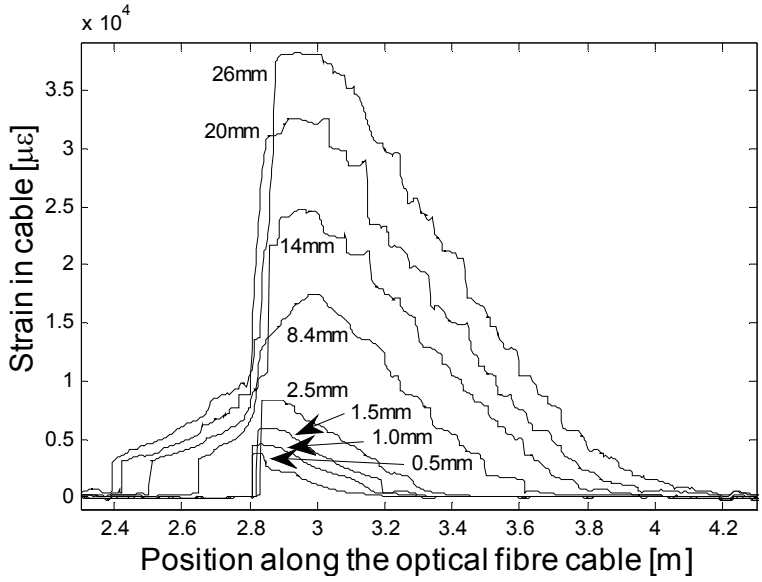

Figure 5-4: Measured strain for each load step δ applied to the fibre cable: For each load step δ distributed measurements was carried out. Measured was obtained using BEDS experimental set-up with 5 cm spatial resolution allowing for at least 20 resolved points per meter. The Brillouin frequency shift was retrieved which gave the information on the amount of strain applied. In the first four steps, the strain behind the fixation point (at 2.8 m) is zero while at larger displacement steps the strain profile propagates

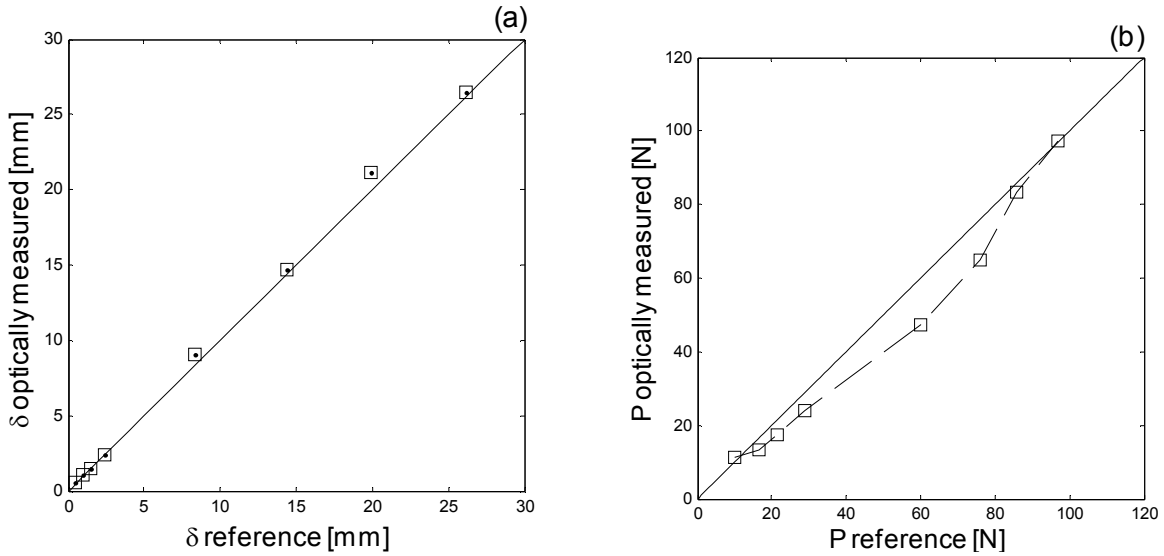

Figure 5-3: (a) Applied displacement as a function of the measured displacement (retrieved from numerical integration of the entire strain in the cable), (b) applied force versus optically measured pullout force. The measured and the applied values are consistent.

Numerical integration of the entire strain in the cable leads to the displacement δ at the fixation point and this can also be compared with the value applied by the step motor (Figure 5-4(a)). By

using the optically-measured maximum fibre strain at each load step, cable force P at the fixation can then be calculated (using the formula $\varepsilon[\mu\varepsilon] = P$ [N]/0.0029 for strain showing elastic range from 0 to 9000 με and $\varepsilon[\mu\varepsilon] = 258P^2[\mathrm{N}]+241P[\mathrm{N}]+870$ for strain showing elastic range above 9000 με [16]) and compared to the applied load measured by the load cell (Figure 5-3(b)). As can be seen, for both values (P, δ) the agreement between the optically and conventionally measured values is very good. Geotechnical interpretation can also be find in Ref [7].

5.2 Brillouin gain spectrum measurements in Photonic crystal fibre using BEDS

5.2.1 Background

From the introductory chapter, we know that low-loss single-mode optical fibres exist since 1970. Four years later (i.e 1974), Air-silica microstructure fibres (ASMF) were developed with the interest of their unique optical properties and ability to manipulate light [8]. These fibres are typically all-silica optical fibres with air-holes introduced in the cladding region that run along the length of the fibre. Since then, we have seen the advent of air-clad optical fibres, microstructured optical fibres (sometimes called photonic crystal fibre when the arrays of holes are periodic and resemble a crystal) and many other subclasses [9]. Photonic-crystal fibre (PCF), a term first coined by Philipp Russell in 1995-1997 [9], is a new class of optical fibre based on the properties of photonic crystals. More specific categories of PCF include photonic-bandgap fibres (PCFs that confine light by band gap effects), hollow core fibres (PCFs using air holes in their core), hole-assisted fibres (PCFs guiding light by a conventional higher-index core and low index cladding modified by the presence of air holes), and Bragg fibres (photonic-bandgap fibres formed by concentric rings of multilayer film). Because of its ability to confine light in hollow cores or with confinement characteristics not possible in conventional single-mode optical fibres, PCF is now

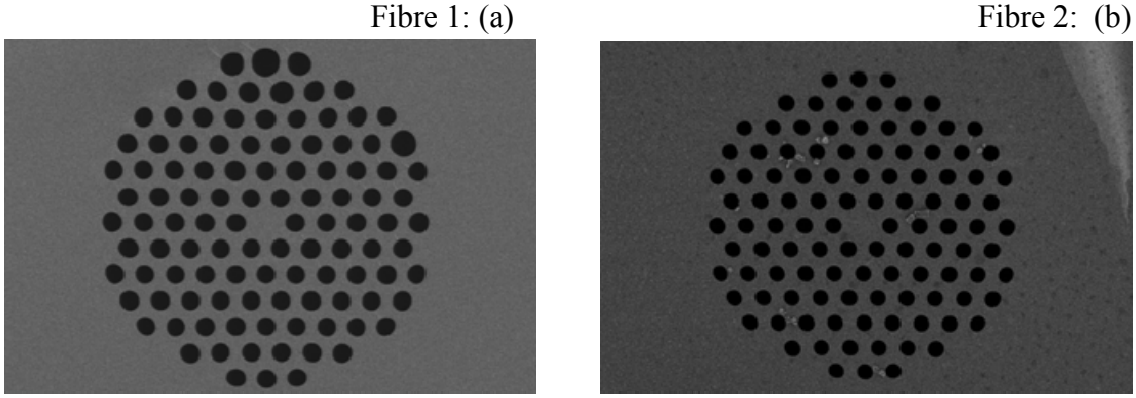

Figure 5-5: Scanning electron micrograph (SEM) of the solid core PCF fibres, a)Fibre 1: 100°m length and b)Fibre 2: 400°m length.

finding applications in optical fibre communications, fibre lasers, nonlinear devices (high efficiency gas-Raman cells), high-power transmission, highly-sensitive gas sensors, metrology and sensing [10]. In fact the multi-peak Brillouin spectrum exhibited by small core PCF due to the periodic air-hole microstructure can be an advantage for the simultaneous strain and temperature measurements. However, when these multi-peaks overlap, the Brillouin spectrum broadens and it becomes detrimental for the information extraction. In addition, the in-homogeneity of opto-geometrical parameters over the fibre has a major influence on the Brillouin frequency shift. This is even more crucial since we know that the actual challenge for higher dimensional photonic crystals fibres is in the fabrication of these structures with sufficient precision to prevent scattering losses blurring the crystal properties, and in drawing processes that can be as robustly mass produced as for standard single mode fibres (SMFs).

As a matter of fact, using the BEDS technique with high spatial resolution (30 cm spatial resolution), it has been possible to get a distributed characterization of two PCFs fibres (solid-core fibres category) provided by a partner company Crystal Fibres [11]. The impact of structural irregularities and strain on the Brillouin frequency shift has been evidenced. In addition, long- and short-scale [9] fluctuations in Brillouin frequency shift have been observed. We further show that it is possible to extract the effective refractive index all along the fibre from the distributed BFS measurements, which yields a quantitative estimation of fibre irregularities. With these measurements performed at our laboratory at EPFL with the team of the laboratory of Besançon, we were able to draw conclusions about the PCF fibre in-homogeneity induced by the drawing process [12-13].

5.2.2 Mapping of two PCF fibres

The two PCF fibres under mapping are 100 m (Fibre 1) and 400 m (Fibre 2) in length, respectively, have a hexagonal holey structure and whose scanning electron micrographs are shown in Figure 5-5. The two PCF fibres originated from the same stack but from different intermediate canes. The cane used to manufacture Fibre 1 was 3.8 mm in outer diameter and drawn at a relatively high temperature (low tension). For Fibre 2, the cane was drawn with the same parameters, but the temperature was much lower than that used for Fibre1, leading to a much higher tension during the drawing process. At this stage, the outer diameter fluctuations of both canes were comparable, but the air holes were slightly smaller in the cane of Fibre1 than that of Fibre2. The canes were then inserted into jacketing tubes and drawn down into fibres. Both fibres were drawn with comparable parameters, although a slightly higher pressure was used for Fibre1 to inflate the air holes. The outer diameter fluctuations measured during the drawing process were about 2% for Fibre1 and less than 1% for Fibre2. Other parameters of the two fibres are given in Table 5-1.

[9] Short-scale longitudinal fluctuations were studied in Ref [8]. However it is the first time that short-scale fluctuations were investigated in optical fibres using distributed measurements.

Table 5-1: Parameters of PCF Fibres 1 and 2.

Fibre parameters	Fibre 1	Fibre 2
Lenght	100 m	400 m
Att @ 1550nm	5 dB/km	8.6 dB/km
Aeff @ 1550nm	15 μm^2	16 μm^2
Zero dispersion wavelength	1060 nm	1060 nm
Core diameter	5.5 μm	5.5 μm
Hole diameter	2.7 μm	2.3 μm
Pitch	4.1 μm	3.9 μm

Figure 5-6 provides the 2 D distribution of Brillouin gain along along the 100 m PCF fibre showing the longitudinal fluctuations of the Brillouin frequency shift. As can be seen in Figure 5-7, the distribution exhibits both long- and short-scale longitudinal fluctuations that are due to diameter fluctuations. Particularly for Fibre1, we can identify long-scale sinusoidal variations of about 8 MHz with a half-period of the strain induced by the fibre coiling, as a half of the fibre length is coiled on the other half. This is easily confirmed by inverting the input and output in the measurement system. On the other hand, the short-scale longitudinal fluctuation seen in Figure5-7 (a) (about 5±1 MHz every 2 m) indicates a random geometric variation of the air-hole microstructure. By analyzing the observation, it cannot be attributed to the influence of birefringence in the PCF, since the variation on the refractive index can be estimated to $7x10^{-4}$ (using Eq. 2.24) which is well above the birefringence of the PCF (estimated phase birefringence by simulation: $\approx 1.5x10^{-5}$, measured group birefringence $\approx 5x10^{-6}$).

Figure5-7 (b) shows a 5 MHz shift in Brillouin frequency shift for Fibre 2 between 80 m and 180 m which corresponds to one layer of the fibre coil. Therefore, we are able to detect the strain applied to one layer. The short-scale fluctuation is smaller (3±1 MHz, every 2-3 m of the fibre) and can be attributed to geometrical fluctuations of the air-hole microstructure. Of the foregoing, we can say that the longitudinal fluctuations in Brillouin frequency shift are less significant for Fibre 2 than for Fibre 1 as the drawing process was better controlled in the former. This is verified by studying the fast Fourier transform of the Brillouin frequency shift trace shown in the insets of Figure 5-7. We notice that for Fibre 1, the frequencies pedestal around the main peak is wider than for Fibre 2.

In order to obtain an estimation of the diameter or microstructure fluctuations along the fibres, the distributed effective refractive index n_{eff} from the distributed Brillouin frequency shift have been derived using two assumptions:

(i) The main contributions to these fluctuations are due to homothetic variations of the microstructure (i.e. to fluctuations of the outer diameter only).

(ii) Possible longitudinal in-homogeneities of individual air holes or pitch, as well as possible twists induced during the drawing process have been neglected.

The variation of the effective refractive index can therefore be due to different causes: applied strain, temperature variation, longitudinal variations of the microstructure, individual air hole in-

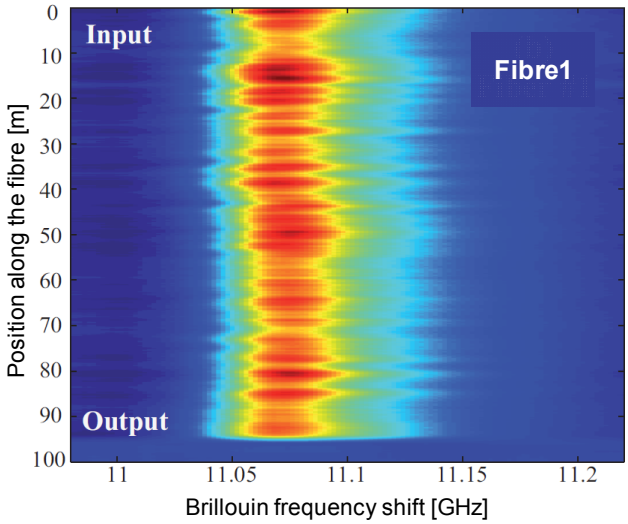

Figure 5-6: 2 D distribution of Brillouin gain along along the 100 m PCF fibre. The spatial resolution and the frequency resolution are respectively 30 cm and 2 MHz.

homogeneities or variation of the pitch. Considering that the temperature does not influence the experiment because of the short experiment duration, the impact of strain was observed in long-scale fluctuations which indicate the effect of the fibre coiling. Moreover, the variation of the pitch has an important impact on the effective refractive index [14].

However, several SEM-images at different sections of the fibres show that there is no measurable variation of the pitch and singular air holes. From numerical simulation and numerical software (Comsol), it was found that the variation of the microstructure scale is the main cause of the variation of the effective refractive index. Thus the scale of the microstructure has been varied since this seemed to be the most general variation. To relate geometrical variations to n_{eff}, the dependency of n_{eff} on the microstructure scale has been computed by using the PCF cross-section of the two two fibres via Comsol software. A simulation based on the original image (corresponding to 100%) provides a certain value for n_{eff} (1.434 for Fibre 2 and 1.432 for Fibre 1). By varying the scale of the original SEM-image, different n_{eff} were obtained. We have computed the local derivation of the obtained relation between n_{eff} and the geometrical scale around 100%. We found that the effective refractive index changes by 2.2 $\text{x}10^{-4}$ (Fibre 1) and 2.0x 10^{-4} (Fibre 2) for 1% diameter change, when compared to the fluctuations of the effective refractive index in the fibres using the Brillouin frequency shift formula (Eq. 2.22). The variation of the short-scale fluctuations (5±1 MHz for Fibre 1 and 3±1 MHz for Fibre 2) corresponds respectively to 2.9±0.6% and 1.9±0.6% of scale or diameter fluctuations. The large-scale variation is 4.7% (8 MHz for fibre1)

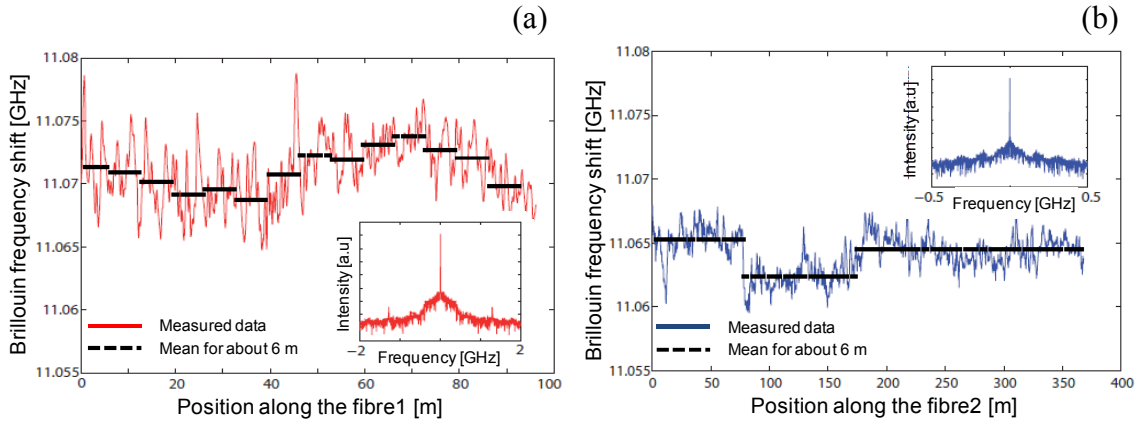

Figure 5-7: Mapping of the Brillouin frequency shift along the a) Fibre 1 and b) Fibre 2 showing the effect of in-homogeneities and strain. The insets show the Fourier transforms.

and 3.2% (5 MHz for Fibre 2). This means that the maximum core diameter fluctuation is 5.5±0.3 µm (Fibre 1) and 5.5±0.2 µm (Fibre 2).

Since polarization and strain can influence the variation of the effective refractive index the contribution of the structure size is expected to be below these values. This estimation confirms the higher quality of the drawing process obtained for fibre2. Note that the fluctuations measured in the present work are in good agreement with the specifications from state-of-the-art PCF manufacturers [11, 15].

Table 5-2: Summary of the PCF fibres' retrieved characteristics

Fibre parameters	**Fibre 1**	**Fibre 2**
Fibre length	100 m	400 m
Short-scale fluctuations	5±1 MHz	3±1 MHz
Scale/ diameter fluctuations	2.9±0.6%	1.9±0.6%
Large-scale fluctuations	4.7% (8 MHz)	3.2% (5 MHz)
Core diameter	5.5±0.3 µm	5.5±0.2 µm

5.3 Acoustic life-time and Brillouin spectrum measurement in Photonic crystal fibres using BEDS

From Section 5.2.2, it turned out that the Brillouin gain exhibits large- and short-scale fluctuations and some long-scale fluctuations are due to the effect of structural irregularities.

Using the BEDS technique, it was also possible to observe (using the set-up described in Figure 4-8) at the fibre output end a damping of the scattered signal which was different to the acoustic phonon lifetime t_A. The effect of the second echo appears in Figure 5-8 (b) because of the damping of the acoustic wave as explained in Chapter 4. Nevertheless, an asymmetric Brillouin spectrum all along the fibre, with a mean FWHM width of 50 MHz - larger than in SMF - can be observed. Figure 5 - 8(a) represents the Brillouin gain spectrum of Fibre 1 at a propagation distance of 85 m. The black curve in Figure 5-8 (b) represents the maximum Brillouin gain of the same fibre at its resonance frequency (11.059 GHz), the red line represents an exponential fit of the damping of the scattered wave. From the same figure the acoustic lifetime t_A is found to be equal to ~3.8°ns which is not directly linked to the 50 MHz line-width giving an acoustic lifetime of ~3.18 ns. However in a single mode fibre using the same approach, the measured line-width, 28 MHz, is intimately linked to the acoustic lifetime which was measured to be ~5.98 ns described in Section 2.2.1.4. This may prouve that there is more than one acoustic mode interplaying each other, so more than one Brillouin spectrum. These new characteristics mainly rely on the air-hole periodic microstructure which impacts on the acoustic modal distribution and leads to a strong coupling between the longitudinal and transverse acoustic modes. Since the width of the Brillouin spectrum is defined by the damping of the acoustic wave, this effect artificially modifies the acoustic lifetime at the Brillouin resonance. As a consequence, the Brillouin spectrum broadening may be linked to the superposition of different Lorentz shape with a line-width equal to the silica value. The distribution

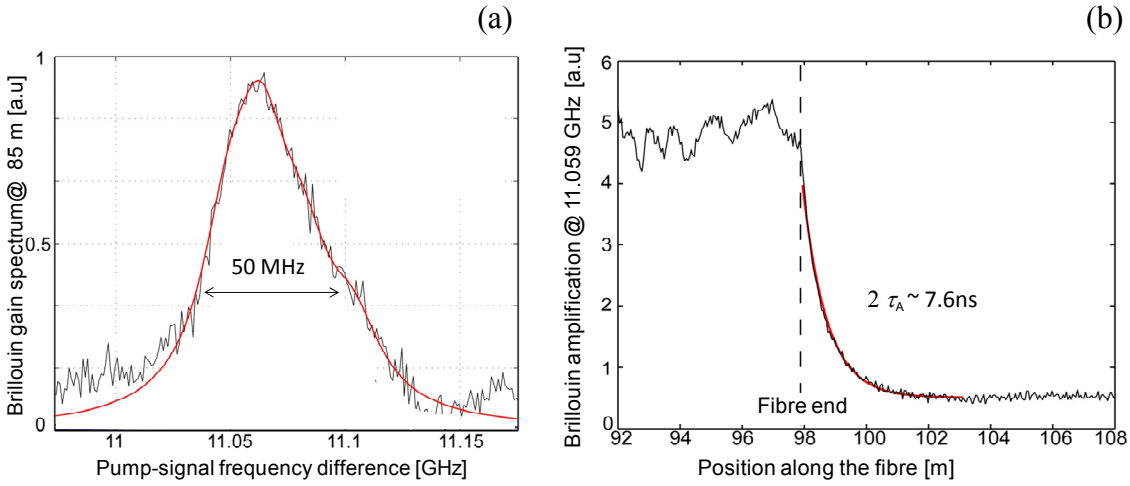

Figure 5-8: a) Brillouin gain spectrum at position distance of 85 m with a line-width of 50 MHz b) experimental Brillouin gain in the time domain at the fibre output end and at the peak gain frequency. The red line represents the exponential decay fit curve to estimate the acoustic lifetime. The set-up is described in Figure 4-8.

of the acoustic modes is related to the propagation waveguide characteristics due to the air-hole microstructure.

5.4 Conclusion

Throughout this chapter, we have seen the potential of the latest BEDS technology provide solutions in real contexts. Using the BEDS technology in landslide monitoring, the cable is itself both the structure and the strain gage, allowing for at least 20 measuring points per meter, without affecting the stiffness of the cable or the soil. For the first time it became possible to observe the failure propagation at the laboratory scale with an accurate precision. Furthermore, using BEDS we have proposed and demonstrated the possibility of mapping geometrical structure fluctuations along a photonic crystal fibre. We have been able to identify and quantify both long- and short-scale longitudinal fluctuations in the Brillouin frequency shift resulting respectively from residual strain due to fibre coiling and air-hole microstructure or diameter fluctuations. The homogeneity of two solid-core photonic crystal fibres drawn from the same preform, but with a different drawing process, has been investigated and the fluctuations logically found to be less important in the case of a fibre fabricated with a better process control. Our results finally demonstrate the great potential of the Brillouin echoes distributed sensing technique for small-scale optical fibre characterization. Moreover, these results show the need for characterization of structural irregularities in fibres before they can be used for distributed sensing. We have carried out a high spatial resolution distributed measurement of the Brillouin gain spectrum in a photonic crystal fibre. BEDS also allowed the direct experimental measurement of the acoustic phonon lifetime and the observation of Brillouin linewidth broadening. In this way BEDS, can help in the fundamental understanding of SBS and in the design of PCF in view of applications to optical-strain/temperature sensing.

Bibliography

[1] Inaudi D. and Vurpillot S., 1999. Monitoring of concrete bridges with long-gage fibre optic sensors. Journal of Intelligent Material Systems and Structures 10, 4:280–292.

[2] Measures R.. *Structural Monitoring with Fiber Optic Technology*. Academic Press, USA (2001).

[3] Niklès M., Ravet F., 2010. Depth and sensitivity. Nature Photonics, 4, 431-432.

[4] http://www.omnisens.ch/ditest/31-home.php

[5] http://www.ozoptics.com/products/fiber_optic_distributed.html

[6] http://www.yokogawa.com/

[7] Iten M., Puzrin A.M., Hauswirth D., Foaleng S. M., Beugnot J.C. and Thévenaz L., 2009. Study of a progressive failure in soil using BEDS. In Proceding of SPIE, 7503, 20th International Conference on Optical Fibre Sensors, Edinburgh, UK.

[8] Kaiser P.V., Astle H.W., 1974. Bell Syst. Technology Journal, 53, 1021–1039.

[9] Russel P. ST. J., 2007. Photonic Crystal Fibers: A Historical Account" IEEE LEOS Newsletter, 1-15.

[10] Russel P. ST. J., 2010. Photonic Crystal Fibres in Sensing and Metrology. OSA/SENSORS, STuA1-A2.

[11] Crystal Fibres, http://www.nktphotonics.com/.

[12] Stiller B., Foaleng S. M., Beugnot J.-C., Lee M. W., Delqué M., Kudlinski A., Thévenaz L., Maillotte H. and Sylvestre T., 2010. Photonic crystal fiber mapping using Brillouin echoes distributed sensing. Optics Express, 18, 19:20136-20142.

[13] Beugnot J.-C., Stiller B., Foaleng S. M., Won Lee M., Delqué M., Kudlinski A., Maillotte H., Laude V., Thévenaz L. and Sylvestre T., 2010. Observation of Brillouin linewidth broadening in photonic crystal fiber. 36th European Conference and Exhibition on Optical Communication, pp. 1-3.

[14] Poletti F., Furusawa K., Yusoff Z., Broderick N. G. R., and Richardson D. J., 2007. Nonlinear tapered holey fibers with high stimulated Brillouin scattering threshold and controlled dispersion. JOSA B, 24, 9:2185–2194.

[15] Euser T. G., Chen J. S. Y., Scharrer M., Russell P. S. J., Farrer N. J., and Sadler P. J., 2008. Quantitative broadband chemical sensing in air-suspended solid-core fibers. Journal of Applied Physics 103, 10:103108–103108-7.

[16] Iten M. 2011. Novel Applications of (distributed) Fiber Optic Sensing in Geotechnical Engineering. Dissertation. ETH Zurich, Switzerland.

6 Optical sampling applied to optical distributed fibre sensors

As presented in the previous chapters, novel time domain fibre sensors show sub-metric spatial resolutions requiring a pulse width of 1 ns and shorter. The detection and acquisition stages must be adapted accordingly, resulting in a bandwidth (BW) of several GHz and a sampling rate of many Gigasample/s. This has of course a great impact on the cost of the system. The response and the noise in the detection stage also degrade proportionally to the BW, while the sensor response also decays linearly with decreasing pulse widths. In this chapter[10] we propose a technique developed to acquire fast optical signals using low frequency detection and acquisition. It is based on optical sampling that creates a replica of the fast signal on a much slower time scale by a strobe effect. The performance is illustrated by comparative measurements using a Brillouin high resolution distributed fibre sensor.

[10] This chapter is based on:
Foaleng S. M., Beugnot J-C. and Thévenaz L. (2009). Optical sampling technique applied to high resolution distributed fibre sensors. Proc.OFS20, SPIE 7503, 750369-4.

6.1 Background

As presented in the previous chapters, a substantial effort has been made for developing distributed fibre sensors, working towards longer range and better spatial resolution. As already known, in classical time-domain techniques the spatial resolution is given by the temporal width τ_1 of the pulse activating the measuring process. As a result of the group velocity in an optical fibre, a 1 m spatial resolution corresponds to a 10 ns pulse width. The detection stage must offer a sufficient bandwidth (BW) to resolve a transition that will span over a minimum distance given by the pulse width. A traditional relationship from signal theory fixes the minimum bandwidth necessary to resolve the pulse as BW = $0.35/\tau_1$, so that a 1 m spatial resolution requires at least a 350 MHz bandwidth in the detection stage. Identically, the data acquisition requires a minimum sampling rate to resolve all changes in the signal activated by the pulse and returned from the fibre to the detector. The Nyquist-Shannon theorem provides the condition that the sampling rate fs must be at least equal to twice the maximum frequency contained in the signal, thus f_s = 2 BW = $0.7/\tau_1$. A 1 m spatial resolution will thus requires a minimum sampling rate f_s = 0.07 Gigasample/s in the acquisition stage. For recently novel configurations showing submetric spatial resolutions, pulse duration shorter than 1 ns is used. The detection and acquisition stages must be adapted accordingly, resulting in a bandwidth of several GHz and a sampling rate of many Gigasample/s. This has of course a great impact on the cost of the system, since the needed devices required to enter in a superior category in terms of performances, with price multiplied by a very substantial factor. Even worse, the response and the noise energy of the detection stage also degrade proportionally to the bandwidth, while the sensor response also decays linearly with decreasing pulse widths. These combined effects make the SNR of the global sensor response depend on the pulse width as $\tau_1^{3/2}$ in identical experimental conditions.

To alleviate this problem we propose a technique that offers the possibility to detect and sample a signal covering a bandwidth of several GHz using an arbitrary low bandwidth detection stage and a low sampling rate acquisition card. The potential and the relevance of the technique are illustrated on a Brillouin optical time domain analyzing system (BOTDA), by comparing the response given by a classical direct detection and the optical sampling technique. The latter has been widely used in optical communication [3-5] for measuring the eye diagram, in pump-probe spectroscopy [6-7], in Fourier-transform infrared spectroscopy [8], and in electronic THz spectroscopy [9] for rapid data acquisition. To our knowledge, it is the first time that the optical sampling technique has been proposed in distributed fibre sensors.

6.2 Principle and theory

The principle of optical sampling can be found in many scientific contributions [3-10]. Here, we are going to describe the technique and focus on its adaptation to the distributed optical fibre sensing. Figure 6-1 depicts the principle of the optical sampling. The upper part of the figure shows an optical signal (which can be the temporal Brillouin gain signal) which can be for instance a repetitive signal with period T_1. Before detection this periodical signal passes through a fast optical gate that is opned with a periodicity T_2 chosen close but different to T_1. The gate is in off-sate most

of the time except for bried time intervals τ_2. If the width of the optical signal is much shorter than the typical duration of the optical signal τ_1, as shown in Figure 6-1, only a brief fraction of the optical signal is sliced out in the time domain. A sample of duration τ_2 is so sliced from the optical signal and is transmitted to the detector. Since the sample periodicity is slightly different to the signal period, a sample shifted in time is extracted at each signal period. After a low pass filtering a replica of the original signal is obtained on a multiplied time scale, in full similarity with a stroboscopic effect.

Let N be the number of time resolved points to extract from the signal in the time domain. The sampling period T_2 can be expressed as follows:

$$T_2 = T_1 + \frac{T_1}{N}, \tag{6.1}$$

This means that after each period T_1, the optical gate is time-shifted by T_1/N. If T_{acq} is the real time necessary to display the signal replica on the scope after sampling and acquire it, then $T_{acq} = N.T_1$ and N true signal periods are required to scan the entire signal. If the signal must be displayed and acquired only over a time window $T_e < T_1$ randomly positioned along the entire waveform, T_2 is expressed in this case as follows:

$$T_2 = T_1 + \frac{T_e}{N}, \tag{6.2}$$

The parameter T_1 is fixed by the total length L of the sensing fibre and is given by the following relation $T_1 > \frac{2L}{V_g}$, where V_g is the group velocity of the light in the fibre.

Fully sampling the signal over the analyzing window requires a burst of N sampling pulses and the repetition frequency f_B of the burst sequence must satisfy the condition $f_B \leq 1/T_{acq}$ to avoid any temporal superposition.

The proper setting of the sampling technique requires a special care, suggesting some comments and guidelines:

- The gate window τ_2 must be shorter than the activating pulse width τ to preserve the instrumental spatial resolution.
- The acquisition time T_{acq} depends on the fibre length L that fixes the signal repetition rate T_1, as in a classical detection scheme, but also on the number of sampling points N since T_{acq} =N.T_1.
- The low pass filtering must be low enough to smooth the response from the gating device, but large enough to observe a change at each sample step. These two competing conditions result in a strict value for the bandwidth of the detection stage that must be exactly $BW_{det} = 0.35/T_1$.

To give an example how the system must be properly set, the parameters selected for the illustrative measurements shown below were calculated as follow.

$L = 2.2\,\text{Km} \rightarrow T_1 = T_e = 25\,\mu\text{s} \rightarrow BW_{\text{det}} = 14\,\text{kHz}$ $N = 2500 \rightarrow T_2 = 25.010\,\mu\text{s}$; $T_{\text{acq}} = 62.5\,\text{ms}$; $f_B = 13\,\text{Hz}$

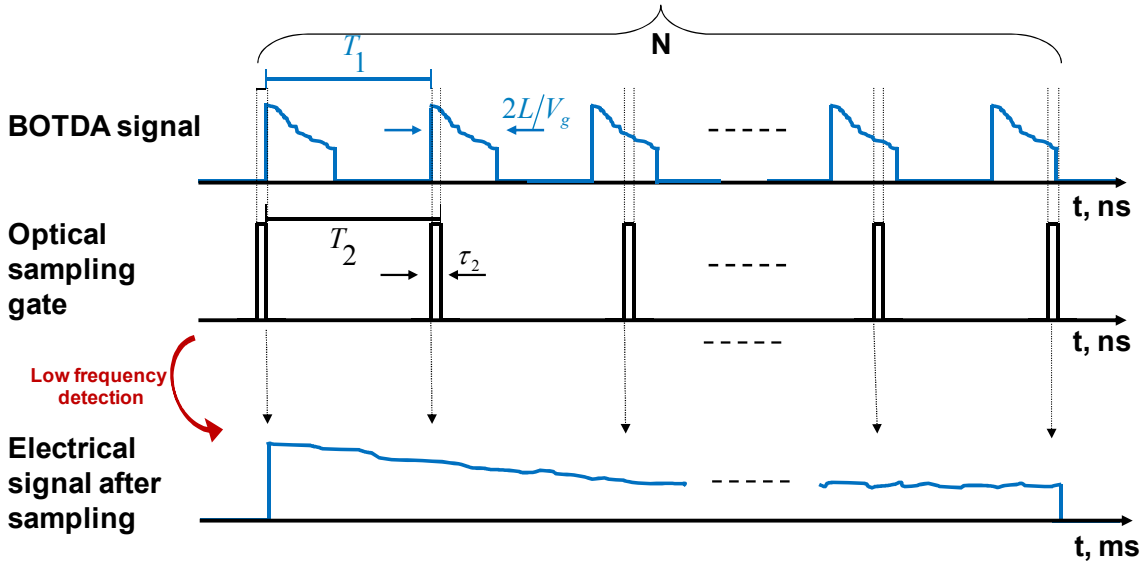

Figure 6-1: Set-up of generation of the optical sampling signal.

6.3 Experimental set-up

Figure 6-2 represents the experimental set-up used for demonstrating the potentiality of the optical sampling technique. The first box represents a classical time-of-flight distributed measurement system, in the present case a low noise BOTDA system described in detail in chapter 3 (Figure 3-10) was used. Generator-1 supplied the activating pump pulses of width τ_1. In the BOTDA system the pump pulse width τ_2. The second part describes the specific sampling configuration where a semiconductor optical amplifier (SOA) is used to create an optical gate driven by bursts of short electrical pulses (width τ_2) on its electrodes supplied by Generator-2. The gate window τ_2 was set to 8 ns which is the shortest pulse width supplied by Generator-2. Time jitter was minimized by using a 10 MHz master clock to drive both generators.

A low frequency detection stage was used to allow a high gain and low noise detection for the optical signal. The gain of the preamplifier was set, so that the bandwidth of the detection stage exactly matches the bandwidth required for the acquisition. The sampled and filtered signal is then visualized on a low frequency oscilloscope triggered by the master clock.

In the BOTDA system the pump pulse width τ_2 was set to 20 ns (2 m spatial resolution); therefore the 8 ns gate width τ_2 does not limit the spatial resolution. A special test fibre arrangement made of 2 m, 1 m and 0.5 m sections of G657B fibres placed in the middle of a 2.2 km G652D

fibre, as depicted in Figure 6-3, was analyzed. The Brillouin frequency of the short sections is shifted by 173 MHz compared to the rest of the fibre.

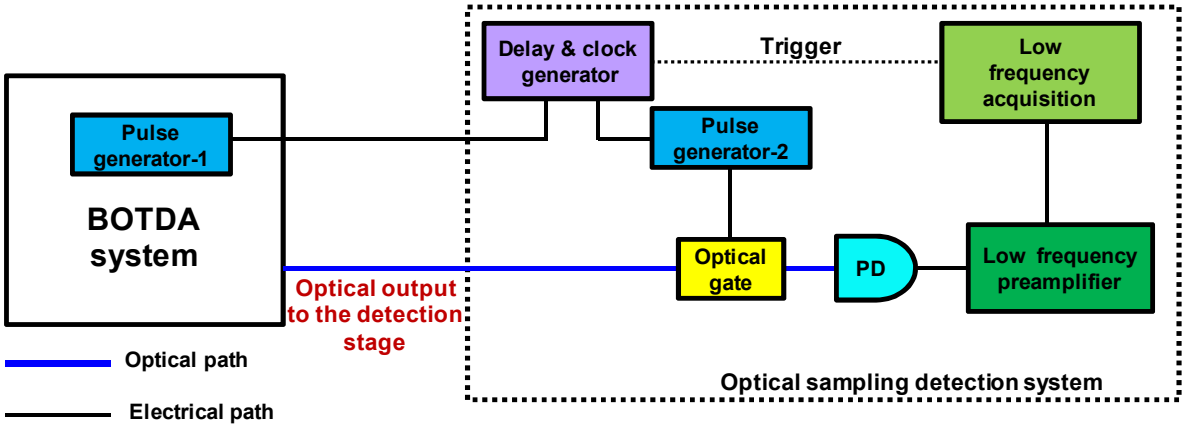

Figure 6-2: Complete set-up for optical sampling applied to distributed Brillouin sensing system. BOTDA: Brillouin time domain analysis.

6.4 Experimental results and discussion

A special test fibre arrangement made of 2m, 1m and 0.5m sections of G657B fibres placed in the middle of a 2.2km G652D fibre, as depicted in Figure 6-3, was analyzed. The Brillouin frequency of the short sections was shifted by 173MHz compared to the rest of the fibre. Figure 6-4 represents the 3D Brillouin gain distribution as a function of frequency and distance along the fibre. The measurement performed with a 2 m spatial resolution clearly shows the presence of the Brillouin frequency shifted segments. The 2 m section is fully resolved, while the 1 m and 0.5m sections are only partially resolved but still clearly detected. The time traces shown in Figure 6-5 (a) and (b) represent the detected local Brillouin gain measured at the resonance frequencies of the G657B fibre by respectively using a classical detection scheme and the optical sampling technique.

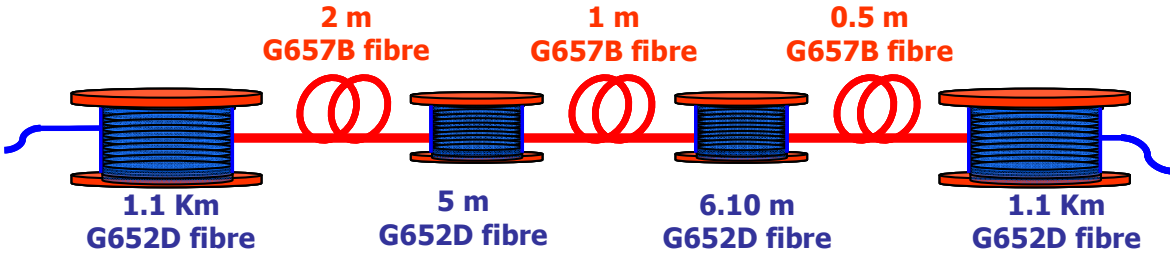

Figure 6-3: Fibre sensor arrangement used for the comparative tests. At a wavelength of 1557 nm the Brillouin resonance of the fibres is ν_B = 10.693 GHz for the G652D fibre and ν_B = 10.520 GHz for the G657B fibre.

The fluctuations observed in these two traces are due to the fact that SBS is inherently dependent on the polarization [12].

Figure 6-5 (a) is a Brillouin gain measurement performed by using a classical detection scheme using a 125°MHz bandwidth detector. The corresponding optical signal measured using the optical sampling technique (100°kHz), a low frequency detector and a low performance digital oscilloscope at the frequency resonance of the long segment fibre (10.693°GHz) is shown in Figure 6-5 (b). The fluctuations observed in the two traces are due to the fact that SBS is inherently dependent on the polarization [12]. The aspect of the two traces is very similar and the noise looks much better controlled in the case of the optical sampling.

To check the adequacy of the optical sampling technique with a complete Brillouin analysis and the possibility of measuring an arbitrary time window, measurements have been realized using the same test fibre by scanning the signal frequency around the Brillouin Stokes frequency of the two types of short section fibres (G657B) and by restricting the acquisition on a time window centered on the 2 m, 1 m and 0.5 m fibre segments. The time traces shown in Figure 6-6(a) and (b) represent the local Brillouin gain measured at the resonance frequencies in the G652D fibre. These measurements were performed by a classical detection scheme using a 125 MHz bandwidth detector (Figure 6-6(a) and the corresponding optical signal measured using the optical sampling technique with a low frequency detector (100°kHz) and a low performance digital oscilloscope (Figure 6-6(b)).

The aspect of the two traces is very similar. The time scale is expanded over more than 3 decades and the original time value can be easily retrieved from the relations given in section 2 by simply dividing the acquisition time scale by *N*. However, a critical point is the acquisition time that is clearly extended as a result of the time scale expansion. A simple inspection of the situation shows that the noise reduction results in a reduced number of averaging that exactly compensates the extra acquisition time when compared to the direct detection technique.

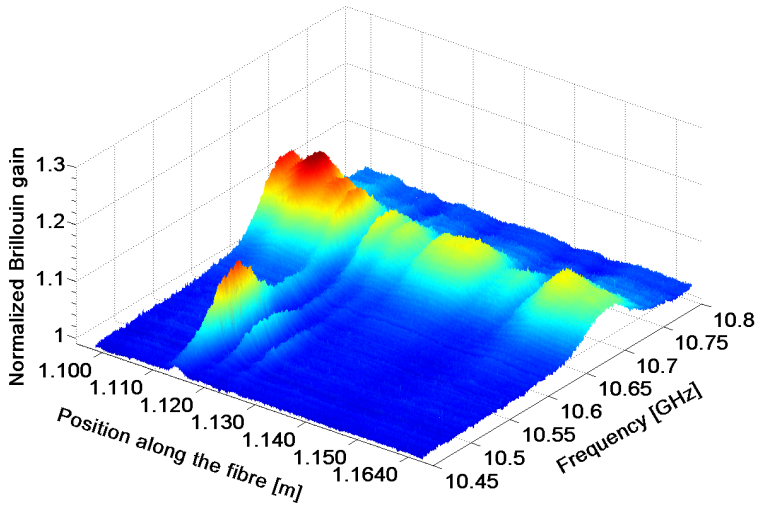

Figure 6-4: 3D plot of the distribution of the Brillouin gain of the central region of the fibre arrangement shown in Figure 6-3. The short segments made of distinct fibres are clearly visible. The acquisition is realized using the optical sampling technique with a 64 times averaging.

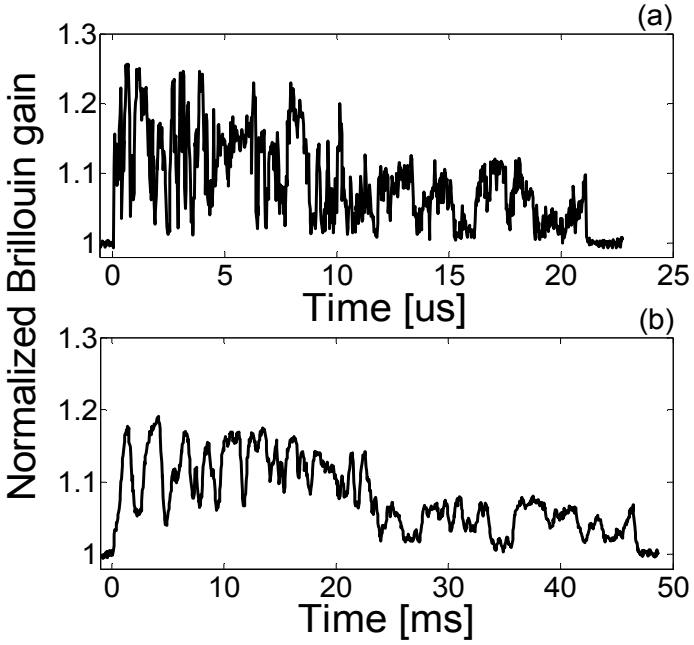

Figure 6-5: Brillouin gain as function of the position in the fibre at the frequency resonance of the long segment fibre (10.693 GHz) measured (a) using direct detection i.e. high frequency detector; (b) using the optical sampling technique and a low frequency detector.

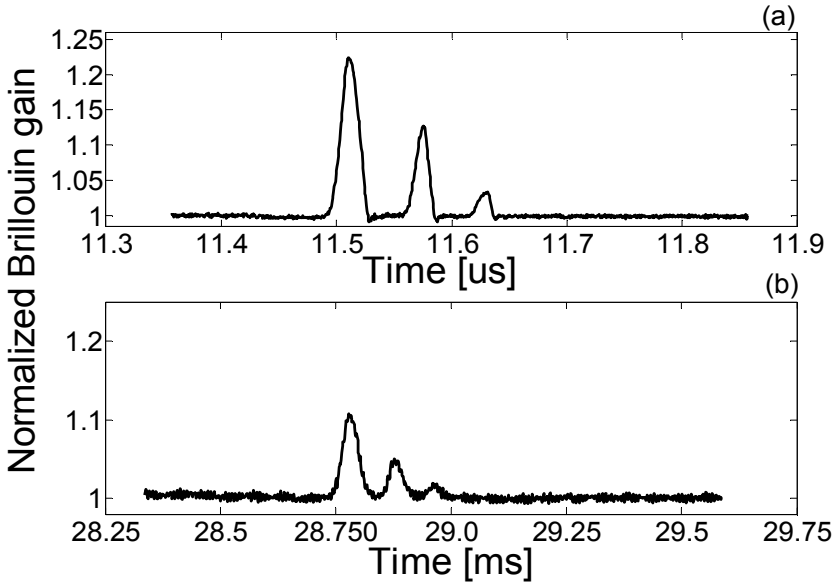

Figure 6-6: Brillouin gain as function of the position in the fibre at the frequency resonance of the small segment fibre (10.520GHz) measured (a) using direct detection, i.e. high frequency detector; and (b) the corresponding optical signal measured using the optical sampling technique and a low frequency detector with a 64 times averaging.

6.5 Conclusion

The possibility of using the optical sampling technique for distributed fibre measurements at high spatial resolution was the purpose of this chapter. This technique can offer an attractive solution to circumvent the problem of fast electronics that is not widely available, expensive and limited in performance in terms of sensitivity and noise. The only fast electronic device is the pulse generator that must be capable of generating pulses at the sampling resolution. The optical sampling technique offers the advantage of optimizing the bandwidth performance of the system, and consequently of maximizing the available gain in a given configuration. A rapid analysis of the technique shows that the effective electrical signal at the output of the detection stage is of similar amplitude for the direct and the sampling techniques: the amount of light on the detector is reduced by a factor equal to the duty cycle of the optical gating, but the gain on the pre-amplification stage can be raised in the same proportion as a result of the bandwidth reduction. It can thus be concluded that the optical sampling technique does not cause any impairment of performance if it is properly set up and brings the decisive benefit to improve the potential resolution of a distributed sensor without requiring an advanced instrumentation, however the jitter can be a big issue. Optical sampling offers an attractive solution for the next generation of high spatial resolution optical fibre sensors.

Bibliography

[1] Brown A. W., and Colpitts B. G., 2007. Dark-Pulse Brillouin optical Time-Domain Sensor with 20-mm Spatial Resolution. Journal of Lightwave Technology 25, 381-386.

[2] Foaleng S. M., Tur M., Beugnot J-C. and Thévenaz L. 2010. High spatial and spectral resolution long-range sensing using Brillouin echoes. . IEEE Journal Lightwave Technology, 28, 20:2993-3003.

[3] Li J., Hansryd J., Hedekvist P. O., Andrekson P. A., and Knudsen S. N., 2001. 300 Gbit/s eye-diagram measurement by optical sampling using fiber-based parametric amplification. IEEE Photonics Technology Letters 13, 987-989.

[4] Shirane M., Hashimoto Y., Yamada H., and Yokoyama H., 2000. A compact optical sampling measurement system using mode-locked laser-diode modules. IEEE Photonics Technology Letters 12, 1537-1539.

[5] Dorrer C., Kilper D. C., Stuart H. R., Raybon G., and Raymer M. G., 2003. Linear optical sampling. IEEE Photonics Technology Letters 15, 1746-1748.

[6] Elzinga P. A., Kneisler R. J., Lytle F. E., Jiang Y., King G. B., and Laurendeau N. M., 1987. Measurements of atomic sodium in flames by asynchronous optical sampling: theory and experiment. Applied Optics 26, 4303-4309.

[7] Takagi Y. and Adachi S., 1999. Subpicosecond optical sampling spectrometer using asynchronous tunable mode-locked lasers. Rev. Sci. Instrum. 70, 2218.

[8] Keilmann F., Gohle C., and Holzwarth R., 2004. Time-domain mid-infrared frequency-comb spectrometer. Optics Letters 29, 1542-1544.

[9] Van der Weide D. W., Murakowski J., and Keilmann F., 2000. Gas-Absorption Spectroscopy with Electronic Terahertz Techniques. IEEE Trans. Microwave Theory Technology MTT-48, 740-743.

[10] Foaleng S. M., Beugnot J-C. and Thévenaz L., 2009. Optical sampling technique applied to high resolution distributed fibre sensors. In Proceding SPIE 7503, 750369-4.

[11] Diaz S., Foaleng S. M., Lopez-Amo M., and Thevenaz L., July (2008) "A High-Performance Optical Time-Domain Brillouin Distributed Fiber Sensor," IEEE Sensors Journal 8, 1268-1272.

[12] Thévenaz L., Foaleng S. M. and Niklès M., 2007. Fast measurement of local PMD with high spatial resolution using stimulated Brillouin scattering. In Proceding ECOC'07, 10.1.2.

7 Conclusion

«Ce qui est simple est toujours faux, mais ce qui ne l'est pas est inapplicable»
PAUL VALÉRY, 1942

By proposing an interesting approach to solve the problem of the spatial resolution in distributed Brillouin sensors, this thesis has resulted in a number of contributions that may help to better understand the Brillouin sensor and to build a better set-up. Moreover, throughout this work, we have pointed out the problems and propose solutions to resolve the raised questions. In this chapter we will summarize the work presented in previous chapters, discuss the overall significance of our findings and how they can inspire the future technology.

7.1 Original contributions

The distributed optical fibre sensor based on the properties of Brillouin scattering is the central object of this thesis.

A full development of a groundbreaking technique in optical fibre sensors has been performed, designated as "Brillouin Echo Distributed Sensing (BEDS)", making possible continuously distributed measurements with a high spatial resolution (down to 5cm) over a long distance (5 km), representing 100'000 resolved points has been performed.

The key of the entire idea resides in the exploitation of the inertial behaviour of the acoustic wave in the optical fibre with respect to the optical wave in an optimized configuration, using π-phase pump pulses. This has made possible to break the trade-off between the spatial resolution and the measurand accuracy related to the effective Brillouin linewidth. This not only represents an innovative approach, but also brings significant improvements in terms of spatial resolution, dynamic and distance range in the Brillouin sensing systems.

Modelling and experimental demonstration have lead to the evidence that non-linear effects as pump depletion due to SBS, modulation instability and Raman scattering are the most limiting phenomena on the performances of the Brillouin Sensors.

7.1.1 Brillouin sensor and its limitations

We have first investigated the limitations to the classical Brillouin sensor. When intense pump pulses propagate along the fibre, however, the optical signals can be seriously degraded by several nonlinear interactions occurring within the fibre. The most critical nonlinear effects are those in which the background noise is amplified while co-propagating with the pump pulse such as pump depletion due to stimulated Brillouin scattering, the self-phase modulation (SPM), the modulation instability (MI), which occurs only in fibres presenting an anomalous dispersion at the pump wavelength, and Raman scattering (RS).

- For the effect of pump depletion we have pushed the modeling to obtain analytical expressions that are useful for the proper design of a BOTDA sensor and for the determination of its immunity to depletion. This model is informative on the conditions maximizing the depletion effect; therefore a standard configuration can be defined to control the depletion according to the chosen configuration (one sideband or two sidebands CW signal), made of a long uniform fibre having a length equivalent to the claimed range. The Brillouin frequency at the far end of this fibre is shifted by locally modifying the temperature or the applied strain over a short section, albeit longer than the spatial resolution. The amount of shift must be $\delta\nu=\Delta\nu/4$ and the measured Brillouin shift must correspond to the real value that can be obtained by measuring the short segment only. A common accuracy claimed in most reports and commercialized instruments are 1 MHz on the peak gain frequency. A CW signal power must not exceed 95 μW (-10.2 dBm) to ensure that the depletion never exceeds 14% in a very long fibre ($L > L_{eff}$ =20 km). This value is fairly low and is actually far from being proved to be met in the vast majority of publications and commercial instruments. They are thus all potentially subject to biasing errors related to depletion, errors that are only rarely observed since the worst case situation is very unlikely to occur in real conditions. Experimental and theoretical studies have shown that using one sideband as CW signal the

depletion does not depend on the pump power. The contrary effect is observed when two sidebands are used, however in this case the depletion is much smaller in the comparative situations.

- SPM-induced spectral broadening can have a significant effect on the effective gain linewidth measured by Brillouin sensors. Modeling and experiments have undoubtedly demonstrated that the effective gain linewidth can easily experience a two-fold increase in standard conditions when the pulse intensity profile is Gaussian. At power and spatial resolutions used in standard configurations, spectral broadening can be observed typically from a 5 km distance. Practically the problem can be circumvented by using a clean rectangular pulse with very sharp rising and falling edges.
- MI and forward RS in distributed BOTDA sensors systems are detrimental and have been evaluated experimentally and compared to a theoretical model giving a simplified expression to predict the critical power for a given distance range. In a practical sensor the critical distance must be longer than the actual fibre length and is bound by the nonlinear fibre length, fixing a maximum pump power. MI turns out to be the dominant nonlinear limitation since it shows the lowest critical power, but it can be avoided to a wide extent by using the fibre in the normal dispersion spectral region such as a DSF in the C-band. However, Raman scattering can be avoided only by limiting the optical pump power and therefore is the ultimate nonlinear limitation in a distributed sensing system. Under similar conditions RS shows a critical power ~5 times larger than MI.

7.1.2 Toward high performances sensor: Brillouin Echoes

- A general analytical solution for Brillouin distributed sensing in optical fibres with sub-meter spatial resolution is obtained by solving the acoustical-optical coupled wave equations by a perturbation method. The Brillouin interaction of a triad of square pump pulses with a continuous signal is described, covering a wide range of pumping schemes. The model predicts how the acoustic wave, the signal amplitude and the optical gain spectral profile depend upon the pumping scheme. Sub-meter spatial resolution is demonstrated for bright-, dark- and π-shifted interrogating pump pulses, together with disturbing echo effects, and the results compare favorly with experimental data. This analytical solution is an excellent tool not only for optimizing the pumping scheme but also in post-processing the measured data to remove resolution degrading features.
- Brillouin echo distributed sensing (BEDS) has proved to be a powerful solution to realize sub-metric spatial resolutions in Brillouin distributed measurements. An optimized configuration, using π-phase pump pulses, was experimentally tested down to a spatial resolution of 5 cm, with a clear margin for further improvement down to a real centimetric spatial resolution. This optimized configuration will produce the best contrast independently of the pulse intensity, with a factor 2 of improvement compared to other techniques based on the same approach (dark pulse, bright pulse). This extends the dynamic range by 3 dB, which corresponds in standard loss conditions to a 5 km extension of the sensing range.
- Major difficulties are related to the restoring of the acoustic wave which manifests itself as a secondary trailing echo in the response. During about 10 years specialists did not define strategies to suppress this secondary echo. However a clean explanation gave by us in chapter 4 has allowed understanding the physics behind, suppress it and find a clever way to increase the

performances of the sensor. This was successfully done by using our differential gain approach or a high pass numerical filter proposed in chapter 4. This has limited excessive pump depletion and made it possible to extend the range -with 5 cm spatial resolution - up to 5 km limited by the instrumentation and non-linear effects (which was limited to much less than 1 km using a continuous pump or a de-convolution method). This corresponds to 100,000 independent resolved points along the fibre and a range extension to 10 km looks perfectly feasible, so that a system with one million resolved points along a standard single mode fibre is likely to be proposed in the near future. A techniques as dynamic grating has allowed spatial resolution down to 1 cm but requires special polarization maintaining optical fibres. In addition, for practical point of view users will prefer standard optical fibre for economical reasons and availability. In all cases distributed measurements in optical fibre with spatial resolution below 3 cm becomes meaningless since the heat naturally propagates over ~3 cm in optical fibre. It appears that BEDS systems can become a key and powerful configuration for the next generation of Brillouin fibre distributed sensors, combining simplicity in the hardware implementation, kilometric sensing ranges and centimetric spatial resolution, with a temperature/strain resolution unchanged when compared to a classical BOTDA system, as summarized in the table here after.

Technology	**BOTDR**	**BOTDA**	**BOFDA**	**BOCDA/ BOCDR**	**BEDS**
Meaning	**Brillouin Optical Time Domain Reflectometry**	**Brillouin Optical Time Domain Analysis**	**Brillouin Optical Frequency Domain Analysis**	**Brillouin Optical Correlation Domain Analysis/ Reflectometry**	**Brillouin Echo Distributed Sensing**
Accuracy	20 με to 40 με	20 με to 10 με	20 με to 40 με	60 με/100 με	10 με to 20 με
Spatial resolution	**1 m**	**1 m**	**2 m**	**1.6 mm/13 mm**	**0.05m**
Range [km]	30 km	30 km	5 km	5 m/7.6 m	Up to 5 km with 5 cm
Availability	**Commercialized**	**Commercialized**	**Laboratory prototype**	**Laboratory prototype**	**Laboratory prototype**
Propriety	One fibre end	Loop required	Loop required	Loop required/ one fibre end	Loop required

- The potentialities of BEDS technology provide solutions in real contexts. Using the BEDS technology in landslide monitoring, the cable is itself both the structure and the strain gage, allowing for at least 20 measuring resolved points per meter. For the first time it became possible to observe the failure propagation at the laboratory scale with an accurate precision. Furthermore, using BEDS we have proposed and demonstrated the possibility of mapping geometrical structure fluctuations along a photonic crystal fibre and get an accurate estimation of the microstructure longitudinal fluctuations. The homogeneity of two solid-core photonic crystal fibres drawn from the same perform, but with a different drawing process, has been investigated and the fluctuations logically found to be less important in the case of a fibre fabricated with a better process control. This demonstrates the great potential of the Brillouin echoes distributed sensing technique for small-scale optical fibre characterization and show the need for characterization of structural irregularities in fibres before they can be used for distributed sensing. The reported observation of Brillouin linewidth broadening of a PCF fibre can help in the fundamental understanding of SBS in PCF and design them in view of applications to optical-strain/temperature sensing.

7.1.3 Outlook and future directions

For the future research on Brillouin sensor my vision is that the challenge remains opened upon very long detection distances since we now know that the major factor that limiting the detection distance is not necessarily the linear loss in the optical fibre, but rather non-linear effects such as pump depletion due to SBS itself, SPM, MI (that we know how to control and overpass from the previous section), and finally RS. This later is very critical since for the moment it is very difficult to overcome it. Techniques such as pump pulse coding or the technical transparency of the fibre have been recently developed precisely to bypass the use of high pump powers. Another solution could be a design of a special optical fibre to completely avoid non-linear effects.

Appendix

In this appendix we give the details' derivation of the three coupled SBS equations presented in Chapter 2 following by the details of the analytic calculations leading to the general solution of a time-domain pump pulse coding used in Chapter 4.

A Derivation of the three coupled waves equations

- **Slowly varying envelopes approximations (SVEA):**

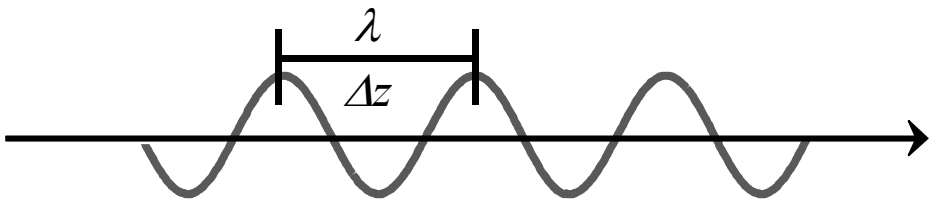

Let us consider A the complex envelope of an electric field $\vec{E}$ such as:

$$\vec{E}=A(z,t)\exp\left[j(\omega t+kz)\right]+c.c., \tag{A.1}$$

where ω and k are respectively the angular frequency and the wave vector of $\vec{E}$.

$A(z)$ slowly vary over the distance $\Delta z=\lambda$ as sketched in the figure above means: $\Delta A \ll A$ over the length $\Delta z \Leftrightarrow |\Delta A| << |A|$.

$$\text{By definition, } \Delta A=\left(\frac{\partial A}{\partial z}\right)\Delta z=\left(\frac{\partial A}{\partial z}\right)\lambda \quad \Rightarrow \left(\frac{\partial A}{\partial z}\right)=\left(\frac{\Delta A}{\lambda}\right)<<\left|\frac{A}{\lambda}\right|<|kA|$$
$$\Rightarrow \left(\frac{\partial A}{\partial z}\right)<<|kA|, \tag{A.2}$$

Of the forgoing, if A varies slightly over the distance λ, the first z derivative of A takes very small values in comparable units. Consequently, using Eq. (A.2) the second z derivative reads as:

$$\left|\frac{\partial^2 A}{\partial^2 z}\right| = \frac{\left|\frac{\partial A}{\partial z_1} - \frac{\partial A}{\partial z_2}\right|}{\Delta z} < \frac{\left|\frac{\partial A}{\partial z_1}\right| + \left|\frac{\partial A}{\partial z_2}\right|}{\Delta z} \simeq \frac{2\left|\frac{\partial A}{\partial z}\right|}{\lambda} << k^2 |A|, \tag{A.3}$$

then driving to the slowly varying envelopes approximations (SVEA) expression,

$$\left|\frac{\partial^2 A}{\partial^2 z}\right| << k^2 |A|. \tag{A.4}$$

Let us consider the first derivative of E which reads as:

$$\frac{\partial \vec{E}}{\partial z} = \frac{1}{2}\left[\frac{\partial A}{\partial z} e^{i(\omega t + kz)} + ikAe^{i(\omega t + kz)}\right], \tag{A.5}$$

The second derivative of E reads as:

$$\begin{aligned}\frac{\partial^2 \vec{E}_p}{\partial^2 z} &= \frac{1}{2}\left[\frac{\partial^2 A_p}{\partial^2 z} e^{i(\omega_p t + k_p z)} + ik_p \frac{\partial A_p}{\partial z} e^{i(\omega_p t + k_p z)} + ik_p \frac{\partial A_p}{\partial z} e^{i(\omega_p t + k_p z)} + i^2 k_p^2 A_p e^{i(\omega_p t + k_p z)}\right] \\ &= \frac{1}{2}\left[\frac{\partial^2 A_p}{\partial^2 z} e^{i(\omega_p t + k_p z)} + 2ik_p \frac{\partial A_p}{\partial z} e^{i(\omega_p t + k_p z)} - k_p^2 A_p e^{i(\omega_p t + k_p z)}\right]\end{aligned}, \tag{A.6}$$

By applying the SVEA, Eq.(A.6) can be rearranged and becomes simply:

$$\frac{\partial^2 \vec{E}_p}{\partial^2 z} \overset{\text{SVEA}}{=} ik_p \frac{\partial A_p}{\partial z} e^{i(\omega_p t + k_p z)} - \frac{1}{2} k_p^2 A_p e^{i(\omega_p t + k_p z)}, \tag{A.7}$$

Now let us consider the two optical waves $\vec{E}_p$ and $\vec{E}_s$ and the acoustic wave $\vec{\rho}$ (which orientations is described in Figure above (representing the orientation of the wave vectors involved in stimulated Brillouin scattering in optical fibre) involved in the SBS process as described in Eqs (A.8) as:

$$\vec{E}_p = e_p A_p(z,t)\exp\left[j\left(\omega_p t + k_p z\right)\right] + c.c., \tag{A.8.a}$$

$$\vec{E}_s = e_s A_s(z,t)\exp\left[j\left(\omega_s t - k_s z\right)\right] + c.c. \tag{A.8.b}$$

$$\Delta\vec{\rho} = Q(z,t)e^{i(\Omega t + qz)} + cc \tag{A.8.c}$$

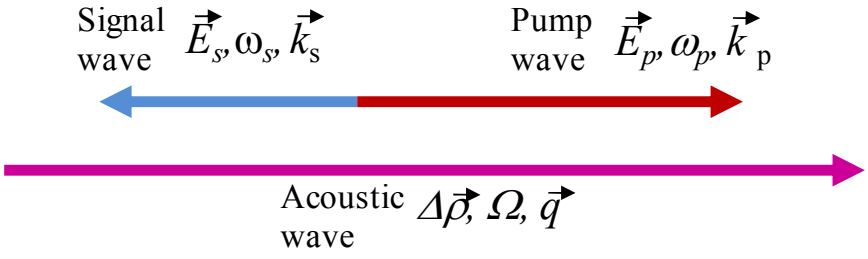

where e_p and e_s are respectively the unit polarization vectors for the pump and the signal waves. A_p and A_s and Q are respectively the complex envelopes of the pump, signal and acoustic waves. Their wave vectors are defined as: $\vec{q}=\vec{k}_p-\vec{k}_s$. Theirs wave numbers are defined as $q=|\vec{q}|=|\vec{k}_p|+|\vec{k}_s|-2|\vec{k}_p||\vec{k}_s|\cos\left[\left(\widehat{|\vec{k}_p||\vec{k}_s|}\right)/2\right]=|\vec{k}_p|+|\vec{k}_s|=k_p+k_s$ at the Brillouin resonance when $\Omega=\omega_p-\omega_s=\Omega_B$. The propagation of the three waves is given by the following equations [2]:

$$\nabla^2\vec{E}_p-\frac{n^2}{c^2}\frac{\partial^2\vec{E}_p}{\partial t^2}=\mu_o\frac{\partial^2\vec{P}_{NL,p}}{\partial t^2}, \tag{A.9.a}$$

$$\nabla^2\vec{E}_s-\frac{n^2}{c^2}\frac{\partial^2\vec{E}_s}{\partial t^2}=\mu_o\frac{\partial^2\vec{P}_{NL,s}}{\partial t^2}, \tag{A.9.b}$$

$$\frac{\partial^2\Delta\vec{\rho}}{\partial t^2}-\Gamma'\nabla^2\frac{\partial\Delta\vec{\rho}}{\partial t}-V_a^2\nabla^2\Delta\vec{\rho}=-\nabla.\vec{F}, \tag{A.9.c}$$

where c/n and V_a are respectively the speed of light and the acoustic wave in the optical fibre. Γ' is the acoustic damping time related to the acoustic damping parameter by $\Gamma'=q^2\Gamma_B$. P_{NL} is the non linear part of the polarizations of the pump and the signal. $\nabla.\vec{F}$ is the divergence of the electrostrictive for $\vec{F}=\nabla P_{st}$ with $P_{st}=-\gamma\left(\langle\vec{E}_{total}^2\rangle/8\pi\right)=-\gamma_e\left[\langle\left(\vec{E}_p+\vec{E}_s\rangle\right)^2/8\pi\right]$.

We begin with the equation driving the excitation of the acoustic field (Eq. (A.9.c)).

- ✓ We first solve the right-hand component.

$$\begin{aligned}\nabla\vec{F}&=\left(\frac{\partial}{\partial x}+\frac{\partial}{\partial y}+\frac{\partial}{\partial z}\right)\vec{F}=\nabla\left(\nabla p_{st}\right)\\&=\left(\frac{\partial^2}{\partial x^2}+\frac{\partial^2}{\partial y^2}+\frac{\partial^2}{\partial z^2}\right)p_{st}=\frac{\partial^2}{\partial z^2}\left[-\gamma_e\frac{\langle\left(\vec{E}_p+\vec{E}_s\right)^2\rangle}{8\pi}\right],\\&=\frac{-\gamma_e}{8\pi}\frac{\partial^2\langle\left(\vec{E}_p+\vec{E}_s\right)^2\rangle}{\partial z^2}\end{aligned} \tag{A.10}$$

Since

$$\begin{aligned}E_{tot}^2&=\left[\frac{1}{2}A_pe^{i(\omega_pt+k_pz)}+\frac{1}{2}A_se^{i(\omega_st-k_sz)}\right]^2\\&=\frac{1}{4}A_p^2e^{i2(\omega_pt+k_pz)}+\frac{1}{4}A_s^2e^{i2(\omega_st-k_sz)}+\frac{1}{2}A_pA_se^{i(\omega_p+\omega_s)t+(k_p-k_s)z},\\&=\frac{1}{4}A_p^2e^{i2(\omega_pt+k_pz)}+\frac{1}{4}A_s^2e^{i2(\omega_st-k_pz)}+\frac{1}{2}A_pA_s^*e^{i\underbrace{(\omega_p-\omega_s)}_{\Omega}t+(\underbrace{k_p+k_s}_{q})z}\end{aligned} \tag{A.11}$$

$$\frac{\partial E_{tot}^2}{\partial z}=\frac{1}{4}\left[\frac{\partial A_p^2}{\partial z}e^{i2(\omega_p t+k_p z)}+2k_p iA_p^2 e^{i2(\omega_s t+k_p z)}+\frac{\partial A_s^2}{\partial z}e^{i2(\omega_p t-k_p z)}-2ik_s A_s^2 e^{i2(\omega_s t-k_s z)}\right]$$
$$+\frac{1}{2}\left[\frac{\partial A_p}{\partial z}A_s^* e^{i(\Omega t+qz)}+\frac{\partial A_s^*}{\partial z}A_p e^{i(\Omega t+qz)}+i(k_p+k_z)A_p A_s^* e^{i(\Omega t+qz)}\right], \quad \text{(A.12)}$$

Since for $2\Omega_B$ frequency, there is no excitation, all terms at that frequency can be ignored.

$$\frac{\partial^2 E_{tot}^2}{\partial z^2}=\frac{1}{2}\left[\frac{\partial^2 A_p}{\partial z^2}A_s e^{i(\Omega t+qz)}+\frac{\partial A_s^*}{\partial z}\frac{\partial A_p}{\partial z}e^{i(\Omega t+qz)}+iqA_s^*\frac{\partial A_p}{\partial z}e^{i(\Omega t+qz)}\right]$$
$$+\frac{1}{2}\left[\frac{\partial^2 A_s^*}{\partial z^2}A_p e^{i(\Omega t+qz)}+\frac{\partial A_p}{\partial z}\frac{\partial A_s^*}{\partial z}e^{i(\Omega t+qz)}+iqA_p\frac{\partial A_s^*}{\partial z}e^{i(\Omega t+qz)}\right]$$
$$-\frac{1}{2}\left[q^2 A_p A_s^* e^{i(\Omega t+qz)}+iqA_s^*\frac{\partial A_p}{\partial z}e^{i(\Omega t+qz)}+iqA_p\frac{\partial A_s^*}{\partial z}e^{i(\Omega t+qz)}\right], \quad \text{(A.13)}$$
$$=-q^2 A_p A_s^* e^{i(\Omega t+qz)}+2iqA_s^*\frac{\partial A_p}{\partial z}e^{i(\Omega t+qz)}+2iqA_p\frac{\partial A_s^*}{\partial z}e^{i(\Omega t+qz)}+2\frac{\partial A_p}{\partial z}\frac{\partial A_s^*}{\partial z}e^{i(\Omega t+qz)}$$
$$\overset{SVEA}{=}-q^2 A_p A_s^* e^{i(\Omega t+qz)}$$

then,

$$\nabla\vec{F}=+\frac{\gamma_e q^2}{8\pi}A_p A_s^* e^{i(\Omega t+qz)}+c.c., \quad \text{(A.14)}$$

- ✓ First term of the left-hand component

$$\frac{\partial^2\Delta\vec{\rho}}{\partial t^2}=\frac{1}{2}\left[\frac{\partial^2 Q}{\partial t^2}e^{i(\Omega t+qz)}+i\Omega\frac{\partial Q}{\partial t}e^{i(\Omega t+qz)}+i\Omega\frac{\partial Q}{\partial t}e^{i(\Omega t+qz)}-\Omega^2 Qe^{i(\Omega t+qz)}\right], \quad \text{(A.15)}$$
$$\overset{SVEA}{=}i\Omega\frac{\partial Q}{\partial t}e^{i(\Omega t+qz)}-\frac{1}{2}\Omega^2 Qe^{i(\Omega t+qz)}$$

- ✓ Third term of the left-hand component

$$\frac{\partial^2\Delta\vec{\rho}}{\partial z^2}\overset{SVEA}{=}iq\frac{\partial Q}{\partial t}e^{i(\Omega t+qz)}-\frac{1}{2}q^2 Qe^{i(\Omega t+qz)}, \quad \text{(A.16)}$$

- ✓ Second term of the left-hand component

$$\frac{\partial}{\partial t}\frac{\partial^2\Delta\vec{\rho}}{\partial z^2}=iq\frac{\partial}{\partial t}\frac{\partial Q}{\partial z}e^{i(\Omega t+qz)}-q^2\Omega\frac{\partial Q}{\partial z}e^{i(\Omega t+qz)}-\frac{1}{2}q^2\frac{\partial Q}{\partial t}e^{i(\Omega t+qz)}-\frac{1}{2}iq^2\Omega Qe^{i(\Omega t+qz)}$$
$$\overset{SVEA}{=}-q\Omega\frac{\partial Q}{\partial z}e^{i(\Omega t+qz)}-\frac{1}{2}q^2\frac{\partial Q}{\partial t}e^{i(\Omega t+qz)}-\frac{1}{2}iq^2\Omega Qe^{i(\Omega t+qz)}+iq\frac{\partial}{\partial t}\frac{\partial Q}{\partial z}e^{i(\Omega t+qz)}, \quad \text{(A.17)}$$

Finally inserting Eqs. A.14, A.15, A.16 and A.17 in Eq. (9.c), we obtain:

$$i\Omega\frac{\partial Q}{\partial t}-\frac{1}{2}\Omega^2 Q-\Gamma'\left(iq\frac{\partial}{\partial t}\frac{\partial Q}{\partial z}-q\Omega\frac{\partial Q}{\partial z}-\frac{1}{2}q^2\frac{\partial Q}{\partial t}-\frac{1}{2}iq^2\Omega Q\right)-V_a^2\left(iq\frac{\partial Q}{\partial z}-\frac{1}{2}q^2 Q\right)=\frac{\gamma_e q^2}{8\pi}A_p A_s^* \tag{A.18}$$

$\Leftrightarrow$

$$i\Omega\frac{\partial Q}{\partial t}-iV_a^2 q\frac{\partial Q}{\partial z}+\frac{1}{2}\left(\Omega_B^2-\Omega^2-i\Gamma_B\Omega\right)Q=\frac{\gamma_e q^2}{8\pi}A_p A_s^*, \tag{A.19}$$

Rearranging Eq we obatain:

$$\begin{gathered}\frac{\partial Q(z,t)}{\partial z}+\frac{\partial Q(z,t)}{\partial t}+\Gamma_A Q(z,t)=ig_1 A_p(z,t)A_s^*(z,t);\\ \Gamma_A=i\frac{\Omega_B^2-\Omega^2-i\Omega\Gamma_B}{2\Omega},\ g_1=\frac{\gamma_e q^2}{8\Omega\pi}\end{gathered}, \tag{A.20}$$

Taking into account the quasi-static of the acoustic field during the interaction $V_a << c \Rightarrow \frac{\partial Q}{\partial z}=0$, we obtain the equation for the quasi-static acoustic wave:

$$\begin{gathered}\frac{\partial Q(z,t)}{\partial t}+\Gamma_A Q(z,t)=ig_1 A_p(z,t)A_s^*(z,t);\\ \Gamma_A=i\frac{\Omega_B^2-\Omega^2-i\Omega\Gamma_B}{2\Omega},\ g_1=\frac{\gamma_e q^2}{8\Omega\pi}\end{gathered}, \tag{A.21}$$

We follow with the equation driving the optical field (Eq. (9.a)): pump

- ✓ We first solve the right-hand component.

$$\begin{aligned}\vec{P}_{NL,p}&=\frac{\gamma}{4\pi Q_0}\frac{\partial^2\Delta\vec{\rho}\vec{E}_s}{\partial t^2}=\frac{\gamma}{16\pi Q_0}\left(Qe^{i(\Omega t+qz)}A_s e^{i(\omega_s t-k_s z)}\right)\\&=\frac{\gamma}{16\pi Q_0}QA_s e^{\overbrace{i(\Omega+\omega_s)}^{\omega_p}t}e^{\overbrace{i(q-k_s)}^{k_p}z}\end{aligned}, \tag{A.22}$$

then,

$$\frac{\partial^2 \vec{P}_{NL,p}}{\partial t^2} = \frac{\gamma}{16\pi Q_0}\left[\begin{array}{l} \frac{\partial^2 Q}{\partial t^2} A_s e^{i(\omega_p + k_p z)} + \frac{\partial A_s}{\partial t}\frac{\partial Q}{\partial t} e^{i(\omega_p + k_p z)} + i\omega_p A_s \frac{\partial Q}{\partial t} e^{i(\omega_p + k_p z)} \\ + \frac{\partial^2 A_s}{\partial t^2} Q e^{i(\omega_p + k_p z)} + \frac{\partial Q}{\partial t}\frac{\partial A_s}{\partial t} e^{i(\omega_p + k_p z)} + i\omega_p Q \frac{\partial A_s}{\partial t} e^{i(\omega_p + k_p z)} \\ + i\omega_p \frac{\partial Q}{\partial t} A_s e^{i(\omega_p + k_p z)} + i\omega_p Q \frac{\partial A_s}{\partial t} e^{i(\omega_p + k_p z)} - \omega_p^2 Q A_s e^{i(\omega_p + k_p z)} \end{array}\right]$$

$$\overset{SVEA}{=} \frac{\gamma}{16\pi Q_0}\left(2\frac{\partial A_s}{\partial t}\frac{\partial Q}{\partial t} e^{i(\omega_p + k_p z)} + 2i\omega_p A_s \frac{\partial Q}{\partial t} e^{i(\omega_p + k_p z)} + 2i\omega_p Q \frac{\partial A_s}{\partial t} e^{i(\omega_p + k_p z)} - \omega_p^2 Q A_s e^{i(\omega_p + k_p z)}\right) \tag{A.23}$$

✓ Left-hand components.

The left-hand components can be easily derived from Eq. (A.6):

$$\nabla^2 \vec{E}_p - \frac{n^2}{c^2}\frac{\partial^2 \vec{E}_p}{\partial t^2} = ik_p \frac{\partial A_p}{\partial z} e^{i(\omega_p t + k_p z)} - \frac{1}{2}k_p^2 A_p e^{i(\omega_p t + k_p z)} + \frac{n^2}{c^2}\left[i\omega_p \frac{\partial A_p}{\partial t} e^{i(\omega_p t + k_p z)} - \frac{1}{2}\omega_p^2 A_p e^{i(\omega_p t + k_p z)}\right]$$

$$= ik_p \frac{\partial A_p}{\partial z} e^{i(\omega_p t + k_p z)} + \frac{i\omega_p}{(c/n)^2}\frac{\partial A_p}{\partial t} e^{i(\omega_p t + k_p z)} \tag{A.24}$$

Finally by inserting Eq. (A.23) and Eq. (A.24) in Eq. (9.a), we obtain:

$$ik_p \frac{\partial A_p}{\partial z} e^{i(\omega_p t + k_p z)} + \frac{i\omega_p}{(c/n)^2}\frac{\partial A_p}{\partial t} e^{i(\omega_p t + k_p z)} = -\frac{\gamma}{8Q_0 c^2}\left(\omega_p^2 Q A_s e^{\overbrace{i(\Omega+\omega_s)t}^{\omega_p}} e^{\overbrace{i(q-k_s)z}^{k_p}}\right) \tag{A.25}$$

then,

$$k_p \frac{\partial A_p}{\partial z} + \frac{\omega_p}{(c/n)^2}\frac{\partial A_p}{\partial t} = \frac{i\gamma}{8Q_0 c^2} Q A_s\,, \tag{A.26}$$

then considering $k_p = 2\pi/\lambda_p$, we obtain the equation for the forward propagating pump:

$$\frac{\partial A_p}{\partial z} + \frac{n}{c}\frac{\partial A_p}{\partial t} = \frac{i\gamma\omega_p}{4Q_0 n c} Q A_s \tag{A.27}$$

We follow with the equation driving the optical field (Eq. A.9.b): signal

✓ We first solve the right-hand component.

$$\begin{aligned}\vec{P}_{NL,s} &= \frac{\gamma}{4\pi Q_0}\frac{\partial^2 \Delta\vec{\rho}^{*}\vec{E}_p}{\partial t^2} = \frac{\gamma}{16\pi Q_0}\left(Qe^{-i(\Omega t+qz)}A_s e^{i(\omega_p t+k_p z)}\right) \\ &= \frac{\gamma}{16\pi Q_0}Q^{*}A_s e^{\overbrace{i(\omega_p-\Omega)}^{\omega_s}t}\ e^{\overbrace{-i(q-k_s)}^{k_s}z}\end{aligned}, \tag{A.28}$$

then,

$$\frac{\partial^2 \vec{P}_{NL,p}}{\partial t^2} \overset{SVEA}{=} \frac{\gamma}{16\pi Q_0}\begin{pmatrix} 2\dfrac{\partial A_s}{\partial t}\dfrac{\partial Q^{*}}{\partial t}e^{i(\omega_p+k_p z)} + 2i\omega_p A_s\dfrac{\partial Q^{*}}{\partial t}e^{i(\omega_p+k_p z)} \\ +2i\omega_p Q^{*}\dfrac{\partial A_s}{\partial t}e^{i(\omega_p+k_p z)} - \omega_p^2 Q^{*}A_s e^{i(\omega_p+k_p z)}\end{pmatrix} \tag{A.29}$$

✓ Left-hand components.

The left-hand components can be easily derived from Eq. (A.6)

$$\nabla^2\vec{E}_s - \frac{n^2}{c^2}\frac{\partial^2\vec{E}_s}{\partial t^2} = -ik_s\frac{\partial A_s}{\partial z}e^{i(\omega_s t+k_s z)} + \frac{i\omega_s}{(c/n)^2}\frac{\partial A_s}{\partial t}e^{i(\omega_s t+k_s z)} \tag{A.30}$$

Finally by inserting Eq. (A.23) and Eq. (A.24) in Eq.(A.9.a), we obtain:

$$ik_s\frac{\partial A_s}{\partial z}e^{i(\omega_s t+k_s z)} - \frac{i\omega_s}{(c/n)^2}\frac{\partial A_s}{\partial t}e^{i(\omega_s t+k_s z)} = -\frac{\gamma}{8Q_0c^2}\left(\omega_s^2 Q A_s e^{\overbrace{i(\Omega+\omega_s)}^{\omega_p}t}\ e^{\overbrace{i(q-k_s)}^{k_p}z}\right) \tag{A.31}$$

after some simplification

$$k_s\frac{\partial A_s}{\partial z} - \frac{\omega_s}{(c/n)^2}\frac{\partial A_s}{\partial t} = -\frac{i\gamma}{8Q_0c^2}\omega_s^2 Q A_p\,, \tag{A.32}$$

then considering $k_s=2\pi n/\lambda_s$, we obtain the backward equation for the signal wave

$$\frac{\partial A_s}{\partial z} - \frac{n}{c}\frac{\partial A_s}{\partial t} = -\frac{i\gamma\omega_s}{4Q_0 nc}Q^{*}A_p\,, \tag{A.33}$$

The three couples waves are then resume using Eqs. (A.21), (A.27) and (A.33) as:

$$\begin{aligned}&\frac{\partial A_p}{\partial z} + \frac{n}{c}\frac{\partial A_p}{\partial t} = ig_{2,p}QA_s \\ &g_{2,p} = \frac{\gamma_e\,\omega_p}{4Q_0 nc}\end{aligned}, \tag{A.34.a}$$

$$\frac{\partial A_s}{\partial z}-\frac{n}{c}\frac{\partial A_s}{\partial t}=-ig_{2,s}Q^*A_p \quad , \qquad g_{2,s}=\frac{\gamma_e\,\omega_s}{4Q_0 n\,c} \tag{A.34.b}$$

$$\frac{\partial Q(z,t)}{\partial t}+\Gamma_A Q(z,t)=ig_1 A_p(z,t)A_s^*(z,t); \quad \Gamma_A=i\frac{\Omega_B^2-\Omega^2-i\Omega\Gamma_B}{2\Omega}, g_1=\frac{\gamma_e\,q^2}{8\Omega\pi} \tag{A.34.c}$$

B Acoustic field solution

Starting with the acoustic field, Laplace transformation over time applied to both Eq. (4.9b) and Eq. (4.10) leads to the Eqs. (B.1) and (B.2):

$$s\tilde{Q}(z,s)+\Gamma_A(z)\tilde{Q}(z,s)=ig_1(z)\tilde{A}_p(z,s)\tilde{A}_s^0, \tag{B.1}$$

$$\begin{aligned}\tilde{A}_p(z,s)&=A_p^0\left[-\alpha\frac{e^{-\frac{z}{V_g}s}}{s}\left(1-e^{t_0 s}\right)+\beta\frac{e^{-\frac{z}{V_g}s}}{s}\left(1-e^{-Ts}\right)+\gamma\frac{e^{\left(-\frac{z}{V_g}-T\right)s}}{s}\right],\\&=A_p^0\left[\frac{\alpha}{s}e^{-\frac{z}{V_g}s}+\frac{\beta-\alpha}{s}e^{\left(-\frac{z}{V_g}-t_0\right)s}+\frac{\gamma-\beta}{s}e^{\left(-\frac{z}{V_g}-t_0-T\right)s}\right]\end{aligned} \tag{B.2}$$

where the sign "~" denotes the Laplace transform, and s is the Laplace variable. Inserting Eq. (B.2) in Eq. (B.1), and performing the inverse Laplace transformation, the time domain solution for the acoustic amplitude is:

$$Q(z,t)=ig_1(z)\frac{A_p^0 A_s^{0*}}{\Gamma_A(z)}\left\{\begin{aligned}&\alpha\left(1-e^{-\Gamma_A(z)\left(t+t_0-\frac{z}{V_g}\right)}\right)u\left(t+t_0-\frac{z}{V_g}\right)\\&+(\beta-\alpha)\left(1-e^{-\Gamma_A(z)\left(t-\frac{z}{V_g}\right)}\right)u\left(t-\frac{z}{V_g}\right)+(\gamma-\beta)\left(1-e^{-\Gamma_A(z)\left(t-T-\frac{z}{V_g}\right)}\right)u\left(t-T-\frac{z}{V_g}\right)\end{aligned}\right\}, \tag{B.3}$$

C General solution for Signal amplitude

We first perform the Laplace transform of the right-hand term of Eq. (4.9a). Considering the following equality, $u(t-t_1)u(t-t_2)=u(t-t_1)$, valid when $t_1>t_2$, we obtain Eq. (B.4):

$$A_p(z,t)Q^*(z,t) = -ig_1(z)\frac{A_p^0 A_s^{0*}}{\Gamma_A^*(z)}$$
$$\left\{\begin{array}{l} \alpha^2 u\left(t+t_0-\frac{z}{V_g}\right)+\left(\beta\beta^*-\alpha^2\right)u\left(t-\frac{z}{V_g}\right) \\ +\left(\gamma\gamma^*-\beta\beta^*\right)u\left(t-T-\frac{z}{V_g}\right) \\ -\mathrm{e}^{-\Gamma_A^*(z)\left(t-\frac{z}{V_g}\right)}\left[\beta\left(\beta^*-\alpha\right)u\left(t-\frac{z}{V_g}\right)+\left(\gamma-\beta\right)\left(\beta^*-\alpha\right)u\left(t-T-\frac{z}{V_g}\right)\right] \\ -\mathrm{e}^{-\Gamma_A^*(z)\left(t-T\frac{z}{V_g}\right)}\left[\gamma\left(\gamma^*-\beta^*\right)u\left(t-T-\frac{z}{V_g}\right)\right] \end{array}\right\}, \quad \text{(B.4a)}$$

To continue, we first need to calculate the Laplace transform of Eq. (4.9a), which is given by:

$$\frac{\partial\tilde{a}_s(z,s)}{\partial z}-\frac{s}{V_g}\tilde{a}_s(z,s) = -i\frac{1}{2}g_2\tilde{A}_p(z,s)\tilde{Q}^*(z,s), \quad \text{(B.4b)}$$

The homogeneous part of Eq.(A.4) is readily solved and gives

$$\frac{\partial\tilde{a}_s(z,s)}{\partial z}-\frac{s}{V_g}\tilde{a}_s(z,s)=0, \quad \tilde{a}_s(z,s)=C_s(z)e^{+\frac{z}{V_g}s}, \quad \text{(B.5)}$$

where $C_s(z)$ depends on the right term of the Eq (B.4a). By inserting Eq. (B.4.a) in Eq. (B.5), we obtain:

$$\frac{\partial C_s}{\partial z}e^{+\frac{z}{V_g}s} = -i\frac{1}{2}g_2\tilde{A}_p(z,s)\tilde{Q}^*(z,s), \quad \text{(B.6)}$$

By using Eqs. (B.5) and (B.6), the Laplace transform of the signal amplitude change is given by the following expression:

$$\tilde{a}_s(z,s) = -\frac{1}{2}g_1^0 g_2\frac{\left|A_p^o\right|^2 A_s^o}{\Gamma_A^*(z)}e^{-\frac{z}{V_g}s}$$
$$\left[\begin{array}{l} \alpha^2 e^{\frac{t_0 s}{s}}+\frac{\beta\beta^*-\alpha^2}{s}+\left(\gamma\gamma^*-\beta\beta^*\right)\frac{e^{-Ts}}{s+\Gamma_A^*(z)} \\ -\frac{\beta\left(\beta^*-\alpha\right)}{s+\Gamma_A^*(z)}-\left(\gamma-\beta\right)\left(\beta^*-\alpha\right)\frac{e^{-Ts}}{s+\Gamma_A^*(z)} \\ -\gamma\left(\gamma^*-\beta^*\right)\frac{e^{-Ts}}{s+\Gamma_A^*(z)} \end{array}\right]\int g_1(z)e^{-\frac{2\Delta z}{V_g}s}dz, \quad \text{(B.7)}$$

The round-trip time $t=2\Delta z/V_g$, characteristic of the pump-signal technique is clearly visible. According to the configuration of a time-domain pump pulse coding described in Figure 4-4, we integrate the signal gain from high z values ($z_0+\Delta z$) to small z values (z_0). Then, by solving the integral of the right-hand part of Eq. B.7 we obtain:

$$\int g_1(z) e^{-\frac{2z}{V_g}s}\,dz = g_1^0 \int_{z_0+\Delta z}^{z_0} e^{-\frac{2z}{V_g}s}\,dz = -\frac{V_g g_1^0}{2}\frac{e^{-\frac{2z_0}{V_g}s}}{s}\left[1-e^{-\frac{2\Delta z}{V_g}s}\right], \tag{B.8}$$

Now let us consider that Δz is much shorter than the distance over which light propagates during the pump pulse length T and the acoustic time τ_A, Eq. (B.8) becomes

$$\int g_1(z) e^{-\frac{2z}{V_g}s}\,dz \overset{\Delta z \ll 1}{\simeq} -g_1^0 \Delta z e^{-\frac{2z_0}{V_g}s}, \tag{B.9}$$

Considering that Δz is very small and is a homogeneous segment as formerly (meaning that Ω_B remains constant) assumed, the expression for signal gain (Eq. (B.7)) in the time-domain can be read as:

$$\begin{aligned} a_s(z,t) = -\frac{1}{2\Gamma_A^*} g \left|A_p^o\right|^2 A_s^o \Delta z \\ \left\{ \begin{aligned} &\alpha^2 - \left[u\left(t-\frac{z}{V_g}\right) - u\left(t-T-\frac{2z_o-z}{V_g}\right)\right] \\ &+\left[\beta\beta^* - \beta(\beta-\alpha)\mathrm{e}^{-\Gamma_A\left(t-\frac{2z_o-z}{V_g}\right)}\right]\left[u\left(t-\frac{2z_0-z}{V_g}\right) - u\left(t-T-\frac{2z_o-z}{V_g}\right)\right] \\ &+\left[\gamma\gamma^* - \gamma\beta^*\left(1-e^{\Gamma_A^* T}\right) - \left(\alpha-\gamma^* e^{\Gamma_A^* T}\right)\mathrm{e}^{-\Gamma_A\left(t-\frac{2z_o-z}{V_g}\right)}\right] u\left(t-T-\frac{2z_o-z}{V_g}\right) \end{aligned} \right\} \end{aligned} \tag{B.10}$$

where $g = g_1^0 g_2$. The general solution for the signal amplitude and for a homogeneous long-finite segment Δz is then given by

$$
\begin{aligned}
a_s(z,t) = &-\frac{1}{4\Gamma_A^{*2}} V_g g \left|A_p^o\right|^2 A_s^o \{\Gamma_A^* \alpha^2 \frac{2\Delta z}{V_g} \\
&+\left[\Gamma_A^*\left(\beta\beta^* - \alpha^2\right)\left(t - \frac{2z_o - z}{V_g}\right) - \beta\left(\beta^* - \alpha\right)\left(1 - \mathrm{e}^{-\Gamma_A\left(t - \frac{2z_o - z}{V_g}\right)}\right)\right] u\left(t - T - \frac{2z_o - z}{V_g}\right) \\
&-\left[\begin{array}{l}\Gamma_A^*\left(\gamma\gamma^* - \beta\beta^*\right)\left(t - T - \frac{2z_o - z}{V_g}\right) \\ \quad -\left(\left(\gamma - \beta\right)\left(\beta^* - \alpha\right)e^{-\Gamma_A^* T} + \gamma\left(\gamma^* - \beta^*\right)\right)\left(1 - \mathrm{e}^{-\Gamma_A^*\left(t - \frac{2z_o - z}{V_g}\right)}\right)\end{array}\right] u\left(t - T - \frac{2z_o - z}{V_g}\right) \\
&-\left[\begin{array}{l}\Gamma_A^*\left(\beta\beta^* - \alpha^2\right)\left(t - \frac{2z_o - z + 2\Delta z}{V_g}\right) \\ \quad -\beta\left(\beta^* - \alpha\right)\left(1 - \mathrm{e}^{-\Gamma_A^*\left(t - \frac{2z_o - z + 2\Delta z}{V_g}\right)}\right)\end{array}\right] u\left(t - T - \frac{2z_o - z + 2\Delta z}{V_g}\right) \\
&-\left[\begin{array}{l}\Gamma_A^*\left(\gamma\gamma^* - \beta\beta^*\right)\left(t - T - \frac{2z_o - z + 2\Delta z}{V_g}\right) \\ \quad -\left(\left(\gamma - \beta\right)\left(\beta^* - \alpha\right)e^{-\Gamma_A^* T} + \gamma\left(\gamma^* - \beta^*\right)\right)\left(1 - \mathrm{e}^{-\Gamma_A^*\left(t - \frac{2z_o - z + 2\Delta z}{V_g}\right)}\right)\end{array}\right] u\left(t - T - \frac{2z_o - z + 2\Delta z}{V_g}\right)\}
\end{aligned}
\tag{B.11}
$$

where we neglected the offset term since the information is located in the fluctuations. In the experiments this offset is removed by an electrical low-pass filter (see Section 4.5).

Since a real fibre is a concatenation of many short segments, extending from position z_n to $z_n+\Delta z_n$, (n=0 to N, N being a natural integer), each segment with its own g_1, Ω_B and Γ_B, the appropriate solution a_s can be obtained by summing solutions, separately calculated for each of the short segments:

$$
a_s(t,z) = \sum_{n=0}^{N} a_s\left(t, z \le z_n\right) - a_s\left(t - \frac{\left[z_n + \Delta z_n\right] - z}{V_g}, z_n + \Delta z_n\right) u\left(t - \frac{z_n + \Delta z_n - z}{V_g}\right), \tag{B.12}
$$

D Impact of the coherence´s source light

The temporal coherence τ_c is the time over which the phase relationship of the light remains nearly constant. It is approximately equal to $1/\Delta\nu$, where $\Delta\nu$ is the bandwidth of the source. This implies that the spectrum of the laser must as narrow as possible to have high τ_c. To illustrate this concept, we used the pump-signal technique presented in Chapter 3 and we recorded the signal intensity in two different conditions: the signal is in and out of the Brillouin gain spectrum. Figures

here below confirm that for a coherent pump laser like a frequency-stabilized external cavity laser with a linewidth of only 23 kHz, there is no difference between the two traces when the signal is in or out of the Brillouin spectrum. In the case that the pump linewidth is large (3 MHz) the Brillouin gain is noisy resulting from the random phase shift induced by the incoherence of the distributed feedback laser (DFB).

Explanation: when the coherence time τ_c of the source laser is comparable to the acoustic lifetime τ_A, the phase of the pump will changed at the same time than that of the acoustic wave resulting to a noise signal. However if τ_c is higher that τ_A, the acoustic wave will have enough time to return to it initial phase before that the phase of the pump changes again.

(i) Laser Source: DFB laser ($\Delta\nu$~3 MHz)

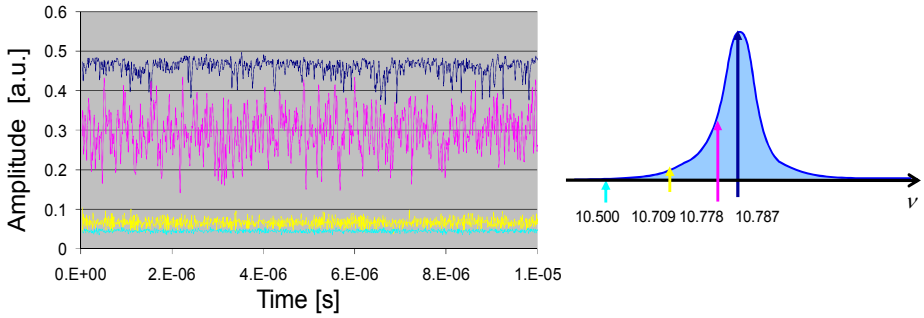

(ii) laser source: External cavity laser ($\Delta\nu$~23 kHz)

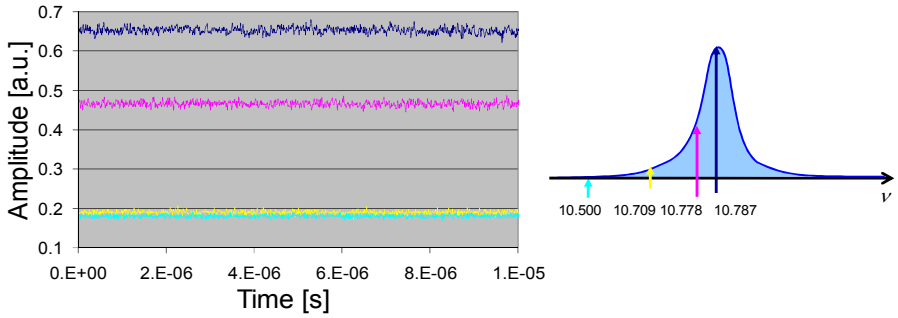

(iii) Comparison of the two pump source lasers

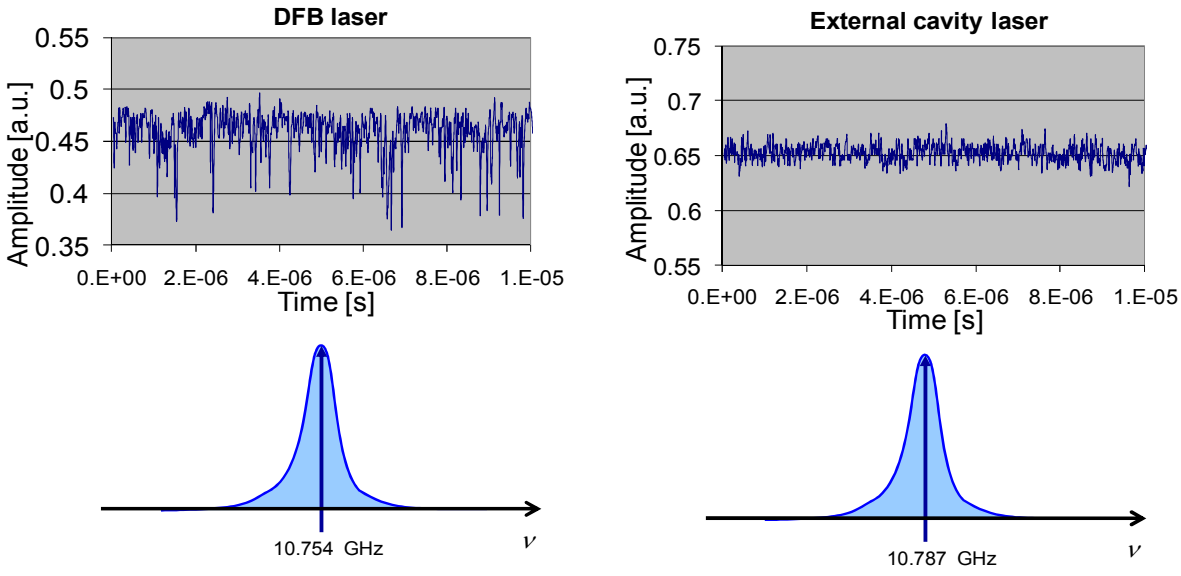

Glossary

List of acronyms and abbreviation used troughout this thesis.

Acronyms	Meaning
A/D	Analog/digital
BEDS	Brillouin Echoes Distributed Sensor
BFS	Brillouin frequency shift
BGS	Brillouin gain spectrum
BW	Bandwidth
BOCDA	Brillouin Optical Correlation Domain Analysis
BOCDR	Brillouin Optical Correlation Domain Reflectometry
BOFDA	Brillouin Optical Frequency Domain Analysis
BOTDA	Brillouin Optical Time Domain Analysis
BOTDR	Brillouin Optical Time Domain Reflectometry
BP	British Petroleum
CW	Continuous wave light
DFB	Distributed feedback
DGA	Differential Gain approach
DPP	Differential pulse-width pair
EDFA	Erbium dopped fibre amplifier
EOM	Electo-optic modulator
ETHZ	Eidgenössische Technische Hochschule Zürich "Swiss Federal Institute of Technology Zürich"
FBG	Fibre Bragg grating
FWHM	Full width at half maximum
FWM	Four wave mixing
GeO_2	Germanium oxide or Germanium dioxide
GFO	Goup For Fibre Optics
IFFT	Inverse Fast Fourrier transform
ITU	International telecommunication union
LD	Laser diode
MI	Modulation instability
NWA	Network anlyzer
OTDR	Optical time domain reflectometry
SBS	Stimulated Brillouin scattering
SFG	Sum frequency generation
SHG	Second harmonic generation
SMF	Single mode fibre
SRS	Stimulated Raman scattering
SOA	Semiconductor optical amplifier
SPM	Self-phase modulation
PCF	Photonic crystal fibre
PD	Photo-diode
PM	Polarisation maintained
SNR	Signal to noise ratio
THG	Third harmonic generation

FOALENG Mafang Stella

Rue du Valentin 21
1004 Lausanne, Suisse

+41 765264007
mfoaleng@hotmail.com

EDUCATION

2006–2011 **PhD in Photonic**
Swiss Federal Institute of Technology – Lausanne, Switzerland (**EPFL**)
Best ranking and score student paper Award at the 20th International Conference in Optical Fibre Sensors OFS in Edinburgh (2009)
Research domain: Non-linear fibre optics, distributed fibre optic sensing

2003-2006 **Master's degree in Electrical and Electronic Engineering**
Swiss Federal Institute of Technology (**EPFL**)– Lausanne, Switzerland
Thesis title: "Antenne multifréquences SSFIP intégrant des filtres"

2000-2003 **Laurea in Ingegneria dell'Informazione (equivalent to Junior Engineer)**
Università degli Studi di Perugia, Facoltà di Ingegneria – Perugia, Italy (**UNIPG**)
Thesis title: "Le techniche per guarantire la qualità del servizio su Internet"

PROFESSIONNAL EXPERIENCE AND INTERNSHIP

2006–2011 (4.1 years) **EPFL, GFO** (Group for fibre optics, Lausanne-Switzerland), **PhD ASSISTANT**

- Development of a groundbreaking technique in optical fibre sensors "Brillouin Echo Distributed Sensing (BEDS)".
- Author and co-author of more than 15 scientific publications in International conferences and meeting and 6 scientific journals papers.
- Awarded in 2009 as Best ranking and score student paper at the 20th Conference in Optical Fibre Sensors, OFS, in Edinburgh.
- Involved in 2 industrial projects and 2 European projects.
- Contribution on the study of progressive failure in the soil-structure interaction in collaboration with the geotechnical institute at ETH in Zurich.
- Contribution on the study of inhomogeneities' effect in photonic crystal fibres in collaboration at EPFL with St-Femto at Franche-Comté University.
- Teaching assistant and preparation of experimental demonstration for lectures.

2005 (2.5 months) **EPFL, LCAV,** (Audio-visual communication laboratory, Lausanne-Switzerland), **TRAINEE**

- Measuring radio propagation for wireless sensor network applications (using system PXI & Labview environment).

2004 (3 months) **PHONAK COMMUNICATIONS SYTEMS,** (R&D division Morat-Switzerland), **TRAINEE**

- Study of the possibility to replace a Hearing Aid hardware interface (HiPRO) for a miniature FM-Receiver by a high speed interface.

2002–2003 (5 months) **FACOLTÀ DI INGEGNERIA UNIPG, CASI** (Centro di Ateneo per i Servizi Informatici, Perugia-Italia).

- Part-time administrative work.

INVOLVED PROJECTS

10.2006-09.2007	• Industrial project with Ominisens SA: "High resolution distributed fibre optic sensors"
02.2006-02.2010	• COST 299 Fides:"New generation of distributed fibre optic sensors"
06.2008-06.2009	• Interreg IV: "Capteurs distribués à fibre microstructures"
2010-onwards	• Indutrial project NCCR-QP: "Extended performance in fibre optics distributed sensors using time-frequency coding"

COMPUTER SKILLS

Simulations	• Matlab, RF and microwave simulation (Ansoft Design), Labview+PXI, Pspice.
Office	• Word, Power Point, Excel, Windows (95, 98, 2000, XP, 7), Linux, Latex.
Network protocols	• Transmission control protocol (TCP), Internet protocol (IP), User datagram Protocol (UDP).

LANGUAGES

French	• Native language
English	• Good knowledge
Italian	• Fluent
German	• Basic knowledge

ACTIVITIES AND INTERESTS

- Member of the Female Scientists' Network (FSN) of EPFL, Electrical Engineering Student Association EPFL (ADELE) and of the SHARE-EPFL association.
- Worked as a repeater during 3 years for scholar integration of young students (CVAJ).
- Dance, badminton, reading scientific magazines.

PERSONAL

- Born in 1979, Cameroonian, married.

List of publications

Journals papers

1. **Foaleng S. M.**, Rodríguez F., Martin Lopez S., González Herráez M., Thévenaz L., 2011. Impact of self phase modulation on the performance of Brillouin distributed fibre sensors. Optics Letters, 36, 2:97-99.
2. **Foaleng S. M.**, Tur M., Beugnot J-C. and Thévenaz L., 2010. High spatial and spectral resolution long-range sensing using Brillouin echoes. Journal of Lightwave Technology, 28, 20:2993-3003.
3. Stiller B., **Foaleng S. M.**, Beugnot J-C., Lee M. W., Delqué M., Kudlinski A., Thévenaz L., Maillotte H. and Sylvestre T., 2010. Photonic crystal fiber mapping using Brillouin echoes distributed sensing. Optics Express, 18, 19:20136-20142.
4. Beugnot J-C., **Foaleng S. M.**, Moshe T. and Thévenaz L. General analytical model for distributed Brillouin sensors with sub-meter spatial resolution. In preparation
5. Diaz S., **Foaleng S. M.**, Lopez-Amo M., Thévenaz L., 2008. A High-Performance Optical Time-Domain Brillouin Distributed Fiber sensor" IEEE Sensors journal, 8, 7:1268-1272.
6. Beugnot J-C, Alasia D., Maillotte H., Sylvestre T., Laude V., Monteville A., Provino L., Traynor N., **Foaleng S. M.**, Thévenaz L., 2007. Complete experiment characterization of stimulated Brillouin scattering in photonic crystal fiber. Optics Express, 15, 15517-15522.

Conference papers

1. **Foaleng S. M.**, Thévenaz L., 2011. Impact of Raman scattering and modulation instability on the performances of Brillouin sensors. In procedimg of SPIE, 21st International Conference on Optical Fiber Sensors, Ottawa, Canada, 7753-226.
2. Thévenaz L., **Foaleng S. M**, Lin J., 2011. Impact of pump depletion on the determination of the Brillouin gain frequency in distributed fiber sensors. In procedimg of SPIE, 21st International Conference on Optical Fiber Sensors, Ottawa, Canada, 7753-210.
3. **Foaleng S. M.**, Rodríguez F., Martin-Lopez S., González Herráez M., Thévenaz L., 2010. Impact of self phase modulation on the performance of Brillouin distributed fibre sensors. In proceding of European Workshop in Optical fibre sensors, EWOFS, Porto, Portugal.
4. Thévenaz L., **Foaleng S. M.**, Song, K.-Y., Chin, S., Primerov, N., Beugnot, J-C. and Tur, M., 2010. Advanced Brillouin-based distributed optical fibre sensors with sub-meter scale spatial resolution. In proceding of 36th European Conference and Exhibition on Optical Communication, pp. 1-6.

5. Beugnot J.-C., Stiller B., **Foaleng S. M.**, Lee, M.W., Delque M., Kudlinski, A., Maillotte H., Laude V., Thévenaz L. and Sylvestre, T., 2010. Experimental observation of Brillouin linewidth broadening and decay time in photonic crystal fiber. In proceding of 36th European Conference and Exhibition on Optical Communication, pp. 1-3.

6. Thévenaz L., **Foaleng S. M.**, Song K.-Y., Chin, S. Primerov, N. Beugnot, J-C. and Tur M. (2010) "Advanced Brillouin-based distributed optical fibre sensors with sub-meter scale spatial resolution". In proceding of 36th European Conference and Exhibition on Optical Communication, pp. 1-6.

7. Stiller B., Beugnot J.C., **Foaleng S.M.**, Lee M.W., Delqué M., Kudlinski A., Maillotte H., Laude V., Thévenaz L., Sylvestre T., 2010. Observation of Brillouin Linewidth Broadening and Decay Time in Photonic Crystal Fiber. Fiber Optics - IEEE Photonics Society Summer Topical Meeting Series, Mexique [hal-00541831 - version 1].

8. Stiller B., Delqué M., Lee M., **Foaleng S. M.**, Beugnot J.-C., Kudlinski A., Thévenaz L., Maillotte H., Sylvestre T., 2010. Effect of inhomogeneities on backward and forward Brillouin scattering in photonic crystal fibers. Procceding SPIE - Photonic Crystal Fibers IV, Belgique [hal-00503913 - version 1].

9. **Foaleng S. M.**, Beugnot J-C. and Thévenaz, L., 2009. Optimized configuration for high resolution distributed sensing using Brillouin echoes. In proceedings of SPIE, 20th International Conference on Optical Fibre Sensors, 7503.

10. **Foaleng S. M.**, Beugnot J-C. and Thévenaz L., 2009. Optical sampling technique applied to high resolution distributed fibre sensors. In Proceedings of SPIE, 20th International Conference on Optical Fibre Sensors, 7503.

11. Iten M., Puzrin D. M. S., **Foaleng S. M.**, Beugnot J-C. and Thévenaz L., 2009. Study of progressive failure in soil using BEDS. In Proceedings of SPIE, 20th International Conference on Optical Fibre Sensors, 7503.

12. Chin S.-H., Dicaire I., Beugnot J-C., **Foaleng S. M.**, Gonzalez-Herraez M. and Thévenaz L., 2009. Experimental verification of the effect of slow light on molecular absorption. Proceedings of SPIE, 20th International Conference on Optical Fibre Sensors, 7503.

13. Chin S., Dicaire I., Beugnot J-C., **Foaleng S. M.**, Gonzalez-Herráez M. and Thévenaz L., 2009. Material slow light does not enhance Beer-Lambert absorption. In Slow and Fast Light, Technical Digest (CD), SMA3.

14. Thévenaz L., **Foaleng S. M.**, 2008. Distributed fiber sensing using Brillouin echoes. In proceding of SPIE, 19th International Conference on Optical Fibre Sensors, 7004, 70043N-4.

15. Thévenaz L., **Foaleng S. M.** and Niklès M., 2007. Fast measurement of local PMD with high spatial resolution using stimulated Brillouin scattering. In proceedings of the 33rd European Conference on Optical Communication ECOC'2007, Berlin, Germany.

16. Diaz S., **Foaleng S. M.**, Lopez-Amo M and Thévenaz L., 2007. High performance Brillouin Distributed fiber sensor. In proceedings of the 32nd European Conference on Fiber Optic Sensor EWOFS'2006, Naples, Italy.

17. Beugnot J-C, Sylvestre T., Maillotte H., Laude V., Provino L., Traynor N., **Foaleng S. M.**, Thevenaz L., 2007. Distributed measurement of Brillouin Gain Spectrum in photonic Crystal Fibre. OFMC', Teddington, UK.

Technical meeting presentations

1. **Foaleng S. M.**, Beugnot J-C. and Thévenaz L., 2009. Experimental demonstration of 5 cm spatial resolution using Brillouin echoes distributed sensing (BEDS). Technical meeting COST Action299 "FIDES"(Optical Fibers for New Challenges Facing the Information Society), Larnaca, Cyprius, April 2nd-3th.

2. Chin S.-H, Dicaire I., Beugnot J-C., **Foaleng S. M.**, Gonzalez-Herraez M. and Thévenaz L., 2009. Material Slow Light Does Not Enhance Beer-Lambert Absorption. Technical meeting COST Action 299 "FIDES"(Optical Fibers for New Challenges Facing the Information Society), Larnaca, Cyprius April 2nd-3th.

3. **Foaleng S. M.**, Beugnot J-C., Moshe T., and Thévenaz L., 2009. State of the art on Brillouin Echo Distributed Sensing (BEDS). Technical meeting COST Action 299 "FIDES"(Optical Fibers for New Challenges Facing the Information Society) Wroclaw, Poland, Sept. 9-11.

4. Beugnot J-C, Moshe T., **Foaleng S. M.** and Thévenaz L., 2009. Distributed Brillouin sensing with sub-meter spatial resolution: Modeling and Processing. Technical meeting COST Action 299 "FIDES"(Optical Fibers for New Challenges Facing the Information Society), Wroclaw, Poland, Sept. 9-11.

18. Chin S.-H., Dicaire I., Beugnot J-C, **Foaleng S. M.**, Gonzalez-Herráez M. and Thévenaz L., 2009. Effect of slow light on molecular absorption. Research Day & Photonics Day, EPFL, Oral section.

5. **Foaleng S. M.**, S-H Chin and Thévenaz L., 2007. Photonic timing + Optical storage. Science et Techniques de l'Ingénieur (STI) Seed Fund, EPFL, CH, Oct. 22nd.

Invited papers

1. Thévenaz L., **Foaleng S. M.**, Song K. Y., Chin S., Primerov N., Beugnot J-C., and Tur M., 2010. Advanced Brillouin-based Distributed Optical Fibre Sensors with Sub-Meter Scale Spatial Resolution. Proceedings of European Conference on Optical Communications, Tu.3.F.1, Torino, Italy, 19-23. Invited paper.

2. Thévenaz L., **Foaleng S. M.**, Song K.-Y., Chin S., Primerov N., Beugnot J-C., and Tur M., 2010. Advanced Brillouin-based distributed optical fibre sensors with sub-meter scale spatial resolution. In proceding of the 36th European Conference and Exhibition on Optical Communication, pp. 1-6. Invited paper.